Characterization of Ultrasound Pressure Fields, Microbubbles and Their Interaction

Camilo Perez

A dissertation

submitted in partial fulfillment of the

requirements for the degree of

Doctor of Philosophy

University of Washington

2015

Reading Committee:

Lawrence A. Crum, Co-Chair

Thomas J. Matula, Co-Chair

Andrew A. Brayman

Program Authorized to Offer Degree:

Bioengineering

University of Washington

Abstract

Characterization of Ultrasound Pressure Fields, Microbubbles and Their Interaction

Camilo Perez

Co-Chairs of the Supervisory Committee:

Dr. Thomas J. Matula

Applied Physics Laboratory

Dr. Lawrence A. Crum

Bioengineering

Ultrasound's therapeutic applications are increasing daily, and have spread in different medical fields, such as cardiology, sports medicine, urology, oncology, and even the field of cosmetics. Focused ultrasound (FUS) has shown the ability to target a millimeter-size spot inside the body without damaging intervening tissue, generate cavitation bubbles, or activate exogenous bubbles (*e.g.*, ultrasound contrast agents) to enhance therapeutic effect. Although the mechanisms by which FUS creates therapeutic effects are known to be thermal and mechanical, every modality enhances

different aspects of the mechanical or thermal effects. For this reason, it is essential to characterize the ultrasound pressure field of different clinical devices, as each one can provide insight of the physical mechanism for its therapeutic application. Ultrasound contrast agents (UCA's) are encapsulated gas bodies with a thin shell that stabilizes them, ranging in size from 1-10 μm in diameter. Their initial clinical application was for medical imaging of the heart muscle. For therapeutics, microbubbles have the potential to become drug vehicles, mechanical actuators, and cavitation nuclei inside the body to induce mechanical changes. In order to use microbubbles more effectively for both imaging and therapeutic applications, in is essential to know how the material properties of their stabilizing shells can influence their dynamical behavior and how to characterize and control their size. With newer contrast agents having loaded drugs, targeted ligands and fluorescent molecules loaded on their shell, there is a need to characterize and understand how these systems respond to ultrasound. Whether the biomedical application is imaging or therapeutically related, the aim of the research in this thesis is to understand ultrasound pressure fields and its interaction with microbubbles. I have adapted specific tools to explore these areas, including high speed imaging, fiber optic probe hydrophone, laser Doppler vibrometry, finite element modeling, and flow cytometry.

TABLE OF CONTENTS:

List of Figures

List of Tables

ACKNOWLEDGEMENTS

First of all, I would like to thank my main advisors: Drs. Thomas J. Matula and Lawrence A. Crum for giving me the opportunity to grow as a researcher and trusting my ability to do research. I would also like to thank my supervisory committee: Andrew Brayman, Lilo Pozzo, Matthew O'Donnell, Ruikang Wang, Jarred Swalwell, and Randall LeVeque for all of their time and support. In particular, I would like to thank Dr. Crum for his advice and Dr. Matula for his constant support in every single project that we tackled together, regardless of the challenges. I want to thank Dr. Andrew A. Brayman for his constant support as an academic mentor through all of my projects and for his life advice throughout my stay in CIMU. I would like to thank Drs. Yak-Nam Wang and Wayne Kreider for their support. I would also like to thank Drs. Oleg Sapozhnikov and Vera Khokhlova for their continuous help in every project. Furthermore, I would like to thank Barb Purington and Lisa Day Mercer for making me feel at home at CIMU from the very first day. I would also like to thank Brian MacConaghy for his help throughout this process. Also, thanks to Drs. Michael Bailey Tanya Khokhlova and Adam Maxwell for always being willing to answer questions or offer help with an experiment. I want to thank my collaborators in other departments: Chen-Wei Wei, Michael Lombardo, Suzie Pun, James-Kevin Tan, or in other Universities: Juan Tu, Cheng-Hui Wang, Matthew Butts, the Biolase group, and Bastien Arnal. I want to thank the Bioengineering department for giving me the opportunity to become a TA, an experience that helped me grow tremendously. I want to thank all my mentors throughout this past five years: Rusty, Bastien Arnal, Chen-Wei Wei, Hong Chen, Tong Li, Navid Farr, Juli Simon, and many other talented postdocs/students who have taught me many different aspects of research. Finally, I would like to thank my family, and friends, who have unconditionally supported me and kept me sane throughout this journey to a PhD. You are the most important part of my life.

CHAPTER 1

Introduction

1.1 Motivation

Ultrasound in medicine has been around for more than a century[1]. Whether it is for medical imaging applications or for therapeutic applications (shockwave lithotripsy, high intensity focused ultrasound, *etc.*), ultrasound is a modality that is considered inexpensive, portable and also minimally invasive[2]. Ultrasound's therapeutic applications are increasing daily, and have spread in different medical fields, such as physical therapy, sports medicine, urology, oncology, and even the field of cosmetics (*e.g.*, breaking down fat or face lift applications). The biomedical industry is starting to feel the surge of very successful companies that utilize therapeutic ultrasound for several applications and conditions, with many devices already FDA or CE approved for use in different countries.

Focused ultrasound (FUS) has shown the ability to target millimeter-size spots inside the body without damaging intervening tissue, to generate cavitation bubbles, or to activate exogenous bubbles (*e.g.*, ultrasound contrast agents) to enhance therapeutic effect. There are different modalities and several parameters that change between different treatments. Although the mechanisms by which FUS creates therapeutic effects are known to be thermal and mechanical [3], every modality enhances different aspects of the mechanical or thermal effects. For this reason, it is essential to characterize the ultrasound pressure field of different clinical devices, as each one can provide insight of the physical mechanism for its therapeutic application.

Ultrasound contrast agents (UCA's) are encapsulated gas bodies with a thin shell that stabilizes them, ranging in size from 1-10 μm in diameter. Their initial clinical application was for medical imaging of the heart muscle and chambers. For therapeutics, microbubbles have the potential to become drug vehicles, mechanical actuators, and cavitation nuclei inside the body to induce mechanical changes [4]. In order to use microbubbles (MBs) more effectively for both imaging and therapeutic applications, it is essential to know how the material properties or the shell materials can influence MB dynamical behavior and how to characterize and control their size. With newer contrast agents having drugs, targeted ligands or fluorescent molecules loaded on their shells, there is a need to characterize and understand how these systems respond to

ultrasound. Whether the biomedical application is imaging- or therapeutically-related, the aims of the research presented here are to: (1) characterize ultrasound pressure fields associated with different sources; (2) quantify how the microbubbles respond dynamically to those pressure fields, and (3) use the results to determine the mechanical properties of ultrasound contrast agent shells from those dynamical responses. I have adapted specific tools to explore these areas, including high speed imaging, finite element modeling, laser Doppler vibrometry, fiber optic probe hydrophones, and flow cytometry.

The thesis will be organized as follows: Chapter 2 will cover a thorough background of many of the topics discussed in detail in the next chapters 3-7. Those chapters are further divided into 2 main topics: The first is characterization of the ultrasound fields of clinically-available medical devices by both high speed imaging and hydrophone pressure measurements, which are covered thoroughly in Chapters 3 and 4. The second is to understand the interaction between ultrasound pressure fields and contrast agents, and to develop a tool to characterize the contrast agents, topics which are covered in chapter 5, 6 and 7. The specific work described by the thesis is detailed next, by chapter.

Chapter 3 focuses on characterizing and modeling the acoustic field of a clinical shockwave therapy device. Progress toward understanding the mechanisms of bioeffects requires accurate characterization of the parameters of ultrasound fields generated by clinical devices. Thus, while self-reported results by manufacturers are useful, independent characterization is needed. The acoustic field of a clinical portable ESWT device (Duolith SD1) was characterized. Simulations were carried out for the short standoff by matching a Khokhlov-Zabolotskaya-Kuznetzov (KZK). Chapter 3 also provides an *ex vivo* experiment using the device characterized previously (in the same chapter) as an example highlighting the importance of characterizing therapeutic fields.

Chapter 4 focuses on characterizing the acoustic field and bubble dynamics in the cavitation field of a clinical dental laser. The FDA-approved laser is used in the field of periodontics and endodontics. Therefore, a new application to use the laser photoacoustic acoustic interaction to destroy biofilm was envisioned. In order to test the idea, similarly with Chapter 3, a pressure field characterization setup and a high-speed-imaging setup to measure the bubble dynamics were developed. In addition, a model using heat and mass transfer was implemented to understand and optimize the system's response to develop an optimal laser pulse to destroy biofilm in periodontal and endodontic diseases.

Chapter 5 focuses on characterizing ultrasound contrast agents using flow cytometry. The initial version of the system is introduced and shown to be capable of characterizing custom-made protein shelled microbubbles. The properties obtained with the acoustically-adapted flow cytometer were validated with Atomic Force Microscopy techniques described in Chapter 5. Also, an overview of the system instrumentation, improvements to the system and sizing capabilities compared to the current sizing the gold standard (Coulter Counter) are performed.

Chapter 6 initially describes the transient and steady state characterization steps of the pressure field inside the modified flow cytometer system. It presents a combined measurement and model approach to validate the internal pressure. This characterization step is an improvement in the speed of the mechanical property fitting for microbubbles; for the remainder of Chapter 6 the focus is on several applications of the calibrated system: The pressure dependence of the shell mechanical properties for Optison microbubbles and harmonic analysis for different lipid and protein bubbles are presented. It is shown that the flow cytometer can detect changes in MB shell mechanical and spectral properties slight modifications in the shell. The last section in chapter 6 describes a future work application for the acoustic flow cytometer and presents some preliminary evidence and proof of concepts. The main hypothesis is that acoustic flow cytometry is an adequate tool to characterize bound targeted UCA-cell, binding rate, binding efficiency and differentiate within targeted UCA-cell and regular cell.

In Chapter 7, the focus is on the characterization of a therapeutic nano-agent for ultrasound and photoacoustics. High speed imaging and cavitation threshold characterization of a dual ultrasound/photoacoustic contrast agent is performed. The mechanism by which this therapeutic agent breaks blood clots is determined *via* high speed imaging. Significant non-linear contrast enhancement in photoacoustic molecular imaging with the agent is obtained and described. The main outcome in this chapter is that a combination of ultrasound pressure waves and a laser pulses can achieve droplet vaporization using pressures and fluences below the maximum allowed ultrasound mechanical index (FDA limitation for ultrasound imaging) and permissible optical fluence exposure, respectively. The nano-agent is fully characterized *in vitro* with dual ultrasound-laser energy activation parameter scans. Also, since the nanoemulsion acts as a microbubble when activated with both light and sound, a non-linear imaging technique for the dual ultrasound and photoacoustic contrast agent is introduced.

Finally, in Chapter 8, a summary of the work in this thesis and some reflections are provided, as well as future visions of the potential new projects and direction of the presented research and the biomedical ultrasound field.

CHAPTER 2

Background and Significance

2.1 Background

2.1.1 Therapeutic Ultrasound:

Therapeutic ultrasound has been around for longer than ultrasound imaging (since 1950), even though imaging had a much earlier clinical adoption [1]. Within the last 20 years, therapeutic ultrasound has been clinically adopted in different countries for several modalities, such as shockwave lithotripsy, extracorporeal shockwave therapy (ESWT), and pancreatic cancer ablation, and is being explored in the research field for some others such as sonothrombolysis, drug delivery, vascular calcification treatment, hyperthermia induced cancer treatments, and acoustic hemostasis [5,6].

With the development of new therapeutic devices, there are new ultrasound-guided systems, and new ways to focus the ultrasound in complicated areas such as the brain (time reversal techniques, [7,8]) or through the ribs [9]. Along with exciting applications and new research comes the extremely important concern of ultrasound pressure field characterization for safety and understanding. Previous reports of independent characterization of therapeutic ultrasound clinical devices have shown inconsistency while corroborating measurements with the reported manufacturer specifications of energy and pressure outputs [10–12]. For these reasons, characterizing and understanding the physical ultrasound parameters is essential to the successful development of new applications.

In addition, characterization of the acoustic pressure output of medical ultrasound devices is fundamental to the advance of the therapeutic field, to start understanding bioeffects that the treatment may cause, and to obtain ideas of the physical mechanism that can be causing these bioeffects[1]. In Fig. 1, two different modalities for therapeutic ultrasound treatments are compared in order to highlight the importance of thorough characterization. Although both shock wave therapy and high intensity focused ultrasound (HIFU) modalities might reach comparable peak pressure levels, they can have dramatically different effects due to the number of cycles, length of positive and negative tails, and nonlinear content present on their positive and negative cycles.

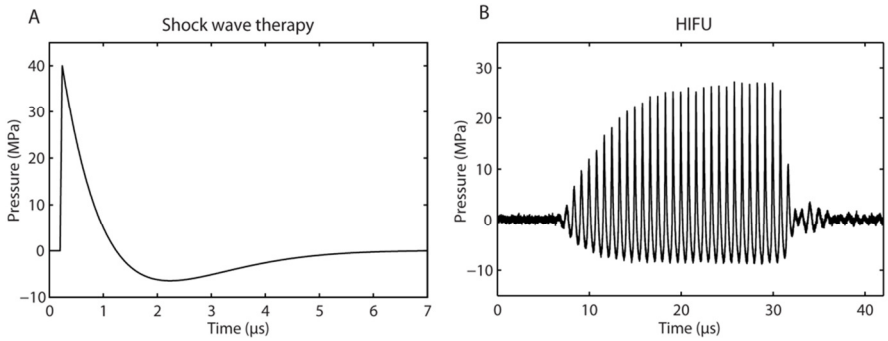

Figure 1. Comparing two modalities of therapeutic ultrasound. A) Shock wave therapy, and B) High intensity focused ultrasound (HIFU), courtesy of Wayne Kreider.

2.1.2 Challenges of Therapeutic Ultrasound: Mechanisms and Bioeffects

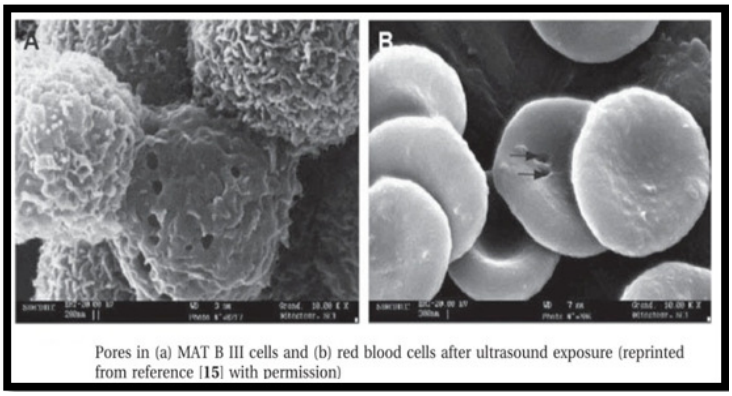

Figure 2. Effects of cavitation in proximity to cells. Figure adapted from Mehier-Humbert *et al.* [13] with permission.

There are two main challenges for therapeutic ultrasound in clinical applications. First, there is poor guidance or monitoring. It is difficult to rely on MRI or other expensive methods for monitoring, therefore there is a clear need for ultrasound guided devices. The other problem is the fear of bioeffects due to tissue motion, which brings non-targeted tissues into the focus. There are also possible bioeffects outside the focal region caused by tissue inhomogeneity, air gaps and undesired reflections have made these high intensity applications for direct tumor ablation challenging to become clinical trials.

There are well known effects of tissue damage due to therapeutic ultrasound, where tissue thermal necrosis or tissue emulsification/erosion can be observed depending on the parameters of the acoustic pressure pulse. For applications where ablation is desired, transducers are usually piezo-ceramic and operated in the frequency range between 1 - 10 MHz, using spatial average intensities in the order of 1000-10000 W/cm^2 [5,14–17]. However, this thermal bioeffect will also be accompanied with mechanical forces such as cavitation, radiation force, streaming, such as in histotripsy[18] or boiling histotripsy [19]. Another common example where cavitation is

present is shockwave lithotripsy, where the mechanical action of ultrasound comminutes the kidney stone and therefore provides a great platform and alternative treatment of certain stone sizes for clinical urologists.

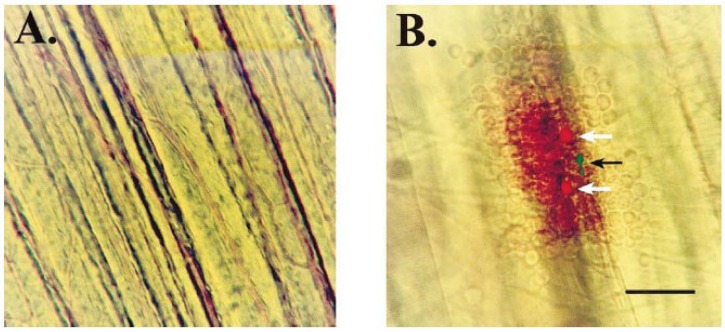

Figure 3. Microvessel rupture after ultrasound exposure in the presence of microbubbles. A) Before ultrasound, B) After ultrasound. Figure adapted from Skyba *et al.* [20] with permision

Cavitation: Acoustic cavitation occurs whenever a gas body in a fluid is acted upon by an acoustic field. Microbubbles can be induced, or pre-exist. There is an operation distinction of cavitation into 'types' that are dependent on the characteristics of the bubble growth and collapse under the influence of the acoustic field. A bubble grows during the tensile phase of an ultrasound pulse, the negative pressure. A bubble collapses during the positive pressure, bubble compression phase. This oscillation creates streaming effects with some shear rates proportional to the amplitude of the oscillations.[21]

Although it may seem insignificant, if we take an example of a bubble that is 8 µm in diameter and consider its oscillation of 2 µm in diameter then we could be talking about shear rates in the order of 10^{-7}/s, which is sufficiently strong to destroy a cell or vesicle that could be close to the bubble. This microstreaming forces in liquids are known as “small scale eddies”.[22] Inertial cavitation is caused by the increase mainly in the negative pressure of the pulse, so that it reaches a level where the bubble expands and then collapses at speeds that can reach up to 20m/s. Figure 2 shows pores created by 2.5 MHz ultrasound in MAT B cells and red blood cells after the ultrasound exposure.[13] Possible ways in which cavitation can aid drug delivery include shear forces, direct collapse from a jet formation, an increase in local temperatures, endocytosis due to bubble shell proximity to the cell membrane, and conformational changes in the proteins of the cell membrane.

The idea of noninvasive immunotherapy was proposed by cavitation studies, where the strength of the cavitation might rupture some of the cell proteins and markers, which might activate pathways to involve the immune system to provide antitumor effects.[23] Finally, one common effect that has been shown is the use of lower intensity transcutaneous ultrasound to enhance

the permeability of cells and tissues. All these effects can be produced by the adjusting of parameters mentioned above and it is critical to understand how to produce them. Figure 3 shows microvessel rupture caused by ultrasound activation of microbubbles inside small vasculature, which indicates an exogenous kind of cavitation caused by the interaction of ultrasound and the injected contrast agents. In summary, the main effects that ultrasound have in broad categories are heating of tissues, cavitation effects, and sonoporation effects.[24] As we can see from Figure 2, sonoporation is a physical method, by which ultrasound enhanced with oscillation of cavitation nuclei can open up transient pores in the membrane of cells. Although previous studies have shown that at different exposures the transient pores can remain open for a few seconds, the length of the pore formation is not well characterized.[13]

Acoustic Radiation Force: Radiation force occurs when the ultrasound wave transfers the momentum to the medium where it is propagating, generating a unidirectional force or push mechanism.[5,6] Radiation force is proportional to the absorption coefficient of the medium and to the rate of applied energy, but inversely proportional to the speed of sound of ultrasound in the wave medium, mostly due to an impedance mismatch.[5,6] Acoustic streaming has been observed to reduce heating from exposure to ultrasound through the process of increasing advective heat loss as well as increasing the mass transport of nanoparticles for improved transdermal delivery.[25] Finally, radiation force has shown to widen intracellular space by increasing the distance through shear forces. Ferrara *et al.* have demonstrated that the so called primary radiation force [25,26] is the pushing effect, and that secondary radiation force is the effect of agglomeration of particles, caused when they are flowing due to this ultrasound trap. Radiation force produced by insonation with a pressure as low as 100 kPa and a duty cycle less than 0.1% can result in rapid translation of small, highly compressible objects such as contrast agents in saline or whole blood with optimized parameters [25,26]. The acoustic field produced by a clinical transducer can cause translation of the agents away from the acoustic source.

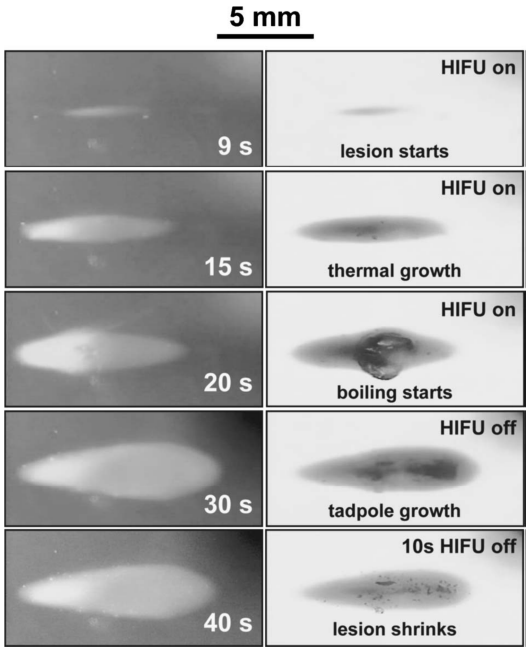

Figure 4. HIFU induced-heating stages of lesion development. Figure adapted from Khokhlova *et al.* [27] with permission.

Heating: The ultrasound heating or hyperthermia field has had several advances in the past years. Khokhlova has developed outstanding numerical methods to study the complex acoustic heating mechanism.[27] From the idea of heating tissue to the point of inducing coagulative necrosis, to the idea of raising the local temperature by only perhaps 2 or 3 degrees, the heating can also be classified between linear or nonlinear heating depending on the regime used. Figure 4 shows an example of heating lesion development as a function of time in a non-degassed gel. Destructive hyperthermia occurs when temperature is raised up to 57 ˚C for a few seconds. Nondestructive hyperthermia is gaining popularity for drug delivery since temperature is raised to between 39 and 41 ˚C, and it can activate the release of drug carriers like doxorubicin-loaded liposomes [28,29].

Such is the one used for temperature-sensitive liposomes, which are drug containers made out of lipid that open up when temperature is raised slightly from body temperature, for a controlled release at tumor site [5,30–32]. There are several mechanisms by which bubbles can cause local heating: 1) absorbing energy, converting it to heat due to damping and viscosity in the bubble and nearby 2) scattering very high frequencies that are absorbed more strongly than the transmitted US by the surrounding tissue, when a bubble is excited.[24] Although cavitation and heating are typically described as separate events, one could lead to the other depending on the pressure field and the parameters used to send the ultrasound wave.

2.1.3 Ultrasound Contrast Agents (UCA) or Microbubbles (MBs)

Ultrtasound contrast agent microbubbles are gas bubbles stabilized by a protein or lipid shell, used in diagnostic imaging typically ranging between 1 – 10 µm in diameter [33–35]. Commercially available thin phospholipid- MBs are currently used in clinical imaging. Currently, in the United States, there are only three clinically approved contrast agents by the Food and Drug administration (FDA)[36]: album-shelled Optison TM (GE Healthcare, Princeton, NJ, optisonimaging.com) approved for left ventricular opacification/endocardial border definition (LVO / EDB), lipid shelled Definity® (Lantheus Medical Imaging, N. Billerica, MA, lantheus.com) and lipid-shelled agent called Lumason® (previously known as SonoVue®, Bracco, Milan, Italy, braccoimaging.com) mainly for echocardiography applications. Outside the United States there are several other commercial agents and many other indications where the same contrast agents can be applied clinically.

For example, in Japan, surfactant-shelled Sonazoid®, Daiichi Pharmaceutical Co., LTD, Tokyo, Japan www.daiichisankyo.com (manufactured and distributed in partnership with GE Healthcare) is used to treat focal liver and breast lesions. The lipid-shelled contrast agent SonoVue® (Bracco International, Milan, Italy, braccoimaging.com) is approved in the European Union, Norway, Switzerland, China, Singapore, Hong Kong, S. Korea, Iceland, India and Canada for the following conditions: LVO/EBD, breast, liver, portal vein, extracranial carotid, peripheral arteries (macrovascular and microvascular); It is also approved in Canada for LVO/EBD and diagnostic assessment of vessels. Table 1 shows shell, gas composition and typical size for common contrast agents used world-wide.

The design and characterization of the physicochemical properties of MBs' shell are crucial because of the composition of the shell (i) provides stability during administration and circulation through the vasculature (ii) greatly affects the MBs' response to ultrasound and (iii) provides a backbone for conjugation of ligands and drugs. Besides Microbubbles (MBs) clinical use for Contrast Enhanced Ultrasound (CEUS) imaging, there are new applications for targeting and drug/gene delivery [37–39]. These gas-filled agents are coated with a thin viscoelastic albumin, lipid, or polymer shell. Characterizing the viscoelastic shell parameters is important for theorists developing bubble dynamics models, as well as manufacturers who need to understand and optimize MB stability for imaging and targeting applications.

Table 1. Commercially available UCA material, composition and size.

Name	Shell	Gas	Mean Size (μm)
Optison	Albumin	Octafluoropropane	2–4.5
Definity/Luminity	Lipid/surfactant	Octafluoropropane	1.1–3.3
Sonovue (Lumason)	Lipid	Sulfur hexafluoride	2–3
Levovist	Lipid/galactose	Air	2–4
Sonazoid	Lipid/surfactant	Decafluorobutane	—
Imagify	PLGA* polymer	Decafluorobutane	—

* **PLGA, polylactide *co*-glycolide.** Source, [40]

2.1.4 Flow Cytometry: A Tool to Characterize Microbubbles and Nanoparticles.

Flow cytometers are tools that measure cells or small particles as they pass through in a single file in a fluid stream [41]. Typically a particle or cell passes trhrough a laser interrogation region (Figure 5, below) and scatters light. With the aid of side and forward scattering detectors and optics, these devices can obtain scattering information (relative size and granularity) of different cell-types or even detect the finest change in the cell division cycle within the same type of cell[41]. Multispectral interrogation and fluorescence detectors [42] can be implemented for to analyze the presence or absence of several biological markers in cells, microbes or other particles [43,44], making cytometry a robust and appealing platform to test multiple research questions using a single tool [41]. Fig. 5 illustrates the principle of light scattering in flow cytometry (FC).

There are several tools used to characterize microbubble size and population statistics. Each one involves different physics in order to obtain size. One of the most popular is the Coulter Counter, which uses electrozone sensing (impedance electrical measurement) to obtain the size of the particle passing through a small aperture. Other tools can use light obscuration techniques and photon correlation techniques, which are also commercially available such as the Accusizer and conventional DLS, respectively. Finally, there are acoustic spectroscopy commercial devices called dynaflow, which also are able to size MB. Sizing the microbubble is essential to its characterization since size dramatically affects the MBs echogenic properties for ultrasound and harmonic imaging.[45,46] It was recently demonstrated that flow cytometers can also be used to size microbubbles [47–49].

There are several methods used to characterize average mechanical properties of the shell such us ultrasound attenuation and scattering [50–52], photomicrography (high speed imaging) [53–55], atomic force microscopy [49,51,56–58], and active light scattering [59,60]. However, there is a need for high throughput characterization for microbubbles. Out of these methods, light scattering is

the only method that allows high throughput measurements. With a flow cytometer (Fig. 5), the bubble size, dynamical response and shell properties can be obtained [48,49]. For these reasons, flow cytometry is a suitable platform for characterizing microbubbles. There are several studies that have investigated MB characterization in flow cytometry as a powerful tool.[47–49]

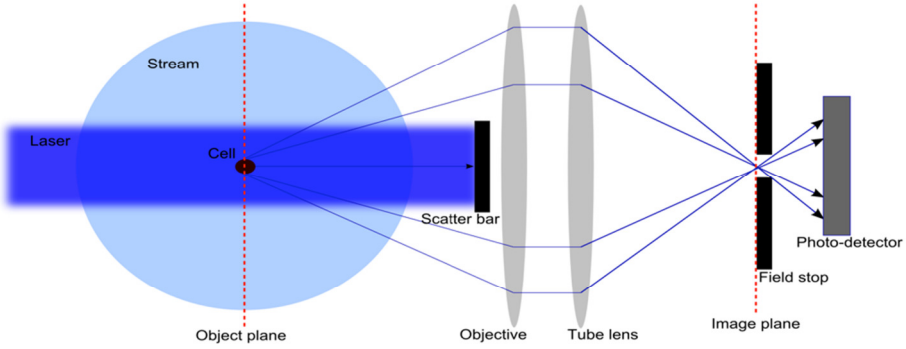

Figure 5. Principle of flow cytometry: Particles such as cells or bubbles travel in a stream (into the page) and are individually interrogated by a laser beam which causes scattering at all angles. These scattering can be collected at 0 and 90 degrees by photomultiplier tubes (PMT's). Courtesy of Jarred Swalwell.

2.2 Significance and Innovation

Characterizing the pressure and cavitation fields of medical devices provides a better understanding of the physical mechanisms of therapeutic ultrasound induced bioeffects. In addition, independent machine characterization of medical devices highlights the need of proper ultrasound metrology for new devices available in the clinic. This thesis uses several methods, tools and algorithms to perform proper acoustic and high speed imaging characterization of therapeutic ultrasound clinical devices. With proper metrology, relevant clinical results can be linked to particular features of the different modalities in therapeutic ultrasound, thus helping advance the field's knowledge. Finally, the models developed to validate the measurements are important tools to optimize the treatments and to predict the acoustic pressure field *in vivo*, where the measurements are not possible.

Characterizing ultrasound contrast agents' (microbubbles) can also improve current contrast enhanced ultrasound imaging detection techniques and understanding of the agent's response to different ultrasound pressure fields. Developing a platform where contrast agents of different shell materials, loadings, and fluorescent markers can be analyzed, sized and resolved at a high throughput provides an all-in-one tool for advancing physical characterization and understanding of contrast agents. In addition, it also provides a new avenue for pharmaceutical

industries interesting in attaching drugs or molecules into contrast agents and quickly assesses, confirm and characterize their binding and response. The acoustically adapted flow cytometer has the potential to be a stand-alone tool to characterize loaded ultrasound contrast agents in the fields of molecular imaging and drug delivery.

CHAPTER 3

Acoustic Field Characterization of the Duolith: Measurements and Modeling of a Clinical Shockwave Therapy Device.

3.1 Introduction

Extracorporeal shock wave therapy (ESWT, or SWT) is a noninvasive technology used to treat several musculoskeletal disorders, including chronic plantar fasciitis,[61,62] tendonitis of the shoulder,[63] lateral epicondylitis,[64,65] achilles tendinopathy,[66,67], nonunion of fractures of long bones[68], and even cardiac conditions such as ischemic heart disease (IHD)[69–73]. Therapeutic bioeffects induced by ESWT include angiogenesis,[74–76] osteogenesis,[77–79] and antinociceptive effects.[79–81] Several studies suggest that ESWT is associated with up-regulation of proteins like vessel endothelial growth factor (VEGF),[75,76] bone morphogenic protein (BMP),[77,78,82] osteogenic protein (OP),[77,78] and nitride oxide synthases (NOS) in multiple tissues,[80,81] and these might activate pathways to induce beneficial bioeffects.[78,81] Although some of these bioeffects have been identified, the actual physical mechanisms of ultrasound action on bones and surrounding tissues in ESWT remain unknown. The problem is exacerbated from clinical reporting of ESWT effects. Clinical studies often do not report acoustic parameters and treatment protocols used for trials, which may lead to conflicting therapeutic interpretations.

Progress toward understanding the mechanisms of bioeffects requires accurate characterization of the parameters of ultrasound fields generated by clinical devices. ESWT devices include electromagnetic, electrohydraulic, ballistic, and piezoelectric sources.

[A] Work published in part in:
C Perez, H Chen, TJ Matula, M Karzova, VA Khokhlova Acoustic field characterization of the Duolith: measurements and modeling of a clinical shock wave therapy device. The Journal of the Acoustical Society of America 134 (2), 1663-1674
C Perez, H Chen, TJ Matula, Characterization of the acoustic field of a clinical electromagnetic shockwave therapy device. The Journal of the Acoustical Society of America 129 (4), 2679-2679
H Chen**, C Perez**, TJ Matula, High speed imaging of shockwave-induced dynamics of cavitation bubbles and vessel wall. The Journal of the Acoustical Society of America 129 (4), 2374-2374
Nazer B, Ghahghaie F, Kashima R, Khokhlova T, **Perez C**, Crum L, Matula T, Hata A. Therapeutic Ultrasound Promotes Reperfusion and Angiogenesis in a Rat Model of Peripheral Disease. Circ J 2015;

The acoustic output from similar devices used for shockwave lithotripsy have been measured,[83–85] but independent measurements of clinical ESWT devices have not been done for several machines that are commercially available. In one independent study, Chitnis and Cleveland reported that the electrohydraulic source of the Equitron/Evotron system produces an output that does not change by varying device settings.[11]A second publication by the same group showed that the ballistic source of the same system generates a wave that does not resemble a shock front.[12] Thus, while self-reported results by manufacturers are useful, independent characterization is needed. Towards that goal, the acoustic field generated by the electromagnetic therapy head of the Duolith SD1 T-Top (Storz Medical AG, Tägerwilen, Switzerland) was characterized.

The Duolith SD1 T-Top device has dual modes of operation, one called “focused shockwave therapy” (focused electromagnetic head), and the other “radial shockwave therapy” (ballistic head). The focused therapy head is composed of a cylindrical coil and a parabolic reflector. A coil excites a cylindrical membrane, which generates a wave that is focused, similar to lithotripsy spark sources, by a parabolic reflector.[86] The ballistic source consists of an air-pressure driven projectile that impacts a metallic applicator and distributes a pressure wave when contacted against the treatment area. Some studies have addressed clinical aspects such as efficacy and safety of the focused head,[87–91] but to my knowledge, no independent studies of the acoustic output at various machine settings, measured or modeled, have been published.

Treatment parameters for ESWT range from low energy to high energy settings, comparable to the higher levels reached by the measured device.[92–97] ESWT treatment parameters for the Duolith SD1 reported in the literature span several output settings. High nominal levels of 43 MPa have been used for studies that explored the potential of shockwaves to remove calculi and biofilms,[88] and for case reports on the treatment of pseudoarthrosis[82,98] Lower settings are more common with more recent studies: A nominal level of 25 MPa was used in studies of chronic pelvic pain syndrome,[90,91] systemic sclerosis,[89] and Peyronie’s disease.[99] Nominal levels of 14 MPa to 31 MPa were used to explore shockwave treatment for tibial stress syndrome in athletes.[100] The Duolith SD1 at lower settings was recently used by our group in an *in vivo study* to demonstrate the promotion of angiogenesis and reperfusion after ESWT and focused ultrasound treatments in a rat model of peripheral arterial disease [101].

Characterization of the fields produced by medical devices is usually performed in water and then the results are translated (derated) into tissue, where direct measurements are difficult or impossible. In recent studies, numerical modeling combined with measurements has been actively used to characterize acoustics fields from high-power ultrasound medical devices. Simulation data based on the nonlinear parabolic Khokhlov-Zabolotskaya-Kuznetzov (KZK) type equation that accounts for effects of nonlinearity, diffraction, and absorption in ultrasound beams has been shown to agree well with experimental data. This model has been applied to predict acoustic fields of lithotripters, unfocused transducers, diagnostic ultrasound probes, and high intensity focused ultrasound (HIFU) sources.[102–106] It has been also shown that a critical component for accurate simulations is to define a boundary condition for the model using actual data, obtained from the measurements for that particular device.[39,41,43] Following this approach, modeling was combined with measurements to characterize the nonlinear ultrasound fields generated by the Duolith SD1 electromagnetic head.

3.2 Materials and Methods

3.2.1 Experimental Arrangement.

Measurements were performed on the portable Duolith SD1 T-Top ESWT device (Storz Medical AG, Tägerwilen, Switzerland). The device output has a number of settings, some of which are shown in Table 2. The machine pulse repetition frequency (PRF) ranges from 1 to 8 Hz (in the higher output settings it can only go up to 3 or 4 Hz, depending on the setting). The electromagnetic source provides two different standoffs that require an oil bag attachment as a film coupling to the membrane of the therapy head with lengths of 15 or 30 mm, respectively (Fig. 6). The other therapy head is a ballistic source advertised as a radial shockwave, respectively pressure wave source. The ballistic head has an applicator/transmitter with a diameter of 15 mm, but a number of other transmitters are available. It uses compressed air to fire a projectile against the tip of the applicator, generating a pressure pulse, and can operate at a PRF of 1-21 Hz. A full characterization of a different ballistic head (EMS Swiss Dolorclast Vet) has previously been performed,[12] thus we devote the majority of this work to the focused electromagnetic therapy heads.

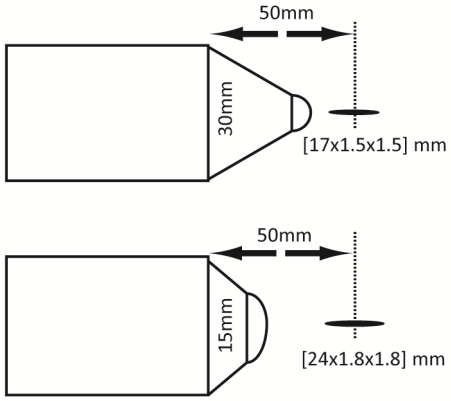

Figure 6. Electromagnetic treatment heads. The -3dB focal zone is shown for the 30 mm (top) and 15 mm (bottom) standoff. The focal dimensions shown were obtained from measurements.

Figure 7 displays the experimental setup: A computer-controlled 3D positioning system (Velmex NF90, Bloomfield, NY) was used to move a fiber optic probe hydrophone (FOPH 2000, RP Acoustics, Germany) for field mapping. The fiber tip was 100 µm in diameter. The step-size increment was 0.5 mm. Alignment of the FOPH to the acoustic field was done by performing a raster scan in two separate planes: One plane intersected the acoustic axis at the focus, with the maximum pressure at the center. The other plane was distal to the first. The beam axis was found as a line crossing the pressure maxima of the two planes. The FOPH was positioned parallel to the axis.

The treatment heads (electromagnetic or ballistic) were located outside the water bath (31 cm long × 18 cm deep × 18 cm wide, maximum degassed level 8% O_2, at room temperature). They were coupled to the bath *via* a Tegaderm (3M, MN, USA) window on one end of the bath and coupling gel. Care was taken to ensure that there were no visible bubbles in the contact area. The bath was large enough to avoid interference from reflections.

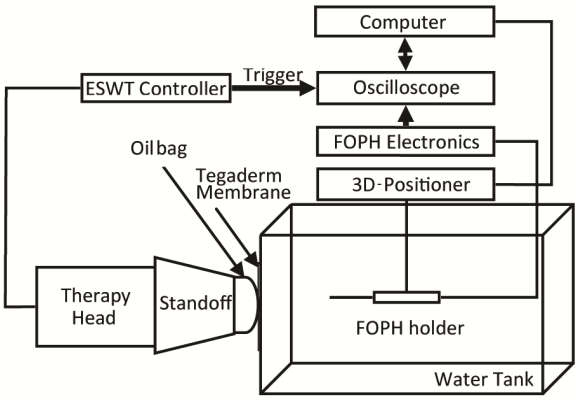

Figure 7. Illustration of experimental setup for the electromagnetic source.

3.2.2 Measurement Protocols and Pulse Definitions

The fiber optic hydrophone (FOPH 2000, RPI Acoustics, Germany) was originally developed specifically as a tool for shockwave measurements.[107] It was also used to measure the field generated by the ballistic source because it is calibrated even at lower frequencies (down to 100 kHz) and provides a broadband (up to 100 MHz) frequency response. An equi-potential discharge pin located on the back of the Duolith was used as a reliable trigger. The FOPH signals were digitized by an oscilloscope (LT344 Waverunner, LeCroy, NY) at 500 MSamples/s. The FOPH 2000 software CALDEC was used to calculate pressure values from the oscilloscope data and to deconvolve the signal to account for the frequency response of the system.[107] Data collection was automated using LabVIEW (National Instruments, Austin, TX).

Acoustic parameters for pressure waveforms associated with the focused electromagnetic source are illustrated in Fig. 8. Peak positive (p^+) or negative (p^-) pressure corresponds to the maximum or minimum pressure value in the pulse. Compression phase duration (t_{p+}) is defined as the length of time between zero crossings for the positive pressure, while tensile phase duration (t_{p-}) is equivalently defined for the rarefaction phase. There is a secondary pulse (characteristic of electromagnetic sources) with a peak pressure p_2^+ and duration t_{t+}. The energy flux density for a pulse was calculated by computing the pulse intensity integral (PII) based on the International Electrical Commission (IEC) standard for shockwave lithotripsy[108] defined as the integral of the intensity over the duration of the entire temporal waveform between time points where the pulse first and last reaches 10% of its maximum pressure value.

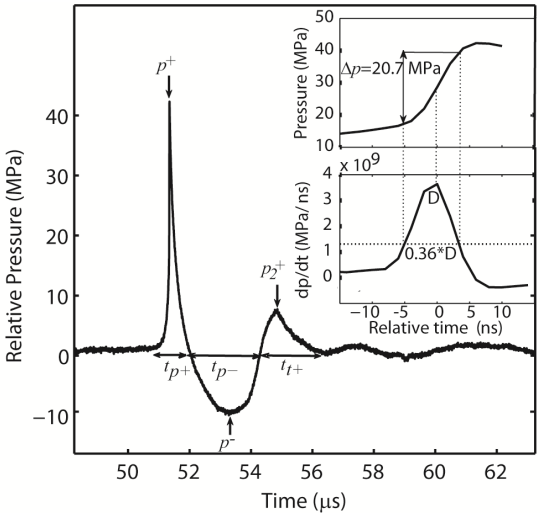

Figure 8. Characteristic pulse at the focus. Typical averaged pressure waveform (25 averages) at the focus (15 mm from the long standoff) at the maximum output setting of the Duolith SD1 T-Top. Inset: Close up of the pulse front of the waveform (top) and its time derivative (bottom).

The rise time of the main pulse at the focus, t_{rt}, was defined from the time derivative of the pulse profile (see Fig. 8 inset). It is given by the duration of the derivative at 0.36 of the maximum derivative value. This definition of the rise time, which corresponds to the steepest region of the front, was recently proposed from laboratory-scale sonic boom studies to characterize shock structures of spark-generated pulses propagating in air.[109,110] The definition is equivalent to the classical definition (time needed for the pressure at the shock of the amplitude A_s to increase from $0.1 \cdot A_s$ to $0.9 \cdot A_s$) for shocks governed by the stationary solution of the Burgers equation: [111]

$$p(\tau) = \frac{A_s}{2}\left\{1+\tanh\left(\frac{\beta A_s}{2b}\tau\right)\right\} = \frac{A_s}{2}\left\{1+\tanh\left(\frac{\tau}{\tau_0}\right)\right\}, \qquad (3.1)$$

where p is the acoustic pressure, $\tau = t - z/c$ is the retarded time, z is the propagation distance, c is the propagation speed of the shock, the parameter τ_0 is introduced as $\tau_0 = 2b/\beta A_s$ β is the coefficient of nonlinearity of the propagation medium, and b is the thermoviscous absorption of the medium. Classical weak shocks, Eqn (3.1), with short rise times form when high amplitude acoustic waves propagate in a nonlinear thermoviscous medium.[111] Nonlinear effects tend to steepen the shock, while thermoviscous effects of energy absorption at the shock tend to smoothen it. The balance of these two effects creates a shock of quasi stationary thickness, inversely proportional to the shock amplitude. The 10% to 90% rise time of the pressure Δp at the shock in Eqn (3.1) is the length of time for the function $\tanh(\tau/\tau_0)$ to change from -0.8 to 0.8, and is equal to $2.2 \cdot \tau_0$. The time derivative of Eqn (3.1) is $\partial p/\partial\tau = A_s/2\tau_0 \cdot \cosh^{-2}(\tau/\tau_0) = A_s/2\tau_0 \cdot \left(1-\tanh^2(\tau/\tau_0)\right)$. It is equal to 0.36 of the maximum value of the derivative when $\tanh(\tau/\tau_0)$ is equal to plus or minus 0.8. For a stationary shock such as governed by Eqn (3.1), these two definitions are equivalent. In estimating the rise time of the experimental waveforms (Fig. 8), the definition based on the time derivative is more accurate, as it rejects the smooth “pedestal” rise that precedes the sharp pressure jump; this pedestal is often in excess of 10% of the shock front amplitude. The presence of the pedestal in the focal waveform is typical for electromagnetic sources and leads to overestimation of the rise time if it is defined from 10% to 90% of the peak positive pressure (shock amplitude). On the contrary, the time derivative definition leads to an estimate for the characteristic time width of the steepest part of the shock front. For example, in water $c = 1486$ m/c, $\beta = 3.5$, and $b = 4.33 \cdot 10^{-3}$ kg·s^{-1}·m^{-1}; $\Delta p = 0.8 \cdot p^+ \approx 20$ MPa (see inset to Fig. 8). If a shock front is formed with $p^+ = 25$ MPa, and its steepness is balanced by nonlinear and thermoviscous effects, the theoretical rise time would be about 0.27 ns.

3.2.3 Numerical Model and Experimental Data Processing for the Model.

Numerical modeling of the nonlinear propagation of focused acoustic pulses generated by the electromagnetic source in water was performed using the KZK nonlinear parabolic equation:

$$\frac{\partial}{\partial\tau}\left(\frac{\partial p}{\partial z}-\frac{\beta}{\rho_0 c_0^3}p\frac{\partial p}{\partial\tau}-\frac{b}{2\rho_0 c_0^3}\frac{\partial^2 p}{\partial\tau^2}\right)=\frac{c_0}{2}\left(\frac{\partial^2 p}{\partial r^2}+\frac{1}{r}\frac{\partial p}{\partial r}\right). \quad (3.2)$$

Here r is the radial distance from the beam axis, c_0 is the ambient sound speed, ρ_0 is the density in water, and other variables are the same as used in Eqn (3.1). The equation accounts for the combined effects of nonlinearity, diffraction, and weak thermoviscous absorption in water. The key component for using Eqn (3.2) to simulate the experiment was to set a boundary condition for the model. The most accurate way is to obtain the boundary condition directly from measurements.[102,104,106]

To set a boundary condition at some initial plane, pressure waveforms were measured radially in a plane as close to the therapy head as possible for the existing experimental arrangement, which was approximately 5 mm from the short standoff. A total of 71 waveforms (each an average of 20 individual waveforms) was measured in increments of 0.2 mm radially away from the axis of the beam up to 14 mm. Signals were sampled at 500 MSample/s. Radial symmetry was assumed after initial experiments (not shown) confirmed that the field emitted from the device was symmetric. Measurements of waveforms were carried out up to 14 mm from the beam axis; measurements at longer distances from the axis were not obtained because of low signal-to-noise levels. Representative examples of averaged waveforms collected from the experiment, along with the model fits, are shown in Figs. 9. To facilitate the modeling effort by reducing the noise level in the measured signal, each experimental waveform was further numerically smoothed 3 times over 5 points in the region around the maximum peak positive pressure (within 1.25 μs) and 3 times over 30 points in the other smoother parts of the pulse.

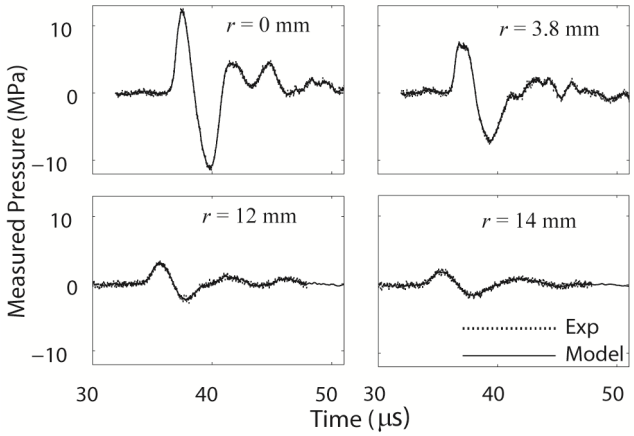

Figure 9. Waveforms comparison from short standoff. Selected radial scan averaged waveforms collected from the measurements in a plane 5 mm from the short standoff, along with simulation fit from model.

The general properties of the solution to the KZK equation assumes that the time integral over the pulse is equal to zero, as the zero frequency component in the FFT series expansion of the signal is eliminated by diffraction. To ensure that the pulses used for the boundary condition satisfy this requirement, a tail of Δt = 30 μs duration was added at the end of each pulse as:

$$p(t) = p_1 \cos^2(\pi t/2\Delta t) - (p_1 + \frac{2S}{\Delta t})\sin^2(\pi t/2\Delta t) \qquad (3.3)$$

Here p_1 is the pressure value at the last measured time point of each waveform, t is the time counted from this last point, S is the integral over the averaged waveform. The absolute value of the maximum pressure in the tail did not exceed 1.6 MPa, *i.e.* it was of the same order as the level of noise in the measured waveforms (± 0.7 MPa). To account for non-measured waveforms in the radial scan from 14 mm to 20 mm from the axis, additional waveforms were numerically introduced in the boundary condition by taking the very last radial waveform at 14 mm and exponentially decreasing its amplitude along the radial coordinate with a linear time delay that followed the overall geometry of the measured field. The radial step in the numerical modeling was refined by adding 36 waveforms in between each two experimental waveforms in the neighboring spatial points with linear interpolation of pressure for each time point. The boundary condition map for the modeling algorithm is shown in Fig. 10, where every vertical line depicts a pressure waveform at a certain radial distance from the beam axis.

The KZK equation (Eqn 3.2) with the boundary condition described above was simulated using an algorithm previously described in detail.[112–114] A method of fractional steps with an operator splitting procedure was used to march the solution over the axial coordinate z. A combined time and frequency domain solution was used. The effect of diffraction was calculated in the

frequency domain for each harmonic using a finite-difference implicit backward algorithm at shorter distances from the initial plane (up to 4.4 mm) and then using the Crank–Nicholson algorithm. Absorption was also calculated in the frequency domain using the exact solution for each harmonic. Nonlinear effects were calculated in the time domain using a Godunov-type scheme. Transition between the spectral and time domains was performed using the fast Fourier transform. Simulations were run in water with physical parameters introduced earlier in this section. The parameters for the modeling were: 16384 harmonics, 32768 time-steps, 65.5 μs time window, 2 ns time step, 43.2 mm radial window, 8000 radial grid points, 5.4 μm radial step, and 0.11 mm axial step.

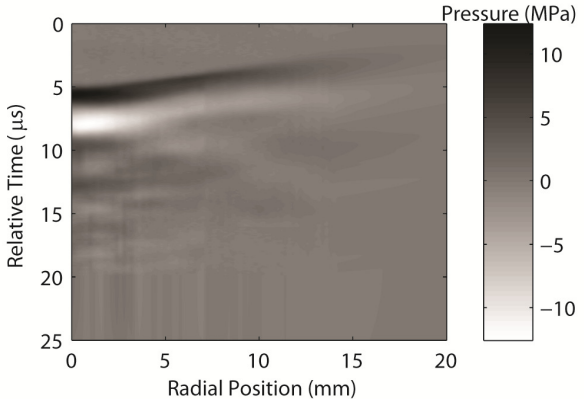

Figure 10. Boundary condition map for the modeling algorithm. Experimental pressure waveforms were measured 5 mm from the short standoff along the radial (transverse) coordinate out to 14 mm. Waveforms are represented by vertical lines; pressure is shown as in grey scale; The time axis is relative to the time in Fig. 9 where the "0" corresponds to a time shift by 32 microseconds from the data in Fig. 9

3.3 Results and Discussion

Experimental results were obtained for the long and short standoffs. Given the relatively small difference between the measured fields from different standoffs, numerical simulations are provided only for the short standoff.

Measurements of individual waveforms were used to present the results with means and standard deviations. However, in many cases, to reduce noise levels for figure presentation or for collecting boundary condition waveforms, waveform averages were used. It was thus important to determine whether or not the waveform average affected the actual peak amplitudes or rise times. The peak amplitudes and rise times of an averaged pulse were compared to those of an individual pulse. The averaged amplitude was at most 1.2% lower than the peak amplitude of an individual pulse and no difference in rise times was observed; this can be explained by two factors. First, the electromagnetic source is stable, much more stable than an electrohydraulic source. Second, the FOPH is band-limited at 100 MHz, therefore the

measured rise time was most probably overestimated and limited by the hydrophone bandwidth in both cases. It is further instructive to examine the jitter by taking the time derivative of each individual pulse and computing the time difference between the maxima of the resulting derivative. The maximum jitter at the highest output setting of the machine was on the order of 5 ns.

A typical (averaged) waveform measured at the focus (15 mm from the long standoff) at the highest output setting of the machine (#7, Table 2), is displayed in Fig. 8. This characteristic waveform has a rapid rise in positive pressure, followed by a negative tail, and then a second trailing pulse that is characteristic of electromagnetic shockwave devices.[86] The measured peak positive pressure in the pulse is p^+= 42.3 MPa (for the individual pulses, p^+= 42.7 ± 1.2 MPa); the positive phase lasts about 1 µs (t_{p+}) for the highest machine setting (#7, Table 2) and 1.4 µs for the lowest setting (#1, Table 2). The negative tail has a peak amplitude of p^-=-9.9 MPa (for the individual pulses, p^-= -9.9 ± 0.24 MPa) and lasts 2.2 µs (t_{p-}) for the highest setting and 1.8 µs for the lowest setting. The secondary pulse has a peak positive pressure of p_2^+= 7.0 ± 0.4 MPa. The ratio of the tensile tail length to the positive tail length (t_{p-}/t_{p+}) increases from 1.2 to 2.1 with increasing machine output setting and the pressure ratio between peak positive and peak negative pressures (p^+/ p^-) increases from 0.8 to 4.3 with increasing machine output setting. The secondary pulse becomes a significant fraction of the maximum peak pressure (p_2^+/ p^+) as the energy setting of the machine decreases, ranging from about 17% of the peak positive pressure at the highest output setting (#7, Table 2) to almost 62% at the lowest machine output setting (#1, Table 2). The length of the secondary pulse t_{t+} decreases as the machine setting decreases from 1.4 µs to 0.8 µs.

Table 2 lists a few of the device settings, and the corresponding measured peak positive and negative pressures at the focus, as well as calculated energy densities (pulse intensity integral) from the measured waveforms (the energy density is a common parameter found in ESWT literature). In addition, the measured (averaged) waveforms at the focus for all machine settings are shown in Fig. 11. Three particular waveforms are also displayed in the inset, corresponding to high, medium, and low output settings (bold curves in Fig. 11). The results of the measurements show that the peak positive pressures and energy densities are not in quantitative agreement with the manufacturer machine settings.

Table 2. Selected output settings of the Duolith SD1 discussed throughout the results and discussion sections.

Nominal Settings***			Measured Parameters, 30 mm Standoff				Measured Parameters, 15 mm Standoff			
#	p^+, MPa	ED, mJ/mm^2	p^+, MPa	p^-, MPa	p-to-p, MPa	ED, mJ/mm^2	p^+, MPa	p^-, MPa	p-to-p, MPa	ED, mJ/mm^2
1	3	0.01	1.8	-2.3	4.1	0.01	2.1	-2.0	4.1	0.01
2	10	0.07	5.7	-5.0	10.7	0.04	5.7	-4.7	10.4	0.03
3	31	0.3	17.5	-8.0	25.5	0.12	17.4	-7.3	24.7	0.11
4	36	0.35	20.3	-8.3	28.6	0.13	19.5	-7.7	27.2	0.13
5	51	0.45	29.9	-9.2	39.1	0.19	26.3	-8.6	34.9	0.17
6	56	0.5	35.8	-9.5	45.3	0.21	30.8	-8.9	39.7	0.19
7	62	0.55	42.7	-9.9	52.6	0.23	39	-9.3	48.3	0.22

*** According to the manufacturer, in-house measurements were done without the coupling cone.

The inset waveforms (Fig. 11) also illustrate the fact that the secondary pulse becomes relatively more important as the machine setting is lowered. That is, the ratios of the second positive peak to the first peak for the settings #7, #3, and #2 from Table 2 are 17, 37, and 62% respectively; corresponding waveforms are shown in Fig. 11a, b, and c. At the low settings, the device essentially delivers a low-amplitude double pulse. The ratio of the peak positive to the peak negative pressure, on the other hand, decreased from 4.3 at the highest machine output setting to 0.8 for the lowest setting.

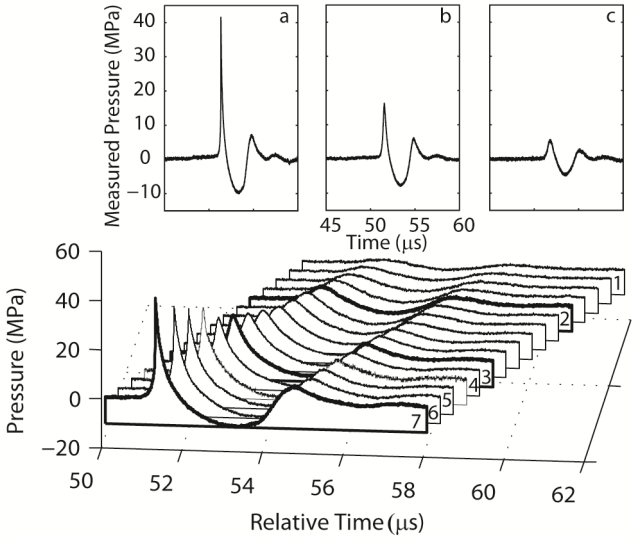

Figure 11. Waterfall plot for all machine output settings from the long standoff. Inset displays averaged waveforms for three different machine settings indicated as dark lines in the waterfall plot. a) Setting #7 of 62 MPa nominal peak positive pressure; b) setting #3 of 31 MPa; c) setting #2 of 10 MPa.

Returning to Fig. 8, the rise time in the experimental waveform was estimated at 8 ns. It was determined by the width of the derivative of the pressure waveform at a level of 0.36 from its maximum value (see discussion in section IIB). This is illustrated in the inset of Fig. 8, where a rapid pressure jump of about 25 MPa at the pulse front occurs. For this setting, the value of 8 ns is over an order of magnitude greater than the theoretical rise time for a shock front of the same amplitude defined from the hyperbolic tangent solution of the Burgers equation (0.27 ns). It was not possible to determine from measurements whether or not the true rise time in the pulse was overestimated because of the limited 100 MHz bandwidth of the FOPH that can provide time resolution of about 10 ns. Thus, it was not possible to determine whether the true weak shock was present in the waveform. This issue is examined further in the discussion section, where numerical modeling was used to show that the waveform was indeed not yet shocked.

3.3.1 Axial and Radial Scans

Axial scans for both the short and long standoffs at the machine's highest output (#7) are displayed in Fig. 12. The axial scans show a clear positive peak corresponding to the focus of the short or long therapy head (the tips of the standoffs are illustrated by the dashed vertical lines). For the short standoff, the spatial maximum for the peak negative pressure is almost 20 mm closer to the standoff than for the peak positive pressure. For the long standoff, there is only the hint of a peak near -9 mm. The peak negative pressure is higher pre-focally than post focally, and not as symmetric as the peak positive pressure along the axis. To prevent damage to the FOPH, the tip was never brought into contact with the standoff. Thus, there is some uncertainty in the exact location of the tip of the therapy head membrane with respect to the focus (the position represented by the dashed lines in Fig. 12), by as much as ± 1.5 mm.

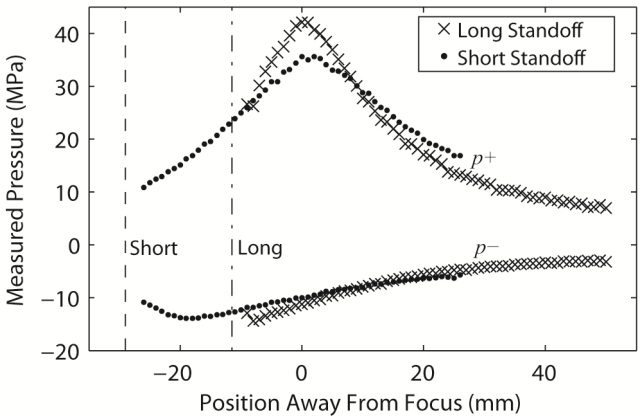

Figure 12. Long standoff vs. short standoff pressure differences away from focus. Axial scans along the beam axis for the focused source using 30 mm and 15 mm standoffs with a 1 mm step-size and 20 averages per location. Measurements include p^+ and p^-. "Short" and "Long" correspond to the position of the tips of the short and long standoffs, respectively. The distance between standoff tips is 15 mm.

A comparison of measurement and modeling results along the axis of the *short* standoff is shown in Fig. 13. The simulation results are in good agreement with the experimental data. There appears to be a systematic shift that biases the simulation to slightly more negative values than the data for peak negative pressures, but the discrepancies are all within experimental error. A comparison of actual waveforms at different distances from the short standoff (along the beam axis) is provided Fig. 14. There is excellent agreement between the measured and modeled axial waveforms, where again, the simulations predict a slightly more negative peak pressure.

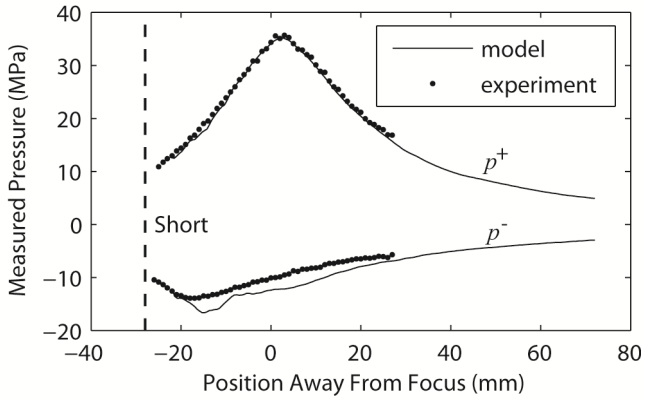

Figure 13. Comparison measured vs. modeled pressures for short standoff. Axial distribution of the averaged peak positive and peak negative pressures measured for the short standoff (black circles) and compared to the modeling results (solid lines) at the highest machine output setting (#7, 62 MPa). ”Short” corresponds to the position of the therapy head edge of the short standoff.

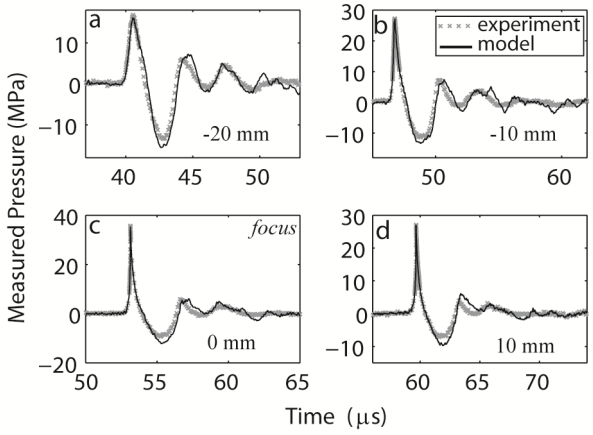

Figure 14. Waveform comparison from short standoff at different distances from focus. Axial waveform measured and modeled for the short standoff at the distances -20 mm (a), -10 mm (b), 0 mm (c, the focus), and 10 mm (d) away from focus at the highest machine output setting (#7, 62 MPa). The experimental waveform was averaged over 25 individual waveforms in order to reduce the noise level.

The radial (transverse) scans for both long (a and c) and short (b and d) standoffs (at setting #7, Table 2) in the focal plane are shown in Fig. 15. For the short standoff, the corresponding simulation results are also shown (represented by the solid line in Fig. 15b and d). The modeling

results are in excellent agreement with the measurements, but the simulations again predict a slightly more negative peak pressure (absolute values are shown).

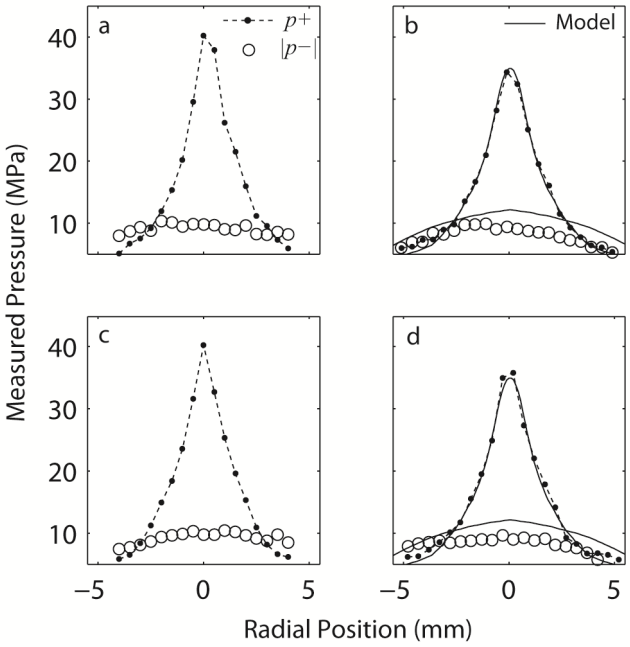

Figure 15. Radial (transverse) scans in the focal plane for both long and short standoffs. The labels and legends apply for all of the plots: a) and c) - x and y scan for the 30 mm standoff; b) and d) - x and y scan for the 15 mm standoff. Modeling results are presented for the short standoff experiments (b and d).

By combining all the measurements together from different axial and radial scans the focal zones were constructed for each standoff, and are shown in the diagram of Fig. 6**.** The focal zone was defined as the -3dB region where peak positive pressures are within 70.8% of their maximum values. The measured -3 dB focal zone is narrower with the 30 mm standoff [17 × 1.5 × 1.5mm] compared to that of the 15 mm standoff [24 × 1.8 × 1.8mm]. While measurements were performed only along the axis and radially in the focal plane, simulations provided full reconstruction of the spatial structure of the field. Shown in Fig. 16 are simulations of the 2D spatial distributions of the peak positive (left) and peak negative pressure fields (middle), and energy density (right) for the short standoff, at the highest machine output. The plots indicate that the spatial distributions of the peak pressures and the energy densities are very different. The spatial maximum of the peak negative pressure is located 20 mm closer to the therapy head than the maximum of the peak positive pressure; the focal region for p^- is much larger (the -3dB focal zone for p^- is >27.6 mm × 4.9 mm compared to the one for p^+ of 23.7 mm × 1.8mm). The energy density has a maximum at -18.3 mm (closer to the head than both p^+ and p^-) and has a -3 dB focal zone of >26.3mm x 5.2mm. The values above, which are extracted from the 2D modeled figures, agree very well with the experimental focal zone measurements already

provided. This may have important consequences for therapy, depending on whether the positive (associated with stress) or negative (associated with cavitation) component is responsible for therapeutic bioeffects.

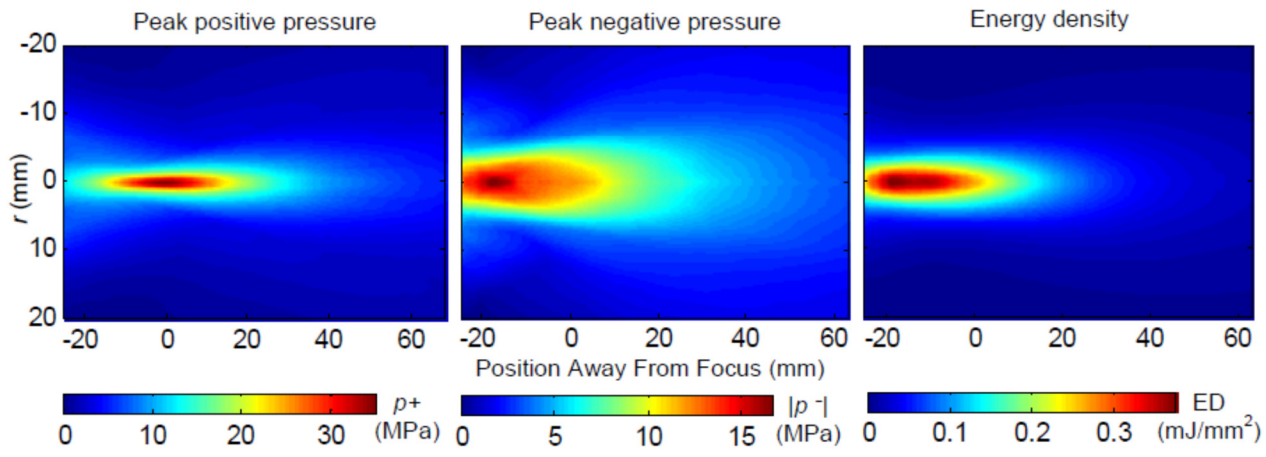

Figure 16. Peak pressures and energy density distributions. 2D spatial distributions of the peak positive (left) and peak negative (middle) pressures, and energy density (right) in the field generated with the short standoff obtained in the modeling. Color on-line.

3.3.2 Peak Pressures at Different Machine Settings

The peak positive and negative pressure and calculated energy density at the focus at each setting for both standoffs are shown in Fig. 17. Because the position of the focus on the beam axis changes due to nonlinear wave propagation, the hydrophone was scanned for each new setting to find the spatial maximum of the peak positive pressure. A total of 25 waveforms were independently recorded at each machine output setting. The means and standard deviations are displayed.

The results shown in Fig. 17a indicate that neither standoff generates peak positive pressures that correspond to the machine display settings shown by the dashed line and labeled as 1:1. The measured pressure, except at the extreme lowest machine settings, is always less than the displayed setting. The peak negative pressures increase as the machine setting is increased. The trends for both standoffs are *quantitatively* the same. On the other hand, the peak positive pressures diverge slightly at higher machine settings, with the long standoff having slightly higher pressure amplitudes. As the machine settings were increased, the peak negative pressures increased at a slower rate than peak positive pressures.

The Duolith settings also display an energy level (in mJ/mm^2). Fig. 17b compares the pulse intensity integral calculated from the actual waveform to the machine display. Again, the measured energy density was much less than the displayed setting at all levels except the lowest.

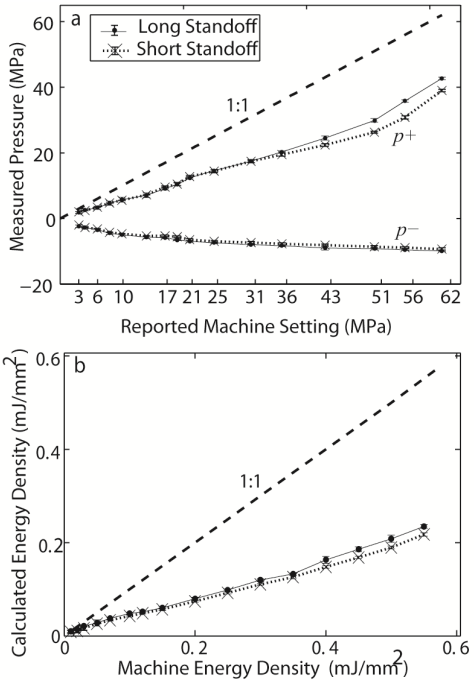

Figure 17. Peak pressures and energy density plots. (a) p+ and p$^-$ pressures measured at each machine output setting for both standoffs. (b) Calculated energy density (E.D.) at each machine setting for both standoffs. 1:1 line plotted for comparison on each plot.

3.3.3 Variation of Peak Pressures at Different Pulse Repetition Frequencies

Three different machine settings were compared to determine if the pulse repetition frequency (PRF) affected peak positive or negative pressures (Fig. 18). The measurements were done at the focus using the long standoff. The PRF setting affected the peak positive pressures only when the PRF was set above 2.5 Hz. The maximum amplitude reduction was between 9 and 15%. 3 Hz was the maximum PRF available for these settings.

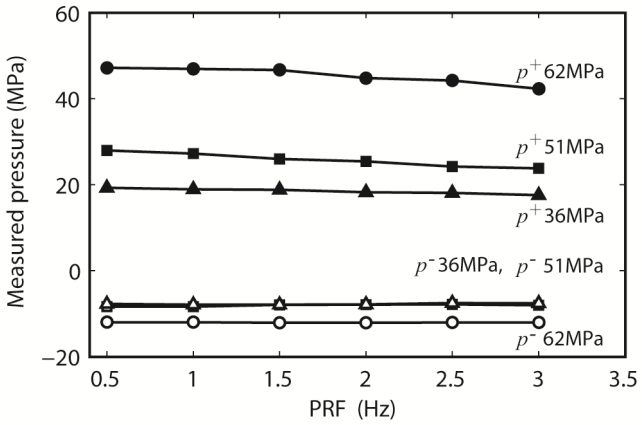

Figure 18. Illustration of peak pressure changes corresponding to changes in machine PRF. Change in p^+ (solid symbols) and p^- (open symbols) pressure with respect to a change in machine PRF for three selected machine output settings: 62MPa (#7), 51MPa (#5), and 36MPa (#4). The long 30 mm standoff was used for these measurements. Data acquired shows averaged pulses (50 pulses averaged) at a specific PRF. Means and STDs are less than 2% in all the cases.

3.3.4 Rise Time Measurements

The rise times were calculated using the long standoff for most machine settings following the definition described in Section IIB along with the traditional definition for comparison, and are shown in Fig. 19. However, because there is noise in the measured waveforms, the derivative will also have noise. To reduce the noise levels for settings below #5, FIR filtering was implemented to smooth out the function around the peak in the derivative (see Fig. 8, inset). In general, as the output levels decreased, the rise times increased, from a minimum of 8 ns at setting #7 (Table 2), to almost 500 ns at a low machine setting (not shown in Table 2).

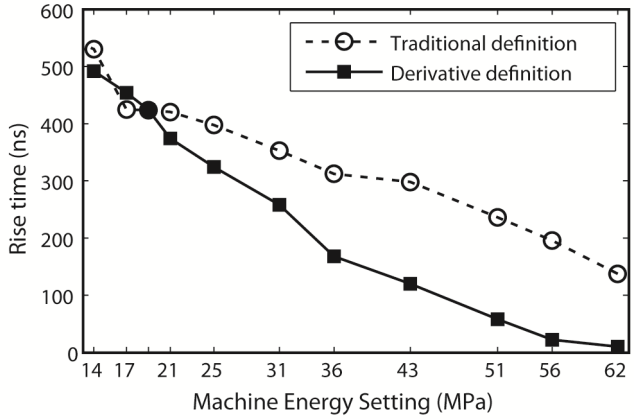

Figure 19. Rise time versus machine setting pressure levels for most of the machine settings using the long standoff. Rise time called “derivative definition” was calculated at the 36% level of the derivative of the pressure wave based on Fig. 8. The “traditional definition” is the standard rise time from 10% - 90% of P+.

Discussion

The pressure field of a clinical shock wave device, the Storz Medical Duolith SD1 T-Top, was studied in detail. In particular, measurements were performed with two standoffs for the electromagnetic therapy head (30 mm and 15 mm in length). Several aspects of the measurements are worth additional discussion, including differences between standoffs, and comparisons with simulations.

The Duolith SD1 has several operating modes. The electromagnetic handpiece can be configured without a standoff, or with one of two different length standoffs. The standoffs are advertised as a way to mechanically change the "therapeutic penetration depth". My goal was not to measure every possible configuration. Instead, I compared some aspects of the two standoffs, and at other times, performed detailed measurements from one or the other standoff.

The SD1 output can be displayed in units of pressure (MPa) or energy flux density (mJ/mm^2). Peak pressure amplitudes (or calculated energy densities based on the measured waveform) measured in this study were lower than the values displayed on the device (see Fig. 17). However, the focal lengths for the two standoffs were similar to device specifications. There is a large discrepancy between my measurements and those reported by the manufacturer. Their in-house measurements were performed without a coupling cone; the measurement equipment was different as well, but not specified by the manufacturer. These differences in experimental conditions may account for the major discrepancies observed. (Personal communication with Storz)

There is also a difference in p^+ between the two standoffs at the higher machine settings (Fig. 17). This may be due to extra focusing and stronger nonlinear effects caused by the difference in the lengths of the standoffs (15 mm). That is, each standoff is filled with oil (proprietary information); the sound speed for some oils (*e.g.* silicon oil, 1350 m/s) is lower than in water. The linear focusing gain, which is inversely proportional to the sound speed, is thus increased for the longer standoff. In addition, nonlinear effects are also stronger in a medium with lower sound speed, leading to further enhancement of the focusing gain.[106,113] The difference in standoff lengths also resulted in a slight narrowing of the focal region of the beam in the axial scan (Fig. 12). But the differences are not large. This suggests that selection of a particular standoff is indeed related to the advertised function of mechanically changing the focus.

Peak positive and negative pressures measured at different PRFs showed relatively little change (Fig. 18). There is only a slight drop off in pressure amplitude at the highest PRFs (maximum drop was 15% for p^+ at the highest setting). The drop-off may be a function of the device electronics, but also, at higher PRFs, cavitation may occur. Signals affected by cavitation can show a reduction in level, but our observations of signals affected by cavitation usually result in a much different waveform, not just a slight reduction in signal amplitude; this was not observed. The amplitude reduction could be a function of the device itself.

One of the important issues of using shock wave therapy devices is the question whether or not they actually produce shock waves. In addition to being an intriguing question in terms of nonlinear wave physics, it also has an important clinical implication, as the width of the shock might be responsible for various bioeffects. This is worth some discussion.

The potential for shock formation was evaluated by examining the rise time of the acoustic pulse at several machine settings. Details of the procedure used to calculate the rise time is discussed in Section IIB and III. The standard definition from 10% to 90% of the peak positive pressure is not accurate if the shock wave is superimposed with an earlier-arriving smooth pressure-wave (the “pedestal”) as observed in Fig. 8. This slow rise may be due to capacitive effects, or perhaps the inertia of the cylindrical coil plate that has to expand and generate the cylindrical wave. Electrohydraulic lithotripters do not have a pedestal wave as spark discharges are generated almost instantaneously. Furthermore, the propagation distance to the focus is longer in lithotripters than in ESWT devices and thus nonlinear effects, which are cumulative in nature, are stronger. Once the shock is formed prefocally, it propagates with higher speed than the ambient sound and overrides the preshock low amplitude component of the pulse. When measuring rise times using the traditional definition, the reported measurements for rise times of electromagnetic sources are on the order of hundreds of nanoseconds.[83,84]

When using the proposed definition of rise time that excludes the smooth pedestal part, the values agree with some electrohydraulic and piezo electric shockwave devices in which rise times are tens of nanoseconds or equal to the bandwidth limit of the hydrophone.[83,84] However, the rise time for the electromagnetic device measured at the highest output setting was about 8 ns, which is still 30 times longer than the theoretical rise time of a quasi-stationary shock (0.27 ns) with the same amplitude. Because shorter rise times cannot be measured with the FOPH, the question is whether the shock has not been formed, or was simply not resolved.

The structure of a weak shock in a nonlinear viscous medium is determined by a balance between nonlinear and dissipation effects as the wave propagates in the medium. Dissipation at the shock front is very strong, therefore once the shock is formed prefocally, its propagation is accompanied by energy losses that lead to reduction of the focusing gain of the peak positive pressure.[104,106,113–115] In these previous simulation studies it was shown that the maximum focusing gain of the peak positive pressure is reached at an output level when the shock starts to develop at the focus. Here, additional simulations were performed to determine if a shock would develop if higher pressures were achieved. This was done by scaling the pressure amplitudes of the boundary condition (Figs. 9 and 10) from 0.5 to 2*x* in steps of 0.1. From these scaled pressures, the axial distributions and focusing gain can be compared for increasing source output. Although this linear scaling does not precisely correspond to changing the output level of the device, it was an adequate approach as nonlinear effects were weak at the distance where measurements for the boundary condition were taken.

The results of these additional simulations are shown in Fig. 20. The dashed lines correspond to (simulations of) the experimental conditions for the short standoff at the highest machine output (#7). The inset shows the peak positive focusing gain, given by the ratio of p^+ at the focus to its initial value at the boundary, as a function of the source pressure output. Formation of a shock is expected when the focusing gain curve reaches a maximum. In our case, the experimental conditions correspond to the output level that is lower than the level of the maximum focusing gain, *i.e*. the shock has not yet formed. Unfortunately, it was not possible to resolve the fine structure of shocks with 2 ns time steps used in the modeling, and the simulations became unreasonably long with finer grid. But the focusing gain curve (inset) does suggest that a shock has not formed. Apparently, if the device could generate an extra factor of 2 in pressure at the source, a shock may indeed form at the focus.

Figure 20 also illustrates how the focal zone changes with source pressure amplitude. With an increase in source output, the position of the spatial maximum of p^+ on the beam axis changes non-monotonically. It first moves away from the source and then backward. This effect is typical for nonlinear focused beams and has been observed in the earlier studies.[113,115] The shift away from the source is characteristic for focusing without formation of shocks. It is caused by strengthening of the nonlinear self-refraction phenomenon because the speed of the pulse front depends on its amplitude. At very high source outputs, when a shock is formed prefocally,

strong absorption at the shock results in diminishing of the peak positive pressure and the maximum moves backward. Note also that the maximum shift in the natural focus from the lowest to highest setting is about 6 mm. The peak negative pressure maximum always moves toward the source with the increase of its output.

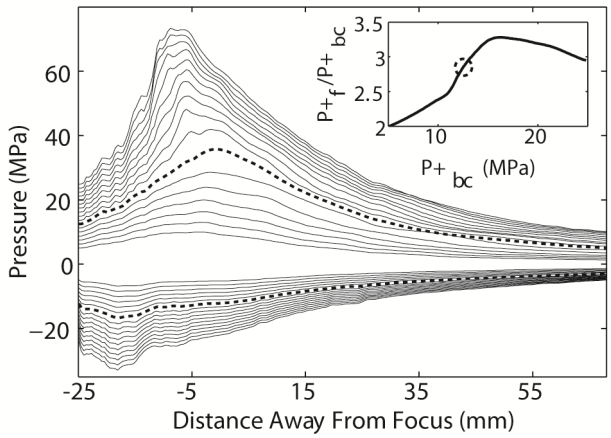

Figure 20. Simulations of the axial peak pressure distributions. Inset: The focusing gain for the peak positive pressure (inset). The dashed lines correspond to the results simulating the experimental conditions for the short standoff at the highest machine output (#7, Table 2). The inset shows the ratio of the peak positive pressure at the focus to its initial value at the boundary as a function of the source pressure output. The dashed circle in the inset indicates the experimental point corresponding to that gain curve.

Therapeutic bioeffects from ESWT are often categorized as being due to the peak pressure (p^+), rise time, or negative pressure (both peak and duration). The peak positive pressure and/or the rise time can generate compressional and shear stresses that might generate a bioeffect. If so, higher settings would most likely generate larger bioeffects, although at low settings, the secondary pulse becomes a significant fraction of the main pulse height (see text describing Fig. 8), suggesting that at these settings the machine generates a pulse 'doublet'. Negative pressures are associated with cavitation. As the machine setting is increased, the peak negative pressure also increases, but also, so does the length of the tensile tail. This suggests that the cavitation fields will have longer characteristic lifetimes, possibly inducing more violent collapses, and more bioeffects. Note also that the size and position of the positive and negative pressure fields differ (Fig. 16). The negative pressure field is broader and is focused closer to the therapy head than is the positive pressure field.

Returning to the rise time, according to our own experimental data shown in Fig. 8, a rise time measurement of 8 ns would correspond to a spatial scale on the order of 10 μm, which is comparable to the typical size of cells (1 – 100 μm). Thus many cells could experience an internal pressure gradient. According to Cleveland and Mcateer,[86] although tissue is usually robust to isotropic compression, a leading shock front with rise times on the order of 70 ns

(spatial scale of 100 μm) suggests that structures in the range of 10 μm to 1 mm will experience a significant variation in stress across them as the shock wave passes. The short rise time associated with the shock will lead to non-uniform straining of the tissue, resulting in shear forces. Lokhandwalla *et al.* showed that hemolysis is directly related to the pressure gradient at the shock and validated shearing as a cell lysis mechanism in SWL.[116] It has also been shown that tissue structures are sensitive to shear stress and that the distortion of tissue by a shockwave can cause damage.[117] I thus hypothesize that mechanical tissue damage is associated with a shock front. In addition, mechanoreceptors in cells can be affected by shear. According to Wang *et al.*, application of a mechanical stimulus like shear stress to a cell turns on mechanosensitive ion channels, heterotrimeric G proteins, protein kinases, and other signaling molecules; these trigger downstream signaling cascades that lead to force-dependent changes in gene expression.[118] Based on all the above I conclude that shear stresses from the shock front might be an active mechanism for ESWT. It is thus important to determine whether or not therapeutic bioeffects are due to the positive (*i.e.,* stress) or negative (*e.g.,* cavitation) pressures in order to optimize ESWT treatments. For example, if shear stress were the major therapeutic mechanism, then treatments for near-surface conditions (*i.e.,* wound healing) might benefit from the longer standoff.

The focus of this chapter has been on the electromagnetic therapy head. The Duolith also comes with a ballistic (termed 'radial shock wave') source. A previous study showed that ballistic sources do not generate a shock wave.[12] For completeness, a characteristic averaged pressure waveform (20 averages) from the Duolith ballistic source is shown at a setting of 5 bar in Fig. 21. The pulse consists of a leading positive phase with p^+ = 8 MPa and duration of 5 us. The trailing negative phase has p^- = -5.7 MPa. The spectrum of the wave is shown in Fig. 21b. Most of the energy is contained at or below 200 kHz. The energy flux density is 0.115 mJ/mm^2, calculated according to the PII described in Section II. The measurements taken here for the ballistic source are similar, but not identical to the ones presented by Chitnis and Cleveland 2007 for the Dolorclast Vet device (our measurements have lower peak negative pressures).[12] Although the signal does not resemble a shockwave, the International Society for Medical Shockwave Treatment (ISMST) defines it as a shockwave.

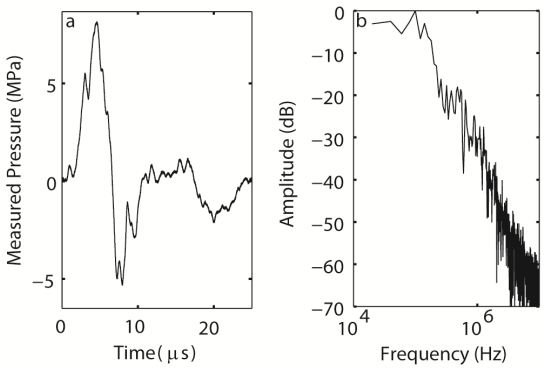

Figure 21. Ballistic source pressure waveform and corresponding spectrum. The pressure waveform (a) and corresponding spectrum (b) measured at a distance of 5 mm from the metal applicator for the ballistic source operated at 5 bar setting level.

The measurements reported here are important for device characterization and understanding wave propagation in water, but for *in vivo* settings, especially in musculoskeletal tissues, the waveform shape and amplitude would be expected to differ greatly from *in vitro* results. Bones and inhomogeneous tissues will create complicated reflections and re-focusing, and shear waves that can disturb the field and shift the focus as well. [119,120]

3.4. *Ex Vivo* Application Using the Duolith SD1 Characterized ESWT Source.

3.5.1 *Ex Vivo* Study Using ESWT

A set of *ex vivo* tissue studies that characterized microbubble oscillations inside a microvessel structure comparing 2 focused ultrasound regimes are presented. Briefly, a rat-mesentery section was obtained and placed in a high speed imaging inverted microscope setup following the protocol thoroughly described elsewhere [121,122]. A pulse from the Duolith (the shock wave therapy device characterized on this chapter) is compared with a regular 3-cycle focused ultrasound pulse at 1 MHz where the peak negative pressure matched the same level. This allowed the comparison of the dynamics of the microvasculature-bubble interaction between two commonly used ultrasound modalities (Fig. 22), focusing on the differences in rise times and shock fronts between ESWT pulses and HIFU pulses, and lengths of the negative tail (see Fig 22 for comparison). The Duolith (ESWT) pressure pulse interacted with exogenous contrast agents (Fig.22, blue) and caused a higher vessel distention compared to previously characterized response to focused ultrasound dynamics with exogenous bubbles [121,122] (Fig. 22, red). The length tensile tail during the Duolith pulse dominated the bubble dynamics (Fig. 22, blue).

It was determined that the vessel distention during the response to the Duolith pulse (Fig. 22, blue) appeared to be a major mechanism for vessel rupture as opposed to vessel invagination, which is the main mechanism reported from focused ultrasound experiments of the same system[121,122]. Maximum radii expansion agreed with the suppression of shocked bubble expansion results due to confinement discussed in the literature. They are also reduced to free bubble results generated by the same device. In this *ex vivo* tissue study I compared the effect of shockwave therapy (using the characterized device on this chapter over previously used high-intensity focused ultrasound (HIFU) in the dynamics of the microbubbles inside microvessels [121,122]. Results were qualitatively consistent with tissue constrained bubble dynamics and simulations by others[123]. The distention for these experiments appeared to be a major mechanism for vessel rupture, in agreement with literature results [124].

3.5.2 Methods

The dynamics of shockwave-induced microbubble-microvessel interactions with ultrasound contrast agents in the microvasculature were explored. The regimens differed in peak positive pressure amplitudes (28 *vs.* 8 MPa) for both signals, but peak negative acoustic pressure amplitudes were comparable, at about 7MPa. The main differences between the two waveforms are the rise time of the p+ front, and the length of the negative tail (Fig 22).

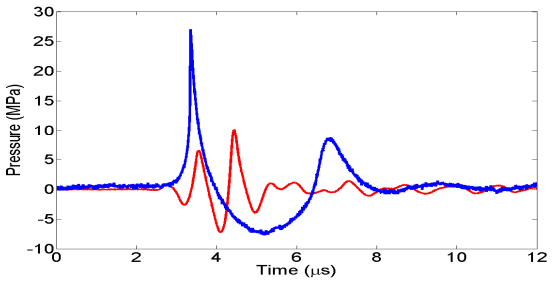

Figure 22. Focused ultrasound pulse using an ESWT medical device. Comparison of a 2-cycle focused ultrasound pulse with an extracorporeal shockwave therapy (ESWT) medical device pulse.

The tissue sample was placed at the focus of an inverted microscope at a 45 degree angle with respect to the ESWT source (Fig. 23a). A flash lamp illuminated the tissue sample while the high speed camera (Imacon 200, Hadland Imaging LLC, Santa Cruz, CA, USA), connected *via* the inverted microscope, captured 12 images of the tissue sample under the exposure of ESWT (Fig. 23b). A regular video camera, connected to the inverted microscope (50/50 splitter) aided with registering specific experimental events and with histological selection at the end of experiments. The image collection/processing techniques followed the detailed methods described elsewhere [121,122].

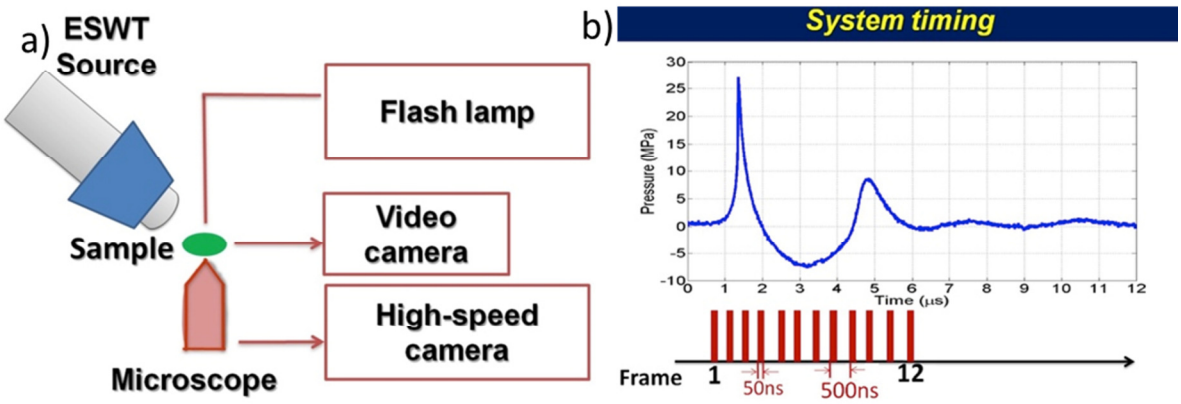

Figure 23. High Speed Imaging Setup(a) and system timing(b): Exposure time (50ns), interface rate (500ns).

System Timing

Fig. 23 (b) illustrates the timing of the high speed imaging system for the Duolith pulse. The upper panel shows the waveform measured at the position of the tissue sample. There were 12 frames of high-speed images are captured in each experiment. The first frame was assigned time point T=0. The exposure time of each frame was 50 ns and the interframe time was 1μs. The total time covered by 12 frames was about 11us. The waveform here is 8mm postfocal (see Fig. 12). The pressure shown in Fig. 23 is reduced by a factor of 2 from the previous measurement shown (Section 3.3) due to the fact that the imaging takes places beyond the focal region. However, the negative tail governs the dynamics of the microbubble and that is about 7 MPa p-.

3.5.3 *Ex Vivo* Results

Clinical ESWT-induced bubble dynamics with the Duolith (described in section 3.2) were explored in vascular environments and compared with previously obtained focused ultrasound results of microbubble-microvessel interactions [121,122]. Invagination, in the previous results, was always found to be larger than distention in 96% of venules[121,122]. With the Duolith pressure pulses, it can be seen from Table 3, that rupture caused by vessel distention was either comparable or at least greater than invagination. Figure 24 shows a classic example of vessel rupture due to ESWT-bubble interaction in a 52 μm microvessel.

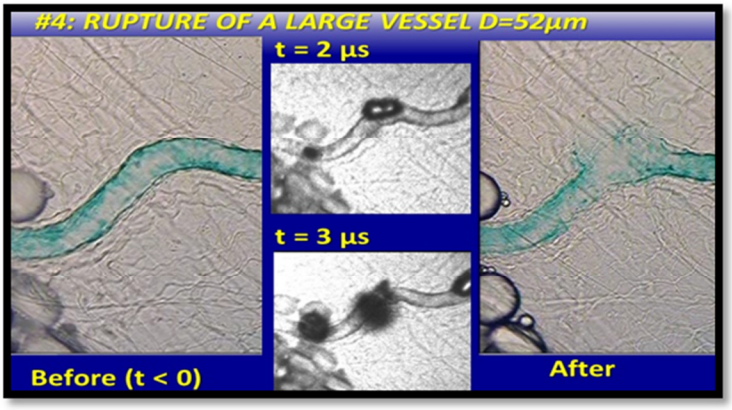

Figure 24. Cavitation can disrupt a vessel. Rupture of a large vessel due to cavitation; images before (left) or after (right) ESWT exposure. The middle picture show 2 consecutive frames showing the growth of the exogenous microbubbles responding to the tensile phase of the waveform (see timing in Fig. 23).

Table 3 shows a summary of the results for the selected studies. The bubble expansion observed is much smaller than what is observed *in vitro*[124], which is displayed for comparison as the last column of the table (free bubble). The R_{max} of an assumed prolate spheroid is measured to be not bigger than 45 µm. Compared with previous work in by Hong Chen, the results indicate that the ratio of invagination to distention is, on average, 0.96, which was not true for the previous studies with HIFU pulses[121,122] (ratio was always greater than one). Distention is a major mechanism of vessel rupture or damage in response to the Duolith ESWT pulse. There is also a clear tissue constraint of the bubble dynamics (R_{max} reaches about 50% of the Rmax of a free bubble, Table 3). These results are qualitatively consistent with the suppression of shocked bubble expansion results due to confinement published by Freund[123]. There is suppression by the vessel and liquid in the entire bubble-vessel dynamics that stops the bubble radii from expanding freely.

Table 3. Summary of selected high speed imaging results for bubble-vessel studies.

Case	Rmax *	Max Invag.	Max Disten.	Rmax Free Bubble
1	36 µm	13 µm	20 µm	78 µm
2	43 µm	23 µm	10 µm	90 µm
3	34 µm	19 µm	16 µm	80 µm
4	45 µm	24 µm	27 µm rupture	67 µm

3.5. Conclusion

In this chapter, it is shown that the combination of measurements together with mathematical modeling provided a suitable tool for acoustic characterization of high intensity pressure fields generated by electromagnetic shockwave medical devices. Acoustic parameters of the field of a

clinical device used to treat musculoskeletal conditions in patients were measured using a fiber optic hydrophone: focal peak pressures, axial and radial distributions, and rise time of the pulse front were determined at several machine power output settings. Radial scanning in the plane close to the therapy head was performed at the highest output setting and the results were used as a boundary condition for an acoustic nonlinear propagation model. The results of modeling were validated by comparing pressure waveforms obtained in simulations and measurements. Simulation data provided additional information on the spatial distributions of the peak pressures and the degree of nonlinear effects to form a shock in the pulse at the focus. It was shown that shock formation did not occur for any machine settings and that a true shock formation could be reached if the maximum initial pressure output of the device is doubled. Although characterization was performed in water and strong distortions of the field occur while propagating through the complicated musculoskeletal geometries and impedances that are present in the human body, this study provides the important steps at calibrating a device toward understanding the pressure field of ESWT clinical devices and developing a model that can become a powerful tool to predict high intensity pressure fields *in vivo*.

CHAPTER 4

Cavitation Dynamics and Acoustic Characterization of a Commercial Dental Laser (Waterlase iPlus, Er,Cr:YSGG) for Orthodontics and Periodontics.

4.1 Laser Generated Shock Wave Therapy Device for Biofilm Removal.

Applications in endodontics and periodontics focus on using erbium lasers in order to effectively kill bacteria and biofilms. Erbium laser-tissue interaction is characterized by an explosive process with a low ablation threshold and a thin coagulation zone along laser incisions. In this section, the acoustic field and the bubble dynamics of a clinical portable dental laser (Waterlase iPlus, Biolase Inc) were characterized in a water tank. The laser is a Er,Cr:YSGG laser. Field mapping was performed for two different tip geometries (flat or tapered) and 3 tip diameters (200, 300, 400 µm) using both fiber optic probe and calibrated needle hydrophones. Peak positive pressures at 5-50 mm away from the tip ranged from 3 to 0.01 MPa, while peak negative pressures ranged from 2.5 to 0.1 MPa. Pulse rise times measured 5-50mm away from the tip ranged from 50 to 1000 ns. The maximum standard deviation in peak pressure was 8%, indicating that the Waterlase iPlus generates stable pulses. Shorter duration laser pulses result in larger pressures. The primary pulse is independent of tip geometry, but generally stronger for smallest tip diameter. The first bubble collapse depends on tip geometry and diameter, whereas bubble rebounds are independent of tip type. A Plesset-Zwick model, which accounts for mass and heat transport, was implemented to further analyze the experimental bubble dynamics and the pressure emissions. The model suggests that heat deposition in the bubble from these relatively long laser pulses is a potentially significant contributor to understanding bubble dynamics and emitted pressures from tapered and flat tips.

The characterization technique was very similar as the one described in Chapter 3, and incorporated the high speed imaging technique. The main goal of these studies was to define the optimal laser parameters and techniques to effectively kill bacteria for endodontics and periodontics indications.

[B] Work published in part in:
C Perez, YN Wang, A Sivriver, D Boutoussov, V Netchitailo, TJ Matula, Acoustic field characterization of the Waterlase2: Acoustic characterization and high speed photomicrography of a clinical laser generated shock wave therapy device for the treatment of periodontal biofilms in orthodontics and periodontics, The Journal of the Acoustical Society of America 136 (4), 2279-2279

4.2 Introduction

High intensity acoustic waves and shock wave therapy (SWT) have been used to break up collagen in various tissues and to accelerate bone healing[67,68]. In addition, the use of focused ultrasound and laser generated shock waves have reported success at disrupting biofilms[125], removing biofilms from medical devices[126], and permeating through the cellular matrix and cell membranes (sonoporation)[127,128]. These high intensity fields are often coupled with endogenous cavitation or exogenous cavitation (*i.e.,* ultrasound contrast agents), and the intensity of bubble collapse has been associated to bioeffects such as degranulation, cytokine release[129], intracellular calcium[127], and chemotactic factor increase[130].

Progress toward understanding the mechanisms of bioeffects requires accurate characterization of the parameters of ultrasound fields generated by clinical devices[10]. "Shockwave" systems include devices that use electromagnetic, electrohydraulic, ballistic, piezoelectric, and laser sources. In this chapter the focus is on a clinical dental laser that generates pressure pulses when in contact with a fluid. The acoustic outputs from similar pulsed laser devices have been measured,[131–134] but independent measurements of clinical devices have not been done for several machines that are commercially available. Several examples exist that show differences between manufacturer and independent-lab measurements.[10,11,12] Thus, while self-reported results by manufacturers are useful, independent characterization is needed.
The typical mechanism for laser-medium interaction is the following: A Er,Cr:YSGG laser generates a pulse, laser absorption in the fluid leads to a primary pressure wave emitted from the absorption region. At higher settings, a vapor bubble is also formed. The growth and subsequent collapse of the vapor cavity leads to secondary pressure waves. High speed imaging of a similar system was qualitatively described[135–137], but characterization of the bubble dynamics or acoustic field mapping was not previously reported. Therefore, the focus of this section is on characterizing the acoustic pressure waves and bubble dynamics caused by the system's laser pulses in water.

Erbium lasers are used in dermatology and dentistry for ablation of soft or hard tissues. With new fiber systems becoming available to transmit wavelengths around 3 µm, there is a growing interest in using of Erbium lasers in a water environment like urology, otorhinolaryngology (ENT), neurosurgery and dentistry. Laser-tissue interaction of ~3µm wavelength lasers is characterized by an explosive process with a low ablation threshold and a thin coagulation zone

along laser incisions[138]. The Waterlase iPlus is an FDA approved medical device, and my work focused on characterizing the acoustic field generated by its laser pulses in order to facilitate identification of optimal laser parameters and techniques to effectively kill bacteria for endodontic and periodontic indications. Several studies have been performed to assess the effectiveness of the Waterlase iplus[139–145]. Previous high speed photomicrography studies using this system[135–137] and other similar systems[146–151] suggest that spherical generated bubbles using short diameter and tapered tips are expected to be more forceful in creating mechanical bioeffects in both hard and soft tissues, however no acoustic pressure measurements have been performed to validate the previous high speed imaging studies.

Shock waves are characterized by high positive pressures with a short rise time (<10ns), and a longer-duration tensile wave (negative pressure)[86]. The short duration positive pressure is associated with shear effects. The tensile wave is associated with cavitation (formation of µm-sized vapor bubbles in liquid) and high tensile stress at interfaces between different materials[152]. Cavitation can lead to rupture of material as the bubble grows explosively. In addition, bubble collapse can lead to large amplitude pressure pulses (even shock waves) that can disrupt tissues from high shear stresses, and bubble micro-jetting that can pierce nearby tissues, or pit hard surfaces such as bone. Beneficial bioeffects of low energy shock waves include osteogenic potential[77–79,94,96,153], neovascularization[74,79,154], and the breakup of bacterial cellular matrix.

In recent studies, numerical modeling combined with measurements has been actively used to characterize acoustic fields from high-power ultrasound medical devices. Simulation data based on variations of a Rayleigh-Plesset type equation that accounts for effects of heat and mass transfer have been shown to agree well with experimental data. This model has been applied to predict bubble response to lithotripter pressure pulses and high intensity focused ultrasound fields.[155,156]

Following this approach, modeling was combined with measurements to characterize the nonlinear ultrasound fields generated by the Waterlase iPlus device. The chapter is organized as follows. The experimental system is described first, followed by the model (Section 4.2.4). Experimental results are provided for various machine settings and lastly compared with modeling at a particular operating level of the device; simulation results are presented to provide more detailed analysis of geometrical differences in tips (tapered vs. flat) reflected on the

measured pressures and temporal characteristics of the R(t) curves (Section 4.4.6). The results are discussed in Section 4.4.

4.3 Materials and Methods

4.3.1 Experimental Arrangement

Measurements were performed using Waterlase iPlus (Biolase Inc, California, USA) with an Er,Cr:YSGG (wavelength λ=2780 nm) laser. Some of the device settings used are shown in Table 4. Diameters of tips were 200, 300 and 400 µm. The laser output energy varied between 0 to 600mJ, measured with a calibrated power meter and sensor (Ophir Photonics, Utah, USA) for each flat tip. There were two options for laser pulse length: H mode, (60 µs long, 6dB level) and S-mode (700 µs long 6dB level). The machine pulse repetition frequency (PRF) used ranged from 5 to 100 Hz. Two different tip geometries (Fig. 25) were tested: the flat-ended tip or radial firing tapered tip (RFT Tapered tip).

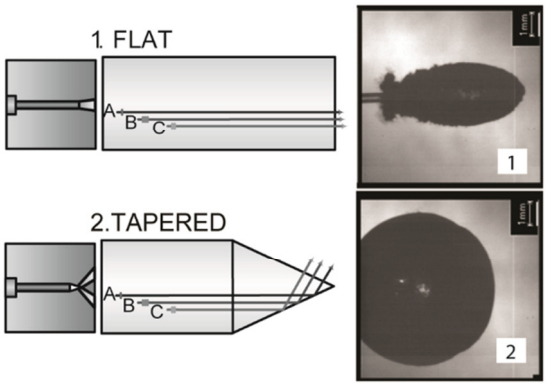

Figure 25. Tip geometries used in the acoustic characterization study. Tip diameters for each of these geometries can be 200, 300 or 400 µm as shown in Table 4. (Right) typical bubbles generated by each geometry (1. Flat tip, and 2. Tapered tip). These particular images are for the 300 µm diameter tip and 300mJ energy setting.

Figure 26 illustrates the experimental setup. A computer-controlled 3D positioning system (Velmex NF90, Bloomfield, NY) with 10µm precision in step accuracy was used to translate a PVDF hydrophone (described below in section 4.3.4). Alignment of the PVDF hydrophone with the laser tip was accomplished by first bringing the hydrophone near the tip, where a camera under high magnification imaged the two tips and a calibration ruler together. Once the initial displacement was known, the hydrophone was scanned in two planes orthogonal to the laser tip. The radial axis (along the laser tip) was defined by co-registration of the two planes with the laser tip.

Table 4. Selected output settings of the Waterlase iPlus discussed throughout the chapter. The table indicates the different settings that were characterized. Abbreviations: power (P) in Watts (W), the pulse repetition frequency (PRF), energy (E), short pulse mode (H), and a long pulse mode (S).

Laser Settings			Tip Geometry / Pulse Mode					
			300µm				200µm	400µm
P (W)	Hz	E (mJ)	Flat		Tapered		Tapered	Tapered
0.10	20	5	S	H	S	H	H	H
0.25	5	50	-		H		H	H
0.50	5	100	H		S	H	H	H
0.75	5	150	-		H		H	H
1.00	5	200	H		S	H	H	H
1.25	5	250	-		H		-	H
1.50	5	300	H		S	H	-	H
1.75	5	350	-		-	-	-	H
2.00	5	400	-		-	-	-	H

The device handpiece was located outside the water bath, which was 31 cm long × 18 cm deep × 18 cm wide, and had a maximum degassed level of 8% O_2 at room temperature. The head of the device was not watertight and therefore was not inserted in the water – only the tips were inserted. Care was taken to ensure that there were no visible bubbles on the laser tip prior to firing. The bath was large enough to avoid interference from wall reflections, but there were reflections from the top air/water interface (see Fig. 26). By trial and error, it was determined that having the tip inserted at least 12 mm guaranteed that the bubble dynamics were not influenced by the interface. The hydrophone itself was never brought close enough to interfere with a growing bubble (at least > 4mm away for the highest energy settings). Fine-tuning the laser tip position was done with a second 3D-positioning stage.

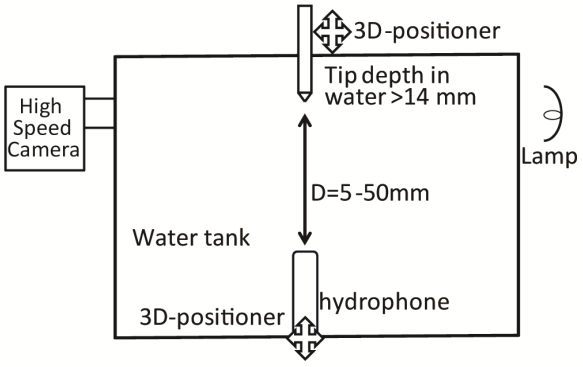

Figure 26. Experimental setup of dual high-speed photomicrography and acoustic characterization of the laser-based system using a calibrated hydrophone. D indicates the distances where the acoustic measurements where scanned along.

The overall objective was to quantify the acoustic wave generated by various laser settings, and to determine if any of the settings generate a shock wave. Parameters tested included pulse duration (H or S mode), tip size (200 or 400 µm), tip shape (flat or tapered), and output energy level. Pulses were isolated by a software-controlled shutter for measurements. The parameter space is illustrated in Fig. 27.

4.3.2 Measurement Protocols and Pulse Definitions

To reiterate, the overall objective was to quantify the acoustic waves generated by various laser settings for different tips. The parameter space is illustrated in Table 11-14 (Appendix A). Data collection was facilitated with a trigger pin located on the back electronics board of the Waterlase iPlus which allowed for triggering of the high speed camera and hydrophone.

In the results and discussion sections there are references to bubble dynamics and emitted pressures from bubble collapses. In order to faciliate these discussions, it is worthwhile describing the general attributes that were observed. A typical analysis of the high speed imaging and hydrophone signals is illustrated in Fig. 27.

First, consider the high-speed image analysis shown in Fig. 27a. As mentioned earlier, the non-spherical bubbles were ‘converted’ to spherical bubbles using an “equivalent area” technique. The equivalent radius of a bubble during the growth, collapse, and rebound stages is shown. The tapered tip data shows a main growth to a maximum bubble size of about 3.25 mm at about t = 300 µs. The main collapse occurs near t = 700 µs. The bubble then rebounds to a local maximum (about 1.9 mm) around t = 850 µs before collapsing and rebounding again.

The corresponding acoustic emission data for the tapered tip is shown in Fig. 27b. There is a signal generated near time t = -100 µs (labeled A), and again near t = 700 µs (labeled B), t = 1050 µs (labeled C), and t = 1200 µs, labeled (D). Signal A corresponds to a thermoelastic pressure pulse generated by the absorption of laser energy in water. Signal B corresponds to the main (first) bubble collapse. Signal C corresponds to the second bubble collapse (which is also the first rebound collapse). Signal D corresponds to the third bubble collapse (or second rebound collapse).

A similar observation can be described for the flat tip, whose radius is shown as open circles and its corresponding acoustic signature is shown in Fig. 27c. The initial pressure pulse during bubble formation occurs at the same time as the tapered tip. However, because the flat tip bubble doesn't grow as large (only 2 mm), it collapses earlier, in this particular case near t = 300 µs (*cf*. the tapered tip, where the main collapse occurs near t = 700 µs). The first rebound occurs near t = 550 µs. The last observed acoustic emission data, labeled D, occurs near t = 650 µs. Note that the images for this collapse are not as well defined, but the acoustic emission shows that there was indeed a collapse strong enough to be detected. Section 3.2.2 defines the acoustic parameters for pressure waveforms associated with the measurements in Fig. 27.

Returning to the bubble dynamics, in all cases at least one rebound is observed, and usually more. And while I often observed a second (and sometimes third) rebound, the data analysis did not extend past the first rebound (specifically signals A, B and C). Note that the minimum bubble size was not observed because of the lower temporal resolution of the image acquisition system. The temporal resolution was however sufficient to quantify the maximum bubble size for the main growth and subsequent rebound.

4.3.3 High Speed Imaging and Analysis

Bubble dynamics were captured with a Photron APX-RS high speed monochrome camera (Photron, San Diego, CA, USA). Image sequences were captured at 30,000 frames per second (FPS) with a resolution of 256x256 pixels (see setup in Fig. 26). A Carl Zeiss lens (Makro-Planar T* 2/100, Thornwood, NY, USA) with a bellows extension was used to provide a resolution on the order of 28 µm/pixel. A continuous, disperse light source (Photogenic PowerLight 2500DR, Bartlett, IL, USA) positioned behind the camera lens was used to backlight the water to air interface. A total of 80 frames at 6 µs shutter speed were captured per laser pulse.

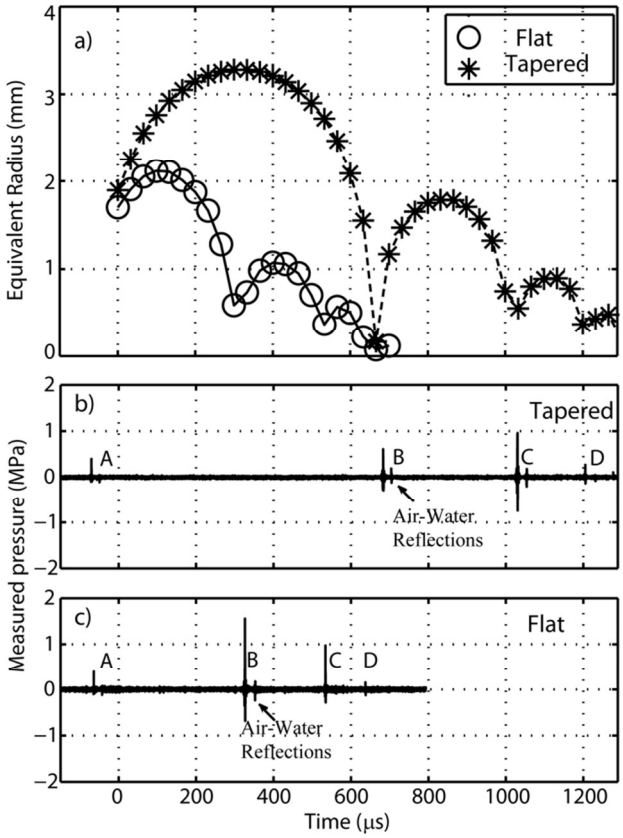

Figure 27. Typical bubble dynamics and acoustic emission plots. (a) "Equivalent" radius bubble dynamics from individual laser pulses at 300mJ energy setting for both tapered (asterisk) and flat (circles) tips having a diameter of 300 μm. (b-c) Corresponding hydrophone acoustic emission measurement of a single pulse from a Tapered tip (b) and a Flat tip (c) measured 15mm away from the laser tip. The initial thermoelastic expansion signal is labeled A, while the bubble collapse-generated pulses are labeled B-D. Pulses reflecting off the air-water interface can also be observed. These reflected pulses from the first collapse are labeled, but all emissions contained reflected pulses.

Image processing was performed using a custom made erosion dilation imaging analysis routine using functions (imerode, imdilate, imfill and bwarea) in Matlab (Mathworks, USA). Typically, a binary algorithm was applied with a threshold to convert bubble interiors to white and surrounding areas to black. A small disk structural element with specified radius of two elements was created and used to dilate the image. Then erosion was performed with a similar disk of eight element radii. Later, the function imfill was used to cover non-bubble spaces created by light artifacts to allow the user to select the bubble element on each frame and then computing its center of mass (using bwlabel and regionprops to compute each bubble's centroid). Finally after identifying the center of mass of each bubble, its pixel area was computed with the bwarea function and then multiplied by the scale/pixel to compute the area in mm^2. To a first approximation, these non-spherical bubbles were represented as spherical

bubbles by equating the measured area to an “equivalent radius” of a sphere (measured area = πR^2). Although inexact, this simple metric has proven useful for analyzing bubbles dynamics using models that are only valid for spherical bubbles. [157] Examples of images and image sequences can be seen in Figs. 25 and 32. Bubble dynamics of the “equivalent” spherical bubbles are shown in Figs. 27, 31, 33, 38, 42, and 43.

4.3.4 Hydrophone Measurements of Pressure Pulses

The bulk of the pressure pulse measurements were obtained with a polyvinylidenfluoride (PVDF) piezoelectric calibrated hydrophone with a 500µm active diameter tip (HNP-series, Onda, USA). The hydrophone and preamplifier (AH-2020, Onda, USA) bandwidth was 25MHz. The hydrophone signals were digitized by an oscilloscope (LT344 Waverunner, LeCroy, NY) at 500 MSamples/s. Full calibration and deconvolution was performed from the PVDF hydrophone’s frequency response. Briefly, the pressure waveform was recovered by computing the inverse Fourier Transform (iFT) of the ratio between the Fourier Transform (FT) of the measured signal divided by the full hydrophone’s frequency response. Data collection was automated using LabVIEW (National Instruments, Austin, TX).

During initial testing, bubble translation *away* from the laser tip during collapse and subsequent rebounds was initially observed. This can be caused by the air/water interface, which is about 14 mm from the laser tip. Additionally, the relatively long laser pulses can impart momentum to the bubble, and during collapse conservation of momentum requires that the bubble translate [158,159]. The first bubble collapse occurred near (but away from) the laser tip, while subsequent rebounds translated even further away.

In order to accurately compare emitted acoustic pressure amplitudes of collapses and rebounds, a correction for bubble displacement was needed. 'Depth correction' was performed by locating the center of mass (centroid) of the bubble at its smallest (most compressed) state from the high speed camera images. This allowed for determining the actual distance between the collapsed (or rebound) bubble and hydrophone. The induced bubble translation also prevented the hydrophone from being brought closer than 4 mm from the laser tip, as that would cause the bubble to envelope the hydrophone, making the signals un-useable. For the PRF studies shown in Fig. 34, a particular PRF was selected (5 to 100Hz) and the oscilloscope recorded 30 consecutive pulse transients in a long time series (shutter open for a collection of

pulses), then each transient was analyzed and the STD computed for display as error bars. For these studies, the hydrophone was positioned 15 mm away from the 200 µm flat tip.

4.3.5 Numerical Model and Experimental Data Processing for the Model

The goal of the model is to 1) predict the bubble dynamics (or R(t)) behavior captured by high speed imaging and 2) predict the emitted pressure by both the laser absorption and subsequent bubble acoustic emissions. As expected, a simple model that does not account for heat and mass transfer (modified Keller model)[157] was unable to match the measured pressures and longer collapse times.

To address the relevant physics, a reduced-order model of a single spherical bubble is used here to gain insight and predict the behavior of these bubbles: The model incorporates phase change at the liquid-gas interface as well as heat and mass transport in both phases. The model captures physics of phase change and diffusive transport compared to several benchmark models and experimental data. These models developed by Kreider *et al*, are described elsewhere [155,156]. Briefly, two models were developed where the SCL model assumes uniform liquid temperature everywhere outside a boundary layer near the bubble wall and Fickian equations take care of thermal conduction. In the "PZ" model [160] (after Plesset and Zwick's approach), no such assumption is made. Rather, an approximate solution is utilized to account for thermal conduction in the presence of convective flow. For mass transport in the liquid, an approach fully analogous to that used in the PZ model is implemented for diffusion of dissolved gases. For completeness the PZ model was used to describe the dynamics of both Tapered- and Flat-tipped bubbles.

The energy of the cavitation bubble is given by:

$$E_B = \frac{4}{3}\pi(p_{stat} - p_v)R_{max}^3 + 4\pi\sigma R_{max}^2 \,, \tag{4.1}$$

where ρ is the density of the liquid, p_{stat} is the static pressure, and P_v is the vapor pressure of the liquid. Typically in Eqn (4.1) the sigma (surface tension term) becomes negligible for large mm sized bubbles produced by our device. Finally the energy loss was calcylated during collapse by comparing the different values of bubble energy before and after. The energy of a spherical acoustic transient as derived by Cole (1948)[161] is

$$E_s = \frac{4\pi r^2}{\rho c}\int p^2 dt, \tag{4.2}$$

Where c represents sound velocity in liquid, and r the distance between the hydrophone and the emission of the transient (collapse location). Combining equation 1 and 2, the fraction of energy loss during the first bubble collapse can be calculated, which is converted into acoustic energy (acoustic efficiency) term $E_s/\Delta E_B$, since the maximum bubble radius before and after the collapse are known (R_{max}, and R_{max} rebound) ΔE_B can be calculated, and termed as the acoustic efficiency. The studies described here focus on the acoustic efficiency of the first and second collapse, which are called EF1 and EF2 respectively. Boundary layer thickness and definitions shown below were used to compare with our experimental data from R(t) oscillations:

$$\delta_{T1} = \left(\frac{k_l}{\rho_0 c_{pl}} \frac{R}{\sqrt{p_i/\rho_0}}\right)^{1/2} , \tag{4.3}$$

$$\delta_{T2} = \frac{4\pi R^2 k_l}{\mathcal{L}|\dot{n}_v|} . \tag{4.4}$$

The assumed boundary layers used in the PZ model are described by Eqn (4.3) and Eqn (4.4). The expected change of temperature across the boundary thickness, ∆T in

$$q = mc_p \Delta T . \tag{4.5}$$

Using basic heat transfer, the relationship between mass, density and volume and Eqn (4.5) the relationship,

$$V = \frac{4}{3}\pi[(R + \delta_{T1})^3 - R^3] , \tag{4.6}$$

Is obtained, where V is the volume of the heated region (assuming a shell of boundary layer thickness, δ1, and q is the calibrated laser input energy (known for flat tips) and approximated (2x-5x) for tapered tips. Using R_{max} of each bubble, ΔT can be computed for a specific tip energy for Biolase and compute the temperature change at a particular boundary layer near that bubble of a relevant timescale dictated by time scale $\frac{R}{\sqrt{p_i/\rho_0}}$. Finally, the energy retained by a bubble through its collapse can be normalized relative to the bubble's initial energy using the volume ratio $(R_2/R_1)^3$. This ratio can be termed "rebound energy".

4.4 Results

Experimental results were obtained for flat and tapered tips at all machine laser energy settings and tip diameters. However, given the large parameter space, numerical simulations are only provided for a representative set of parameters. The primary thermoexpansion pulse is examined, as well as emissions due to the first, second and third collapse. The main results for the pressure characterization for all the tips, energy settings and pulse modes are also provided in Tables 11-14 (Appendix A) as a comparison.

4.4.1 The Primary Pulse (Thermoelastic Expansion Wave)

These studies concentrated on using the H-mode, where the laser pulse length is 60 µsec. Absorption of this laser pulse results in a thermoelastic acoustic emission (pressure pulse) and the formation of a vapor bubble. The thermoelastic effect has been characterized previously in several studies that use similar microwave lasers [162–165]. Although these microwave laser high speed imaging studies used a much longer pulse (60 µs) compared to nanosecond or femtosecond pulsed lasers [131,149], they still generate a thermoelastic pulse. The primary or thermoelastic pulse is the first pulse that is seen by the hydrophone (see Fig. 27, labeled as A). It is due to either heating associated with the absorbed radiation or by nonequilibrium excitation of the electron subsystem (plasma generation). This photoacoustic process causes changes in material density upon laser absorption. In addition, the measured acoustic pulse envelope has been shown to closely match the laser pulse deposition. The spikes, or mode beats, of the laser create a modulation of the photoacoustic pulse at low pressures (unpublished results). The second physical effect, which occurs with increased absorbed energy, is the explosive evaporation related to phase transitions.[163]

The primary pulse A for a 300-µm tapered tip is shown in Figure 28a. The pulse amplitude does not significantly differ with tip geometry. The highest reproducible peak pressures are achieved with the 200 µm tapered tip (comprehensive results of measurements in this rather large parameter space are presented in tabular format in the Appendix A). The pressure amplitude decays as 1/r as the hydrophone distance increases, as shown in Fig. 28b.

Even at the closest hydrophone location of 5 mm, only the primary pulse rise times dropped below 100 ns; therefore only the primary pulse rise times were analyzed to determine if any waveforms were shocked. In particular, the tapered 200 µm tip at the highest energy settings (200 mJ) had the shortest rise times, decreasing down to 40 ns at the closest position. The

method described in reference [10] (associated with Fig. 3 of that paper) was used to analyze the rise times. In this method the derivative of the pressure pulse at a particular width is used to estimate shock fronts. The analysis suggested that there are no shock waves generated by the primary pulse at 5 mm from the laser tip. Previous analysis of bubble collapse shock waves suggests that if the laser does generate a shock wave, it reduces very quickly to a linear pulse with increasing distance from the source, probably becoming linear within a distance of 100 µm.[166,167].

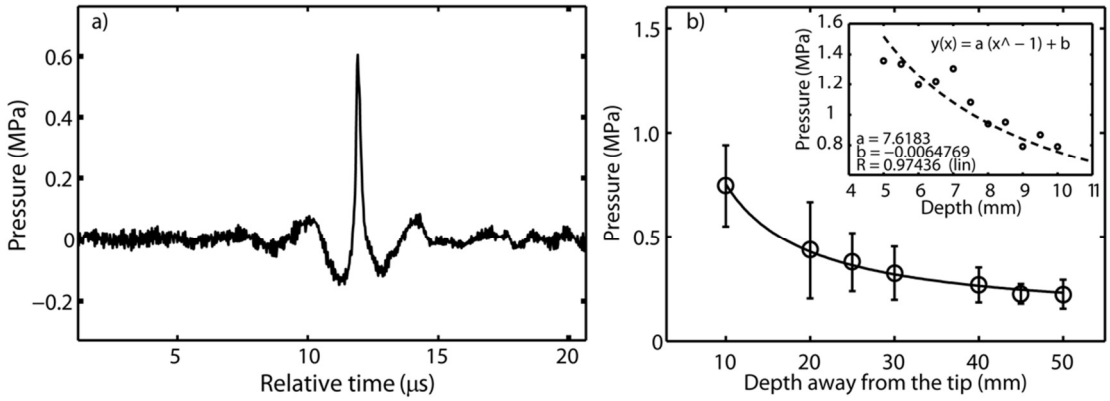

Figure 28. Primary pulse measurements. (a) Characteristic Primary pulse of a 300 micron tapered tip 10 mm away from the source at energy setting of 300 mJ (1.5W, 5Hz PRF). This pulse is a thermoelastic response of laser absorption. [163,164] (b) Pulse amplitude decays as 1/r, even as close as 5 mm from the laser tip.

Figure 27a shows a comparison of the primary pulse peak positive pressure with various tip geometries (Flat, F, or Tapered, T) and diameters for different energy settings (20 - 300mJ). The primary pulse A trends to slightly higher amplitudes with higher laser energy, as expected. There is not a significant difference between tapered and flat tips (Fig. 29a), nor is there a significant difference between tips of different diameters (Fig. 30a). However, the 200 µm diameter tip at its highest allowable energy (200 mJ) setting does appear to increase in peak pressure more than the other tips.

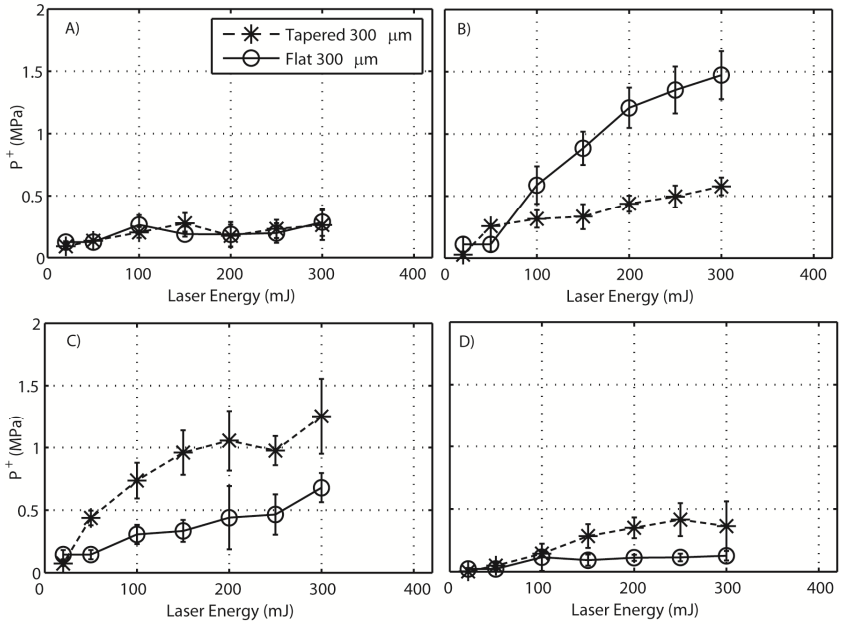

Figure 29. Tip geometry comparison for both tapered (T) and flat (F) tips of the primary pulse. (a), first collapse (b), second collapse (c), and third collapse (d) acoustic pressure (p+) strength pressure maximum as a function of laser energy setting at 15mm distance away. Marker indicates mean of N=6 independent pulses and lines indicate standard error.

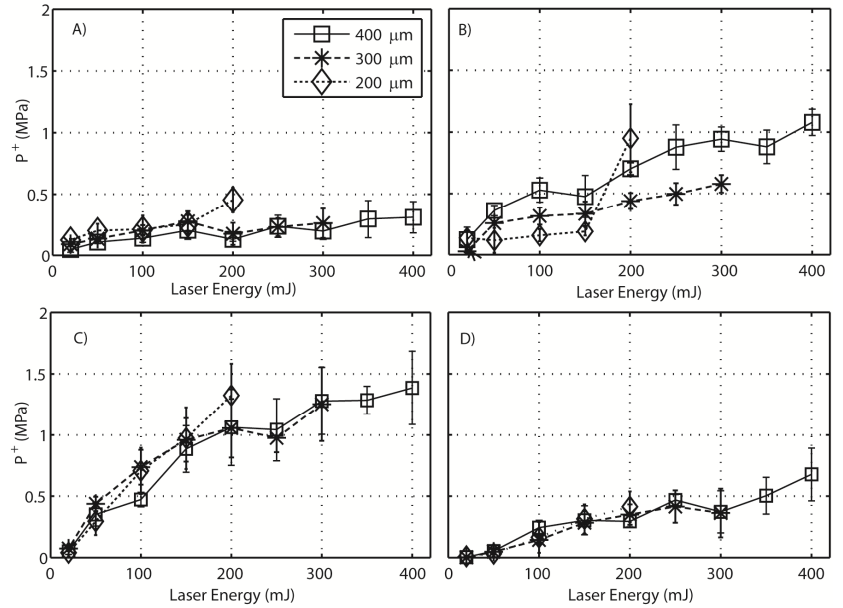

Figure 30. Tip diameter comparison for both tapered (T) and flat (F) tips of the primary pulse. (A), first collapse (B), second collapse (C), and third collapse (D) acoustic pressure (p+) strength pressure maximum as a function of laser energy setting at 15mm distance away. Setting used for both plots are the short pulse (H mode), and 5Hz PRF (Table 4).

4.4.2 The First Bubble Collapse and Rebounds

The vapor bubble that is formed by the laser pulse grows and collapses hundreds of microseconds later, followed by one or more rebounds. Its duration is always related to the

initial growth of the bubble (see Fig. 27). Further, the bubble translates further from the tip with increasing energy output (see *e.g.,* Fig. 32). For tapered tips, the translation during collapse increases from 0.3 to 2 mm as energy setting increases, and from 0.5 to 3.5 mm for the flat tips as the energy setting increases. There is some inertial confinement effect due to the air-water interface on the top of the device as shown on Fig. 26. Also note that the time between the primary pulse A and the first collapse pulse B (first collapse time, t_{c1}) was highly repeatable for all tips and energy settings, with the biggest standard error of the mean being not larger than ±3.5% the mean.

Fig. 29b shows a comparison of the first collapse (labeled 'B' on Figs. 27b and c) peak p+ with varied tip geometries as a function of energy settings (20 - 300 mJ). The highest reproducible peak pressures are achieved by the flat tip. The bubble generated by the flat tip was less spherical and smaller in surface area than that produced by the tapered tip (Fig 27a), and generated stronger first collapses. Fig. 30b shows a comparison of the first collapse peak p+ with varied tip diameters (200, 300 or 400 µm, Tapered, T) as a function of energy settings (20 - 300 mJ). In general, Fig 30b suggests that a larger tip diameter generates stronger first collapses, showing a significant relationship between tip diameter and first collapse strength.
The second collapse (labeled 'C' on Figs. 27b and c) occurs after the first collapse, and its duration is always related to the initial rebound of the bubble. The second collapse time, (t_{c2}), calculated as the time between the first collapse and the second collapse, which is related to the growth and collapse of the rebound bubble, is very repeatable for each fiber tip and each energy setting with the biggest standard error of the mean being not larger than ±2.5%. As before, the distance between the tip and collapse increases with energy setting and tip geometry. For tapered tips, the translation during collapse increases 1 mm to 4 mm as energy increases, and from 2 mm to 4.5 mm for the flat tips as the energy setting increases.

The pressures measured from secondary collapse are higher for the tapered tips regardless the diameters compared to the flat tips (Figure 29c). The second collapse mean values of single pulses (average of n=6), are shown in Figs. 29c and 30c. Fig 30c shows a comparison of the second collapse peak p+ with varied tip diameters (200, 300 or 400 µm, Tapered, T) as a function of energy settings (20mJ-300mJ). In general, Fig. 30c suggests that a larger tip diameter does not influence the second collapses and this effect is also observed in Fig 30d for the third collapse (labeled 'D' on Figs. 27b and 27c), showing no significant relationship between tip diameter and third collapse strength.

The third collapse's duration is always related to the second rebound of the bubble. As seen in Fig 29d, tapered tip measured pressures dominate the third collapse at any particular energy setting, as expected from a larger bubble. The third collapse happens further from the tip of the source. The depth of collapse for the third collapse varies between machine energy settings and also as tip geometries change. For tapered tips, the translation during collapse increases 2.5-5.5 mm as energy setting increases, and from 2.5-5 mm for the flat tips as the energy setting increases. The third collapse time, (t_{c3}), was found to have a SE of the mean being not larger than ±4.7% the mean, making the distance between second collapse and third collapse very repeatable. Third and fourth collapses happened mostly when using tapered tips at higher energy settings (E>50mJ), due to inertia of the initial collapses. For flat tips it is a noticeable effect, but definitely much weaker compared with the tapered tips. The results for all the tips, energy settings and pulse modes are also presented in Table 11-14 (Appendix A) as a comparison.

4.4.3 High-speed Imaging Analysis

The full analyzed sequence of growth, collapse, and rebounds are shown in Fig. 32 for both the Flat and Tapered tips, at 4 different machine energy settings, and for a tip diameter of 300µm. As discussed earlier, all bubble images were converted to an "equivalent" spherical radius in order to analyze their dynamical behavior. The bubble dynamics was very repeatable, with errors in size between 2.5% and 5%. Thus the errors are not shown in the R(t) curves. Bubble growth and collapse is correlated to input energy, while tapered tips generate much larger bubbles than flat tips for the same energy setting.

Typical bubble dynamics sequences for flat and tapered tips are shown in Fig. 31. These images represent only 9 of 43 frames, but illustrate the main characteristics of the growth and first collapse of these laser-generated pulses. For example, the flat tip generated very elongated bubbles, whereas the tapered tip created much more spherical bubbles. Also, one can see the translation of the bubble over the collapse and rebounds, especially for bubbles generated by the flat tip. Filaments between the bubble and laser tip can also be observed.

Researchers will often report collapse times, corresponding to the time between two acoustic emission pulses. These times can be between the primary pulse and first collapse, or between first and second collapse, *etc.* The collapse times are not reported here because the full R(t)

curve is shown. However, the tapered tip-generated bubbles have longer collapse times than those generated by the flat tips, as expected because tapered tips generate larger bubbles, and tip diameter does not affect collapse times significantly.

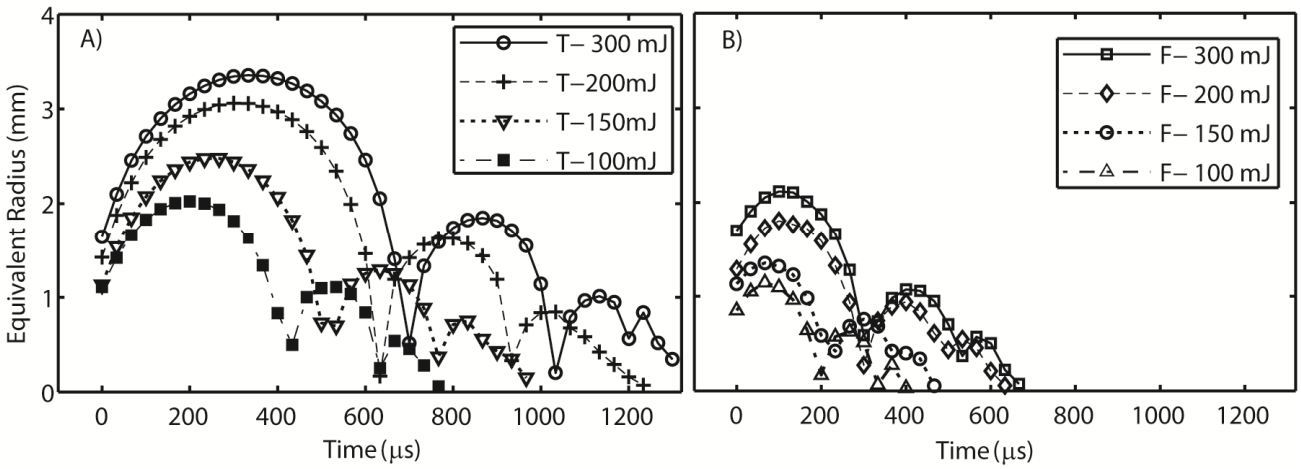

Figure 31. Radius vs. time curves obtained via experimental high speed imaging. A: 300 μm tapered tip generated bubble R(t) curves at four different machine energy settings. Larger machine settings, for the same tip, generate larger bubbles. B: 300 μm flat tip generated R(t) curves at 3 different machine energy settings, larger machine settings, for the same tip, generate larger bubbles. Bubble sizes generated from flat tips (equivalent radii) are smaller at the same machine energy.

4.4.4 Laser Pulse Duration Effect

The iPlus has two laser emission settings, a relatively short “H mode” (~60 μs pulse length), and a longer “S mode” (~300μs pulse length). Fig. 33a presents a comparison of the acoustic emissions from the main bubble collapse for the long and short pulse modes for a 300-μm tapered tip. Note that the longer pulse mode does not generate larger acoustic emissions with increasing laser energy. This can be explained by looking at the bubble dynamics (Fig. 33b). The long laser pulse does not generate bubbles that collapse violently; hence, their acoustic emission is much reduced. Previously reported results [168] indicate that for every measureable pulse emission detected from this process (A, B, C and D), the H mode (shorter pulse duration) was much more efficient than the S mode.

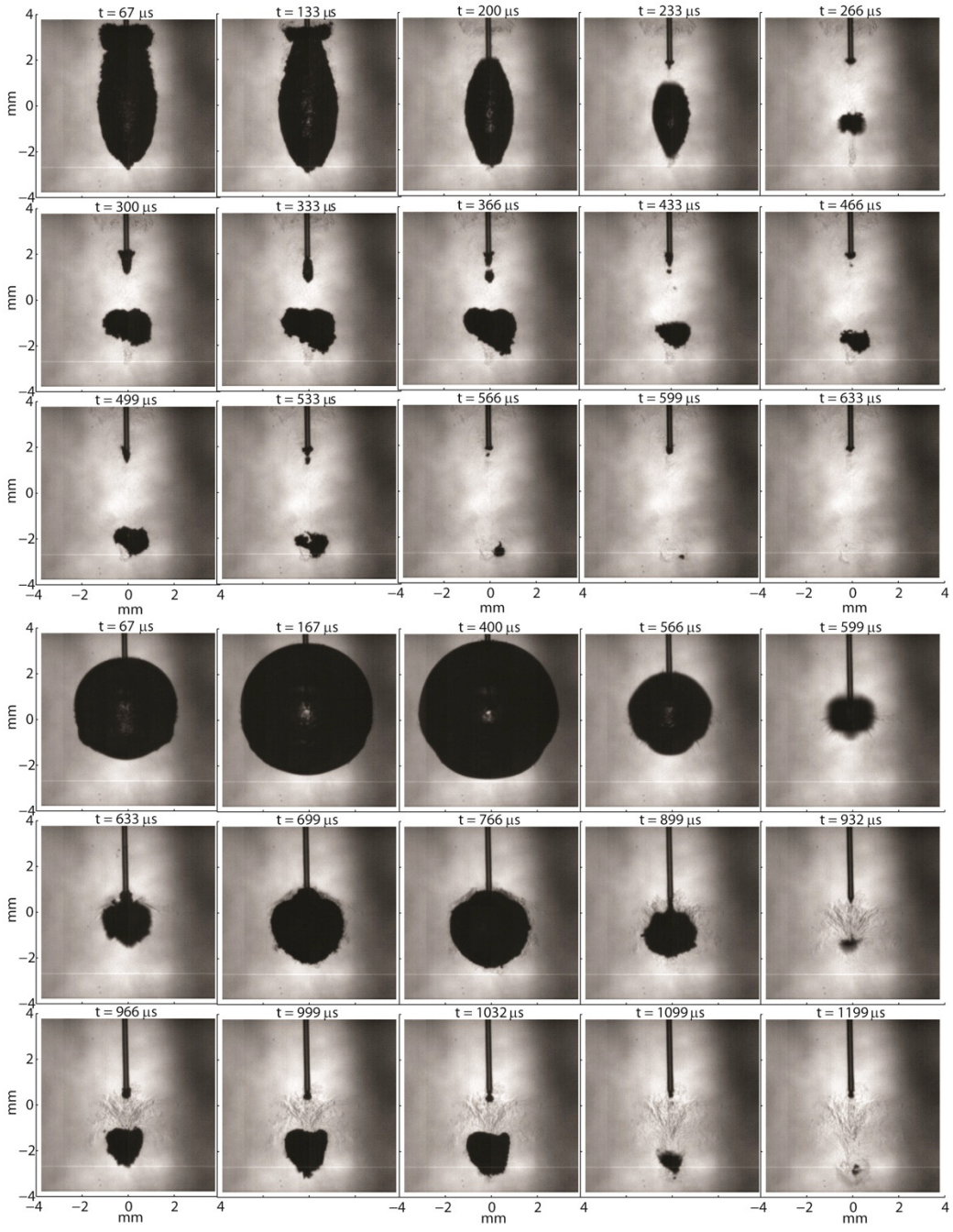

Figure 32. Characteristic high-speed images. Bubble dynamics of a single pulse using a 200µm diameter tip at 200mJ energy setting for the flat (top) and tapered (bottom) tips. The times for flat tip first collapse (labeled 'B' on Figs. 27), second collapse (labeled 'C' on Figs. 27) and third collapse (labeled 'D' on Figs) are (242µs,533 µs and 538 µs, respectively). The times for tapered tip first collapse, second collapse and third collapse are (581µs, 902 µs and 1078 µs, respectively). The primary pulse is not visible in high speed imaging since it occurs before bubble formation, but is always detected as an acoustic signal on the hydrophone pulse for both flat and tapered tips (Fig 27). Collapses, rebounds, and streaming effects are visible in many recorded videos. Jets are visible in t=266µs (flat tip), t=599µs (tapered tip), and t=932µs (tapered tip). Only a select 9 out of 23 images are shown.

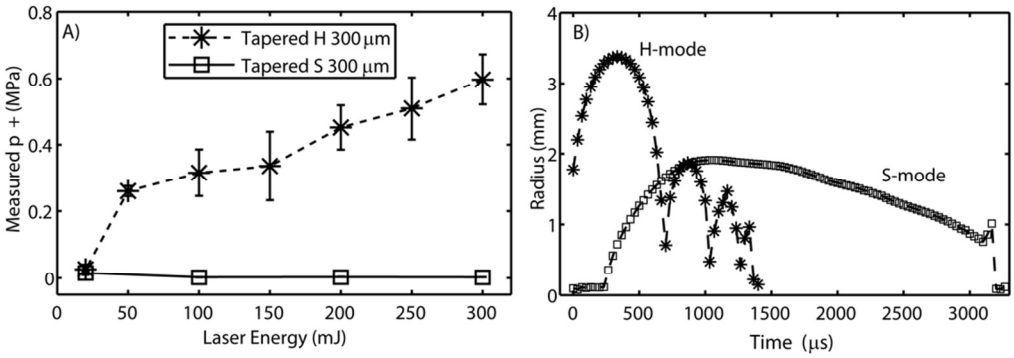

Figure 33. Comparison of the maximum P+ pressure measured as a function of laser energy setting (Power/PRF) between 300 micron Tapered H vs. S mode A) First collapse. The secondary collapse. Third collapses were not observable in the S mode using the high speed camera, and were not strong enough to be distinguished using the hydrophone signal, as compared with the example on Fig. 27. B: Characteristic (typical) Radius vs. Time dynamics between the H-tapered and S-tapered 300 micron tip for one laser energy settings.

4.4.5 Pulse Repetition Frequency Effects (PRF)

The iPlus allows for PRFs from 5-100 Hz. It was hypothesized that bubbles may not dissolve away fast enough at higher PRFs, causing them to interfere with newly created bubbles, reducing their acoustic emission amplitude. To test this hypothesis, a particular PRF was selected and the oscilloscope recorded 50 consecutive Primary pulse (A) and first-collapse (B) transients. The first 5 pulses were not used for the statistics, to allow the system to develop a steady cavitation field. Then, 30 of those remaining transients were collected and each transient was analyzed and the STD computed for display as error bars. The hydrophone was positioned 15 mm away from the 200 µm flat tip. Four different machine PRF settings were compared (Fig. 34). In general, higher PRFs resulted in lower acoustic emissions. From these data it can be concluded that PRF has a mild effect on pressures at lower PRF's but at high settings the repetition frequency effectively reduces the pressure by about 50%. The rebound emissions (C and D) were also significantly reduced at high PRFs (data not shown).

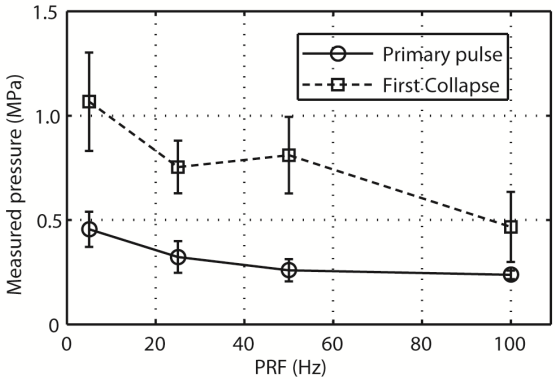

Figure 34. PRF variation plot. Pressure measured 15mm away from a tapered 200 µm tip collapse as a function of increasing pulse repetition frequency (PRF).

4.4.6 Modeling of Heat Transfer

Another way to show some of the data is to compare bubble emissions as a function of maximum bubble size. Figure 35a shows the pressure amplitude from the main collapse (B) for different tip diameters and geometry. Larger bubbles do not necessarily generate larger emitted pressures. For example, consider a maximum bubble size of 1.5 mm. The emitted pressures increase with increasing diameter for tapered tips. Flat-tip bubbles are more difficult to analyze because they are very elongated and do not collapse like a spherical bubble. Nevertheless, assuming equal conditions, one would expect that larger bubbles would generate more intense emissions, and for similar conditions, a bubble of a certain size should emit similar pressures.

If one performs a similar analysis with the first rebound emission (B) from the maximum rebound size, all the data collapse into a single grouping. For example, all bubbles that rebound to 1.5 mm generate the same pressure amplitude upon collapse. There is no tip diameter or geometry dependence. Such a trend implies that all rebounding bubbles have similar attributes.

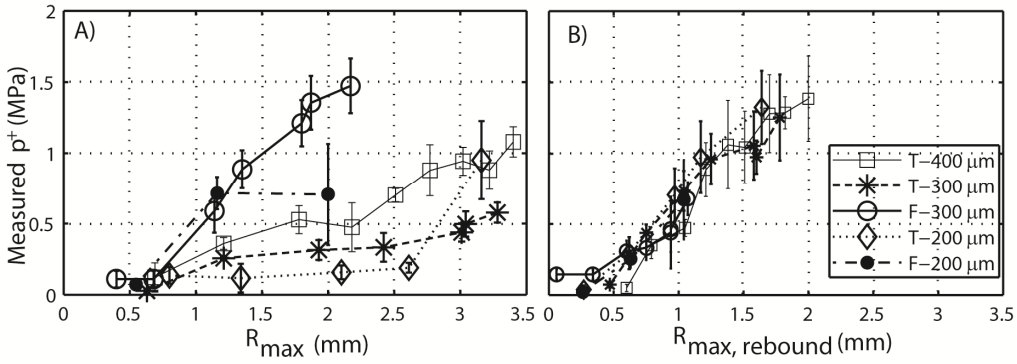

Figure 35. Collapse pressure as a function of maximum bubble radius and maximum rebound plots A. Pressure as a function of R_{max} for different geometries and tip diameters for energies between 20mJ and 400 mJ according to Table 4. B: Pressure as a function of Rrebound for different geometries and tip diameters for energies between all energies.

Another important observation is found by looking at Fig. 27b-c. For flat tips, the first collapse (B) always generates a higher peak pressure amplitude than the following rebound emission (C) for a given tip geometry and diameter. However, for tapered tips, the first rebound emission (C) is *always* higher than the main collapse (B). Yet from Figs. 31 and 35, the main bubble *always* grows to a larger size than the rebound.

Why do larger bubbles from the Tapered tip emit smaller pressures? And from Fig. 35a, why does the emitted pressure from the first collapse depend on the tip, while rebound emissions are independent of tips? The analysis below focuses on the following question: Could heat

retained in the bubble explain the variation in the first collapse and explain why rebound emissions from tapered tips are higher than the main collapse?

These questions motivated modeling the R(t) dynamics using Rayleigh-Plesset type models that describe the oscillation of a bubble as a function of time, including mass and heat transfer. Figure 36 shows some basic effects that the model is capable of describing. Figure 36 shows bubble dynamics of the same bubble at 3 different temperatures (20^0, 70^0 and 90^0 Celsius). With higher temperatures bubbles grow to slightly larger sizes, but more dramatically, they collapse much later. Further, the emitted pressures depend greatly on temperature. Hotter bubbles emit much weaker pulses.

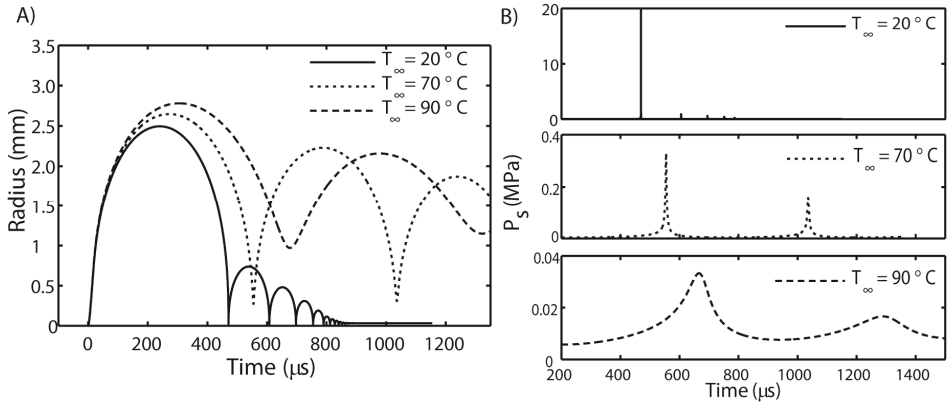

Figure 36. Modeled bubble dynamics at three different temperatures. A: Bubble dynamics of the same bubble at 3 different temperatures using PZ model, R=2.52mm. B: Radiated pressure from a R=2.52mm bubble 15 mm away from its center modeled at 3 different effective temperatures for the same R(t) cases shown in the previous figure (Fig. 27).

In order to compare the experimental data with Kreider's model, one must to calculate the collapse efficiency (Eqn 4.2 /Eqn 4.1, $E_s/\Delta E_B$,) and use the graph in Fig. 37 to calculate the apparent collapse temperature. The PZ model effectively captures the effect of temperature in the surrounding liquid. The bubble dynamics (especially the collapse times as shown in Fig. 36a) vary with temperature. Also, the emitted pressure can vary greatly (Fig. 35b). An example of extracting the relative ambient temperature from experimental data and using Kreider's[155] Fig. 11 is shown in Fig. 37, and although not shown, was also performed for several laser energy settings (see supplementary section 4.6).

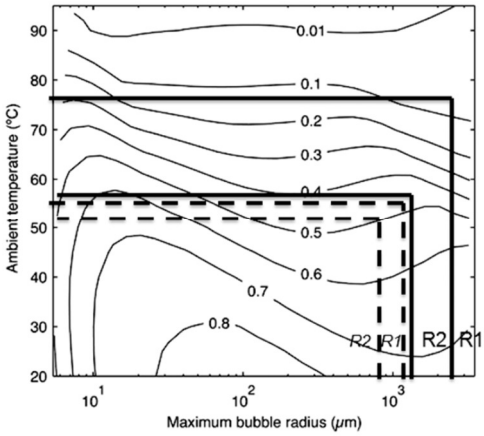

Figure 37. Temperature *vs.* bubble radius relationship. Figure adapted from Kreider et al [155], with their permission, used to determine the relative temperature of a specific collapse efficiency knowing the initial radius and the efficiency of the collapse for each bubble using high speed images and acoustic hydrophone measurements.

Results from flat (top) and tapered (bottom) tips are shown in Fig. 38. Flat: The R(t) curve and fit using a liquid temperature of 55° C. The emitted pressures of the first and second collapse are also similar to the measured pressures. Tapered: It was assume the temperature changed from 70° during the first phase (0<time<550 μsec) to 60° during the second phase (550<time<800 μsec). This is consistent with the bubble cooling down over time. Note also that the relative pressure amplitudes are close to what was measured. In particular, the emitted pressure at 800 μsec is larger than at 550 μsec. This is the lowest-order model that matches our observations. Tapered tips generate a hot surrounding liquid temperature that greatly affects the bubble's dynamics and emitted pressure.

Using Eqn (4.2) and comparing two geometries of laser generated bubbles with the same energy setting, the details of the analysis below using Figure 38 are explained as an example. The acoustic efficiency of a collapse is defined (first or second collapse) as $E_s/\Delta E_B$, since the maximum bubble radius before and after the collapse are known (R1 and R2 for the first collapse, and R2 and R3 for the second collapse). The acoustic efficiency of the first collapse (EF1) and the one of the second collapse (EF2) were calculated for the tapered tip generated bubble: EF1 = 0.06, which using the 2D contour plot (Figure 37) on the right of [155], assuming a bubble of R=2.42mm, leads to a temperature of a bubble collapsing in between T=70-80℃ (Figs. 38c,d) . For the second collapse, the parameters found were: EF2 = 0.46, with $R_{rebound}$ = 1.3mm T = 53 - 58℃, and even higher number for the third collapse, EF3 = 0.58-0.68, T = 35-40℃. Assuming 2-5X fluence compared to the flat tip fluence, for the tapered however it is

found, ΔT= 110-275 (234 with 4.25X fluence), that change of temperature can heat up a boundary layer of δ_{T1}=8.79 μm, in a time scale = 541μs. For the flat tip R(t) and pressure on Figs. 38A and B the parameters found were: EF1 = 0.47, corresponding to a temperature of T = 55-60℃, EF2 = 0.53, T = 53-58℃, and fluence can be calculated as Energy/Surface area of the circular tip cross section ($4\pi R^2$), ΔT= 219, δ_{T1}=7.06μm, Time Scale = 349 μs. The tapered tip modeling (Figs 38 c, d) required a 2 step model. Following the same analysis equivalent results were found for temperatures and excellent fits between the model and experimental R(t)'s and P(t) measured signals.

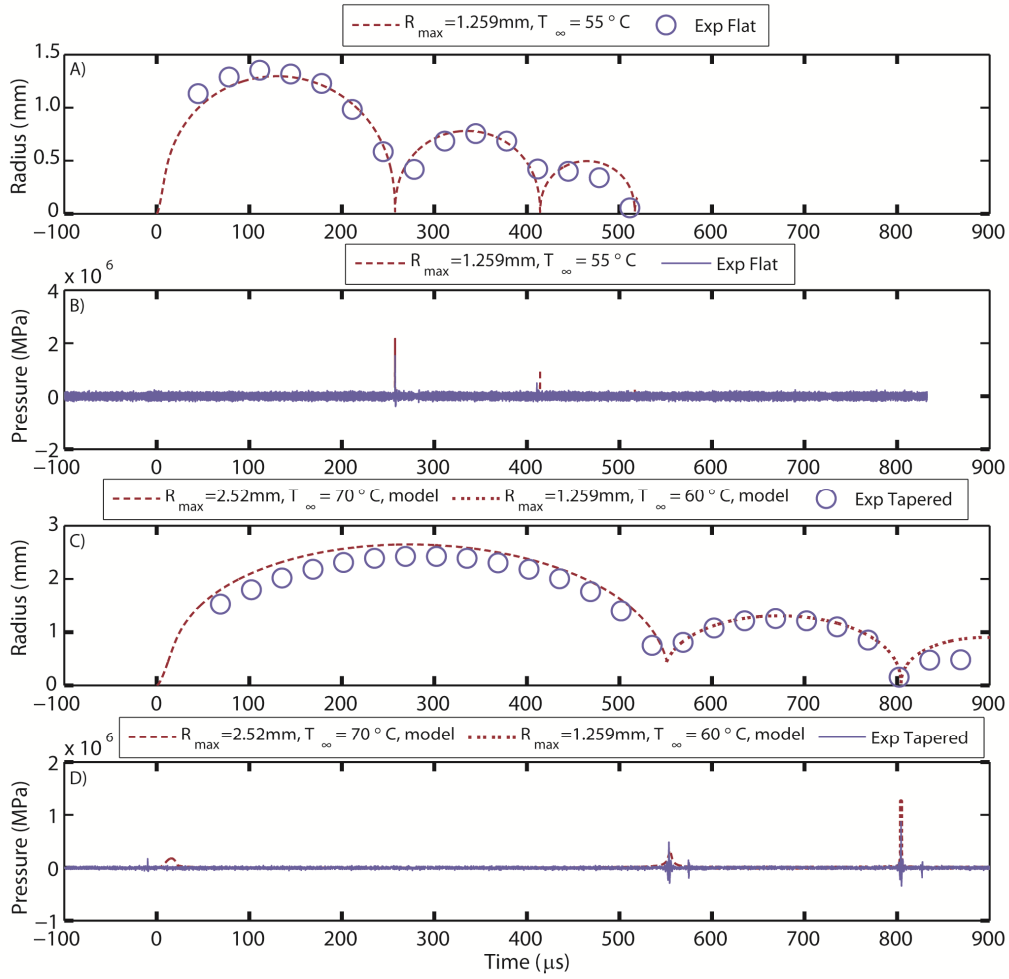

Figure 38. Comparison of tapered and flat tip modeling vs. experiments results. 150mJ setting comparison of tapered vs. flat modeling. Results from flat (top) and tapered (bottom) tips are shown in Figure 39. Flat: The R(t) was fit using a liquid temperature of 55° C. The emitted pressures of the first and second collapse are also similar to the measured pressure. Tapered: The temperature was assumed to change from 700 during the first phase (0<time<550 μsec) to 600 during the second phase (550<time<800 μsec). Tapered requires 2 step model of temperature variations to fit the curve and pressure pulses properly.

4.5 Discussion

The “equivalent” radial dynamics and emitted pressure resulting from a clinical dental laser emission, the Biolase Waterlase iPlus, was studied in detail. In particular, measurements were performed with two tip geometries, flat and tapered, at several diameters and laser parameters (energy, PRF, pulse length). Several aspects of the measurements are worth additional discussion, including differences between geometries, and comparisons with simulations. Our goal was not to measure every possible configuration. Instead some aspects of the two geometries, and at other times, performed detailed measurements from one or the other geometries (*e.g.,* rise time analysis) are compared below.

The primary pulse is independent of tip geometry, but generally stronger for smallest tip diameter. Tapered tips generate larger bubbles which last longer and collapse later. The first collapse is not the strongest (acoustically), but secondary collapses are. Second and third collapses are dominated by bubble rebound initial size (physically expected). First collapse pressure (P+ max) as a function of maximum bubble radius showed that a bigger bubble did not generate a stronger first collapse. There is a tip diameter and geometry dependence on how strong the first collapse is. In addition, as it was shown later, the second collapse could be of the same order or stronger than the same collapse, which is hinting to some process or some physical reason that might be changing the dynamics in the first collapse. The first collapse is not dominated by bubble size. Perhaps it is dominated by boundary effect, bubble temperature, or collapse direction asymmetry.

For the second collapse, the measured radius and pressure are positively correlated, as expected (larger bubble, larger collapse). In this case, a bigger bubble, different from the first collapse shown below, generates a stronger first collapse. There is no tip diameter or geometry dependence on how strong the first collapse is. Tables 11-14 (Appendix A) show maximum rebound radii as functions of energy, tip diameter, and device mode. Figure 27 highlights qualitatively the difference between a tapered and flat tip of the same diameter (300 µm) regarding their first and second collapses, and R_{max}. As it is noticeable the bubble from tapered tip reached a larger surfaces area (larger R-equivalent) compared to the football-shaped flat tip bubble for the shortest pulse length (H mode). However, there is a stronger collapse specifically measured for the first collapse in the flat tip case compared to first collapse in the tapered tip case, even if the surface area of the bubble is smaller than the tapered case. The second collapse, as demonstrated by Figs. 29 c,d, does behave as expected.

Shorter duration laser pulses (H-mode) result in larger pressures (60 µs *vs.* 700 µs) compared to longer laser pulses (S-mode). The primary pulse is independent of tip geometry, but generally stronger for smallest tip diameter. According to the hydrophone measurements, the rise time could be resolved at distances larger than 5 mm away from the source, leading us to understand that if there is a shock, it gets attenuated very quickly and close to its initial location, suggesting the use of Schileren imaging at ultrafast speeds in order to isolate the primary pulse process to determine the shockwave presence and its duration. It is also tells us that 5 mm and further away, targets will experience a pressure wave and not a shockwave as a mechanism of treatment with these type of settings used for the study.

Vogel and Lauterborn[132,133] have analyzed in depth the dynamics of laser-generated cavitation bubbles near solid walls, and its dependence on the distance between the bubble and the wall. Using high speed imaging and pressure hydrophones they were able to determine pressure amplitudes and profiles, and the energy of acoustic transients during collapse. They concluded that sound emission is the main damping mechanism in spherical bubble collapse, but minor in aspherical bubble collapse (less than 10% loss of energy for aspherical bubble, compared with about 73% of the energy in spherical bubbles).

Although sound emission from spherical cavitation bubbles is of no direct interest for the explanation of these bubbles (they collapse close to the fiber tip (a solid boundary), possibly heated, they will always collapse aspherically), it does, however, provide a solid basis to interpret the data for asymmetrical collapses and is still the best way to compare with experimental results.

Axial scans for all the tip diameters at different laser energy settings were performed and are shown below in Fig. 39. The pressure decay is always fitted to a 1/r spherical decay and can be safely assumed since the fits all agree for different tips, energies and fiber orientations up to 4.5 mm away from the tip. To prevent damage to the hydrophone, the tip was never brought into contact with the bubble. Thus, there is some uncertainty in the exact location of the tip of the therapy head membrane with respect to hydrophone, verified by high speed imaging. The specific way the pressure changes when closer than 4 mm away from bubble is unknown since it is to close and can affect the hydrophone. Pressure exhibits a 1/r spherical spreading from 5 mm away going far to 60 mm.

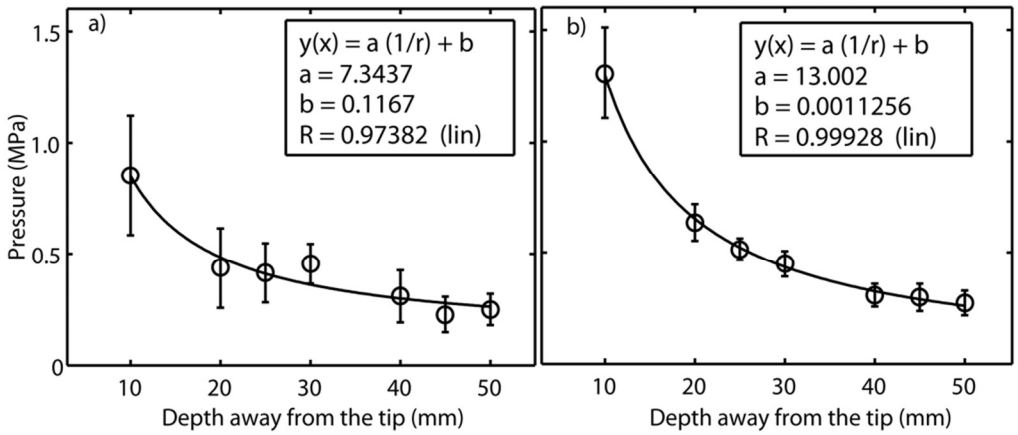

Figure 39. Variation of the peak pressure as a function of distance for the rebounds (A) first collapse (B) and second collapse of a 200 µm tapered tip at 250mJ energy setting. All plots are fitted with a y=1/r + b and error bars indicate +/-STD.

Further discussion on the model of 0-5 mm from the tip is needed here since that is our most relevant distance. Matula and Pencha [166,167] have shown that the shock front from spherical bubble collapse and sonoluminescence phenomena gets absorbed fairly quickly over time (over few nanoseconds, or 40 µm in distance). A shock generated may last up to 40 µm from incident location, therefore for relevant biological distances to biofilm (1-5mm) there might already be a non-shocked or absorbed pressure amplitude. A proper Schileren setup would be required to accurately assess the shock distance from lasing location. Regardless of whether the wave is shocked or not, the pressures (>1MPa) are high enough to generate bioeffects, shown by researchers who have measured the fracture toughness of enamel and dentin as 0.67-3.93MPa and 1.79MPa, respectively.[169,170]

Between 5 and 50mm away from the tip, at the highest setting and tip geometry/diameter combination found from Table 4, the rise time was properly resolved, without reaching bandwidth limits (40 ns). Despite the signal being non-linear the pressure jump, known as ΔP, was defined using the derivative definition of non-traditional shocks and calculated as a function of energy settings (not shown). Rise time seems resolvable by the band-limited hydrophone 5 mm away and beyond (not shocked at this point) although the waveform may be shocked prior near the collapse location.

Regardless of whether it is a shock at distances closer to the tip <4mm, a rise time measurement of 60 ns would correspond to a spatial scale on the order of 80 µm, which is comparable to the typical size of cells (1 – 100 µm). Thus many cells could experience an internal pressure gradient. According to Cleveland and Mcateer,[86] although tissue is usually

robust to isotropic compression, a leading shock front with a rise time on the order of 70 ns (spatial scale of 100 μm) suggests that structures in the range of 10 μm to 1 mm will experience a significant variation in stress across them as the shock wave passes. The short rise time associated with the pressure jump will lead to non-uniform straining of the tissue, resulting in shear forces. Lokhandwalla *et al.* showed that hemolysis is directly related to the pressure gradient at the pressure jump and validated shearing as a cell lysis mechanism in SWL.[117] It has also been shown that tissue structures are sensitive to shear stress and that the distortion of tissue by a shockwave can cause damage.[116] It is hypothesized that mechanical tissue damage is associated with a pressure jump. In addition, mechanoreceptors in cells can be affected by shear. According to Wang et al., application of a mechanical stimulus like shear stress to a cell turns on mechanosensitive ion channels, heterotrimeric G proteins, protein kinases, and other signaling molecules; these trigger downstream signaling cascades that lead to force-dependent changes in gene expression.[118] Based on all the above it was concluded that shear stresses from the shock front might be an active mechanism for SWT. It is thus important to determine whether or not therapeutic bioeffects are due to the positive (*i.e.*, stress-related) or negative (cavitation-related) pressures in order to optimize SWT treatments. For example, if shear stress were the major therapeutic mechanism, then treatments for near-surface conditions (*i.e.*, wound healing) might benefit from the shortest pulse duration (faster rise times, higher pressure jumps) and the smallest diameter tip (fastest rise times in primary pulse measured with 200 μm tip).

Energy calibration is performed with the flat tip, and then the tapered tip is used with flat calibration. Fluence of tapered tip unknown but estimated to be 2-5X higher (according to best fits a value of 4.25X higher fluence than the flat tip case was found, which agrees with Biolase's original estimate of 2-5X). Another argument from the literature that strongly supports the hypothesized idea behind heat deposition affecting the first collapse of the generated bubbles (shown in Fig.7 from [138]) is that if the laser fluence is greater than 1000 J/cm^2, the effect of acoustic collapse is counterproductive (pressure is reduced). For the same reason, long pulse durations are not acoustically efficient for producing strong collapses, due long time heating (Figs. 33 and 41).

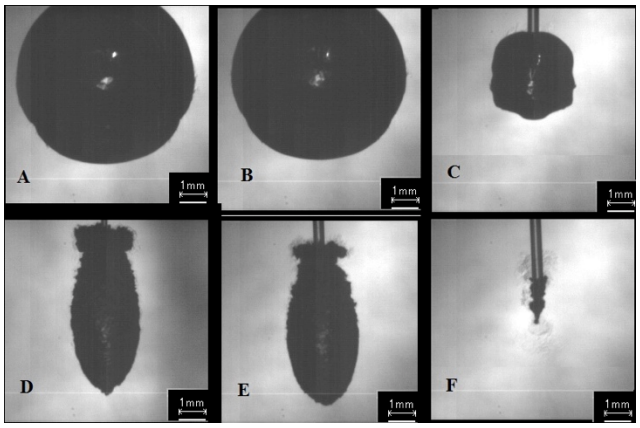

Figure 40. Different types of bubble shape compared at the same laser energy of 200 mJ. A, B are tapered 200, 300 tip under H mode respectively. D and E are 200 and 300 µm flat tips under H mode, respectively. C and F are S mode characteristic patterns of tapered C) and flat (F) 300 µm tips.

4.6 Supplementary Material

Short laser pulse vs. Long laser pulse using flat tips

Comparing the pulse mode H (~60 us pulse length) *vs*. Long laser pulse (~700us pulse length): the 300 µm diameter tips (tapered and flat) are selected as a consistent tip diameter to compare the performance of the long *vs*. short pulse. The results indicate that for every measureable pulse emission detected from this process (namely, PP, FC, SC and TC) the Short laser pulse(shorter pulse duration) was several orders of magnitude more efficient than Long laser pulse. Figure 41 shows the main comparison using the flat tips Using flat tips on Long laser pulse, the Primary pulse, first collapse, secondary and third collapse defined on Fig. 27 can be observed. Finally Figs. 42 and 43 show other best fits from the model and experimental data similar to the one shown on Fig. 38, but in this case for 2 different energy settings, 100 and 200mJ.

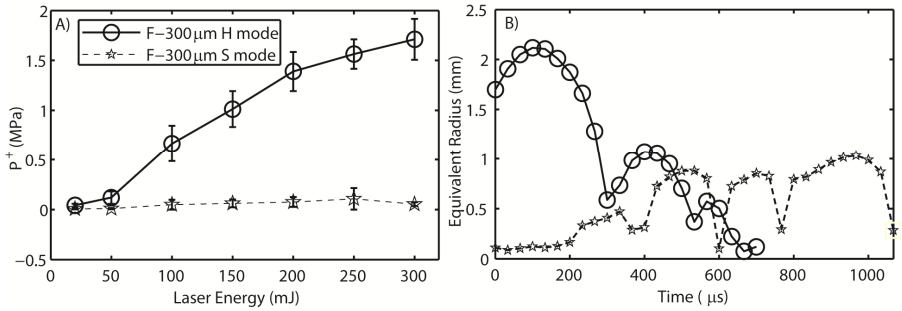

Figure 41. Comparison of short and long laser pulse duration in measured pressure. A: Comparison of the maximum P+ pressure measured as a function of laser energy setting between 300 µm Flat short (H) vs. long (S) laser pulse duration for the first collapse. Right: Characteristic (typical)

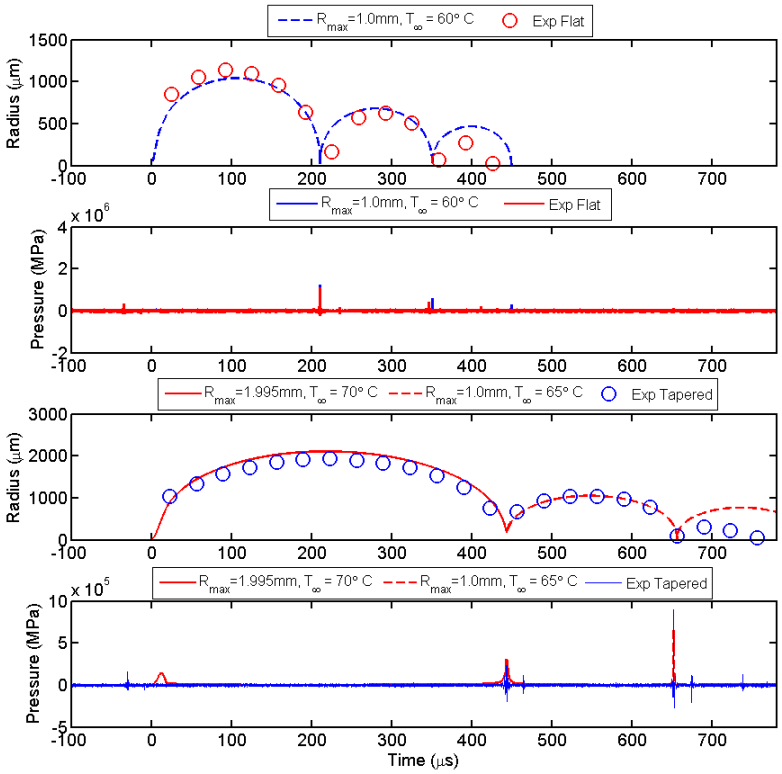

Figure 42. Comparison of tapered and flat modeling vs. experiments results. Results from flat (A and B) or tapered (B and C) tips R(t) and scattered pressure at 100mJ , respectively.

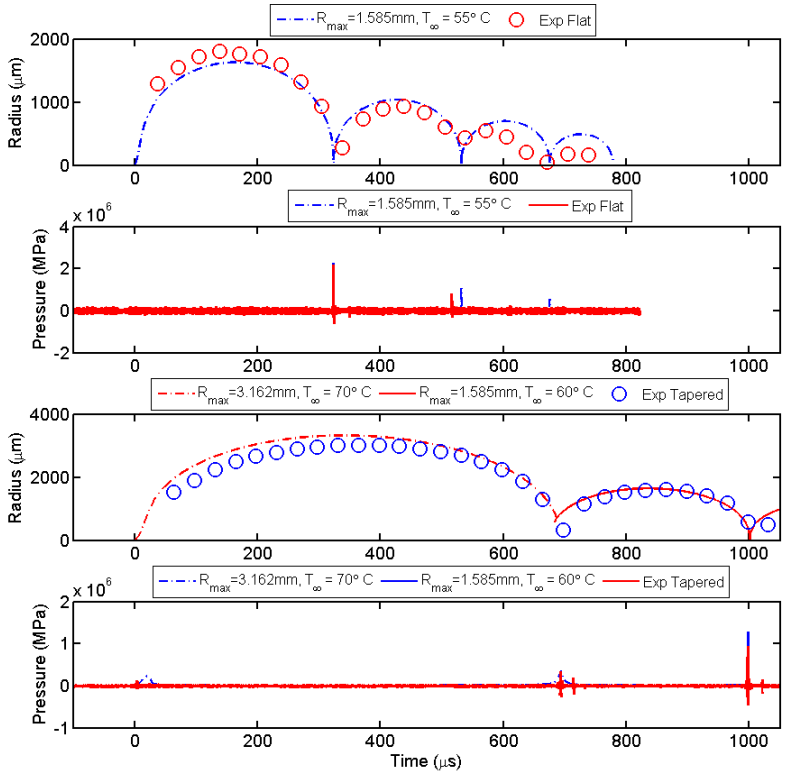

Figure 43. Comparison of tapered and flat modeling vs. experiments results. Results from flat (A and B) or tapered (B and C) tips; R(t) and scattered pressure at 200mJ , respectively.

4.7 Conclusion

In this chapter it was shown that the combination of measurements together with mathematical modeling provided a suitable tool for acoustic characterization of high intensity pressure fields and bubble dynamics generated by a clinical dental laser medical device. The acoustic emissions and bubble dynamics from the iPlus were characterized for different tip geometries and diameters. Both tips generated similar thermoelastically-induced pressure pulses. The main bubble collapse was stronger for flat-tipped bubbles, while the rebound emission is stronger for tapered-tipped bubbles. A nonlinear bubble dynamics model which accounts for heat and mass transfer was used to describe the R(t) dynamics and the emitted pressures. The results of modeling were validated by comparing pressure waveforms obtained in simulations and measurements. Heat deposition in the bubble is a potentially significant contributor to understanding bubble dynamics and emitted pressures from tapered and flat tips. Collapse times and emitted pressure can be explained by bubble temperature. Tapered tips generate much hotter bubbles than flat tips. Hotter bubbles collapse much later, and are much 'softer' than flat tip bubbles. This suggests that reducing the laser pulse length will result in more intense bubble collapses and more intense emitted pressures. Shock waves were not measured for any machine settings as near as 5 mm from the tip.

CHAPTER 5

Optical and Acoustic Characterization of Ultrasound Contrast Agents

5.1: Characterization Microbubble Shells by Flow Cytometry and AFM

5.1.1 Introduction

Ultrasound contrast agent microbubbles (MBs) are gas bubbles stabilized by a protein or lipid shell, and are used in diagnostic imaging.[33–35] MBs have also been developed for targeted imaging and delivery of drugs.[26] The design and characterization of the physicochemical properties of MBs' shell are crucial because the composition of the shell (i) provides stability during administration and circulation through the vasculature (ii) greatly affects the MBs' response to ultrasound and (iii) provides a backbone for conjugation of ligands and drugs. Biopolymer-shelled micro- or nano-bubbles have been synthesized by high intensity ultrasound-induced emulsification and cross linking of lysozyme and other thiolated biopolymers in aqueous solutions.[171–174] In the process of the ultrasonic formation of lysozyme microbubbles (LSMBs), lysozyme assembles at the air-liquid interface and forms a hydrogel-like structure (Fig. 44) stabilized by both newly formed intermolecular disulfide crosslinks and β-sheet domains.[35] The diameter and shell thickness of LSMBs, measured by optical and scanning electron microscopy over a set of 200 MBs, are 2.5 ± 0.5 μm and 150 ± 30 nm, respectively.[173] Compared with the commercial products based on lipid shells and perfluorocarbon gases[26], thick LSMBs offer many structural and functional advantages.

Large scale production of relatively monodispersed and stable micro- and nanometer sized LSMBs is possible using the flow-through sonication technique without the use of perfluorocarbons gases.

[C] Work published in part in:

Reprinted (adapted) with permission from: Cavalieri F, Best JP, **Perez C**, Tu J, Caruso F, Matula TJ, Ashokkumar M. Mechanical characterization of ultrasonically synthesized microbubble shells by flow cytometry and AFM. ACS Appl Mater Interfaces 2013;5:10920–10925. Copyright © 2013, American Chemical Society, DOI: 10.1021/am403108y

C Perez, C Wang, B MacConaghy, J Tu, J Swalwell, TJ Matula, The Journal of the Acoustical Society of America 136 (4), 2095-2095 Characterizing the pressure field in a modified flow cytometer quartz flow cell: A combined measurement and model approach to validate the internal pressure

C Perez, J Swalwell, J Tu, H Chen, A Brayman, TJ Matula, Acoustic and optical characterization of targeted ultrasound contrast agents, Proceedings of Meetings on Acoustics 19 (1), 075016

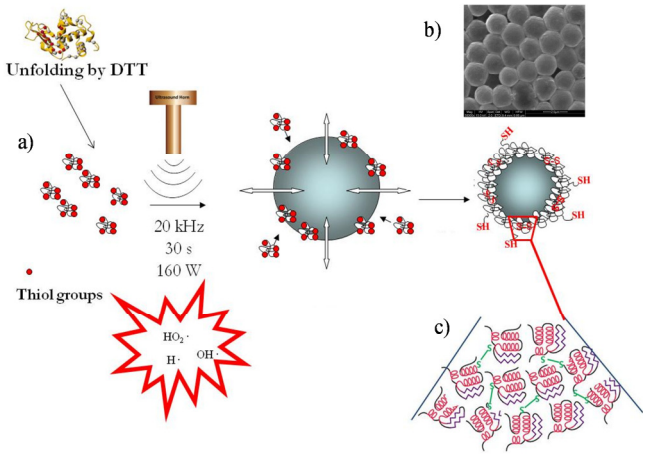

Figure 44. Schematic illustration showing the LSMBs preparation ultrasonic technique. (a), SEM image of dry LSMBs (b); schematic representation of the LSMBs shell structure (c).

LSMBs bear an intrinsic antimicrobial activity,[35] biodegradability and biocompatibility,[175] they are highly stable in aqueous suspensions at room temperature up to two years and possess echogenic properties for ultrasound contrast imaging.[174] The thick protein shell provides a platform for versatile functionalization with nucleotides, proteins[175] and gold nanoparticles.[176] In addition, it has been shown that LSMBs are readily internalized and degraded in SKBR3 breast cancer cells.[177] The emerging challenge is the design of therapeutic MBs which can potentially be transported across vascular walls (extravasation), and move through the tumor's interstitium. Rigid lipid and polymer shelled MBs (10 - 50 nm shell thickness) are not versatile enough to pursue for such innovative applications. The rigidity and elastic moduli of micro- and nanobubbles have been found to tremendously affect circulation lifetime and biodistribution.[178] Softer particles (bubbles) in general circulate longer *in vivo*, evade immune system phagocytosis and pass through narrow microchannels.[179,180] Cellular internalization and trafficking of MBs are also dependent on the particle's elastic modulus.[181] The precise control over the mechanical properties of MBs' shell will lead to the understanding as to how stiffness and deformability of MBs affect circulation lifetime, biodistribution, cellular interaction and adhesion to immune-system cells. The stiffness or rigidity of the shell depends on material composition, porosity and the shell thickness. To characterize the stiffness and elastic modulus of lipid and polymer MBs, AFM[57,58] and flow cytometry[47,48] have been used. Nanointerrogation of MBs using AFM coupled with a thin-shell theory for small deformations allows for the estimation of Young's modulus. AFM offers several advantages as a wide range of forces (from tens of

pico- to μNewtons) can be applied and deformations in the orders of nanometers detected on individual MBs in a suspension.

Thin shelled (30 nm) MBs made from a stiff synthetic polymer, poly(lactide), have a shell stiffness and a Young's modulus of approximately 1 - 7 N/m and 1 - 19 GPa, respectively, when analysed by AFM.[56] The Young's modulus of commercial lipid coated MBs, quantified using AFM nanoindentation, was 133 ± 59 kPa, where a Hertzian deformation was assumed and 19 ± 9 MPa when the elastic membrane theory was used.[58] Shell stiffness of phospholipid coated MBs was also estimated using acoustic interrogation of the shells. An average shell elasticity of 0.5 - 0.7 N/m was deduced.[48] The acoustic interrogation of microbubbles using flow cytometry was developed for phospholipid shells. We have investigated whether this technique can be considered as a versatile method for characterizing a variety of microbubbles such as polymer-shelled microbubble. In this work we show for the first time, the suitability of flow cytometry to determine the rheological properties of biopolymer-shelled microbubbles. We compare and discuss our results with previous studies performed on lipid-shelled MBs. In addition, we compared the mechanical characteristics of LSMBs determined by both flow cytometry and AFM.

5.1.2 Characterization of Lysozyme-Shelled Microbubbles, LSMB.

Appendix B provides details on the synthesis and materials used to produce custom made protein and lipid MBs. The mechanical properties of the shell of LSMBs were measured using a modified flow cytometer. Details of the flow cytometer can be found in the literature.[48] In brief, an InFlux Cell Sorter (BD Biosciences, San Jose, CA) was modified to include a custom-made square quartz flow cell (Hamamatsu Photonics, Japan) with a 150 μm flow channel as a measurement chamber in place of the standard nozzle and fluid jet. Acoustic coupling to the carrier sheath fluid and LSMBs samples occurred through a 0.7 mm thick piezoelectric element that was bonded to one side of the flow cell with epoxy. The source signal to acoustically drive the flow cell assembly was generated by using a function generator (HP 33120A, Agilent Technologies, Palo Alto, CA) connected to an RF amplifier (A150, ENI, Rochester, NY) though an RF step attenuator (837 Attenuator, Kay Elemetrics Corp, Lincoln Park, NJ). The PZT was driven with continuous wave sinusoidal voltages, leading to a variable pressure within the sensing region (ROI) of the cytometer. PMT signals were digitized by a 12 bit PXI- 5105 at 25 MHz for analysis. For the purpose of characterizing the LSMBs in this study, we used the flow

cytometer's side scatter optical path as described in our previous work of MBs characterization.[48]

The optical source was a 500 mW, 488 nm wavelength laser (Sapphire 488-500, Coherent Inc., Santa Clara, CA). PMT signals were routed to a custom high bandwidth (-6 dB at 5 MHz) current to voltage converter and logarithmic preamplifier similar to that described by Shapiro.[41] Custom built LabVIEW (National Instruments, Austin, TX) software was used to control the side scatter PMT gain setting. A National Instruments PXI data acquisition system was used for pulse digitization and storage. The flow cytometer PMT voltage output was converted to radius using Mie scattering theory. A modification of Mie scattering theory, applicable to a coated sphere, was first developed by Aden and Kerker[182] and later applied to coated bubbles by Marston *et al.*[183,184] Our implementation of the model for MBs is based on the equations in a book by Bohren and Huffman.[185] Normally, separate scattering coefficients should be applied to the shell and gas to calculate the relative scattering intensity from MBs. However, the scattering features of small microbubbles of approximately 100 nm thick are almost identical to those of free gas bubbles[59], thus the shell of our microbubbles can be neglected in the calculations. The specific calibration curve for this experiment is shown in Fig. 45.

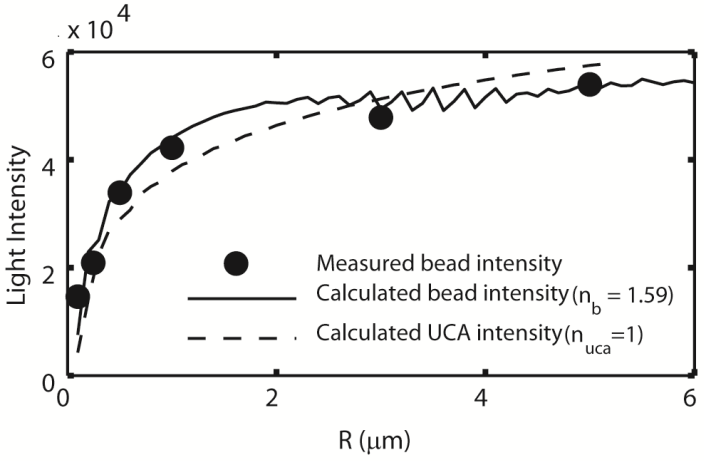

Figure 45. Relative scattered light intensity calculations and measurements as a function of bubble radius. The solid dots represent the light intensity scattered from the calibration beads. The solid line is the calculated Mie Scattering intensity. The dashed line represents the calculated scattering intensity from a MB.

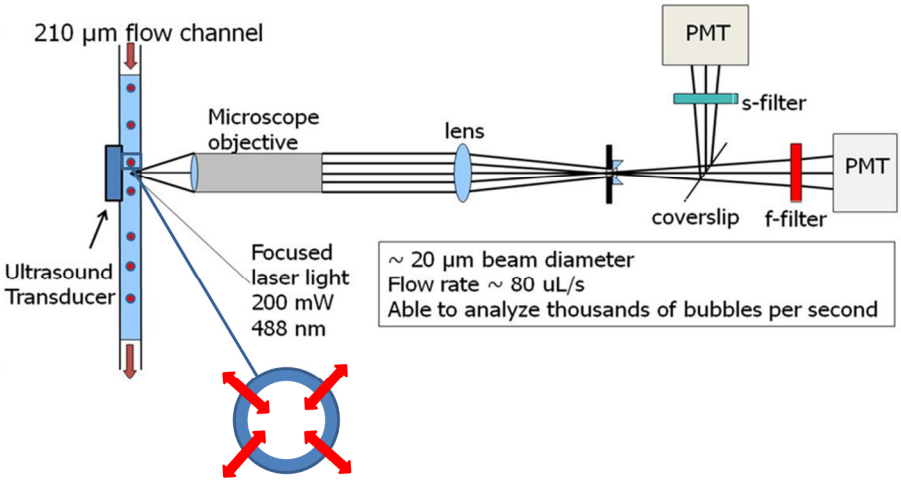

Figure 46. A schematic diagram of the acoustic interrogation apparatus.

For this experiment, the applied frequency was 1.2 MHz. We inserted a FOPH hydrophone, but could not rely on the pressure reading due to the small size of the channel and possible contact with the fiber. The pressure amplitude was then obtained as follows: the driving pressures were measured as voltage amplitudes from the function generator (V_a). We fitted the initial experimental pressure $Pa = kV_a$, where k is a scale value with the units of kPa/mV. The value of k was thus treated initially as a fitting parameter. After several numerical iterations with different data sets, this parameter converged to a value of 0.1 kPa/mV. In all subsequent experiments, we measured the pressure by applying this fitted calibration constant to the voltage signals. That is, knowing the applied voltage, and having found the constant k = 0.1 kPa/mV through iteration, the applied pressure can be determined. That leaves two unknown parameters, the shell viscosity and shell elasticity. Data processing to obtain elasticity and dilatational viscosity (χ (N/m) and κs (kg/s)) is described in more detail next.

Force measurements were performed using a Nanowizard II AFM coupled with a BioCell sample stage (JPK Instruments AG, Berlin, Germany). Measurements were performed using a colloidal probe AFM technique, where the cantilever was prepared by carefully immobilizing a glass bead (diameter 30 to 50 µm, Polysciences Inc., USA) onto the end of a tipless silicon cantilever (CSC12, Mikromasch, Estonia) using a 2-component epoxy adhesive (Selleys super strength, AUS), and the AFM as a micromanipulator. Before bead adhesion, the spring constant of the cantilever was determined using the thermal noise method. For the measurements, a 24 mm diameter round glass slide was used in the BioCell, and the glass substrate and cantilever

were washed using 30% isopropanol and cleaned using reactive oxygen plasma for 3 minutes (O_2 flow rate 0.1 L/min, 29.6 W, 300 mTorr; Harrick Plasma, USA) before measurement. The cleaned substrate was positioned at the top of a MB solution for 30 seconds to allow for positively charged LSMB surface attachment, and was then loaded into the BioCell and 500 µl of Milli-Q water added. The AFM head was connected to a Leica DMI 4000B optical microscope set-up with 40X objective (Leica Microsystems GmbH, Wetzlar, Germany) which allowed for optical visualization, and importantly the alignment of the center of the colloidal probe with the apex of the MBs for uniaxial deformation. Typical compression/retraction cycles were performed using a constant piezo velocity of 625 nm/s.

Collected force spectra were analyzed using JPK data processing software. A baseline was firstly subtracted from the non-contact z-range of the force-displacement data, a probe/surface contact point then assigned, and the effect of cantilever bending subtracted to result in force-deformation (F-δ) data from tip-sample separation data. The particle stiffness (k) was evaluated as the force-deformation gradient over the initial 20 nm of deformation. The Young's modulus (EY) was determined using the Hertz relationship for a spherical indented on a spherical particle, modeled over the first 40 nm of deformation. The Poisson's ratio was assumed to be 0.5, a reasonable value for an incompressible isotropic elastic material. In order to present representative k and EY values for the LSMBs, the force curves for 14 separate MBs were analyzed. Additionally, EMT and the Reissner model were used to verify the Hertzian EY value. Eqns (5.2 and 5.3) were used with the shell stiffness to provide an estimate of the EY over 20 nm of deformation.

5.1.3 Results and Discussion

Stable LSMBs were prepared using a well-established ultrasonic method as described in our previous study[177]. The mechanism responsible for the formation of LSMBs was previously elucidated.[171,176] In brief, two ultrasound-induced phenomena are involved in the process: emulsification and cavitation (Fig. 44). The emulsification depends on the shear forces generated by cavitation bubble collapse. In the second step the crosslinking between the protein aggregates is induced by the HO_2 radicals generated during the acoustic cavitation.

A custom-made flow cytometer was recently developed by Tu *et al.*[48] for analysing the mechanical properties of lipid-shelled MBs. We used this technique to characterize cross-linked protein-shelled MBs. A conventional flow cytometry unit coupled with an ultrasonic transducer

was used as shown in Fig. 46. A small PZT transducer was added to the side of a custom-built quartz flow cell with a 210 µm flow channel. Individual MBs travelling through the flow channel scatter the incident laser light (Fig. 46). The scattered light is collected and focused onto a field stop, then detected by a photomultiplier tube (PMT). As the LSMBs flow through the cell, the incident acoustic energy forces their radial motion. The instantaneous change in their size in response to the acoustic energy is characterized by a change in the scattering signal that could be detected by the PMT.

The rheological properties of LSMBs' shell depend upon the chemical and physical network of the lysozyme shell. The specific geometry of this network is determined by disulfide crosslinks, in addition to hydrophobic and β-sheet domains that hold the protein molecules together. The hydrogel-like architecture of the LSMBs exhibits viscoelastic properties imparted by the disulfide crosslinking and other intermolecular physical interactions. The dynamic acoustic interrogation of LSMBs allows for the determination of both elastic and viscous contributions. When the LSMBs transit through the acoustic "interrogation zone", a modulation in the scattering signal, as shown in Fig. 46, is detected. Light scattering of LSMBs was modelled using Mie theory. The scattering features of MBs of *shell thickness* = 100 nm are almost identical to that of free gas bubbles,[59] thus the shell thickness of the MBs can be neglected in the calculations. From the scattering modulation, a low pass filter provides the initial radius of the bubble using calibration measurements shown in Fig. 45. From the high-pass filtering of the same signal, we extracted the bubble oscillation data in order to obtain a radius versus time (R-t) calibration curve. An example of the best-fit R-t curve and the corresponding best fit parameters are shown in Fig. 47.

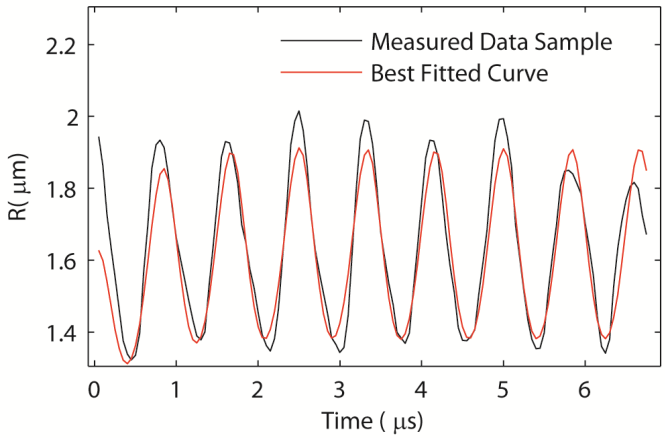

Figure 47. A sample best-fit data for LSMBs using Marmottant's model. The bubble was driven at 1.2 MHz and an acoustic pressure of 290 kPa. The best-fit shell parameters are χ = 0.12 N/m and κs = 9.0 × 10−8 kg/s, with R_o = 1.63 µm.

To obtain the rheological parameters of LSMBs' shell, Marmottant's dynamics Eqn (5.5) was used. Our study suggests that the R(t) curve acquired for LSMBs can be fitted well with the Marmottant model for the estimation of shell parameters. Although developed for phospholipid shells, the results suggest that Marmottant's model may be used for LSMBs shells, at least as a first approximation. Using fits of the experimental R(t) data, the shell elasticity (χ) and the dilatational shell viscosity (κ_s) were extracted. As reported in Table 5 and Fig. 48, the shell elasticity of the LSMBs is 0.15 ± 0.05 N/m, and is independent of the bubble radius to within experimental error. The elastic compression modulus can be related to shell elasticity by χ=Ed, where d is the shell thickness (150 nm). As a fundamental surface physical constant of a material, χ should be independent of the total amount of shell material or its surface area. The results were compared with previous work for shell characterization[48] using commercial ultrasound lipid-shelled MBs (Definity and SonoVue). Significantly higher shell elasticity, 0.5 - 0.7 N/m, and elastic modulus, 125 - 175 MPa, were observed for lipid shelled MBs.

Table 5. Shell mechanical properties of custom-made and commercial UCAs that have been analyzed in our acoustic flow cytometry system. The dynamics of the bubbles have been applied to measure the shell parameters.

UCA	**Shell Elasticity, χ (N/m)**	**E_y, (MPa)**	**Shell Viscosity, κ_s (kg/s)**
Definity (Lipid)	0.7 ± 0.2	175± 50	$3\cdot10^{-10}$ - $9\cdot10^{-9}$
Optison (Protein)	1.04 ± 0.3	69 ± 20	$3\cdot10^{-7}$ – $1.5\cdot10^{-6}$
Sonovue (Lipid)	0.5 ± 0.1	125± 25	$5\cdot10^{-9}$ - $3\cdot10^{-8}$
DSPC/DSPE (lipid)	0.27 ± 0.1	83 ± 33	$5\cdot10^{-9}$ - $7\cdot10^{-8}$
DSPC/DSPE/DSTAP (Lipid)	0.25 ± 0.1	90 ± 33	$1\cdot10^{-8}$ - $1\cdot10^{-7}$
LSMB's (Protein)	0.15 ± 0.05	1 ± 0.3	$1\cdot10^{-8}$ - $5\cdot10^{-7}$

This indicates that lipid assembly at the gas-water interface produces a stiffer membrane compared to the lysozyme hydrogel-like shell. Conversely, the covalent and physical networks of the protein offer a more elastic and softer interface. As for the shell viscosity, the shells of LSMBs are an order of magnitude more viscous than those of lipid MBs. The best-fit results suggest that the shell dilatational viscosity, κ_s, increases with an increase in the radius of the LSMBs (Fig. 49). This is consistent with previous experimental observations on lipid-shelled MBs.[48] Van der Meer *et al.*[186] hypothesized that the variation of shell viscosity with R_0 should be

attributed to rheological effects of shear thinning based on the dependence of shell viscosity on dilatational shear rate.

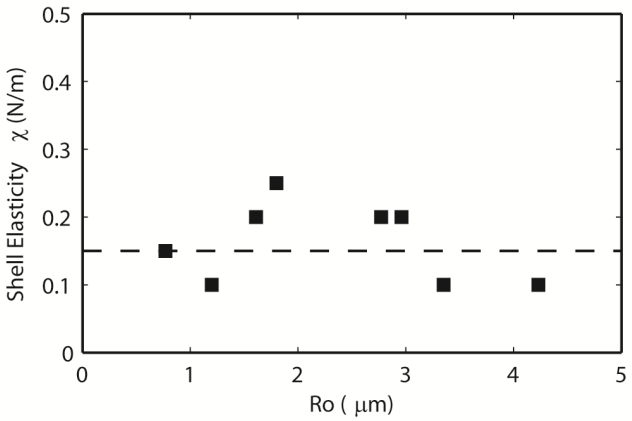

Figure 48. The relationship between LSMBs' shell elasticity and R0. The shell elasticity was obtained by fitting the experimental R(t) curves with Marmottant's model. The dashed line represents the mean of the elasticity values, $\chi = 0.15 \pm 0.06$ N/m.

For a given driving pressure, the shell viscosity does indeed decrease with increasing maximum shear rate (Fig. 49), in agreement with previously published data also using a single driving pressure.[48] To validate the mechanical and rheological properties obtained for LSMBs using the flow cytometry technique, force-indentation measurements were performed using AFM.

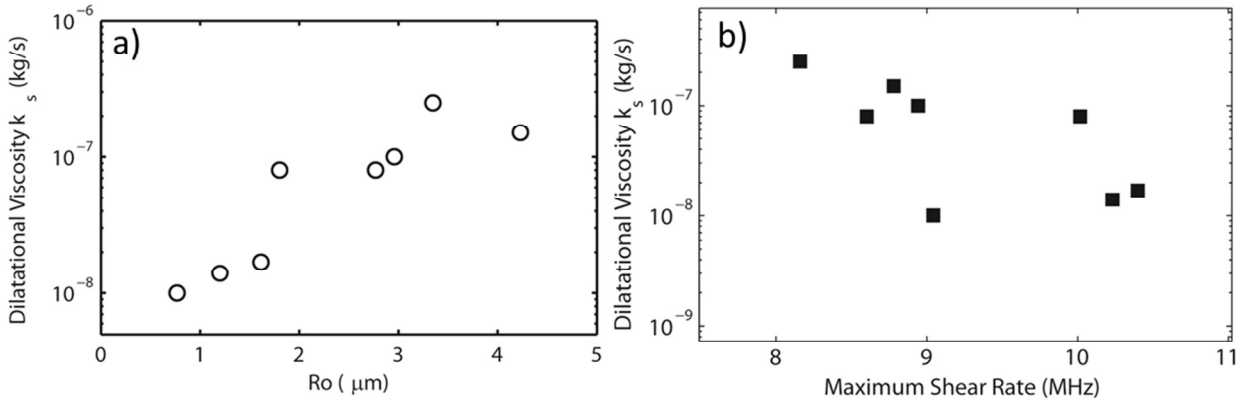

Figure 49. LSMBs shell mechanical properties a) The relationship between LSMBs' shell dilatational viscosity and R_o. b) The relationship between the shell dilatational viscosity and maximum shear rate.

Positively charged LSMBs (radius R_2) were immobilized to a negatively charged O_2 plasma-treated glass substrate to avoid lateral movement during compression. Figure 50 shows a typical force-deformation curve obtained using low-spring-constant cantilevers (k_c ~ 0.32 N/m) for an immobilized LSMBs. Forces of up to 35 nN were applied in order to effect a deformation

approximately equal to the LSMB shell thickness. A constant piezo velocity of 625 nm/s was utilized for all measurements. For all LSMBs studied, the shell elasticity was taken as the initial slope of the force-deformation curve (over ~20 nm).

As the LSMBs are shell-structured materials, the Young's modulus is often elucidated using a Reissner model making use of thin-shell theory[187], elastic membrane theory (EMT)[58,188] or even membrane contact theory for ideal gas compression.[189,190] For LSMBs with diameter 2.5 μm, the shell thickness is ~150 nm, indicating that these systems are outside the range for thin shell models where the maximum limit is often considered as $h/R < 1/20$.[191] In addition, membrane contact theory has only loosely been applied to pressurised capsule systems, as the model ignores fluid permeability through the shell and shell bending during compression, both of which are likely to occur during the deformation experiments. For cells, films and particles, a Hertz model (Eqn 5.1) is often employed for evaluation of the Young's modulus for small deformations, and has also recently been applied to investigate MB shells when treated as homogeneous spheres.[58] Indeed Santos *et al.* compared the use of Reissner (Eqn 5.2), EMT (Eqn 5.3) and Hertz models for understanding the mechanical behaviour of phospholipid microbubbles under a compressive force.[58]

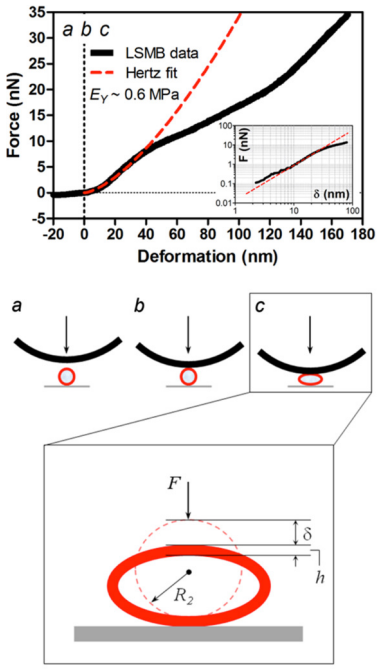

Figure 50. Typical force-deformation curve obtained using low-spring-constant cantilevers. Representative force approach curve and Hertz fit (E_Y ~ 600 kPa) for LSMB indentation and corresponding log-log plot (inset), and schematic representations of the AFM force-indentation measurements. For contact regimes a, b, and c, an illustration is provided, with a magnification of regime c. A colloidal probe with radius R_1 initiates an approach/retract force cycle with a single immobilized LSMB.

$$F^2 = \frac{16\delta^3 R_1 R_2 {E_Y}^2}{9(R_1+R_2)(1-\upsilon^2)^2} \quad (5.1)$$

$$F = \frac{\pi}{2\sqrt{2}} E_Y h^2 \sqrt{\varepsilon} + 4\pi E_Y h R_2 \varepsilon^3 \quad (5.2)$$

$$F = \frac{4(R_1+R_2)\delta h^2 E_Y}{3\sqrt{1-\nu^2} R_1 R_2} \quad (5.3)$$

The Hertz equation for a spherical indenter of radius R_1 cause deformation of a spherical object of radius R_2 is shown above in Fig. 50, where δ is the extent of the deformation for an applied force F, E_Y is the Young's modulus of the object material, and υ the Poisson's ratio of the material assumed here to be 0.5 which holds for an isotropic incompressible gel. It can be seen that for the Hertz model to apply, a linear relationship between force and deformation with a slope of 1.5 should be observed when the F-δ data is subjected to a logarithmic function. As can be seen from Fig. 50 (inset), nanoindentation of LSMBs adheres to Hertzian theory, where for all collected data the mean log-log gradient is found to be 1.5 ± 0.1. We measured shell stiffness and Young's modulus values in the range of 71 ± 21 mN/m and 0.6 ± 0.1 MPa, respectively, with no significant variation with LSMBs radius. This trend is in agreement with results obtained by flow cytometry. Results, as reported in Table 6, show that the Young's modulus was comparable using both methods.

To test the obtained Hertzian E_Y results, we additionally estimated the LSMB elastic modulus using EMT and the Reissner model, using Eqn (5.2 and 5.3), respectively. The shell stiffness (F/δ) was incorporated with the relative deformation ($\varepsilon = \delta/2R_2$) to allow for E_Y elucidation. Compressive deformation modelling using EMT was found to provide an E_Y result similar to the Hertzian value (0.6 ± 0.4 MPa), as shown in Table 6. The elastic modulus determined using the Reissner model was higher than that using both Hertz and EMT modelling, however it was also discussed that the LSMB systems studied here are outside the limits of conventional thin-shell theories. This is the first report of using the Hertz model for the mechanical analysis of a MB shell, presumably due to the large thickness of the LSMBs and the deformation range analyzed.

Analysis of the ratio of bending to stretching components for the EMT, as previously outlined by Lulevich *et al.*,[188] demonstrates that bending resistances dominate in such systems. From Table 6, the shell elasticity evaluated using AFM is however lower than the cytometry result, likely a result of force analysis over a small deformation regime for the microbubble shell. From analysis of the force-deformation curves, it was found that a force hysteresis existed between approach

and retract curves for all indentation experiments. This indicates that microbubble deformation over this range additionally contains a viscoelastic component, consistent with our reported flow cytometry results.

Table 6. LSMBs mechanical parameters evaluated using AFM.

Shell stiffness (mN/m)	Young's modulus (MPa)		
	Hertz	EMT	Reissner
71 ± 21	0.6 ± 0.1	0.6 ± 0.4	1.3 ± 0.6

5.1.4 Fitting Mechanical Properties of LSMB's Acoustic Interrogation Data.

The shell parameters, elasticity and dilatational viscosity (χ (N/m) and κ_s(kg/s)), were optimized with the minimum standard deviation defined in Eqn (5.4) below as:

$$STD = \frac{\sqrt{\sum_{i=t_{start}}^{t_{end}} (R_{exp,i} - R_{calc,i})^2}}{N} \quad , \qquad (5.4)$$

where t_{start} and t_{end} are the starting and ending points of the fitting region; $R_{exp,i}$ and $R_{cal,i}$ are the i^{th} measured and simulated microbubble radius along the time span, respectively; and N is the total number of the fitting points. In this set of experiments, bubbles were driven by 1.2 MHz sinusoidal ultrasound pulses with driving pressures ranging from 176 to 290 kPa, since K_amp converged to a value of 0.1 and the voltages used for both experiments were 2.9 V and 1.76 V, respectively. At 1.76 V we collected several samples and specifically analyzed 9 of them to find shell parameters. Some of the collected samples that were not analyzed did not display oscillations and this might have been caused by the possible fragmentation of the microbubble before arriving to the optical interrogation zone. To obtain shell-specific information, we fit a bubble dynamics equation to the radius-response data obtained from the flow cytometer. There are several models which describe the dynamic response of shelled MBs, considering shell properties such as shell thickness, viscosity, stiffness, friction parameter, and/or surface tension. To be consistent with our previous work, we use the theoretical model proposed by Marmottant *et. al.*[192]:

$$\rho_l \left(R\ddot{R} + \frac{3}{2}\dot{R}^2 \right) = \left[P_0 + \frac{2\sigma(Ro)}{Ro} \right] \left(\frac{R}{Ro} \right)^{-3\gamma} \left(1 - \frac{3\gamma}{c}\dot{R} \right) - \frac{2\sigma(R)}{R} - \frac{4\eta_l \dot{R}}{R} - \frac{4\kappa_s \dot{R}}{R^2} - [P_0 - P_a(t)] \quad (5.5)$$

In Eqn (5.5), R and R_o are the instantaneous and ambient bubble radii, the dots over the R represent time derivatives, ρ_l and η_l are the density and viscosity of a Newtonian liquid, P_o is the ambient pressure, γ is the polytropic exponent of the gas, c is the acoustic velocity in the liquid, κ_s is the shell dilatational viscosity, and the acoustic driving pressure $P_a(t)$ is the sinusoidal incident acoustic pressure. The following are some physical constants used for the simulation: $P_0 = 1.013 \times 10^5$ Pa, $\rho_g = 1.161$ kg/m^3, γ = 1.07, $\rho_l = 10^3$ kg/m^3, c = 1500 m/s, $\eta_l = 2 \times 10^{-3}$ Pa·s. The surface tension model (Eqn 5.6) that considers buckling of the shell and rupture, σ(R) is modeled as:

$$\sigma(R) = \begin{cases} 0 & if\ R \le R_{buckling} \approx R_0 \\ \chi\left(\frac{R^2}{R_{buckling}^2} - 1\right) & if\ R_{buckling} \le R \le R_{break-up} \\ \sigma_{water} = 0.072\ \frac{N}{m} & if\ R > R_{rupture,} \end{cases}, \qquad (5.6)$$

where χ is the shell elastic compression modulus. For large amplitude oscillations, the surface tension varies within an elastic regime until the shell breaks at $R = R_{break\text{-}up}$. Although the initial $\sigma_{break-up} = \chi\left(R^2/R_{breakup}^2 - 1\right)$ should be greater than σ_{water} because of shell cohesion, the surface tension would relax to the value of an uncoated bubble (σ_{water}) after break-up and remain at this value for all $R > R_{rupture}$. Afterwards, the surface tension reversibly returns to the elastic regime during the compression phase as $R_{buckling} \le R < R_{rupture}$, and remains a constant σ_{water} during each subsequent expansion phase as $R \ge R_{rupture}$. Here, $R_{rupture}$ is defined as the bubble radius that can be reached during each oscillation following initial break-up when $\sigma(R) = \sigma_{water}$. For the value of $R_{break\text{-}up}$, two cases are considered in the present work: one is the case in which the shell surface tension σ reaches the critical value of σbreak-up; the other is the case in which the shell breaks up due to violent collapse. Flynn and his coworkers (see[193,194]) established a radial oscillation threshold for $R>2R_0$ for intertial cavitation of free bubbles. Therefore, we set $R_{break\text{-}up}$ to be $\min[R_{buckling}\sqrt{\frac{\sigma_{breakup}}{\chi}} + 1\ ,\ 2R_0]$ in the present work. The value of $\sigma_{break\text{-}up}$ is set to be 1 N/m, reported by Marmottant *et al.* for the resistant shell[192]. To fit the parameters in the model for K_amp we used a range from 0.1 to 1 and had a 0.1 step size. The fitting parameter χ (N/m) had a range of 0.02 to 1 and a step size of 0.02. The fitting parameter κ_s had a range of 10^{-9} to $5\text{x}10^{-7}$ and a stepsize of 10^{-9}.

5.1.5 Sizing, Attenuation and Model-experimental R(t) Curves.

The size distribution of custom-made protein-shelled microbubbles using the acoustic flow cytometer is shown in Fig. 51.

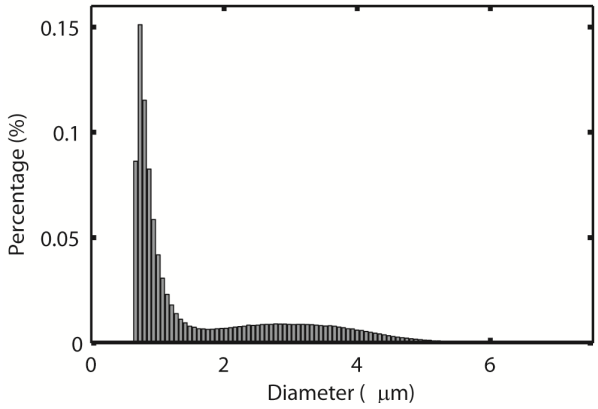

Figure 51. Size distribution of custom-made protein-shelled microbubbles measured with a flow cytometer. The height of each bin shoes the percentage of bubbles within each bin interval.

Several of the curves in Fig. 52 represent a different bubble-model fit for material properties that were shown on Fig. 48-49. Each figure contains the ambient radii and mechanical properties obtained, together with the standard error of the best fit for each bubble.

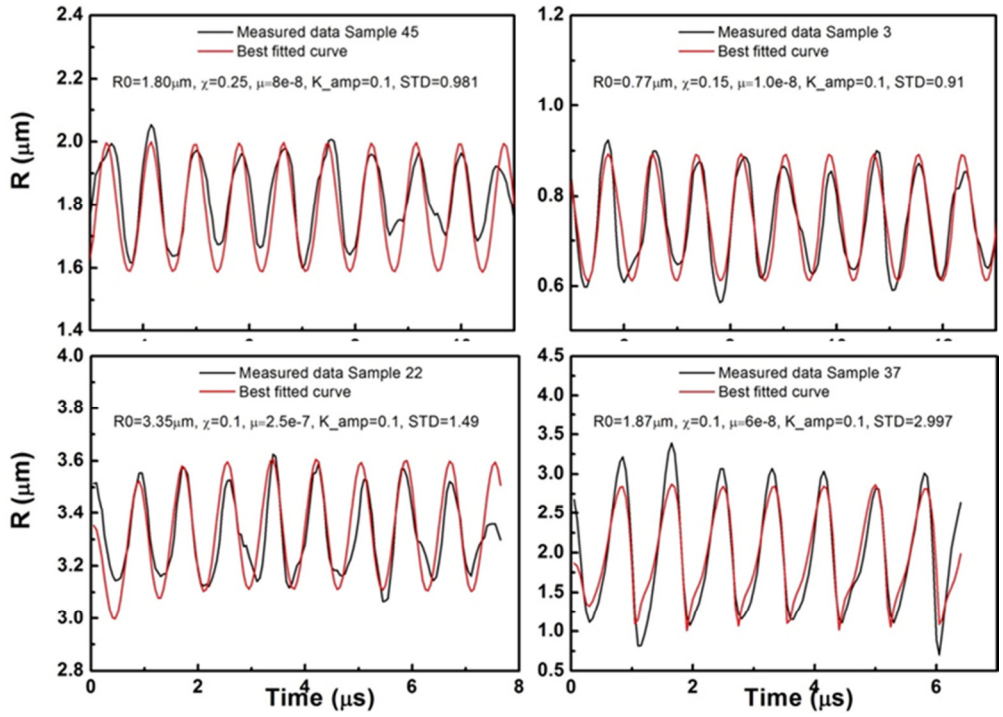

Figure 52. A sample best-fit responses for a protein microbubble using Marmottant's model. The bubbles were driven at 1.2 MHz with Pa = 290 kPa.

The acoustic calipers involved the transmission of ultrasound pulses from one transducer through a cuvette containing microbubbles and receiving the transmitted pulse at a distance d

from the transducer. The simple setup is shown below on Fig. 53a. Frequencies from 1-10 MHz were investigated in a 30 mm cuvette with a suspension of LSMB.

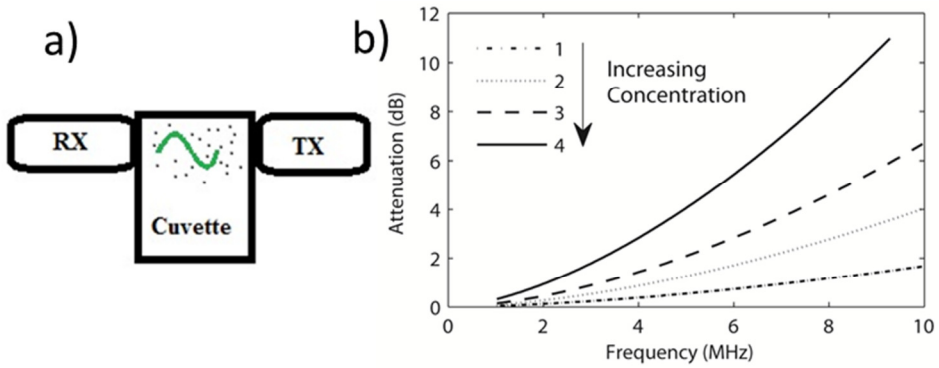

Figure 53. Acoustic calipers setup. a) Tx (transmit) and Rx (receive) transducers are used to interrogate attenuation of a sample due to absorption and scattering of ultrasound, providing information about the sample. b) Attenuation as a function of driving frequency for 4 samples of increasing concentrations.

From Fig. 53 (b) there is no resonance peaks observed within the frequency range scanned. Previous studies [195–197] have shown that for broad distribution of sizes (as shown in Fig. 51) in a solution of contrast agents it is difficult to find a resonant peak; rather, the curve usually looks like the one on Fig. 53 (b).

High speed imaging of LSMB's in response to a single focused ultrasound pulse.

The same high speed imaging setup shown in Figure 28, Ch.3 was used to investigate the response of LSMBs to high pressure pulses. Fig. 54 shows a sequence of high speed imaging frames from LSMBs responding to a single pulse of a ESWT device characterized on Chapter 3. It can be seen from Fig. 54 that most of the LSMB respond to ESWT-like single pressure pulses and that there is evidence of the thick shell of the MBs as is seen in the high-speed images sequences (Fig.54).

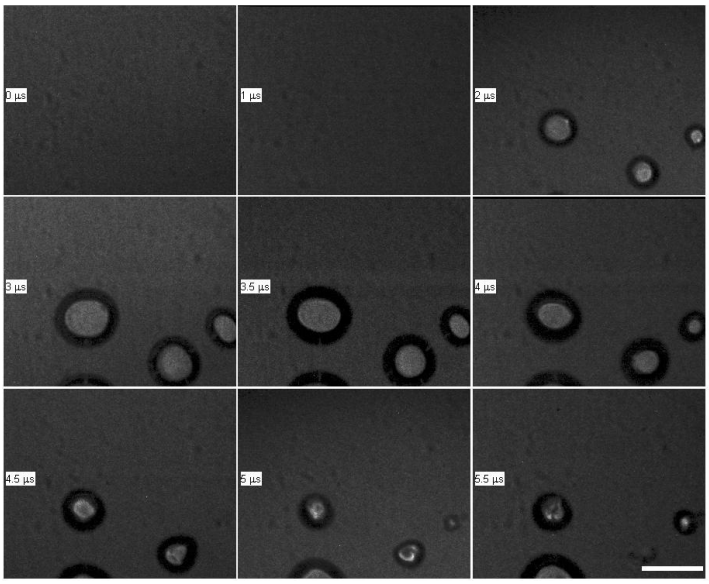

Figure 54. Response of lysozyme protein-shelled bubble to ESWT device at -6MPa characterized in Chapter 3. Each frame is 0.5 µs from each other.

5.1.6 Conclusions

In conclusion, our results suggest that the use of flow cytometry in combination with force microscopy permits the extraction of physically meaningful viscoelastic parameters for LSMBs. The acoustic flow cytometer provides comparable shell elastic moduli to AFM methods. In addition, the acoustic flow cytometer has been used to characterize a thick shelled LSMB, which is the first type of thick-shelled (150nm) MB characterized with this system, since most commercial MBs are have a shell thickness between 3-15nm.

5.2: Optical and Acoustic Flow Cytometer: System Instrumentation Overview

5.2.1 Mechanical/Electrical/Optical Changes

A 500 mW, 457 nm laser (Melles-Griot) was added to the system for both fluorescence excitation and light scattering (see Fig. 56) with capabilities of adjusting the power by small increments and increase photon count on the detectors. The laser beam is directed to the flow cell analysis area *via* optical mirrors and prisms, and focused in the center of the flow cell using a 75 mm focusing lens (Edmund Optics), which for the Gaussian TEM00 laser beam yields a theoretical minimum spot diameter (1/e^2) of 32 µm. The addition of 4 photomultiplier tubes (PMT, C6270, Hamamatsu) allows the current system (Fig. 55) to use several modes of detection: side-scattered and fluorescence signals are emitted at 90 ˚ from incidence and

collected by a 50x long working distance objective (Mitutoyo, 378-805-3) with a shallow 0.9 μm depth of focus. The system can detect fluorescence above 520nm (exchangeable filter). This new arm of the system was added to take advantage of forward-scattering for accurate sizing and discrimination of particles whose size and shape could be completely isolated due to a single parameter (side scatter sometimes is not enough for particles with different indices of refraction, *i.e.* bubbles and cells).

The light emitted in the forward direction was also collected with a 50x objective and focused to a special pinhole described by Swalwell *et al.* [198] that allows for the forward scattered detection and position sensitive detection of particles. Forward scattering together with two position sensitive detectors (see Fig. 58) allows the monitoring and gating of proper counts that go through the center of the square flow cell as demonstrated by Swalwell *et al.* [198]. The addition of one imaging camera to monitor the position of the center of the stream, with respect to the detection pinhole, aided for alignment of the new forward-scattering arm. Specific filters were added at the face of each PMT to detect the correct wavelength desired and block wavelengths that are higher. A light stop filter was added to block 99% of the light going to the forward scattered PMT in order to be able to utilize the laser at full power, and increase photon count for the side scattering arm (always lower photon count due to 90 ˚scattering).

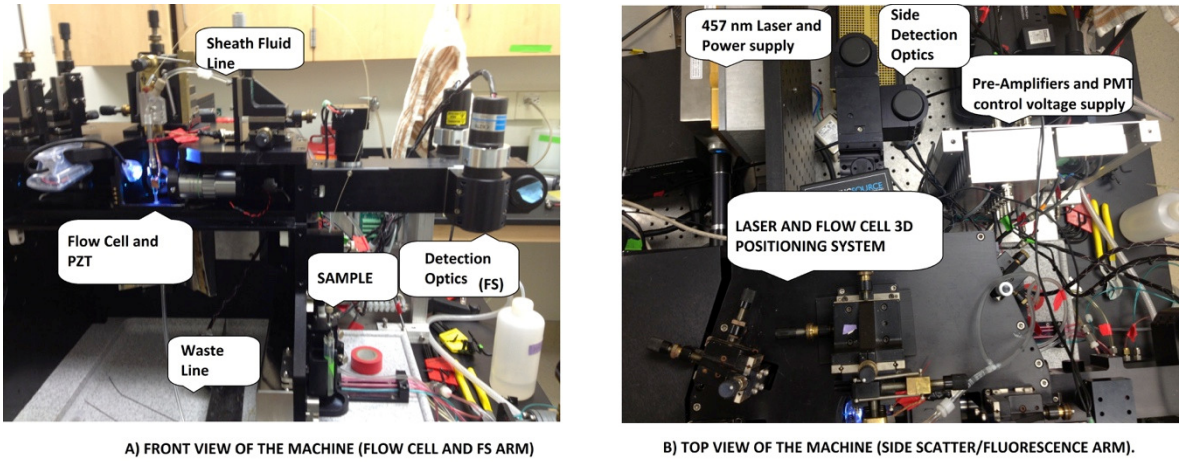

Figure 55. System front and top views. The forward scattered arm (FS) arm is easily observed on the first vie (front view) together with the flow cell. The side scattered arm and fluorescent arm are together and can be observed in the top view of the machine (B)

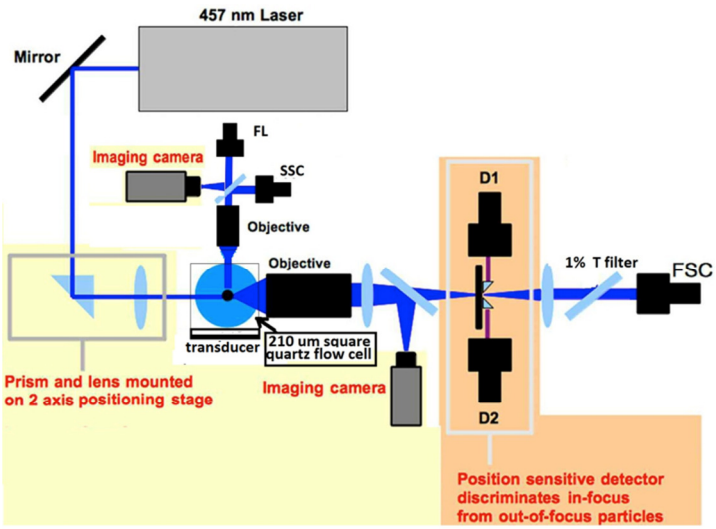

Figure 56. System Instrumentation: The laser is adjusted using prisms, mirrors and focusing lenses. Laser position on the stream is constantly monitored using both cameras (one for FS and one for SS). The position of the particles passing the stream is measured by the 2 position sensitive detectors shown on the forward scattered arm (D1 and D2, as labeled).

5.2.2 Calibration and Data Processing

Mie scattering theory was implemented in order to convert the detected pulses by the photomultiplier tubes into actual bubble radii. The calibration description for the 90 ˚ direction is described by Tu *et al.* [199] , and the addition of a 0˚ scattering arm adds a new calibration curve to the system, as well as a new way to distinguish two objects that might have different indices of refraction that, due to their different sizes, might seem to scatter the same amount of 90 ˚ light. The calibration procedure for this new detection arm was similar to the one described above. For the calibration process we used calibration YG beads (Invitrogen, Carlsbad, CA) of known radii 0.5, 1, 2, 4, 6, 10, or 15 μm. The use of the calibration beads also allows to the determine the system resolution: the ability to use forward scattered (FS) and side scattered (SS) measurements to differentiate different populations of beads, and it can also aid in the calibration of the fluorescence detection since some of the beads contain yellow/green fluorophores.

PMT signals were routed to a custom array of 5 high-bandwidth (–6 dB at 5 MHz) current-to-voltage converter and logarithmic preamplifiers similar to that described by Shapiro [200]. Custom-made LabVIEW (National Instruments, Austin, TX) software was implemented to control the 5 different PMT tube's gain settings. A National Instruments PXI data acquisition system (National Instruments, Austin, TX) was used for pulse digitization and storage. Digitization was performed by a 12 bit PXI-5105 at a 10 MHz sampling rate with 302 points collected per sampling

sequence for the calibration yellow-green fluorescent microspheres (YG beads) and at a 25 MHz sampling rate with 1002 points collection for UCAs, then saved to a computer for post-processing.

5.2.3 Results

System Resolution

It is possible to differentiate beads of different sizes by their scattering properties in very tight groupings (see Fig. 57) without having to add any fluorescence. The differentiation would be difficult at some size ranges if only one of the scattering arms was being used. The new side arms allow for the system to discriminate very well between particles of different sizes. Having two parameters allows flow cytometry to distinguish particles that would otherwise be nontrivial to separate if only one detector (FS or SS) was used. For example, the beads from 2 to 4 µm would lie in a continuous group if the system had not incorporated forward scatter. It can be seen in Fig. 57 that there is tight grouping of most of the beads (2500 per size). Doublets can also be observed and were not filtered out for completeness.

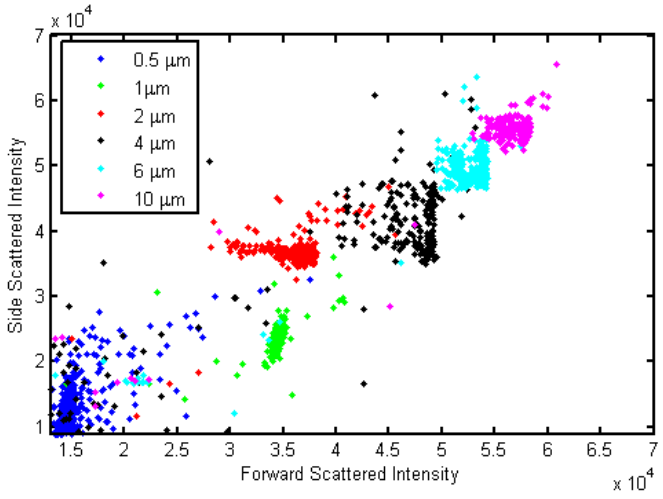

Figure 57. Dot-plot for side scattered *vs.* forward scattered intensity. Each color represents a different size of bead described by the legend in the figure. There are a total of 2500 beads analyzed per size and the results have not been filtered to show the doublets and the raw results of the system without post processing and without position sensing (see below).

Fluorescence Detection Capability

Additional tests were performed to calibrate the fluorescence signal relative to the forward and side scattering signals. These data, illustrated in Figs. 58a, show how different bead sizes have different fluorescence intensities, and can be discriminated completely from each other (again tight grouping as in Fig. 57). Finally, Fig. 58 (b) shows the difference between Optison bubbles

(not fluorescent) and 1-µm diameter fluorescent beads discriminated by the fluorescence detector, which would otherwise cause a confusion in the forward scattered signal detection.

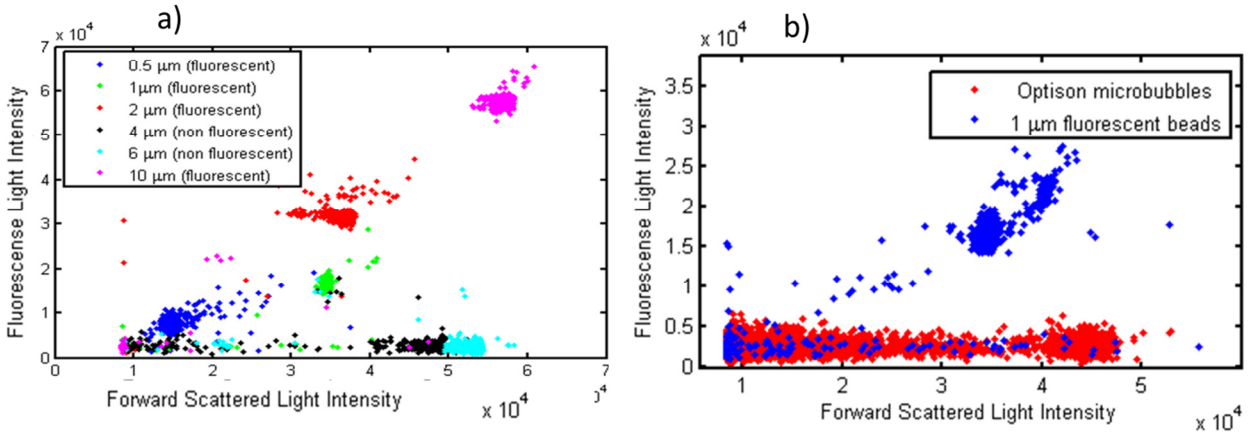

Figure 58. System's fluorescence detection capabilities. a) Dot-plot of fluorescence *vs.* forward scattered intensity for 6 different sizes of µm beads (some with fluorescence as indicated in the legend). The plot indicates the resolution of the system and also how well can it differentiate between fluorescent and non-fluorescent particles. It also provides calibration curves for forward scattering and fluorescence data. Doublets can also be observed and were not filtered out and are shown for completeness. b) Dot-plot of the fluorescence light intensity against the forward scattered light intensity for both fluorescent 1 µm beads and non-fluorescent, commercially available Optison microbubbles. The plot illustrates the forward scattering signal present for both particles, but the difference lies in the lack of fluorescence coming from the microbubbles.

Positioning System

The use of 3 different PMT's allows the proper sensing of a position in the center of the sample stream or outside from it. As shown in Fig. 59, the detectors D1 and D2 will change the amount of light they collect with respect to each other if a particle is displaced from the center of the stream. The functionality of the positioning system with a stream of beads in two different stream paths is shown. This example of particle displacement is illustrated in Fig. 59 for 2 µm diameter beads.

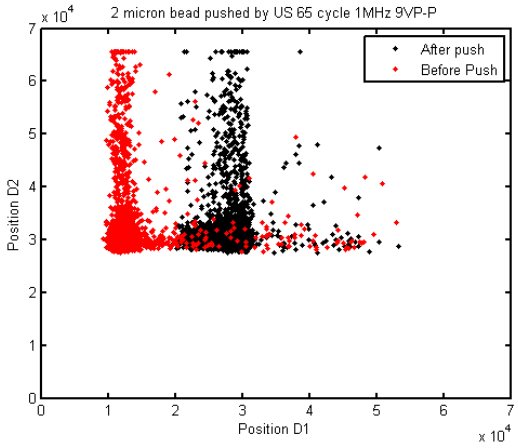

Figure 59. Testing the position detection system using the 2 position PMT's described in Figs. 56. The red colored beads on the dot plot are the position of the beads before flowing through the center of the flow cell. The black beads are the new position of the beads after being translated by a few µm.

The different shelled UCAs analyzed so far using this device are described in Table 5 in Chapter 6.1 (above), together with its obtained shell properties. It is noticeable that the tool is capable of characterizing protein, lipid, polymer, thin and thick shelled microbubbles. However, in some cases there are models that seem to fit a contrast agent better than others. As an example, Optison data (2MHz, 20 cycles, 100mV) was fitted with both Marmottant's and Sarkar's models (see Fig. 60). It seems Sarkar's model fits the data better in this preliminary investigation, although more data needs to be analyzed.

It is important to notice that when the bubbles are driven by a burst and not CW, it is difficult to fit the response using a driving sinusoid wave. Therefore, a Gaussian envelope to the driving signal has been implemented to yield better results. The time history for the pressure pulse has not been determined independently yet.

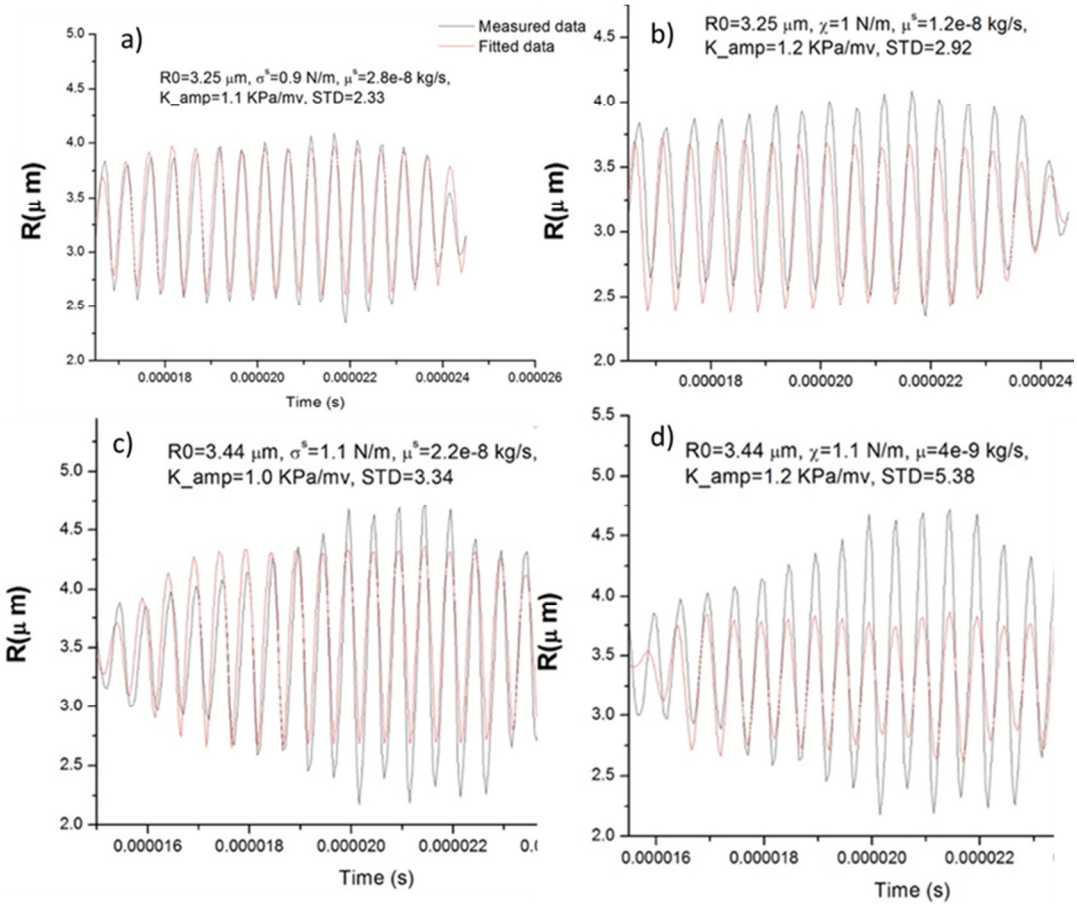

Figure 60. Bubble dynamics comparing the experimental fit of two models: Sarkar's and. Marmottant's model. Bubble dynamics comparison between Sarkar Model (LEFT) and Marmottant's model (RIGHT) for Optison bubbles driven at 2MHz, 20cycles, 100mv bursts. Each plot includes the measured data (blue) and fitted data (red) as well as the measured shell properties with respective standard error. The Sarkar model seems to fit better these bubble oscillations.

Finally, Fig. 61 shows the dynamics of an Optison UCA detected by both the forward scattering arm and the side scattering arm. The difference is due to the nature of the angle at which they scatter, and the additional filter blocking the light in the front scattered arm.

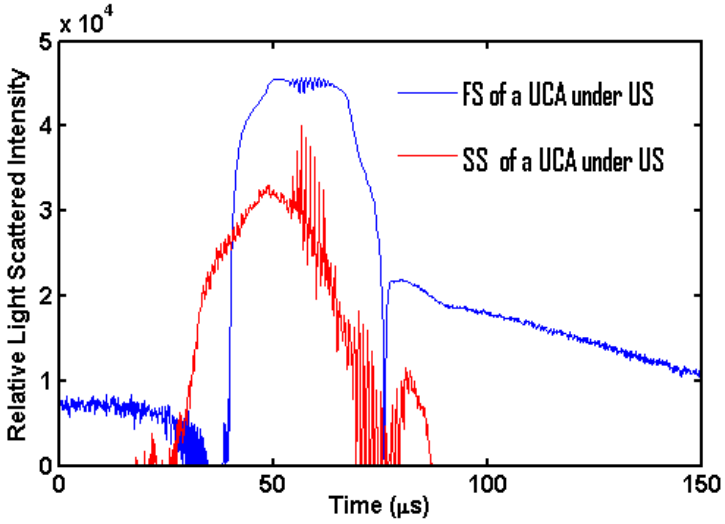

Figure 61. Dynamics of an Optison microbubble detected by the forward scattering and the side scattering arm. Ultrasound bursts of 65 cycles at 1MHz triggered by the side scattering signal at 2E4 level shows the effect and oscillation of the microbubble in both the side and front-scattered signals. The position detectors also show an increase in signal in one of the positions which means slight displacement and the fluorescence detector does not collect any signal since the microbubble does not have fluorophores attached to it.

One limitation from transient fitting is, as seen from Fig. 61, the challenge of fitting burst oscillation as opposed to CW oscillations. Therefore, there is the need to fit the initial pressure as a Gaussian burst instead of a constant sinusoidal pressure. The next chapter (6), where there is an effort to characterize the pressure inside the field, will show that the approximation of a Gaussian pulse is far of the actual field generated by a transient pulse inside the flow channel. The system has many vibrations and beating inside, so it is necessary to use a model. The limitation of this aim is taken to Chapter 6 as a solution.

Finally, the position sensitive detector needs to be calibrated so that a specific amount of light translates directly to a quantifiable distance. Having a calibration curve of light scattering vs. distance in the position detectors will allow radiation force studies using contrast agents and living cells (see Section 6.5) for future directions in this project.

Sizing Capabilities of The Acoustic Flow Cytometer Compared to Coulter Counter:

In the previous section, 5.1, it was demonstrated that the MB size can be obtained in the acoustic flow cytometer (FC) by using a calibration curve as the one shown in Figure 45. In Fig. 62, Coulter Multisizer (M3, Beckman, FL) and acoustic flow cytometry size distributions are compared for commercially available Optison MBs (left) and monodisperse calibration beads (1 or 2 µm) diameter, a and b respectively. It is noticeable that even with individual sized beads both devices have different accuracies (although they have very repeatable measurements).

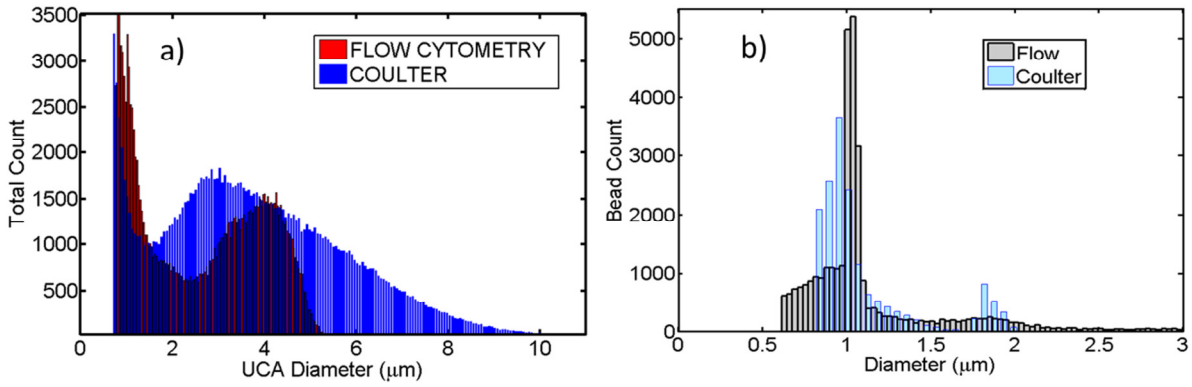

Figure 62. Coulter and FC sizing histograms for Optison microbubbles and monodisperse calibration beads. a): Size distribution comparison for Optison microbubbles between the Coulter Counter and the flow cytometer. b) Size distribution comparison for latex calibration beads of known size (1 or 2 µm) diameter between the Coulter Counter and the flow cytometer.

Fig. 62a reveals a mean shift in the size distributions from electrozone sensing (coulter) compared with flow cytometry (light scattering) techniques. In addition, the broad tail present in the coulter counter is not present in flow cytometry. In Fig. 62b, The Coulter peaks for 1 and 2 micron beads are slightly shifted to the flow cytometry peaks, indicating that even with a very homogenous sample (latex calibration beads), and both techniques show slightly different mean peaks. The differences in sizing from these techniques has already been reported by Satinover *et al.* and Feshitan *et al.* [47,201], who have already shown a discrepancy between flow cytometry sizing, light obscuration techniques, and electrozone (coulter) sizing techniques, in which none of the size distributions has the mean peak in the same location. The differences in peaks revealed by Fig. 62b highlights the high precision of both tool (resolve bead peaks very well), but also reveals the inaccuracy between each other (probably due to systematic errors or physical sizing mechanisms).

5.2.4 Conclusion

Ultrasound contrast agents (UCAs) were detected and analyzed for physical and rheological properties. Preliminary tests were performed at a throughput of 1000 microbubbles/sec. With ultrasound, oscillating MB signals were fitted to a two-parameter bubble dynamics model. Flow cytometry represents a high throughput and robust method for characterizing the size, population and shell properties of UCAs.

Chapter 6

Microbubble Shell Characterization in a Flow Cytometer Using a Combined Measurement-modeling Approach

6.1. Transient Pressure Field Characterization

6.1.1 Introduction

Microbubbles (MBs) are used clinically for Contrast Enhanced Ultrasound (CEUS) imaging. New applications have also been developed for targeting and drug/gene delivery [37–39]. These gas-filled agents are coated with a thin viscoelastic albumin, lipid, or polymer shell. The shell provides a barrier against dissolution in the circulation, affects the dynamical response of a MB to an acoustic pulse, and it is the backbone to which targeting ligands are attached. Characterizing the viscoelastic shell parameters is important for theorists developing bubble dynamics models, as well as manufacturers who need to understand and optimize MB stability for imaging and targeting applications. Methods to characterize the average shell properties of a bubble cluster include acoustic attenuation [52] and scattering [50]. While average properties are useful, measurements of individual MBs can reveal trends and conditions which are important in understanding and optimizing MB behavior. The shell properties of individual MBs have been obtained by atomic force microscopy [49,51,56–58], high-speed photomicroscopy [53–55] and light scattering [47,48,59,60]. As discussed by Chitnis and colleagues [202], AFM provides novel quantitative insight into elastic properties of MB's, but it is difficult to implement efficiently for a large number of MB's, similarly to high speed imaging. Of these, light scattering is the only method that allows high throughput measurements.

D Work published in part or submitted in part in:

C Perez, C Wang, B MacConaghy, J Tu, J Swalwell, A. Brayman, TJ Matula, Submitted to Ultrasound in Medicine and Biology. Microbubble shell characterization in a flow cytometer using a combined measurement-modeling approach. Part I: transient response

C Perez, C Wang, B MacConaghy, J Tu, J Swalwell, A. Brayman, TJ Matula, Submitted to Ultrasound in Medicine and Biology. Microbubble shell characterization in a flow cytometer using a combined measurement-modeling approach. Part II: steady state response.

C Perez, J Swalwell, J Tu, H Chen, A Brayman, TJ Matula, Characterizing the pressure field in a modified microbubble flow cytometer: Using a laser Doppler vibrometer to validate the internal pressure, J. Acoust. Soc. Am. **137**, 2423 (2015)

In particular, flow cytometers are off-the-shelf light-scattering systems that offer the potential of high throughput sensing with minimal refinement [47,48]. The challenge with light scattering in general is that MB properties are obtained by fitting the MB oscillatory response to a bubble dynamics model.

Such an equation typically has several unknown parameters including the ambient bubble size R_0, the driving acoustic pressure P_a, and the shell's viscoelastic properties (*viz.*, elasticity and viscosity). Towards that goal, a flow cytometer was adapted with a transducer affixed to a flow cell. As the MBs enter the interrogation zone, sinusoidal voltages are applied to the transducer, which generates a pressure pulse and drives the MB into oscillation. The oscillatory signal collected by the cytometer detector (ultrasound-activated light scattering signal) is post-processed to extract the relevant parameters (size, number, and shell properties). However, the flow cell's fluid channel is only about 200 μm across, and thus too small to insert a hydrophone for direct measurement of the acoustic pressure inside the flow cell.

In this work, an alternative method for estimating the acoustic pressure P_a at the region of optical MB interrogation within the cytometer cell was developed, so that fitting the experimental data required only the two shell parameters. A COMSOL finite element model was developed to predict the transient vibratory and pressure field generated by the transducer. The model was then validated with measurements *outside* the flow cell. The predicted transient pressure field P_a *inside* the flow cell was finally used in the fitting algorithms. The COMSOL-predicted pressure amplitude was consistent with the older technique of fitting many MBs driven at the same voltage using iterative fitting techniques [48,49].

The goal of this work was to reduce the fitting parameters from a 3-parameter fit of pressure, elasticity and viscosity [Pa, χ, κ_s] to a 2-paramter fit of only the viscoelastic shell parameters. The overarching hypothesis was that the new technique of estimating the acoustic field inside the flow cell would agree with experimental measurements, and would in turn reduce the 3-parameter fit to 2-parameter fit, allowing the shell viscosity and elasticity to be determined on an individual bubble basis, speeding up the fitting time for shell characterization in a high throughput system. The data supported this hypothesis.

6.1.2 Materials and Methods

Experimental Setup for the model calibration step

The experimental setup for the model validation is shown in Fig. 63. The quartz flow cell (Hamamatsu, Japan) with mounted transducer (described below) was removed from the flow cytometer and placed on the surface of a degassed column of water (tank measurements: 22 *x*11*x*11cm). This allowed acoustic waves in the cell to propagate into water and be collected by a calibrated PVDF hydrophone (GL-0150-IA, Specialty Engineering Associates, Soquel, California) with a sensitivity of 0.324 mV/kPa at 1 MHz. The hydrophone output was connected to an oscilloscope (LeCroy 9350AL, Chestnut Ridge, NY) and the data saved for later processing. For scanning purposes, the hydrophone was mounted to a 3D-positioning stage with 10 μm precision and scanned with a minimum step size of 500 μm.

The PZT (Lead-Zirconate-Titanate) rectangular transducer (10 mm x 5 mm, 0.75 mm -thickness and 2 MHz resonance frequency) was supplied with sinusoidal voltages from a function generator (Agilent 33120A, Santa Clara, California), through an RF step attenuator (837 Attenuator, Kay Elemetrics Corp, Lincoln Park, NJ) and amplified by an RF power amplifier (ENI A150 SN 693, Rochester, NY). Input voltages to the amplifier varied from 15.8 to 552 mV peak-to-peak. A second oscilloscope channel was used to measure the voltage at the transducer with a high impedance attenuating probe (10x, 10 MΩ, LeCroy, Chestnut Ridge, NY). The function generator signal consisted of 20-cycle tone bursts at 1 MHz, repeated with a pulse repetition frequency (PRF) of 1 kHz. The frequency of 1 MHz was chosen because a majority of commercial microbubbles (MBs) respond well at that frequency. Both single pulse and 100-pulse averaged waveforms (to reduce measurement noise) were collected. For further system characterization, impedance measurements where obtained using an impedance analyzer (Agilent 4192A LF, Bell Electronics, California). Measurements were done with or without water loading to measure the effect of loading on the system's response.

For hydrophone scans, we defined the starting point (*x,y,z*=0) as 1 mm below the flow cell, at the midpoint of the PZT (see Fig. 63b). Waveforms were recorded along the long (*x*) and short (*y*) axes of the flow cell, as well as two different *z* positions below the flow cell. The collected waveforms were later compared to the COMSOL model, described next.

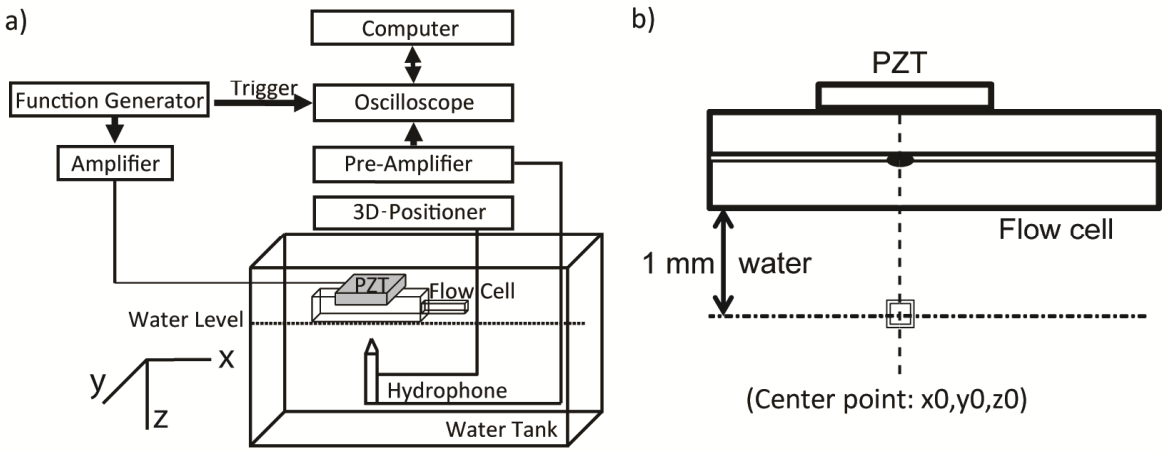

Figure 63. Experimental setup for the model validation. (a) Schematic of the experimental setup. The flow cell is placed against the water surface. Acoustic waves passing through the flow cell and into water are collected with a PVDF hydrophone that can be scanned along the X, Y, or Z axis. (b) The "Center Point" of the scans is located 1 mm below the distal surface, at a point bisecting the center of the PZT (0.7 mm thick). This same line bisects the flow channel at the laser beam interrogation zone (shown as a darkened area in b).

Finite element Model and Setup:

The finite element package COMSOL (4.2a) was used to implement a multiphysics simulation of our experimental setup. This simulation coupled the electrostatics and structural physics of piezoelectricity in the PZT with linear acoustics physics in the quartz and water domains. A schematic of the model setup is shown in Fig. 64. The PZT, quartz and water domains of the model were assigned material properties from the COMSOL built-in materials list of PZT-4, quartz, and water respectively. The electrodes are implemented in COMSOL as a Ground or a Terminal boundary condition within the Acoustic-Piezoelectric Interaction, Transient (acpztd) interface. In order to truncate the water domain below the quartz flow cell, a plane wave radiation boundary condition was applied to the base and sides of the water domain to prevent reflections from the truncated boundary (note that this applies strictly only to normally-incident waves; waves arriving at an angle will generate some reflection, causing errors in the simulations). The top of the water domain and the exterior surfaces of the quartz flow cell were exposed to air in the experiment, so on these surfaces a pressure release boundary condition was applied. The full geometry was meshed using tetrahedral elements, and the element size was dictated by the material sound speed. The refinement of the mesh was chosen to be seven elements per wavelength in each material domain. The time dependent simulation extended out to 30 μs with a time step of 28.57 ns, which produced a CFL number of 0.2 in each domain for this simulation (CFL is essentially the ratio of the distance the acoustic wave travels over the size of the mesh elements).

The input to the simulation is a time dependent voltage (20-cycle tone burst at 1 MHz, between 2 – 50 volts) applied to the positive PZT electrode to match the amplifier input of the experiments. COMSOL solves the stress-charge form of the piezoelectric equations in the PZT and the linear acoustic equations in the quartz and water domains as a function of time. The calculations were performed on a quad core 3.4 GHz processor with 32GB Ram. The specific sound speeds and wavelengths of the 3 materials used in the model are: $\lambda_{(water)}$ = 1.5 mm (C_{water} = 1500 m/s), λ_{Quartz} = 5.5 mm (c_{quartz} = 5500 m/s), and λ PZT = 4.5 mm (c_{pzt} = 4500 m/s).

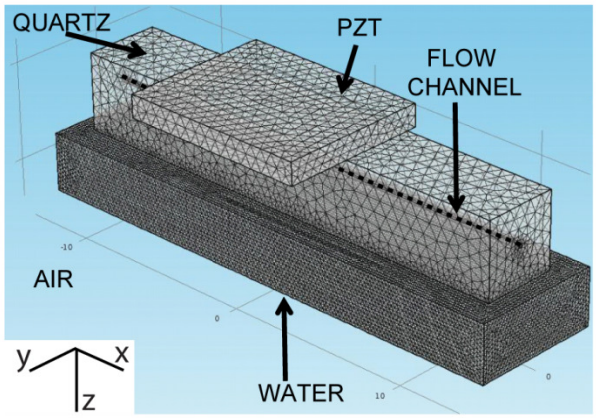

Figure 64. 3D view of the finite element model setup. The system consists of a piezoelectric crystal (PZT) attached to a quartz flow cell. Inside the flow cell, a 200 µm square flow channel filled with water runs through the flow cell. The mesh implemented is a free tetrahedral mesh, with a total of 903709 elements. Each material is meshed corresponding to its own wavelength as the following: $\lambda_{material}/N$, where N=7 for the model above.

Experimental setup for the mechanical property estimation for Optison MBs.

In the experiments, Optison MBs were diluted in 0.45µm filtered Isoton II (Coulter, Miami, FL) electrolyte with an initial concentration (7x 10^8 MBs/mL) determined using a Coulter M3 Multisizer (Coulter, Miami, FL). Experiments were done in triplicate at a sheath pressure of 41 kPa (5.9 PSI) and sample pressure of 43 kPa (6.2 PSI), producing a flow rate of 5 mL/min from the flow cell. Each run at a particular acoustic pressure setting lasted between 3-5 minutes, allowing collection of about 100,000 MB events for each run. For size calibration of the flow cytometer, a calibration kit (nonfluorescent microspheres, Molecular Probes, Eugene, OR) containing six different size populations with diameters from 0.5 - 10 µm was used. The PMT voltage output was converted to a radius using Mie scattering theory [48,59,60].

Additional details of the acoustic and detection system are as follows: The acoustic driving signal consisted of a 20-cycle tone burst at a frequency of 1MHz. The scattered light from the MBs was collected by a PMT and routed to a custom high bandwidth (-6 dB at 5 MHz) current to

voltage converter and logarithmic preamplifier similar to that described by Shapiro [41], and digitized by a 12 bit PXI- 5105 at 20 MHz for later analysis. For the purpose of characterizing the bubbles in this study, the flow cytometer's side scatter optical path was used. Custom built LabVIEW (National Instruments, Austin, TX) software was used to control the side scatter PMT gain setting.

6.1.3 Results: COMSOL Model Validation

System frequency response and pressure-voltage calibration.

The experimental setup for model validation required that the flow cell be removed from the flow cytometer and placed against a water column. This allowed measurement of the acoustic field propagating through the cell and into water. It was assumed that if the model could predict the waveform *outside* the flow cell, it would also be valid *inside* the flow cell where the MBs were being subjected to pulsed ultrasound.

An initial concern was to determine if water loading on one side of the flow cell significantly affected the system's resonance structure. Impedance analysis of the flow cell with or without water loading is shown in Fig. 65. Although the peaks without water loading are sharper and higher (indicating a higher system Q), the effect of loading did not shift the resonance frequency. Thus, results obtained when water-loaded should not differ greatly from the normal *in situ* location of the flow cell.

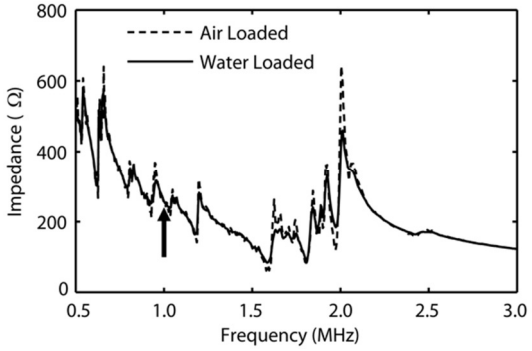

Figure 65. Impedance plot. Impedance measurements in Ohms (Ω) as a function of ultrasound driving frequency for air loaded (dashed line) and water loaded (solid line) cases. The arrow indicates the experimental driving frequency, 1MHz used in the experiments and simulations. Water loading refers to the distal wall of the flow cell being in contact with a layer of water.

The next step was to determine whether there was a linear relationship between input voltage and measured pressure amplitude in the water under the flow cell. Figure 66 illustrates that relationship for the center point. The squares show experimentally measured pressure amplitudes as a function of input voltage to the PZT. The model prediction at the same location

is shown as circles. The offset in amplitude can be explained partially by noting that the simulations use estimates for the PZT and quartz materials, and the epoxy bonding the PZT to the quartz flow cell is not included in the simulations. Thus, one should only expect that the COMSOL simulations fit the experimental results within a constant normalization factor.

The finding of variation in linearity in the simulation in initial experiments was considered probably due to the radiation boundary condition. That condition expects normal incidence acoustic waves along the boundary, so any wave hitting the boundary at an angle will generate a reflection that can interfere with the original signal. Further, the slope differed by 7% from the experimental measurements. Thus, in order to estimate the pressure with COMSOL, the COMSOL predicted peak positive pressure *vs*. voltage relationship was multiplied by a factor 1.1613 and the slope was increased by 7% to match the experimental levels. This setting was applied to *all* subsequent applications of COMSOL.

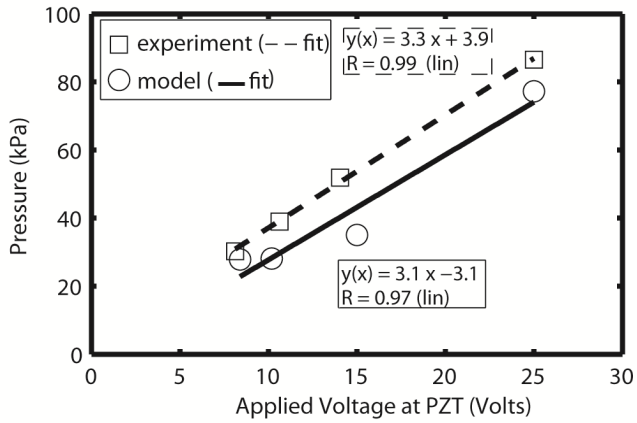

Figure 66. Calibration plot. Relationship between applied voltage at the PZT and pressure amplitude for both the model (circles) and the experimental (squares) setups shown in Figs.63 and 64 at the Center Point (1mm away from the distal face in water, see Fig.63). The lines are a linear best fit. In subsequent applications of the COMSOL model, a normalization factor was added to match the experimental measurements, as described in the text.

Long (*X*) axis scan:

Model validation was performed by comparing the model results with hydrophone measurements at various positions under the flow cell. As an example, Fig. 67 illustrates a comparison of the simulated and averaged (100 waveforms) measured pressure waveforms at the center point. Of greatest interest are the first 20 µs, as this period corresponds to the transit time of a MB through the interrogation laser at the employed particle flow speed of 2 m/s. There is excellent agreement between the measured and simulated fields. The goodness of the fits were determined using a normalized cross correlation technique between the experiment and

modeled waveforms (Eqn 3 in Lubinski *et al.* [203]. The normalized cross correlation value for these two waveforms is ρ = 0.92.

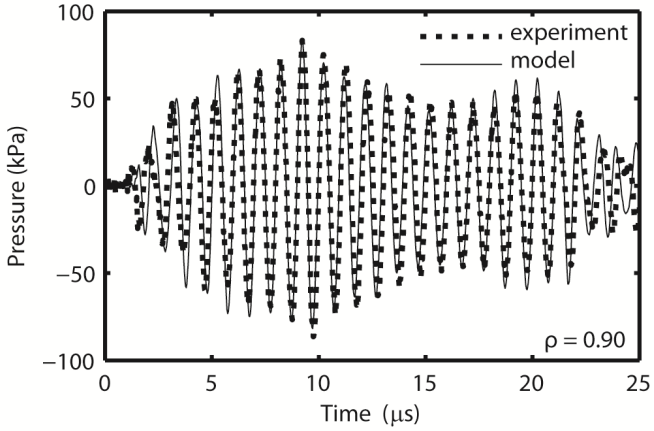

Figure 67. Center point experimental-model transient fit. Comparison of the simulated (solid line) and averaged measured pressure waveform (dashed line) at the Center Point at 25 V input to the PZT. The maximum and minimum pressure amplitudes are P+ = 85 kPa and P- = -87 kPa, with a cross-correlation value of ρ = 0.90.

Comparisons of simulated and measured waveforms at various locations along the *x* axis are plotted in Fig. 68. The measurement position is listed above each plot, relative to the center point. The PZT itself is 10 mm wide, so the scan covers the width of the PZT. Again, there is excellent agreement between the simulated and measured waveforms.

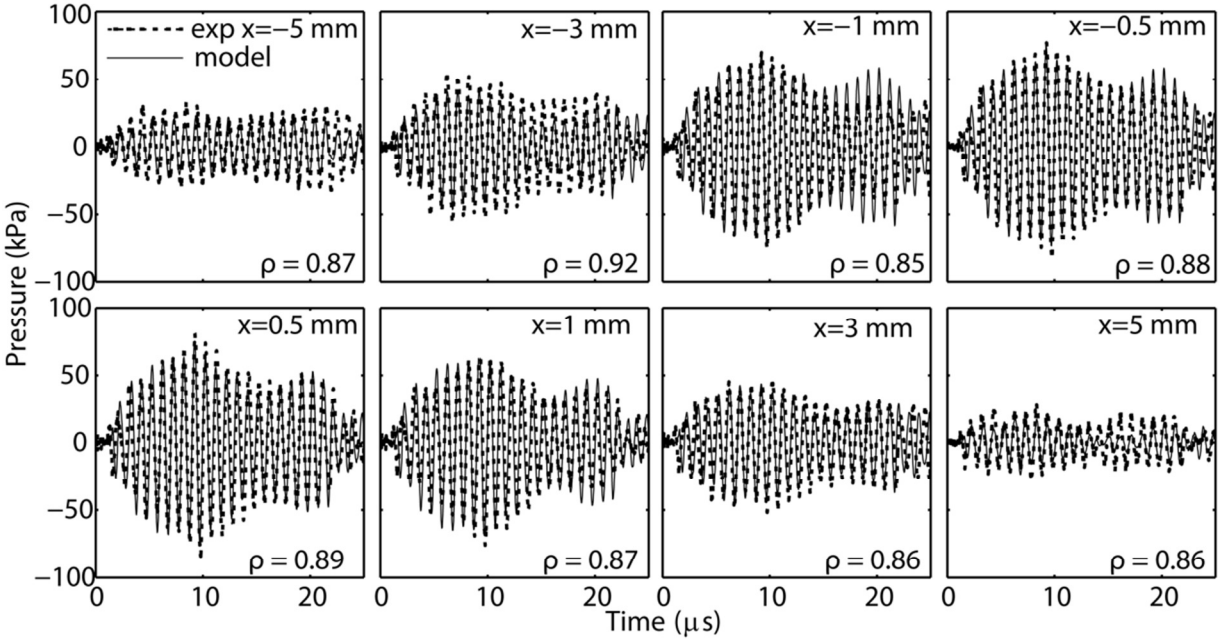

Figure 68. Axial scan model-experiment waveform fits. Axial scan along the long (x) axis (y=0, z=0) as defined in Fig. 63. The position label refers to the distance from the center point. Experimental (dashed line) and model prediction fits (solid line) show good agreement. The axial scan was made with a 0.5 mm step size. The normalized cross correlation parameter, ρ, is indicated on each model-experiment fit.

Instead of showing the actual waveforms, the measured and simulated peak positive pressure amplitudes are compared in Fig. 69, as a function of *x* position. Figure 69a shows the amplitudes associated with the waveforms in Figs. 67 and 68 (at *z* = 1 mm). The results of a second scan at *z* = 2.5 mm are shown in Fig. 69b. Good fits are obtained at both *z* locations. Note that the laser interrogation zone is only 60 µm wide, centered around the center point, while these scans extend to 5 mm away from the center point. Extending the scan out to 5 mm allowed better evaluation of the COMSOL model. Later, when simulating the pressure *inside* the flow channel, the only location of interest is that corresponding to the laser interrogation zone (the line that bisects the center point of Fig. 63b). The normalized cross correlation coefficients, ρ, for all the points in Fig. 69a ranged from 0.82 - 0.93 and in Fig. 69b from 0.80 - 0.93.

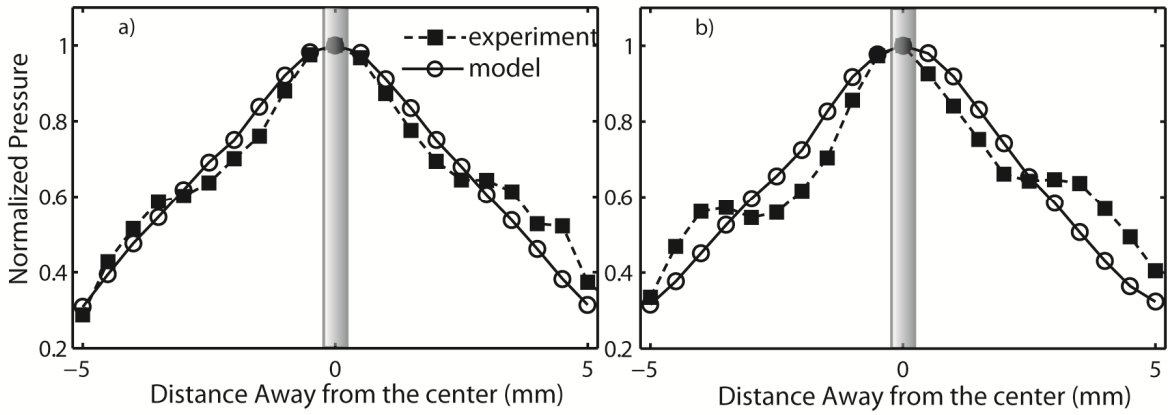

Figure 69. Normalized long axis model-experiment peak pressure fits. (a) Normalized long (x) axis scan of the maximum peak pressure for a depth of z=1 mm below the flow cell. The modeled predictions (circles with solid lines) compare favorably to measured (black squares with dashed lines) values at an input of 25 V to the PZT. Scan step size is 0.5 mm. (b) Similar comparison of peak pressures for a depth of z = 2.5 mm below the wall of the flow cell. The laser spot is 60 µm in diameter.

Short axis (*Y*) scans:

A comparison of experimental and simulated waveforms along the *y*-axis is shown in Fig. 70, while the corresponding normalized pressure amplitudes at two depths along the *y*-axis are shown in Fig. 71. The peak pressure amplitudes decay at a much faster rate away from the center point in this short (*y*) axis compared to the long axis scans. There is also more variation between the fits and measurements along this axis. The normalized cross correlation coefficients ranged from 0.74 - 0.93 in Fig. 71a and 0.76 - 0.92 in Fig. 71b.

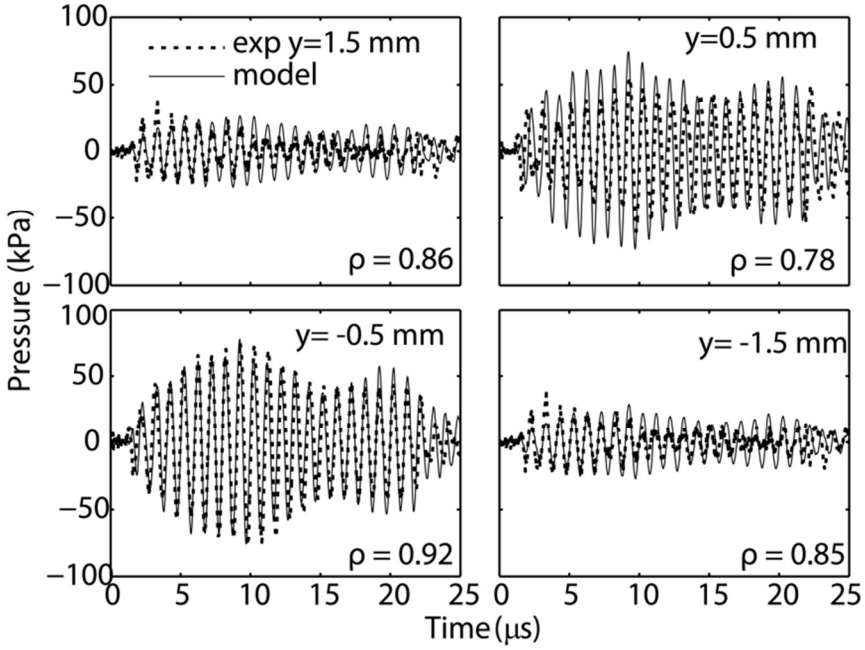

Figure 70. Short axis model-experiment waveform fits. Selection of modeled and measured waveforms along the short (y) axis. Scan step was 0.5mm. The normalized cross correlation parameter, ρ, is indicated on each model-experiment fit.

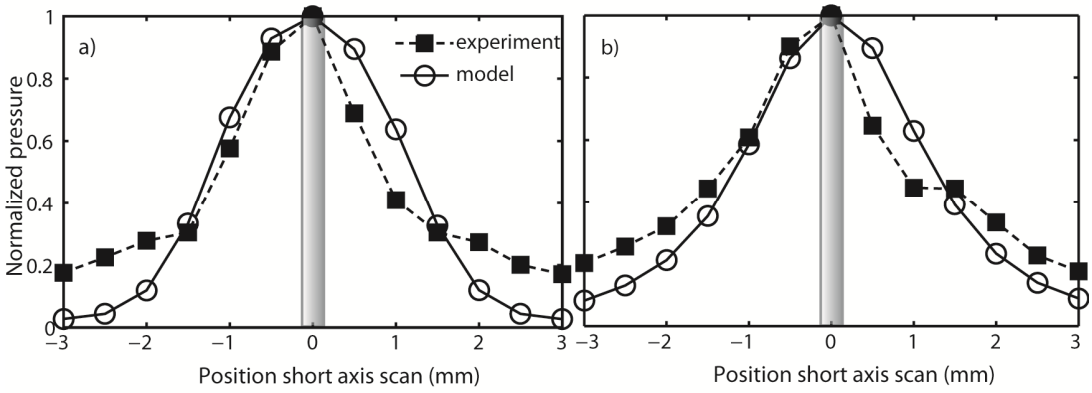

Figure 71. Normalized short axis scan pressure fit. Normalized short axis scan of the peak pressure for a depth of z = 1 mm and b) 2.5 mm. Peak positive pressures measured for short axis (squares) are compared to the respective modeling fit predictions (circles) at an input voltage of 25 V. Scan step size is 0.5 mm.

Internal flow chamber pressure:

Having shown that the model predictions agreed relatively well with experimental measurements of the waveforms *outside* the flow cell, attention was then turned to predicting the waveform *inside* the flow channel at the laser interrogation zone. The predicted waveform is the forcing function that drives the MBs into oscillation. Figure 72a shows a characteristic predicted waveform of a 20-cycle, 16V, 1-MHz tone burst at the center of the flow channel. Figure 72b plots the corresponding predicted peak pressure as a function of driving voltage. Unlike the predicted pressure amplitudes *outside* the flow cell, the predicted pressures *inside*

the flow channel increase linearly with input voltage. This modeled pressure was used as the driving force for simulating the radial dynamics, or R(t) curves of MBs in the laser interrogation zone. That is, we used the Marmottant bubble dynamics model [48,49,192] in which the simulated driving pressure was the input forcing function, and a least squares fitting algorithm was used to extract the viscoelastic shell parameters.

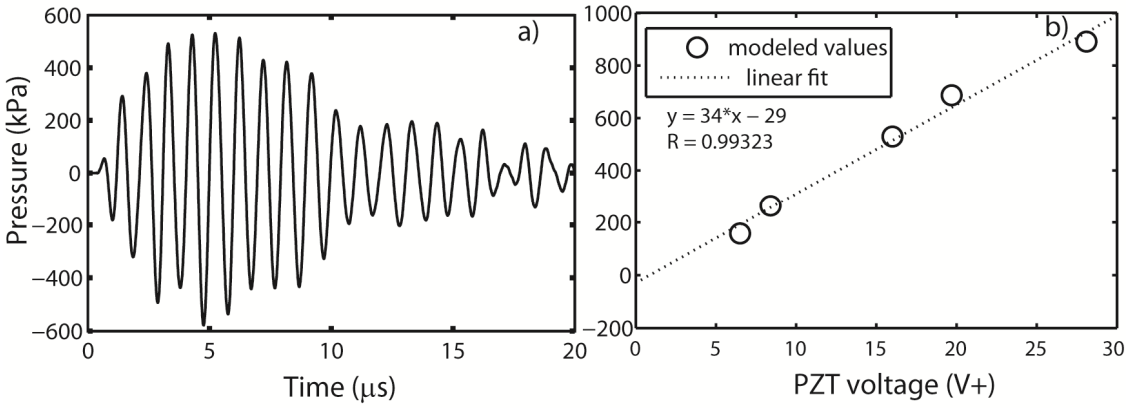

Figure 72. Predicted forcing functions for MB at different pressures. a) At the center point inside the flow channel that drives the MBs for the 16V setting. b) Plot of peak pressure predicted in the center of the flow channel as a function of driving voltage.

6.1.4 Results: Mechanical Property Estimation for Optison MBs.

Returning to the activation of MBs, the ultrasound pulse was initiated as the MBs entered the laser interrogation zone, and the instantaneous scattered light intensity data collected for later processing. Details can be found elsewhere [48,49]. In the earlier work, the driving pressure was a fitting parameter to the measured R (t) curves. In the present study, the pressure was derived from the COMSOL model (Figs. 72 and 73a). Examples of several fitted waveforms are shown in Figs. 73b-f. This technique was applied to a total of 431 MBs of different sizes and driven at different pressure amplitudes, using the STD minimization value described in Eqn (5.4). The best fit minimization values obtained for Figs. 73b-f are in a range of 0.03 - 0.075.

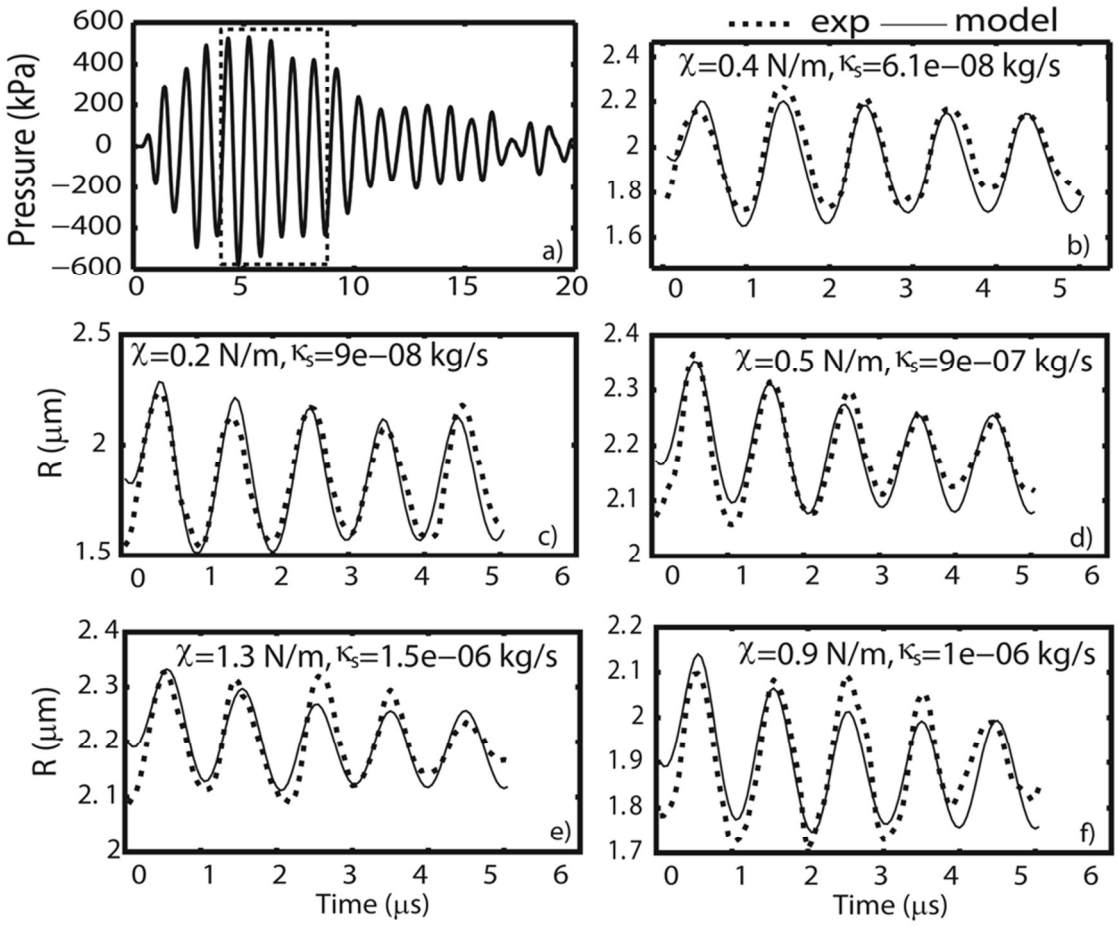

Figure 73. Example of bubble dynamics R(t) fits from transient forcing. (a) The COMSOL-derived forcing pressure was used in the Marmottant bubble dynamics model to fit R(t) curves. The dotted box indicates the fitting window (5 cycles) that was used. (b-f) Best fits and corresponding shell parameters for selected R(t) curves at peak pressures of 158, 264, 529, 687 and 890 kPa, respectively.

The shell elastic modulus, χ, (N/m) and shell dilatational viscosity, κ_s, (kg/s) were extracted for each bubble as a function of size and driving pressure. Statistical analysis software *R* (*R* Core Team, Vienna, Austria) was used to provide descriptive statistics with mean and 95% confidence intervals (see Table 7). Data are also presented in a box-plot format showing the data range, first quartile, median, and third quartile. Initially we conducted normality tests for all groups to ensure that there was a large sample size and the data distribution was approximately normal. Next, a parametric test (one-way ANOVA) was used to investigate the differences between the mechanical property means (elasticity, viscosity and shear rate) as a function of driving pressure for five different pressure groups. If statistical significance was achieved ($p < 0.05$), then between-group comparisons were performed using a Tukey *post hoc* test. We used the STD minimization value described in Eqn (5.4). to determine the quality of the fit between the model and experimental R(t) curves. For a total of 459 bubbles, we discarded any bubble

that did not satisfy, STD < μ + 2SD, where μ is the mean value for all the minimization best fit value (STD) and SD is the standard deviation of the best fits obtained. Six percent of the total data set did not meet this criterion and were discarded, leaving 431 MBs for analysis. These included bubbles that had very large relative radial excursions $(R_{max}-R_o)/R_o > 1$, bubbles exhibiting strongly nonlinear responses, and bubbles with a very large shell elastic modulus (> 3N/m), the latter being usually larger bubbles with very large STD values).

Table 7 shows a summary of the obtained shell properties for Optison at five different peak positive pressure settings, labeled as groups A, B, C, D and E (corresponding to 158, 264, 529, 687 and 890 kPa, respectively) for ease of reporting in the text. The table also shows the input voltage (at the PZT), the predicted peak positive pressure amplitude, number (N) of bubbles analyzed at each pressure, the fitted viscoelastic parameters, and the shear rate (discussed further below). Where appropriate, the 95% confidence interval (CI) is also listed.

Table 7. Summary of the measured properties for Optison ™ MBs obtained with a short pulse.

Group	PZT (V+)	Pressure p+ (kPa)	N	Viscosity κ_s *10^{-7} (kg/s)	Elasticity χ (N/m)	Max Shear Rate (MHz)
A	6.5V	158	57	4.00 [2.92 – 5.08]	0.87 [0.63-1.10]	1.10 [0.93-1.27]
B	8.4V	264	100	5.05 [4.18 – 5.92]	0.93 [0.76-1.10]	1.14 [1.04-1.24]
C	16V	529	105	8.74 [7.32 – 10.2]	1.12 [0.97-1.27]	0.99 [0.88-1.10]
D	19.7V	687	86	9.97 [8.29 – 11.7]	1.10 [0.92-1.28]	1.43 [1.27-1.59]
E	28.1V	890	83	12.0 [9.36 – 14.6]	1.13 [0.99-1.27]	1.51 [1.36-1.66]

Viscosity, elasticity and maximum shear rate are described as means with 95th percentile confidence interval, [95%CI].

The relationship between the shell elastic modulus and MB size is shown in Fig. 74a for N=105 bubbles driven at P+ = 529 kPa (corresponding to third row of Table 7). Within experimental error, the shell elastic modulus was independent of bubble size. We also compared the elastic modulus across different driving pressure groups and observed a nominal increase in the mean value (Fig. 74b and Table 7), but the differences were not significantly different among groups (P-value = 0.14, one-way ANOVA). The albumin shell elasticity of Optison is relatively uniform across MB size and driving pressure, on average 1.04 N/m, 95%CI = [0.96-1.12], which agrees with previous published literature values [197,204,205].

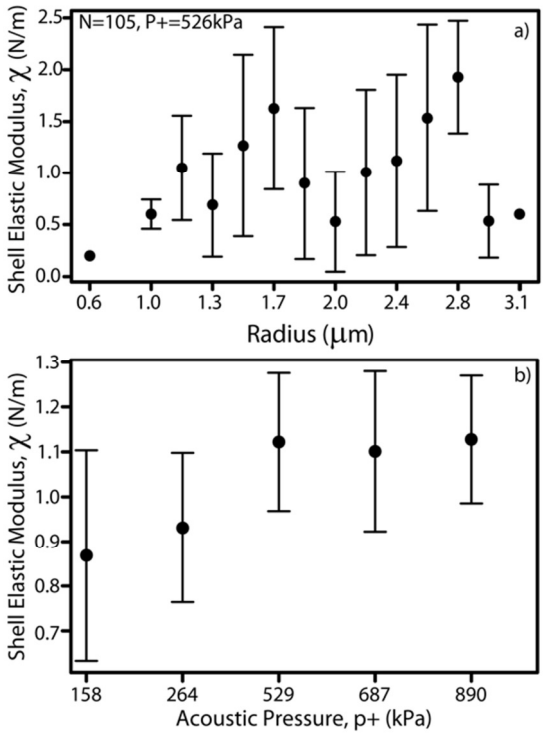

Figure 74. Elasticity plot. (a) Shell elastic modulus vs. Ro for Optison MB's. Standard deviation error bars are used when at least 5 bubbles are binned within 0.18 μm (bin width) of the center radius. (b) Shell elastic modulus vs. driving pressure. Mean and 95% CI (error bars) presented for each pressure group according to Table 7.

The relationship between the shell dilatational viscosity and bubble size is shown in Fig. 75a for three pressure settings (see also Table 7), and shows that the shell dilatational viscosity increases with increasing equilibrium MB size. The family of curves shows a dependence on driving pressure. The mean viscosity across 5 pressure groups was analyzed, revealing statistically significant differences in the means (P-value < 0.0001, one-way ANOVA). Groups C, D and E had statistically significantly higher viscosity than did groups A and B ($P < 0.01$, using Tukey *post hoc* tests). In addition, group D was significantly different from C, ($P=0.036$, Tukey *post hoc* tests).

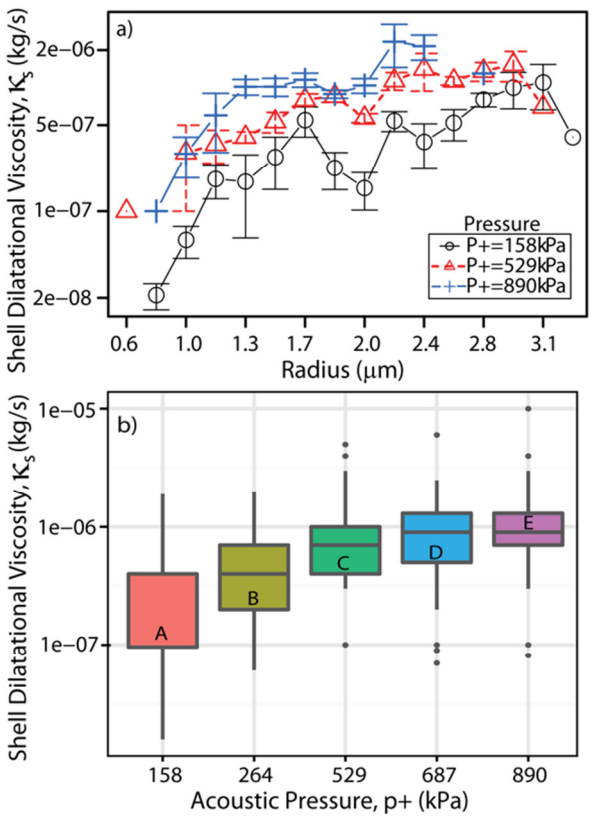

Figure 75. Shell dilatational viscosity plot. a) Shell viscosity *vs*. Ro for Optison MBs, shown for three pressure settings. Standard deviation error bars are used when at least 5 bubbles are binned together. b) Boxplot of the shell dilatational viscosity as a function driving pressure groups (A-E, Table 7). Either the whiskers of a box-plot are drawn out to the maximum and minimum values, or the maximum and minimum values are plotted as individual points (if they are considered outliers). The bottom of the box-plot is the 25th percentile, which defines the first quartile, and the top of the box is the 75th percentile, which defines the third quartile.

Figure 76 illustrates the relationship between the shell dilatational viscosity and maximum shear rate, $max\left(\frac{\dot{R}}{R}\right)$, calculated from each bubble's R (t) curve, for three pressure settings. As expected from the literature [48,49,60,206] the viscosity decreased with increasing shear rate, a behavior characterized as shear thinning. In addition, the maximum shear rate increased with driving pressure.

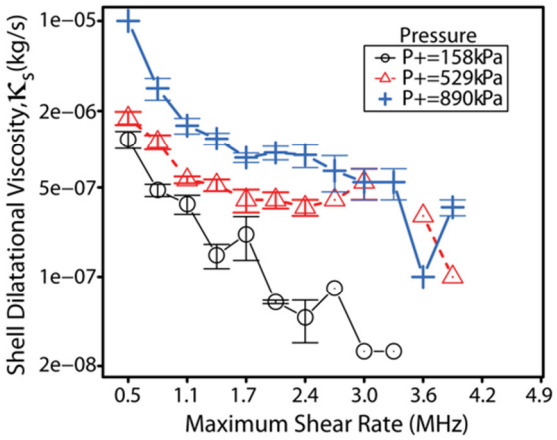

Figure 76. Shear rate plot. Relationship between shell dilatational viscosity and maximum shear rate for Optison, for three pressure settings from Table 7. SD error bars are used when at least 5 bubbles are binned together. A family of shear thinning curves is generated, showing a dependence on driving pressure.

The measured bubble shear rate was also analyzed as a function of different driving pressure groups revealing statistically significant differences (Table 7; P-value < 0.0001, one-way ANOVA). Group E had statistically significantly higher shear rate than groups A, B, and C (P<0.001 for each comparison, respectively Tukey *post hoc* tests). In addition, group D was significantly different from A, B and C (P=0.016, P=0.015, P<0.001, respectively, Tukey *post hoc* tests).

6.1.5 Discussion

The goal of this work was to reduce the fitting parameters from a 3-parameter fit of pressure, elasticity and viscosity [P_a, χ, κ_s] to a 2-parameter fit of only the viscoelastic shell parameters. Here, a complicated 'system' (PZT transducer, quartz flow cell and inner water channel) was modeled with COMSOL to predict the driving pressure in the *inside* flow channel as the forcing function to the bubble dynamics model. The COMSOL model was validated by comparing the simulation results with measurements *outside* the flow cell. Some comments about the validation and use of the COMSOL model are warranted.

First, the multiphysics model appears capable of accurately predicting the experimentally measured pressure. There are good fits to the measured transient pressure field at the center point (Fig. 67), as well as off center in the *x* and *y* directions, and at two *z* locations (Figs. 68 - 71). However, the 'calibration' of the COMSOL model shows that it under-predicts the hydrophone measurements (Fig. 66). There are several possible explanations for this discrepancy. The offset in amplitude can be explained by noting that the simulations use

estimates for the PZT and quartz materials. In addition, there was a layer of epoxy bonding the PZT to the quartz flow cell that was not included in the simulations. The lack of a good linear trend as a function of input voltage is most likely due to the radiation boundary condition. That condition expects normal incidence acoustic waves along the boundary, so any wave hitting the boundary at an angle will generate a reflection that can interfere with the original signal. We tested several models with tapered boundary layers to provide non-normal surfaces and add more reflections and observed significant effects due to the boundary reflections. We ran mesh refinement and mesh optimization together with water domain thickness optimization sweeps to determine the minimum size of the water layer needed to avoid boundary effects. This was done to reduce computational time, which sometimes took over 24 hours to run for a single 20-cycle tone burst, and we were already operating near the limit of our mesh refinement at 1 MHz for our computational power.

An example of the significance of the model can be shown in Fig. 77. Here the model is used to predict the pressure field at the center point of a focused ultrasound transducer in the current flow channel presented in Section 6.12. By using focused ultrasound the flow channel can reach higher pressures (useful where radiation force or bubble dosimeter is needed) and it can also homogenize the field at the center (compare with Fig. 73a).

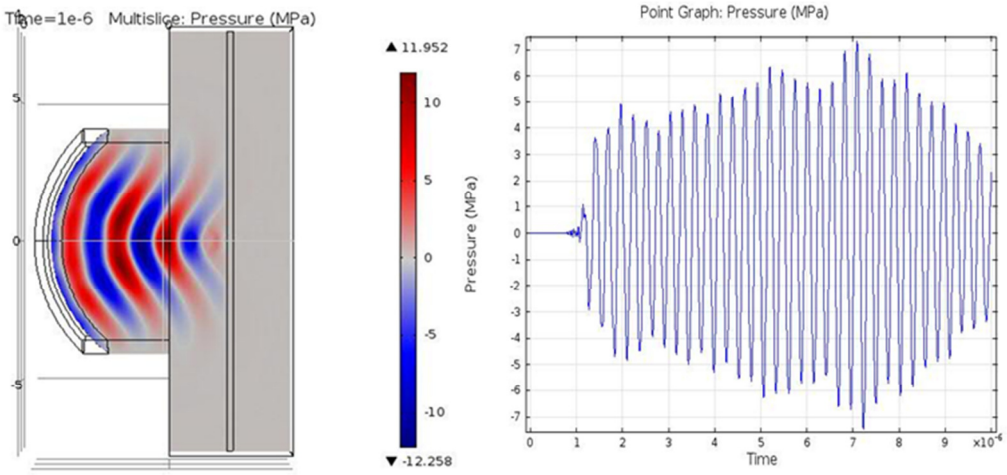

Figure 77. Finite Element Method (FEM) simulations of the acoustic flow channel using Comsol. (left) Transient pressure field of the optimized acoustic setup with a focused (3.5MHz PZT). (right) Pressure-time evolution in the optimized focused system at the interrogation zone.

The flow cell has a complicated resonance structure, as highlighted in Fig. 65. Although not presented here, several attempts were made to match the COMSOL and measurements at

different frequencies. Good fits were obtained at 500 kHz, but not at 2 MHz. It is important to note that the model is 3D and extremely computationally expensive. To mesh for 2 MHz the water layer had to be reduced, which increased the reflections from the plane wave boundary condition. Another difficulty is that the resonance of the system is around 2MHz, and small discrepancies in, *e.g., the* position of the hydrophone will have a large effect on the goodness of the fit. Also, it is a p-wave model that neglects linear elastic waves, which might come into play more at the resonant frequency of the system. For these reasons, and because most studies use MHz frequencies, we restricted our studies to 1 MHz.

The Marmottant bubble dynamics model was derived for a lipid shell coating, not a protein coating. It is not necessarily accurate in describing Optison MBs. Use of a different model might generate a different set of viscoelastic values. Nevertheless, the goodness of our fits suggests that the model is useful for protein shells.

The elastic modulus obtained in this study is similar to previously published results [197,204,205]. For example, the Albumin shell elasticity of Optison is relatively uniform across MB size, on average 1.04 N/m, 95%CI = [0.96-1.12]. There was a nominal increase in mean elasticity with increasing pressure (Table 7), but this was not statistically significant. The present results are in quite good agreement with the manufacturer's elastic modulus estimation of 1.3N/m (internal report), underestimating the latter by only about 15 - 30%. One study suggested that the elasticity of custom-made lipid-coated MBs decreased with increasing pressure [207]. Another study suggested a dependence on MB size R_0 for Albunex MBs, which had the same shell material as Optison [195,208]. We found that the mean elasticity of Optison increased slightly with pressure, and there was no dependence on R_0 (Fig. 74).

The shell dilatational viscosity increases significantly with increasing R_0 (Fig. 75). These results are consistent with previous observations of lipid and protein shells [48,49,53–55,60,206]. In addition, there is a distinct dependence on driving pressure. Figure 75 and Table 7 show that the mean shell viscosity increases by a factor of 3 over a 5.7 fold increase in pressure. Fig. 76 also reveals a significant driving pressure (P_a) dependence on the relationship between the viscous shell term and maximum shear rate, generating a particular family of curves. The particular effect caused by pressure on the offset and shape of the curves in Fig. 76 differ from previous lipid shelled results (Fig. 8a, [48]) where there the curves offset towards a larger shear rate (right) from each other as a function of pressure. In Fig. 76 the curve relationship both shifts towards a larger shear rate, but also towards a larger viscous term as a function of pressure. One possible

explanation for the different family of curves in Fig. 75 and Fig. 76 is the simplified shell viscous term adopted in the Marmottant's model, which might not account for a more complicated rheological nature of viscous stress acting inside the lipid shell, as suggested by Doinikov and Dayton [206]. The dependence of the viscosity on shear rate was found to be similar to previous results and is not further discussed here [48,60].

6.1.6 Conclusion

The goal of this work was to validate a model to estimate the transient pressure field in the flow cell to allow extraction of MB shell viscoelastic parameters. Model validation was performed by measuring the pressure *outside* the flow cell. Once validated, the predicted transient pressure field *inside* the flow cell was used as a known parameter in the Marmottant bubble dynamics model to fit the experimental R (t) curves. The shell parameters for 431 Optison MBs at five different driving pressures were extracted from the fits, and statistical significance obtained. This is an example of the potential for using a modified flow cytometer as a high-throughput tool for characterizing MBs. Although not emphasized, the flow cytometer approach also allowed us to extract the MB size distribution. The combined model-experiment validation appears to be an effective way to predict the pressure inside a small channel inaccessible to a hydrophone.

In the next section we report how a laser Doppler vibrometer combined with a finite element model were used to characterize the steady state vibrations of the system to drive MBs in the acoustic flow cytometer.

6.2: Steady State Pressure Characterization Using Laser Doppler Vibrometry

6.2.1 Introduction

Similar to our previous section (6.1), a flow cytometer was adapted with a transducer affixed to a flow cell. We reported the results of pressure calibration for *transient* sonication [48] in a recent symposium [209] and Chapter 6.1. Here, we report the results of pressure calibration for *steady-state* sonication[210]. However, in contrast to that section which used transient pulses to activate the MBs, this section uses long tone bursts to set up a *steady state pressure field* to drive the MB into oscillation as it flowed through the flow channel. The purpose for using a steady-state pressure field is that the MB experiences a regular sinusoidal forcing, rather than a pulse that includes a ramp up and ramp down phase, which is much harder to model.

As with our previous section, the goal here was to validate a COMSOL Finite Element Model (FEM), and then use that model to predict the pressure experienced by the MB. Modeling was needed to predict the pressure because the flow channel is too narrow to insert a hydrophone. We used a Laser Doppler Vibrometer (LDV) to measure the velocity of a flow-cell wall *in situ*. The COMSOL model of the vibratory modes was then validated and used to predict the pressure in the flow channel. Then, as with the previous section (6.1), 'activated' MBs were fit to a bubble dynamics model and the viscoelastic shell parameters were extracted. Although excellent agreement in fitting the oscillations was achieved, the extracted viscoelastic parameters differ from the transient pulse previous section. We hypothesize that because the flow cell is under steady-state vibration, MBs flowing through the channel experience oscillations before entering the interrogation zone, and thus there is some shell fatigue before the measurements take place.

6.2.2 Materials and Methods

Experimental Setup for the model calibration step

The experimental setup for the model validation is shown in Fig. 78. An Influx Cell Sorter (BD Biosciences, San Jose, CA) was modified to include a quartz flow cell (Model # J11020-040-003, Hamamatsu, Japan) with a 200 µm flow channel as a measurement chamber in place of the standard nozzle and fluid jet. Acoustic coupling to the carrier sheath fluid and MB samples occurred through a mounted transducer bonded to one side of the flow cell. The details of the system and general methods used are described in (Section 6.1). The major difference in setup between the previous section and this one is that instead of validating the COMSOL model with emitted pressure into a water tank, we measured the flow cell's vibration with a Laser Doppler

Vibrometer *in situ*. In addition, the driving signal consisted of a long 300-cycle tone burst rather than a 30-cycle transient tone burst. The longer burst was chosen to allow for the system to reach a steady state velocity field.

LDV *in situ* measurements were performed using the OFV-534 sensor head with OFV-5000 controller and VD 05 decoder (Polytec, Irvine CA). This system performs point-based (rather than scanning) measurements with a frequency detection range up to 10MHz (±0.5 dB frequency response amplitude error) with 100 mm/s/V sensitivity, capable of detecting a maximum velocity of 0.6 m/s. For scanning, the LDV (with either 10X or 50X objective) was mounted to a 3D positioning stage with 10 µm precision and scanned with a minimum step size of 250 µm. The VD 05 decoder (Polytec, Irvine CA) was used. The sensor head was connected to an air corrected, long working distance microscope objective (M Plan APO SL50, Mitutoyo, Japan) to achieve a high sensitivity. The working distance was 20.5 mm and a 1.6 µm depth of focus. A high pass filter of 100 Hz was used to remove low frequency room noise. The output was connected directly to an oscilloscope collecting 5×10^8 samples/s.

The system's jitter was assessed by taking an envelope function of 1000 bursts and measuring the maximum shift between measurements. At an operating frequency of 1MHz, the jitter was below 18ns. For scans, we defined the starting point ($x,y,z = 0$) as a point at the distal wall of the flow cell, at the midpoint of the PZT (see Fig. 78b). Waveforms were recorded along the long (x) and short (y) axes of the flow cell (Figs. 79c,d), and at different voltage levels. Long axis scans included 17 points separated by 500 µm extending 4 mm above and below the center point. The short axis scans included 15 points separated by 250 µm extending across the flow cell passing exactly through the center point. At the center point, the voltage level was swept through seven different voltage levels within the ranges used in the experiments (see Table 8).

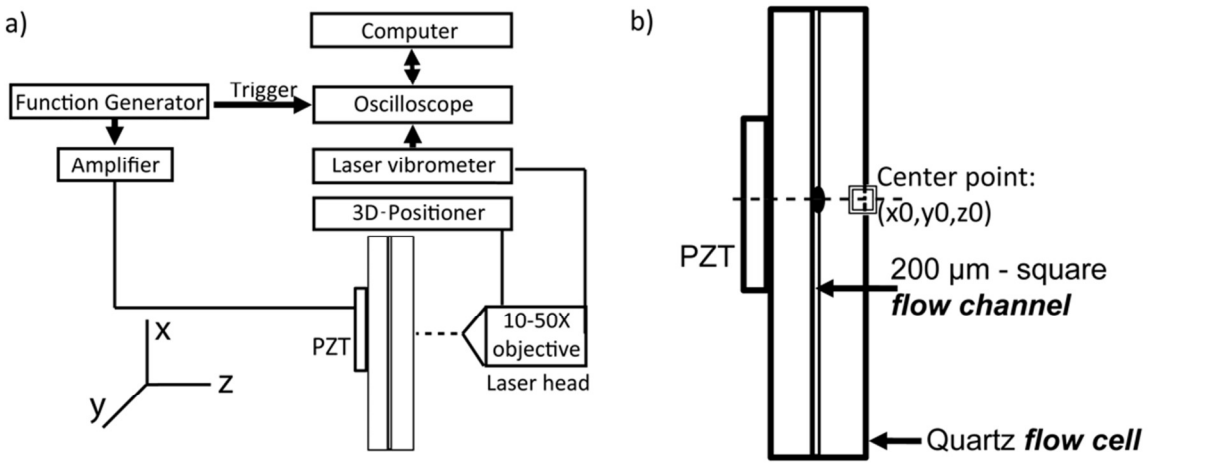

Figure 78. Schematic of the experimental setup. (a) The objective is coupled to LDV system and focused on the distal wall of the flow cell. Velocity vibrations can be measured with an LDV system that can be scanned along the distal surface around the X, or Y axes. (b) The "center point" of the scans is located at the distal surface, at a point bisecting the center of the PZT (0.7 mm thick). This same line bisects the flow channel at the laser beam interrogation zone (shown as a darkened area in b).

Finite element Model and Setup

The finite element package COMSOL (4.2a) was used to implement a multiphysics simulation of the *in situ* flow cell. The simulation couples piezoelectric physics and structural mechanics in the PZT with the structural mechanics in the quartz flow cell and the acrylic mount, and linear acoustics physics in the water domain. The Piezoelectric Devices (pzd) and Pressure Acoustics, Frequency Domain (acpr) physics were implemented in COMSOL for this model. The quartz flow cell was supported by an acrylic mount from above *in situ*. In the model this is implemented by a fixed boundary condition on the top surface of the acrylic; this supports the flow cell as a cantilever. The ends of the flow channel are truncated with a radiation boundary condition. On walls of the flow channel and the structural physics and acoustic physics are coupled with pressure and normal acceleration, respectively. On the PZT domain the electrodes are implemented by a terminal and a ground boundary condition on the large faces of the transducer. A schematic of the model setup is shown in Fig. 79. The PZT, quartz, acrylic and the water within the flow channel were assigned material properties from the COMSOL built-in materials list of PZT-4, quartz, acrylic and water respectively.

The input to the simulation is a steady state sinusoidal voltage (1 MHz, between 4 – 29 volts) applied to the positive PZT electrode to match the amplifier input of the experiments. COMSOL solves the stress-charge form of the piezoelectric equations in the PZT and the structural/elastic vibration, and linear acoustic equations in the water domains as a function of time. The specific

sound speeds and wavelengths of the 4 materials used in the model are: $\lambda_{(water)}$ = 1.5 mm (C_{water}=1500 m/s), λ_{Quartz} = 5.5 mm (c_{quartz}=5500m/s), and λ_{PZT} = 4.5 mm (c_{pzt} = 4500 m/s).

.

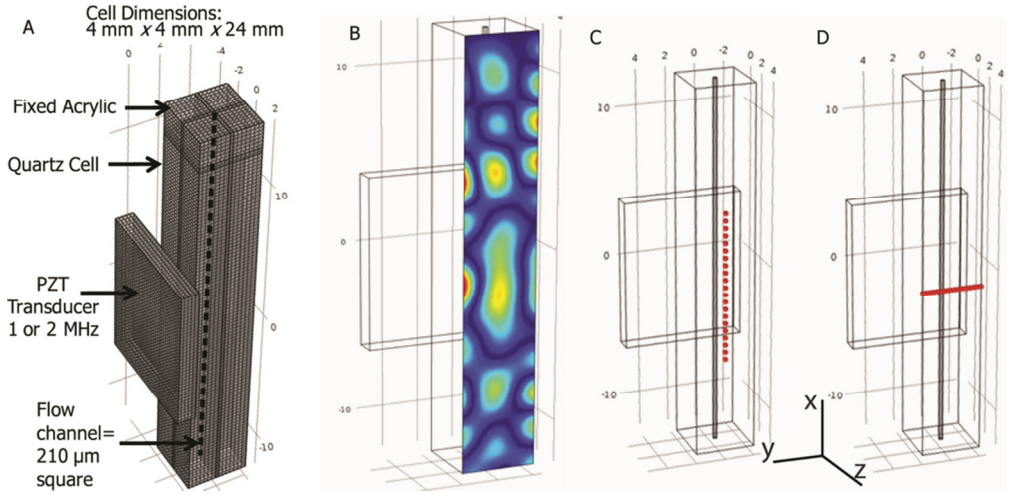

Figure 79. Finite element model setup. a) 3D view of the finite element model setup. The system consists of a piezoelectric crystal (PZT) attached to a quartz flow cell. Inside the flow cell, a 200 µm square flow channel filled with water runs through the flow cell. The mesh implemented is a free tetrahedral mesh, with a total of 903709 elements. Each material is meshed corresponding to its own wavelength as the following: $\lambda_{material}/N$, where N=14 for the model above. b) Velocity field example computed for 1MHz excitations. c) and d) Long and short axis scan compared with experimental measurements, respectively.

Experimental setup for the mechanical property estimation for Optison MBs.

In the experiments, Optison MBs were diluted in 0.45 µm filtered Isoton II (Coulter, Miami, FL) electrolyte with an initial concentration (5.5x 10^8 MBs/mL) determined using a Coulter M3 Multisizer (Coulter, Miami, FL). Experiments were done in triplicate at a sheath pressure of 40 kPa (5.8 PSI) and sample pressure of 41.3 kPa (6 PSI), producing a flow rate of 4.8 mL/min in the flow channel. Each run at a particular setting lasted between 3-5 minutes, allowing collection of about 100,000 MB events for each run. For size calibration of the flow cytometer, a calibration kit (nonfluorescent microspheres, Molecular Probes, Eugene, OR) containing six different size populations with diameters from 0.5 - 10 µm was used. The driving frequency was 1 MHz with pressure amplitudes between 50 - 340 kPa. MB oscillatory behavior was collected by the flow cytometer's laser system, and digitized by a 12 bit PXI- 5105 at 20 MHz for later analysis [41,48,49,209–211].

6.2.3 Results

COMSOL model validation: System frequency response and pressure-voltage calibration.
The experimental setup for model validation was performed *in situ* with the flow cell attached to the flow cytometer. This allowed structural velocity measurements using the exact conditions for MBs experiments. It was assumed that if the model could predict the velocity steady state field *at the distal wall* of the flow cell, it would also be able to predict the pressure field *inside* the flow cell where the MBs were being subjected to ultrasound.

The first step was to determine the system's resonance structure and frequency dependence response measured by the LDV system at the center point. The Admittance Y, defined as the inverse of impedance (Y= 1/Z) measured from the flow cell, was calculated. The admittance magnitude and the center point peak velocity as a function of frequency are shown in Fig 80. Although both plots reveal a peak near the PZT resonance frequency (2 MHz), it is clear that from the velocity plot and the admittance plot that there is a system resonance at 1.6MHz that allows the system to vibrate more efficiently than at the PZT's resonance. It can also be seen that the system has several very sharp peaks (high Q system) at several frequencies, indicating the complicated structure and challenges for modeling. The 1 MHz region chosen to drive the system is not near a strong resonance and shown for Fig 80. There is a strong correlation between the measured admittance and the peak velocity of the system at the center point. The data suggests that either a LDV or an impedance analysis could be a quick way to determine the quality control of the system for future experiments.

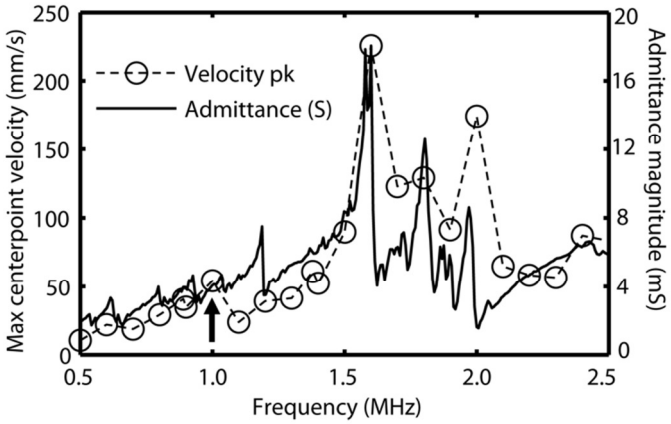

Figure 80. Admittance and maximum velocity plot. Admittance (inverse of impedance) is measured in siemens (S) and plotted in solid lines as a function of ultrasound driving frequency for the *in situ* measurement. Velocity peak(+) shown as dashes and circles vs. frequency at the center point, swept between 0.5 - 2.5 MHz (measured with LDV). The arrow indicates the experimental driving frequency (1 MHz) used in the experiments and simulations.

The next step was to measure the linearity between input voltage and measured velocity amplitude at the distal wall center point. In Fig. 81 the open circles (solid line is a linear fit) show velocity amplitudes, while the model prediction at the same location is shown as filled circles (dashed line is a linear fit). As explained in section 6.1, the COMSOL-predicted peak velocity was corrected by the addition of a constant offset of 5.4 mm/s to match the experimental levels. This setting was applied to *all* subsequent applications of COMSOL.

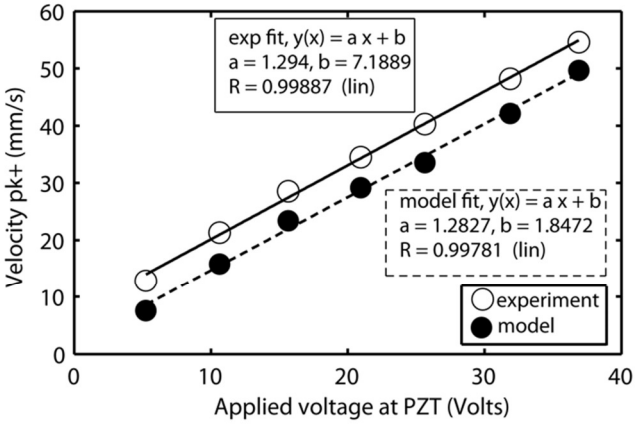

Figure 81. Calibration plot. Relationship between applied voltage at the PZT and velocity amplitude for both the model (solid circles) and the experimental (open circles) setups shown in Figs. 78 and 79 at the center point (center of the distal face, see Fig.78b). The lines are a linear best fit. In subsequent applications of the COMSOL model, a normalization factor was added to match the experimental measurements, as described in the text.

COMSOL model validation: Long (X) and Short axis (Y) scan:

Model validation was performed by comparing the model results with an average of 100 LDV measurements at various positions along the flow cell. Figure 82a shows relatively good fits along the *x*-axis. It's important to note that the laser interrogation zone is only 60 µm centered around the center point, whereas *x*-axis (*y*-axis) scans extend to 4 mm (2 mm) away from the center point. Extending the scan allowed for a more comprehensive evaluation of the COMSOL model. When simulating the pressure *inside* the flow channel, the only location of interest is that corresponding to the laser interrogation zone (the line that bisects the center point of Fig. 78b).

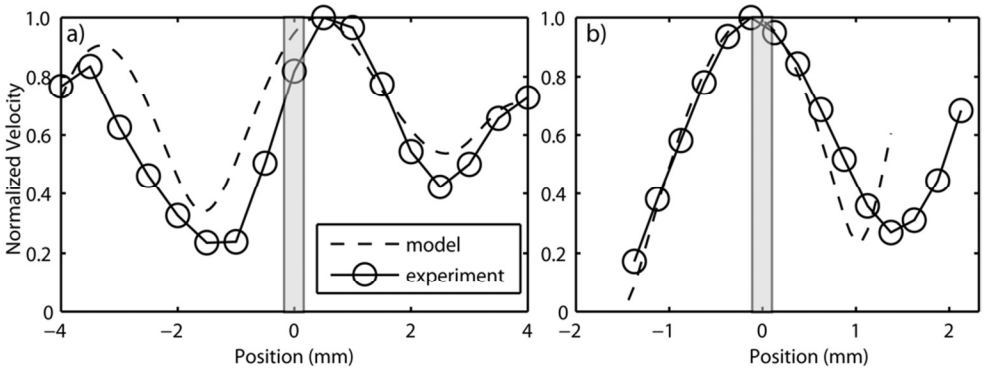

Figure 82. Long and short axes scans. (a) Normalized long (x) axis scan of the maximum peak velocity for at the distal wall of the flow cell (as indicated by Fig. 79c). b) Normalized short axis scan of the peak velocity for at the distal wall of the PZT (as indicated by Fig. 79d). The modeled predictions (dash lines) compare favorably to measured values (circles with solid lines) at an input voltage of 25 V. Scan step size was 0.25mm. The gray bar corresponds to the width of the flow channel where the measurement takes place. The laser spot size at this location was 60 μm in diameter.

With the model validated, we next turned to predicting the waveform inside the flow channel at the laser interrogation zone. The voltage to pressure relationship is summarized by the 3rd and 4th columns of Table 8. The predicted pressure is the forcing function in the bubble dynamics model that drives MBs into oscillation. We implemented the Marmottant bubble dynamics model [48,49,192], and used a least squares fitting algorithm to extract the best-fit viscoelastic shell parameters.

Mechanical property estimation for Optison MBs.

The details for estimating MB size and mechanical properties using the modified flow cell can be found elsewhere [48,49] In the earlier work, the driving pressure was included as a fitting parameter. In this section and in our previous section, the pressure derived from the COMSOL model is used.

Figure 84a shows a representative example of the predicted steady state pressure. It is worth noting how different this time-based signal is compared to the transient pulse we used in the previous section. That pulse is also shown here for comparison (Fig. 83). The steady state signal is much easier to use in fitting the R(t) dynamics from the Marmottant model.

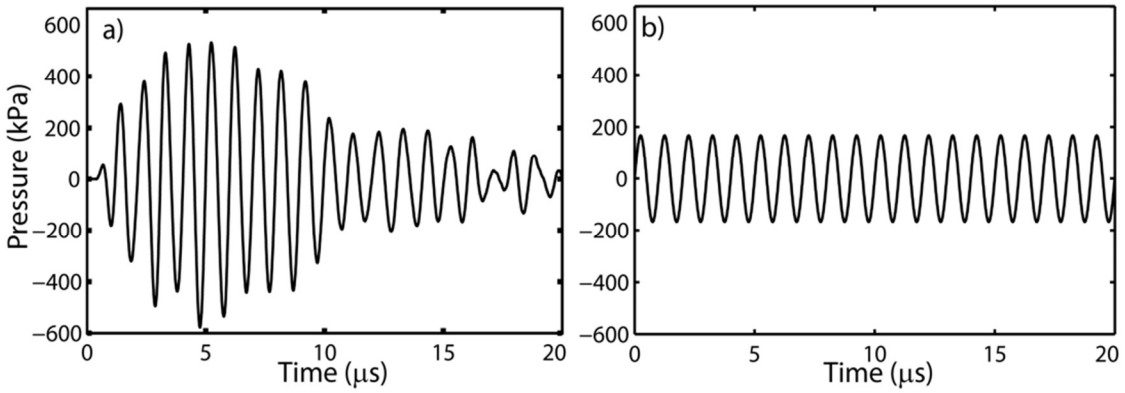

Figure 83. Comparing Comsol predicted driving function for transient vs. steady state. a) 20-cycle 1 MHz pulse, and b steady state sinusoidal at a constant pressure (windowed to 20μs). Both input voltages were near 16V.

Examples of several fitted waveforms are shown in Fig. 84b-f. This technique was applied to a total of 450 MBs of different sizes and driven at different pressure amplitudes. We used the STD minimization value described in Eqn (5.4). The best fit minimization values obtained for Figs. 84b-f are in a range of 0.02 - 0.08.

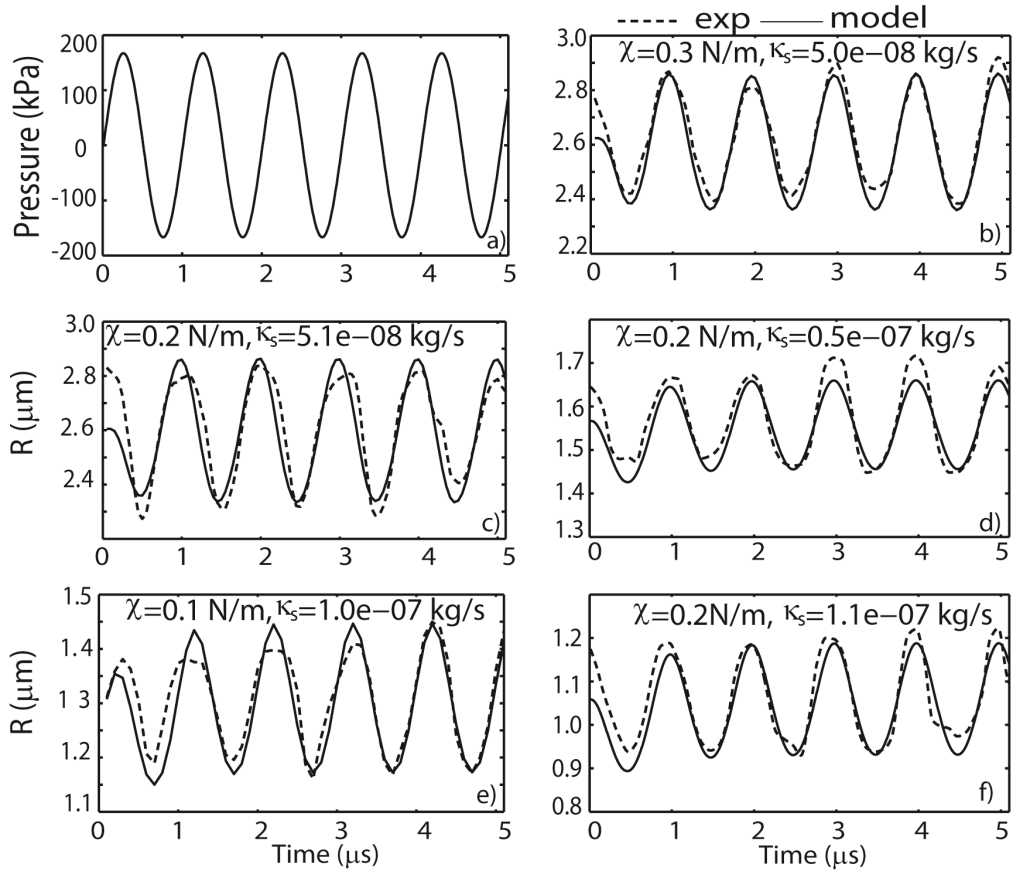

Figure 84. Bubble dynamics fits. (a) The COMSOL-derived forcing pressure was used in the Marmottant bubble dynamics model to fit R(t) curves. The dotted box indicates the fitting window (5 cycles) that was used. (b-f) Best fits

and corresponding shell parameters for selected R(t) curves at peak pressures of 50, 100, 167, 234 or 324 kPa, respectively. The initial size, Ro, of these bubble measured by our system is 2.6, 2.6., 1.6, 1.3 or 1.1 μm for bubbles represented in Panels B-F, respectively.

The shell elastic modulus, χ, (N/m) and shell dilatational viscosity, $\kappa_{s,}$ (kg/s) were extracted for each bubble as a function of size and driving pressure. Statistical analysis performed follows the methods described in Section 6.1.3 to analyze the data. A summary of the steady state results, with mean and 95% confidence intervals is shown in Table 8. For a total of 470 bubbles, we discarded four percent of the total data set that did not meet this criterion presented in 6.1.3, leaving data sets for 450 MBs for analysis.

Table 8 shows a summary of the shell properties for Optison at five different peak positive pressure settings, labeled as groups A, B, C, D and E (corresponding to 50, 100, 167, 234 and 324 kPa, respectively) for ease of reporting in the text. The table also shows the input voltage (at the PZT), the predicted peak positive pressure amplitude, number (n) of bubbles analyzed at each pressure, the fitted viscoelastic parameters, and the shear rate (discussed further below). Where appropriate, the 95% confidence interval (CI) is also listed.

Table 8. Summary of the measured properties for Optison ™ MBs, steady state results.

Group	*n*	PZT Peak Positive Drive Voltage	Acoustic Pressure (P+; kPa)	Viscosity κ_s *10^{-7} (kg/s)	Elasticity χ (N/m)	Max Shear Rate (MHz)
A	62	5.25	50	0.24 [0.17 –0.32]	0.25 [0.15-0.35]	1.87 [1.72-2.02]
B	120	10.6	100	1.08 [0.74 – 1.42]	0.37 [0.29-0.45]	1.27 [1.17-1.37]
C	96	15.6	167	1.40 [0.97 – 1.83]	0.46 [0.32-0.60]	2.20 [1.99-2.41]
D	79	20.9	234	1.65 [1.20 – 2.10]	0.32 [0.24-0.40]	2.23 [2.05-2.41]
E	93	25.6	324	1.97 [1.58 – 2.36]	0.38 [0.25-0.51]	2.38 [2.22-2.54]

Viscosity, elasticity and maximum shear rate are described as means with 95th percentile confidence interval, [95%CI].

The relationship between the shell elastic modulus and MB size is shown in Fig. 85A for N=120 bubbles driven at p+ = 100 kPa (corresponding to the second row of Table 8). Within experimental error, the shell elastic modulus is constant across bubble size. We also compared the elastic modulus across different driving pressure groups and observed a nominal but statistically insignificant increase in the mean value (Fig. 85b and Table 8). The albumin shell elasticity of Optison was relatively uniform across MB size and driving pressure, which is consistent from previous literatures results. However the value obtained in the present study (on average 0.38 N/m, 95%CI = [0.30 - 0.46]), was more than 50% lower than our previous section

results (1.04 N/m with a 20-cycle driving function; Section 6.1), as well as from published literature values [197,204,212]. Potential explanations are presented in the Discussion section.

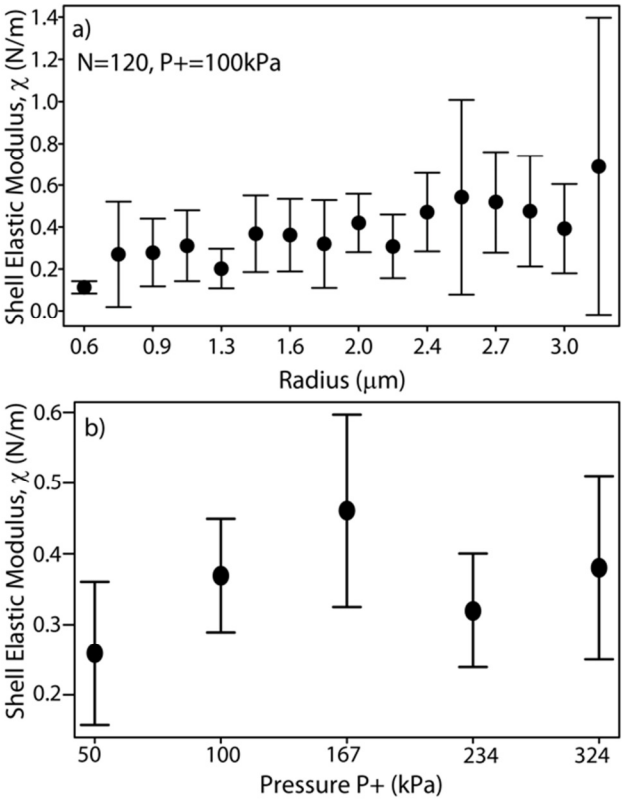

Figure 85. Elasticity plot. (A) Shell elastic modulus vs. Ro for Optison MBs. Standard deviation error bars are used when at least 5 bubbles are binned within 0.14 μm (bin width) of the center radius. (B) Shell elastic modulus vs. driving pressure. Mean and 95% CI (error bars) presented for each pressure group according to Table 8.

The relationship between the shell dilatational viscosity and bubble size is shown in Fig. 86 a for three different pressure settings (see also Table 8), and it shows that the shell dilatational viscosity increases with increasing equilibrium MB size. The family of curves shows a dependence on driving pressure. We analyzed the mean viscosity across five pressure groups (Fig. 86b) revealing statistically significant differences in the means (P-value < .0001, one-way ANOVA). Groups D and E had statistically significantly higher viscosity than groups A and B ($P < 0.01$, using Tukey *post hoc* tests).

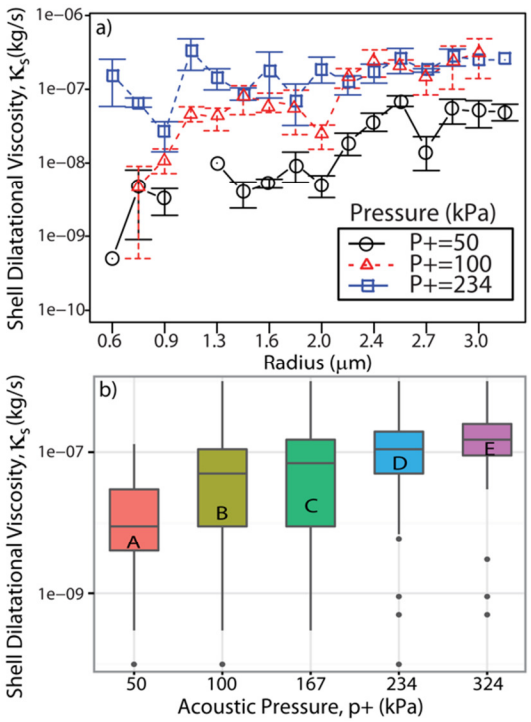

Figure 86. Shell dilatational viscosity plot. A) Shell dilatational viscosity vs. Ro for Optison MBs, shown for three pressure settings. Standard deviation error bars are used when at least 5 bubbles are binned together. B) Boxplot of the shell dilatational viscosity as a function driving pressure groups (A-E, Table 8). Either the whiskers of a box-plot are drawn out to the maximum and minimum values, or the maximum and minimum values are plotted as individual points (if they are considered outliers). The bottom of the box-plot is the 25th percentile, which defines the first quartile, and the top of the box is the 75th percentile, which defines the third quartile.

Finally, in Fig. 87 we plot the relationship between the shell dilatational viscosity and maximum shear rate, $max\left(\frac{\dot{R}}{R}\right)$, (calculated from each bubble's R(t) curve) for three pressure settings. As expected from the literature [48,49,60,206] the viscosity decreases with increasing shear rate. In addition the maximum shear rate increases with driving pressure.

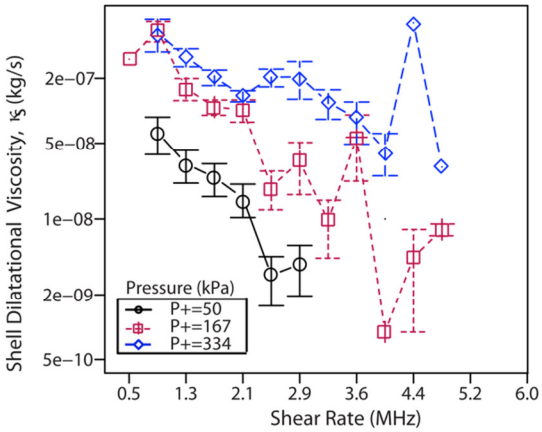

Figure 87. Shear rate plot. Relationship between shell dilatational viscosity and maximum shear rate for Optison, for three pressure settings from Table 8. Standard deviation error bars are used when at least 5 bubbles are binned together. A family of shear thinning curves is generated, showing a dependence on driving pressure.

The measured bubble shear rate was also analyzed as a function of different driving pressure groups revealing statistically significant differences (Table 8; P-value < 0.0001, one-way ANOVA). Group E had statistically significantly higher shear rate than groups A, B, and C ($P < 0.001$ for each comparison, respectively; Tukey *post hoc* tests). In addition, group D was significantly different from A, B and C ($P = 0.016$, $P = 0.015$, $P < 0.001$, respectively, Tukey *post hoc* tests).

6.2.4 Discussion

The goal of this work was to implement a method to characterize ultrasound contrast agent microbubbles (MBs) in a high-throughput fashion. The technique uses light scattering and fitting from a bubble dynamics equation to extract MB size and viscoelastic shell material properties. In particular, we developed a method to allow faster fitting of the data using a COMSOL finite element model to predict the pressure waveform experienced by the MB. The model was validated by comparison to Laser Doppler Vibrometry (LDV), and then used to extract MB properties from hundreds of MBs.

Some comments about the validation and use of the COMSOL model are warranted: First, the multiphysics model appears to predict the LDV measurements fairly accurately. The COMSOL model does show an offset from the LDV measurements; however this can be explained by noting that the model uses estimates for the PZT and quartz materials. In addition, there was an unknown thickness of epoxy bonding the PZT to the quartz flow cell that was not included in the simulations.

The estimation process of mechanical properties has limitations as well. Although 100,000 light scattering events are collected on average for each individual experimental run, the results (Table 8) only report mechanical properties obtained 550 MB best fits. This is because the larger number of pulses contains responsive MBs, debris (albumin clumps), and unresponsive microspheres (*i.e.*, broken shells) which scatter light above a minimum intensity for detection and have to sorted post-processing. After isolating and selecting the responsive MBs, there is a computational time required to find the best-fit mechanical properties. The Matlab implementation used in this study performed a least-squares optimization of the Marmottant model ODE using Matlab differential equation solver (ode45), and for this particular study, required between 8 - 20 minutes to fit one MB. The shell properties were swept through 32 different possible elasticity values (0.1N/m-3N/m) and 42 different shell viscosity values between ($1X10^{-6}$ – $1x10^{-10}$ kg/s). This is more than 1200 combinations, without considering the least squares fitting run-time, the internal Marmottant iterations (*i.e.*, surface tension piecewise

definition which changes for each sampling point in the radius *vs*. time curve), the runtime for ODE45 (computationally expensive), and aligning of the modeled R(t) to the forcing pressure steps. Recent improvements to our code implementation, have allowed us to obtain fits of the mechanical properties in one to five minutes maximum for a single bubble. A future suggestion this work would be to implement the code in C++ language and embed it into the PXI detection hardware that collects flow cytometry pulses to detect and measure mechanical properties in a pseudo-real time fashion (bubble mechanical properties in seconds).

Finally are several findings that were similar in both studies, regardless of the short or long forcing functions used to drive the MBs. We found that the mean elasticity of Optison, although different in absolute value for both studies, was fairly constant across driving pressures and R0. For both studies, the shell dilatational viscosity increased significantly with increasing R0 (Fig. 85). These results are consistent with previous observations of lipid and protein shells [48,49,53–55,60,206]. In addition, both studies show a distinct dependence on driving pressure and a significant driving pressure (Pa) dependence on the relationship between the viscous shell term and maximum shear rate, generating a particular family of curves. The particular effect caused by pressure on the offset and shape of the curves in Fig. 87 differ from previous lipid shelled results (see Fig 8a in [48]), where there the curves offset towards a larger shear rate from each other as a function of pressure. In Fig. 87 the curve relationship shifts towards a larger shear rate and also towards a larger viscous term as a function of pressure. One possible explanation for the different family of curves in Fig. 86a and Fig. 87 is the simplified shell viscous term adopted in the Marmottant's model, which might not account for a more complicated rheological nature of viscous stress acting inside the lipid shell, as suggested by Doinikov [206]. The dependence of the viscosity on shear rate was found to be similar to previous results and is not further discussed here [48,60].

In the next section (6.3), the mechanical properties of Optison using short transient (20 cycles) and long (steady state) acoustic fields are discussed, compared and contrasted.

6.2.5 Supplemental Information

In addition to characterizing the system at 1 MHz, the velocity of the walls of the flow cell was characterized as a response to bursts of 5, 20 and 300 cycles at frequencies between 500 kHz and 2.5 MHz, with 1ms PRF in order to investigate the effect of frequency on the system's vibrational behavior. The frequency sweep included full long and short scans (as defined in Fig. 88c and d) at 0.5, 0.89, 1, 1.38, 1.6, and 2 MHz.

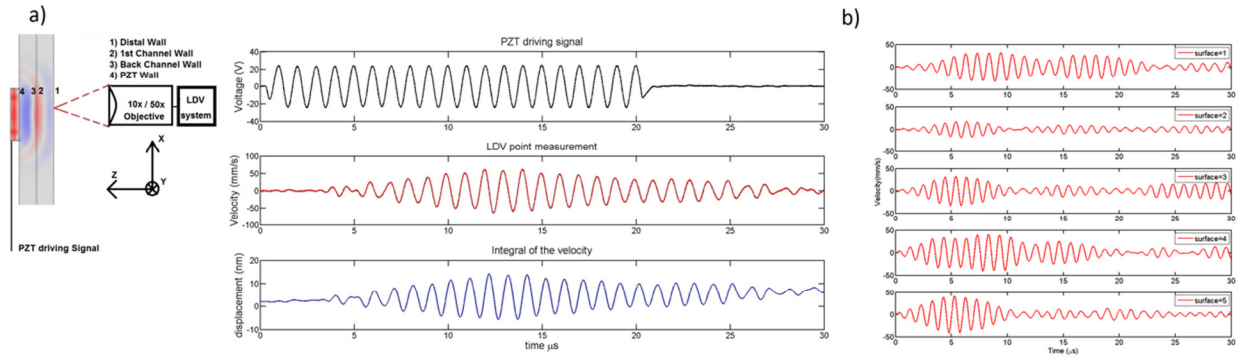

Figure 88. Surface point scanning with the LDV. Measurement of the wall velocity or displacement using a Laser Doppler Vibrometer system. b) Surface velocity scan along the flow cell in response to a short burst, 1MHZ pulse.

Figure 88 shows the representative LDV point measurement of velocity or displacement corresponding to a PZT driving (forcing function) signal of 20 cycles at 1MHz. The same measurement shown was repeated for an orthogonal direction to the sound propagation to investigate the out of the field vibrations in the system. It is very important to note that the mode presented in this section (6.2.2) used to validate the pressure only computed the normal velocity field component, ignoring any velocity small component in the other direction. We confirmed and the component percentage of velocity in the orthogonal direction was less than 8.2 % of the maximum value. Next, the possibility of inserting a fiber optic hydrophone was assessed; the main concern with inserting an object such as a hydrophone inside a cavity is that by inserting it, it will affect the field inside (*i.e.* inserting a 150µm fiber in a 200 µm channel). Velocity measurements were collected with and without fiber at different positions to asses a change in velocity displacement in different surfaces. The results revealed no difference in the distal wall velocity caused by the FOPH. For future studies with a larger flow channel, a FOPH could be inserted to measure the pressure *in situ*.

Figure 89 shows the velocity waveforms measured with LDV at two positions in response to 20 cycle pulses at 1MHz: The center of the distal wall, 600 µm below (x direction), and 1.9 mm below (x direction) to show the qualitative variation off the system even within the PZT region. Every figure in this section is followed by a zoomed version of the first 30 µs.

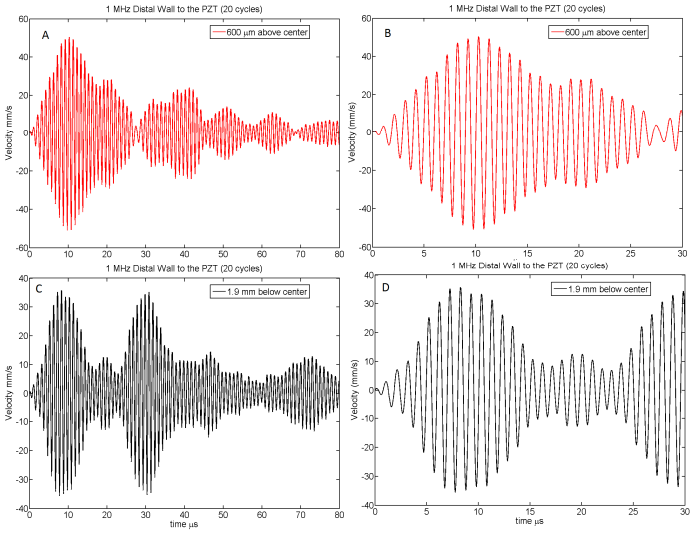

Figure 89. Surface velocity variations along long axis using laser Doppler vibrometer. a) Wall velocity plot at a location 600 µm the center point at the distal wall. b) First 20 µs of a. c) Wall velocity a location 1.9 mm below the center point at the distal wall. d) First 20 µs of c.

Figure 90 shows the summary of a long and a short axes scan performed with the LDV system at 6 different frequencies.

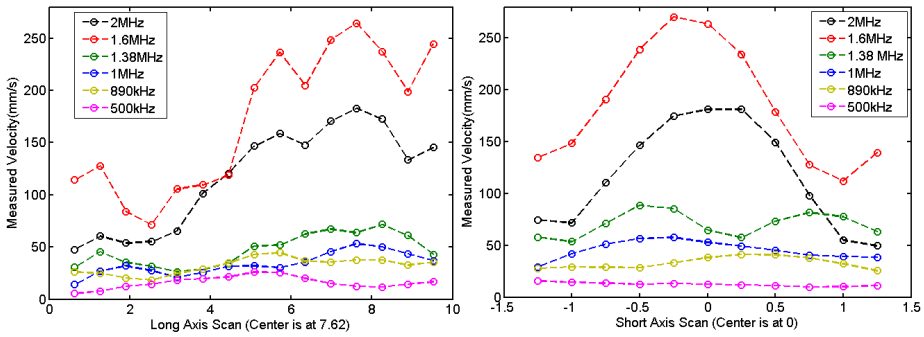

Figure 90. Flow cell velocity scan as a function of frequency. Left: Long axis scan comparing V+ peak at all frequencies. Right: Short axis scan.

The long and short axis were scanned in the PZT walls labeled as 1-4 in Figure 88, but there was a concern that there might be wave mixing of similar order of magnitude than the velocity displacement due to ultrasound local changes on the optical index of the material. Figure 88b shows the scanning along the surfaces initially displayed on Figure 88a. This shows the ability of LDV to focus into a surface and block the light modulated from any other place than the focal region of the objective. One of our possible problems with this results is that the acoustic modulation might be in a similar order of the change in optical index that the device detects, the order of magnitude that ultrasound changes the optical index on the medium as it propagates

can be similar to the change due to velocity vibration, which is the detection mechanism of the vibrometer. For this reason, only distal surface velocity from the vibrometer is shown.

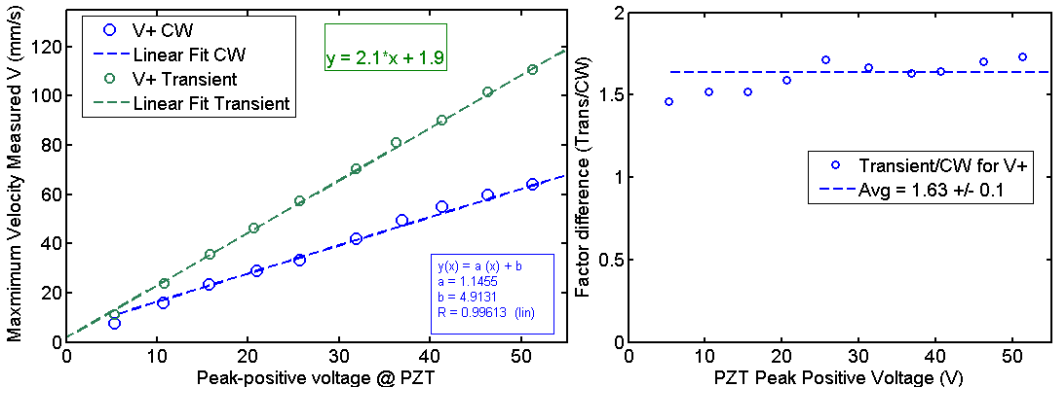

Figure 91. Comparing pulsed *vs.* "steady state" velocities. At the center point for a range of voltages (left) and as a ratio between each point (right).

The ratio between the steady state and transient regions of the center point waveforms shown in Fig. 91; it can be concluded that at a given voltage, there is a fixed linear ratio between the transient/steady state velocity measured by vibrometry. This factor can also be used to estimate the pressure used in the previous section (6.1) compared to the pressure used in this section (6.2). For example, for a voltage setting that would generate 890 kPa p+ in transient regime, if translated to steady state regime, would generate approximately 330kPa. This is another way of confirming the self-consistent calibration results shown in Tables 7 and 8. LDV revealed that CW is more suitable to simulate sinusoidal pressure for fitting material properties, and that burst pulses have a distinct characteristic similar, but not exactly the same as a Gaussian pulse.

6.3: Steady State *vs.* Transient Comparison: Shell Properties and Spectral Analysis

6.3.1 Introduction

In the previous two sections (6.1 and 6.2), the mechanical properties of Optison using short transient (20 cycles) and long (steady state) acoustic fields were extracted. In this section, the focus is on comparing and contrasting the difference in mechanical properties obtained by the two forcing functions (long and short pulses), and on presenting a spectral analysis technique derived from the R(t) curves of the data analyzed both in sections 6.1 and 6.2.

The shell elastic modulus for steady state, was found to be on average χ= 0.38 N/m (Table 8). For the transient case, it was found to be on average, χ= 1.04 N/m (Table 7), which is 2.7 times larger. The shell dilatational viscosity for steady state was found to be within the range of $3x10^{-8}$ – $2.3x10^{-7}$ kg/s (Table 8) and for the transient case, $3x10^{-7}$ – $1.4x10^{-6}$ kg/s (Table 7), which covers a range 1 order of magnitude over the steady state case.

6.3.2 Materials and Methods

Spectral analysis was performed in order to analyze the harmonic content in the radial oscillations of the bubbles, the R(t) signals. An N point FFT algorithm using Matlab (Mathworks, MA, USA) was implemented on the R(t) signal obtained from size calibration of the flow cytometer as shown in Tu *et al.* and Cavalieri *et al.* 2013 [48,49]. The process is illustrated in Fig. 92 below. An initial light scattering pulse (Fig. 92a) is calibrated into size using Mie Scattering theory (Fig. 45, and process shown in as shown in Tu *et al.* [48]), and then high pass filtered to obtain the MHz oscillations superimposed in the flow cytometry pulse (Fig 92b). The filter used is a Chebyshev filter (Matlab function cheby2), in which the filter coefficients are obtained and then filtfilt function is applied to properly high pass filter the calibrated R(t) curve. Finally, FFT is computed (Fig. 92c) and the spectral analysis is performed on the Log converted data ($20Log_{10}(A/A_o)$), in which A is the signal and A_o is a normalizing constant value to make comparison across groups. De-trending the R(t) curve ($R-R_o$) and normalizing by R_o helps removing the offset, as shown in Figure 93, and allows a comparison of the subharmonics ($f_o/2$), harmonics (f_o, f_1, f_2, f_3, …) and ultraharmonics (3/2 f_o, 5/2 f_o, …). The selected values in red indicated in Fig. 93 are the harmonic regions in the computed FFT, where the software implemented calculated the peak values for each MB normalized spectra. This process is repeated for a total of n = 2280 bubbles in the transient study (Chapter 6.1), divided in 6 pressure groups and n = 570 for the steady state study, in 5 pressure groups, and is shown for comparison in Table 9.

Table 9. Harmonic analysis for both transient and steady state Optison,

Transient P+ (kPa)	n	Steady state p+ (kPa)	n
156	93	50	70
269	74	100	134
556	173	167	73
680	255	234	77
890	221	334	109
1300	1464		

The moving window spectral analysis was computed using a Matlab available toolbox called the Time-Frequency Toolbox (TFTB), which is a collection of algorithms developed for the analysis of non-stationary signals using time-frequency distributions. The toolbox contains numerous algorithms which implements various kind of time-frequency analysis with a special emphasis on quadratic energy distributions of the Cohen and affine classes, along with their version enhanced by the reassignment method. Both the short time FFT (tfrstft function, moving window of 32 points) and a moving spectrogram tfrtsp (32 points) were used to analyzed MB R(t) plots sampled at 20MHz from our experiments in section 6.1 and 6.2.

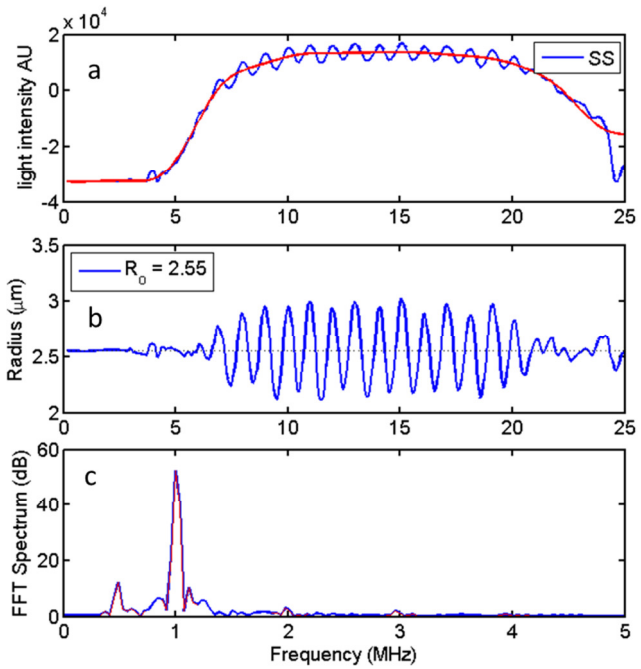

Figure 92. Obtaining R(t) and spectral information from a MB starting from a light scattering pulse. A) A flow cytometry pulse containing ultrasound+light scattering bubble pulse oscillations from an Optison bubble. b) High pass filter output from a), which is a regular R(t) curve. c) FFT of the R(t) curve in b) The red color indicates the harmonics or subharmonic regions analyzed in the next figures below.

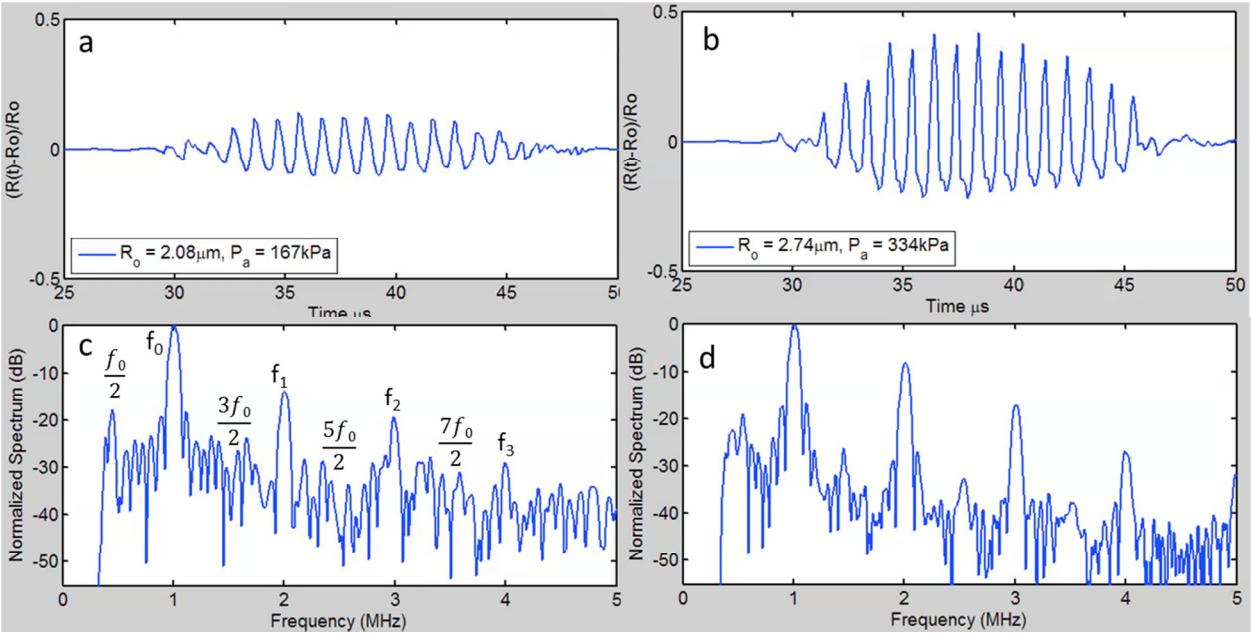

Figure 93. R(t) curves and spectral analysis. a) 2.08 µm initial radius and a larger b) 2.74 µm bubble, both driven at 50 kPa. c) Normalized spectra of a). d) Normalized spectra of b. Harmonic, ultra and subharmonics labeled on c.

6.3.3 Results

Figure 94 illustrates the LDV measurement of the center point velocity at 25V-300 cycle burst at the PZT. Figure 94a shows that the long pulse is clearly divided into a transient region, which is highlighted in Fig. 106c, followed by a steady state region, Fig 94d (until it reaches roughly 300 µs). The main difference in the mechanical properties obtained from the previous sections is due to the forcing functions used to drive MB from section 6.1 (the transient part, Fig. 94c) and section 6.2 (the steady state region, Fig. 94d). Figure 94b shows the calibrated model output at 25 V from Section 6.2, displayed as a contour field color plot, showing steady state surface velocity across the entire distal wall of the flow cell.

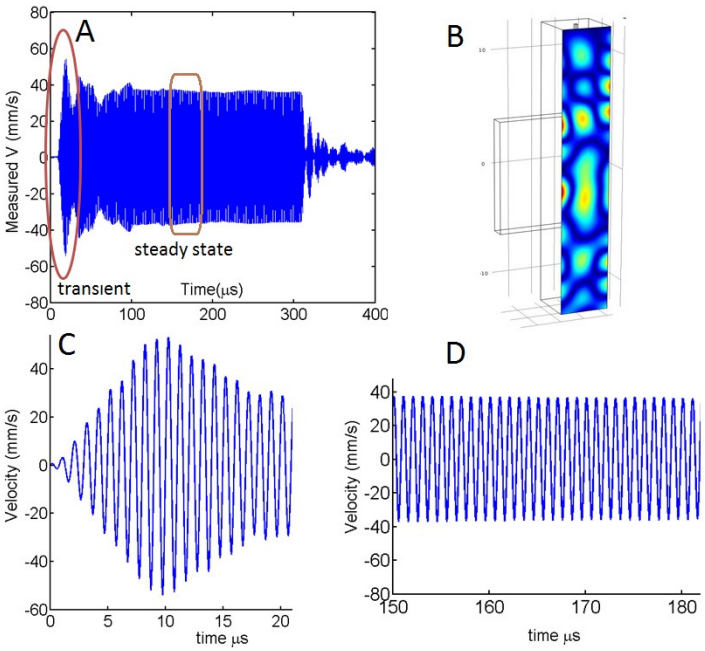

Figure 94. A 300-cycle velocity pulse at the center point showing steady and transient regions. Laser Doppler vibrometer measurement at the center point 1MHz frequency. A) the overview of the 300 cycle signal. B) FEM output at 25V input for 1MHz velocity field map. C) Transient (first 20 cycles) of the signal. D) Steady state region of the signal.

In order to determine the time-scale for shell fatigue, a moving window FFT spectral analysis was implemented for 200 bubbles driven with 20-cycle short pulses, to see if there was any evidence of distortion or evident phase changes at the timescales of the short 20-μs long forcing function. Figure 95 shows the characteristic example of a 2 μm Optison bubble's response to a 167 kPa, 20-cycle burst measured by our acoustic cytometer. The spectral energy density, de-trended R(t) and 2-D spectrogram are displayed together. There was no evidence of shell fatigue or nonlinear distortion (appearance or disappearance of harmonics for the measured R(t)'s at short time scales) for a hundred representative MBs analyzed over this 20 μs timescale.

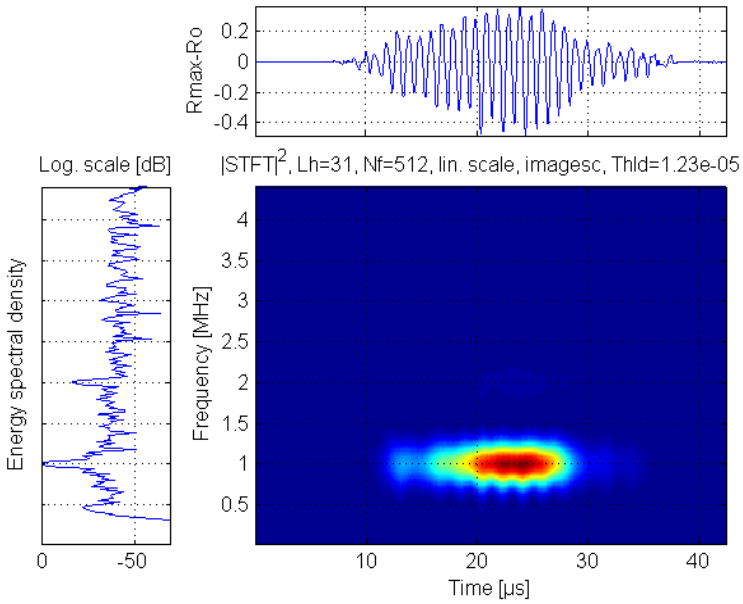

Figure 95. Moving spectral FFT analysis to determine temporal changes of MBs response to a 20-cycle pulse. The R(t) curve is shown on the top, the moving FFT window length was 32 points cycles (3.2µs – over 3 cycles per window). On the left, the spectral energy density for the entire R(t) signal is displayed.

Disapperance and regeneration of subharmonics (SHs)

Figure 96 and 97 show the results for the harmonic analysis of the transient MB and steady state MB, respectively. The mean and SD (circle and error bars) of spectral amplitude as a function of harmonics for a particular driving pressure group (Table 9) are calculated and plotted for each subplot (each harmonic component). Figure 96 illustrates that there is an increased trend of harmonic and ultraharmonic emissions as the driving pressure increases. The relationships are not necessarily linear; sometimes exponential, sigmoidal or power functions provided better fits to the data. However, there is a clear decay (10dB loss, see Fig. 99) in the subharmonic emissions as a function of increasing in pressure, followed by a regeneration of the subharmonic content at the highest pressure.

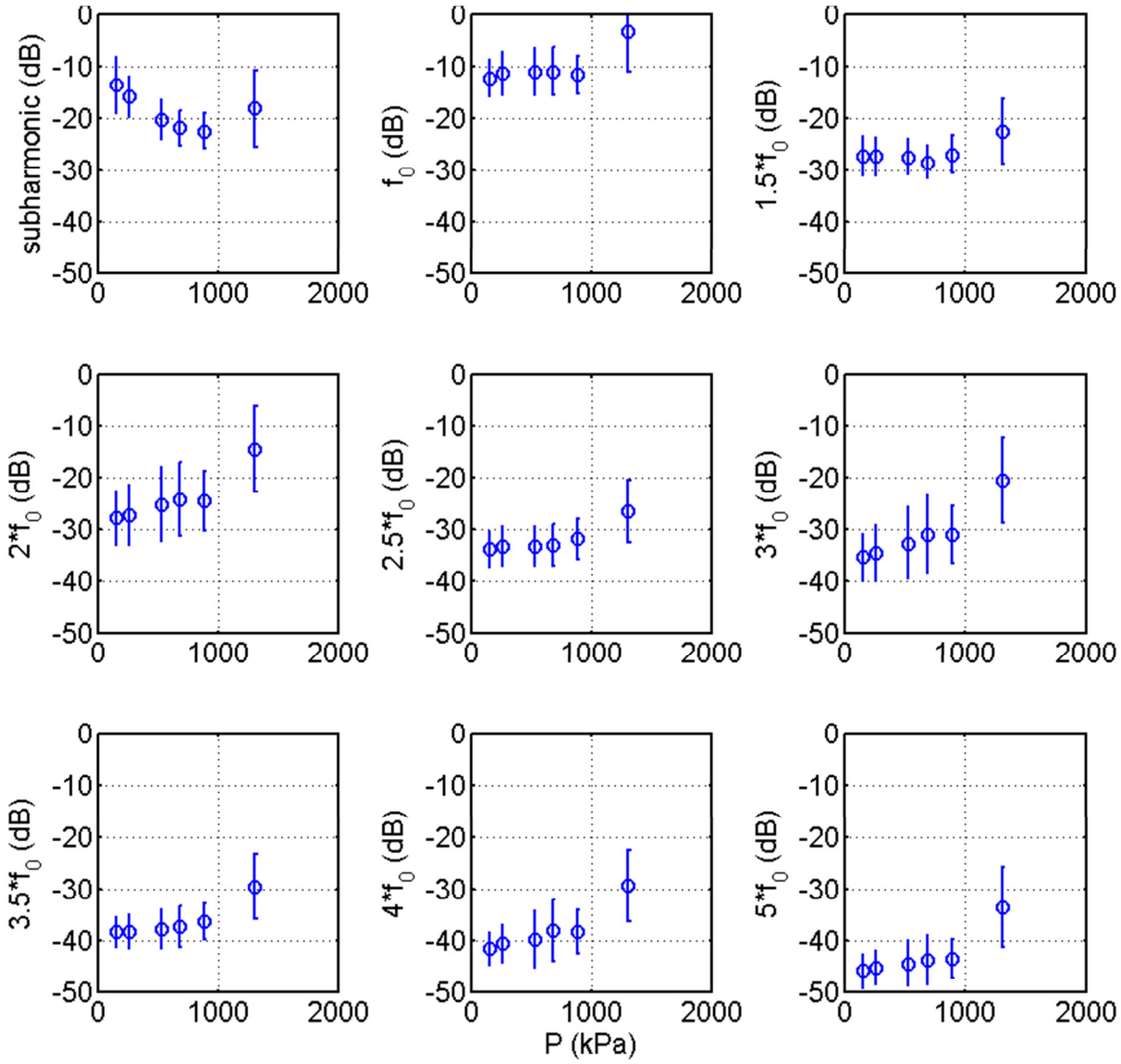

Figure 96. Harmonic analysis for transient study. The subharmonic ($f_0/2$), harmonic (f_o, f_1, f_2… f_4) and ultra-harmonic MEAN and STD error bars values at a particular pressure setting. For each pressure setting a different number of bubbles was used indicated by Table 9 for the transient experiment.

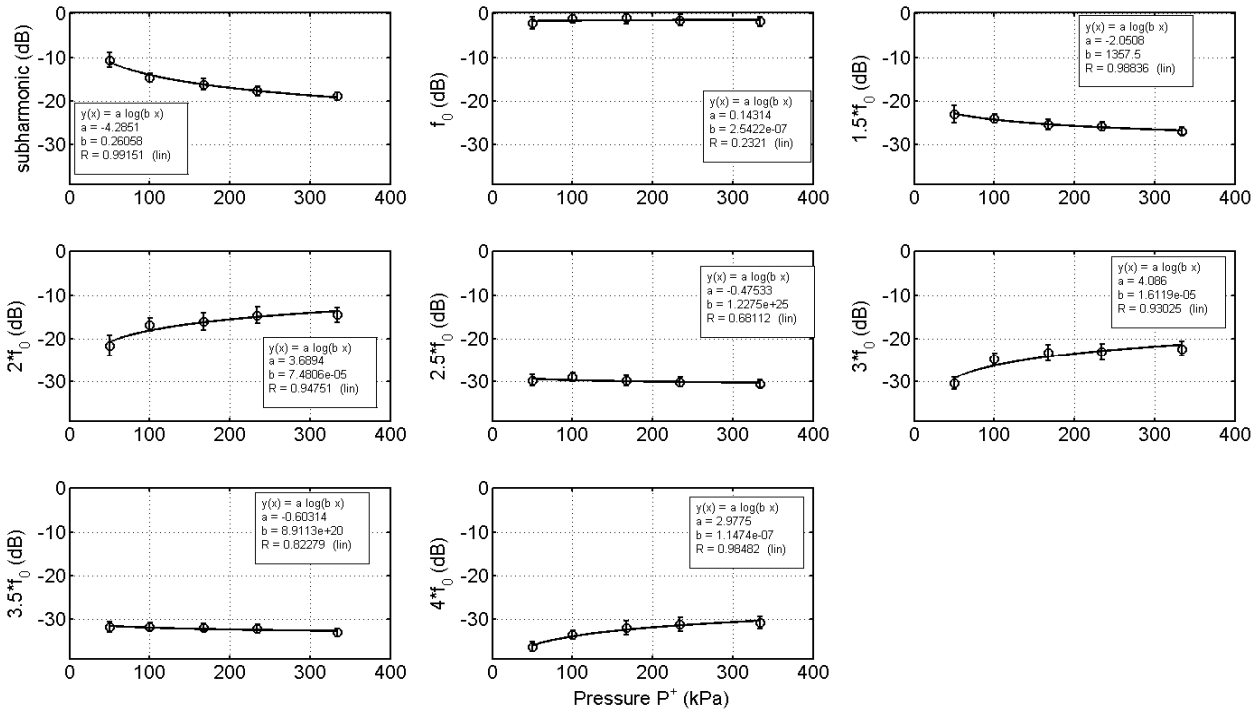

Figure 97. Harmonic analysis for steady state study. The subharmonic (fo/2), harmonic (fo, f1, f2… f5) and ultra-harmonic MEAN and STD error bars values at a particular pressure setting.

In Fig. 97, the harmonic analysis of the steady state MB is shown. Since the pressure range is shorter than in Fig 96, there is only evidence of the disappearance of SH emissions as a function of pressure increase. Having a noticeable decay (10dB loss, see Fig. 99) in the pressure region between 50 and 340 kPa, it confirms that there is a disappearance of subharmonic effect, from both studies shown in Figs. 96 and 97. To our knowledge, this effect has not been shown before experimentally. For example, the studies from Shi and Foster [205,213] looking at Optison subharmonic and harmonic content of UCA are performed on a suspension of bubbles (not individual MBs) inside flow phantoms or inside suspension cuvettes, using imaging systems with limited bandwidth (we have light scattering detection which can detect a broadband signal, not limited to PZT bandwidth).

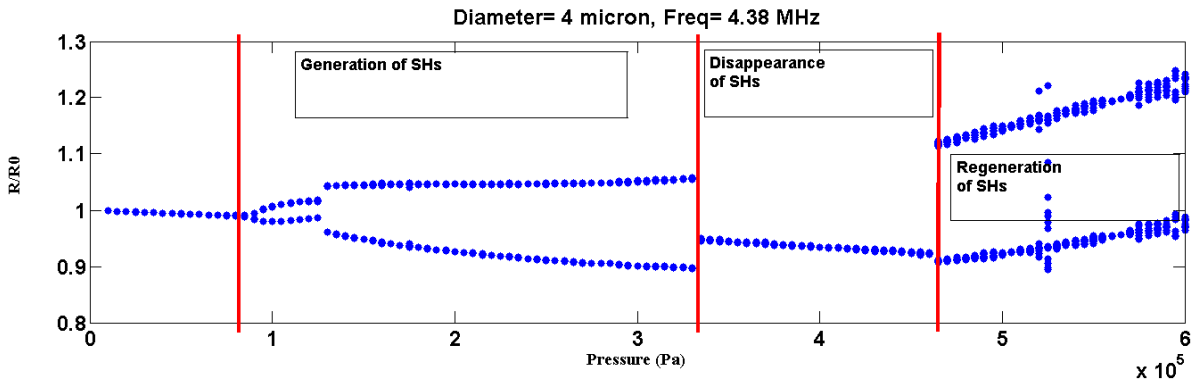

Figure 98. Bifurcation diagram of a 4 micron MB. The frequency of sonication is 4.38 MHz and the bifurcation diagram is displayed as the normalized bubble oscillations (R/R0) versus the acoustic pressure amplitude. Courtesy of: Amin J. Sojahrood

Figure 98 is a modeled bifurcation diagram of a 4 micron MB, courtesy of Amin Jafari Sojahrood. It is shown from Fig. 98 that at pressures lower than 90 kPa the behavior of the bubble is linear. The subharmonics are generated as the pressure increases above ~90 KPa. The bubble exhibits subharmonics for the pressure range of the ~90-340kPa. The subharmonics disappear for pressures above 340 kPa and they again re-appear as the pressure increases above ~470 kPa. Although the frequencies of the modeled behavior are different, and the pressure and sizes modeled are only for a particular case, there is evidence in models of subharmonic disappearance and regeneration, and an opportunity for developing a model that matches our data in terms of disappearance and regeneration of SH is presented here. Figure 99 shows the subharmonics emissions from Figs. 96 and 97 for Optison MBs.

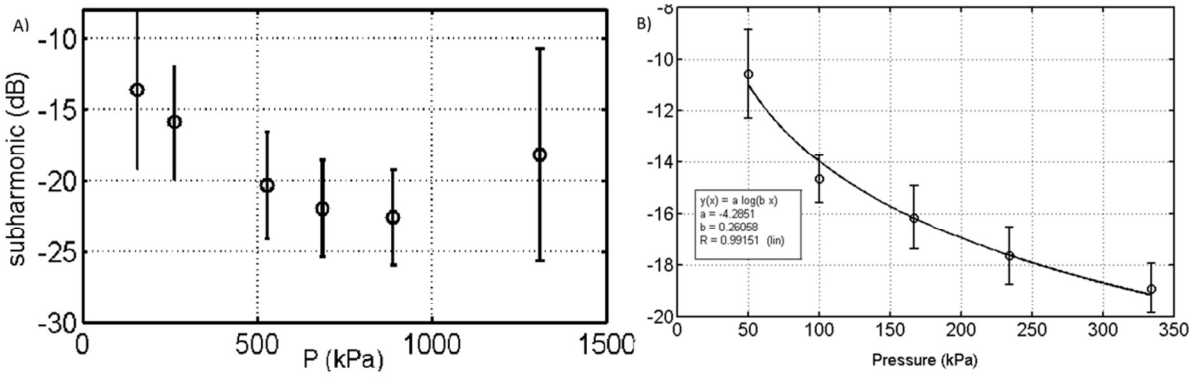

Figure 99. Subharmonic emissions from Optison. a) SH *vs.* pressure for the transient study, b) SH as a function of pressure for the steady state experiment, shown in Table 9.

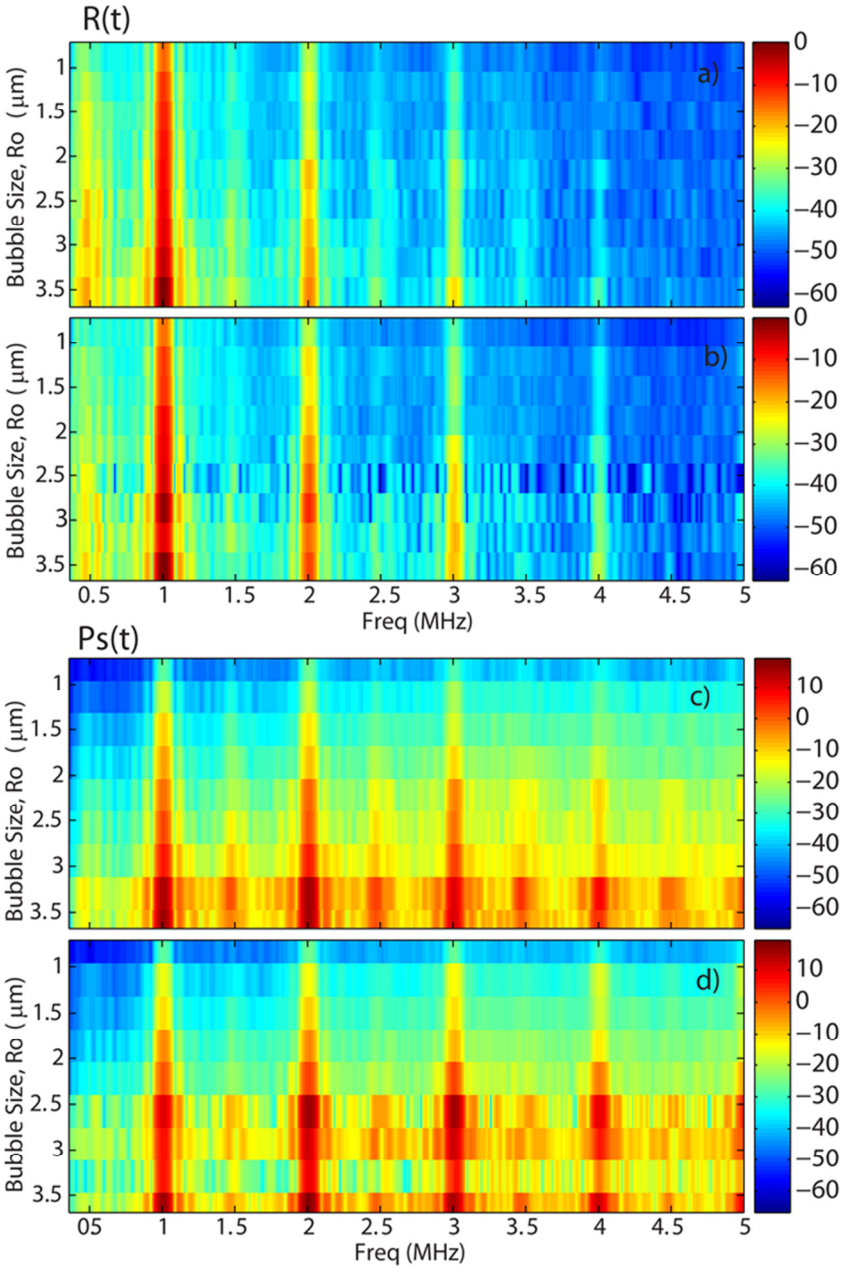

Figure 100. The 2 dimensional FFT for R(t) and predicted bubble scattered pressure. A and C) Bubbles are binned by radius groups and then FFT power is plotted as a function of driving pressure (P=100kPa, a) and P=334kPa (c). b and d) Same groups but FTT is from Ps Scattered pressure, calculated from the R(t) curve and the formula in the text.

In order to visualize the disappearance of subharmonics shown in Fig. 99b, and the dependence of spectral content on MB size, the normalized FFT spectrum power is plotted as a function of bubble size for two driving pressure groups in Figs. 100a and c, respectively. Figures 100b and d show similar content to 100a and c, but now the spectral content is from Ps

(scattered pressure, calculated from the R(t) curve), calculated from: $P_s(r,t) = \frac{\rho R}{r}\left(2\dot{R}^2 + R\ddot{R}\right)$. MBs are binned by radius groups and then FFT power is plotted as a function of driving pressure (P=100 kPa, A and B) or P=334 kPa (C and D). It can be seen that the lower pressure has higher spectral content at the subharmonic region and also around the ultraharmonics. Size dependence resonance shifts by increasing pressure can be visualized comparing the fundamental (fo, 1MHz) intensity shift from A to C, to a lower size bubble. There is also increased broadband noise in the higher pressure setting as expected. Finally, the resonances shift as the pressure increases so the spectral peaks (dark red spots) in the harmonics shift to a lower size as pressure increases. The disappearance of subharmonics as a function of increasing pressure for the steady state experiment can be visualized in Fig. 101 for five different pressure groups. There is also increase in harmonic spectral amplitude as a function of increasing pressure. In addition, at the ultraharmonic, corresponding to 1.5MHz ($1.5f_0$), the spectral amplitude decays from top to bottom according to the colorbar shown below.

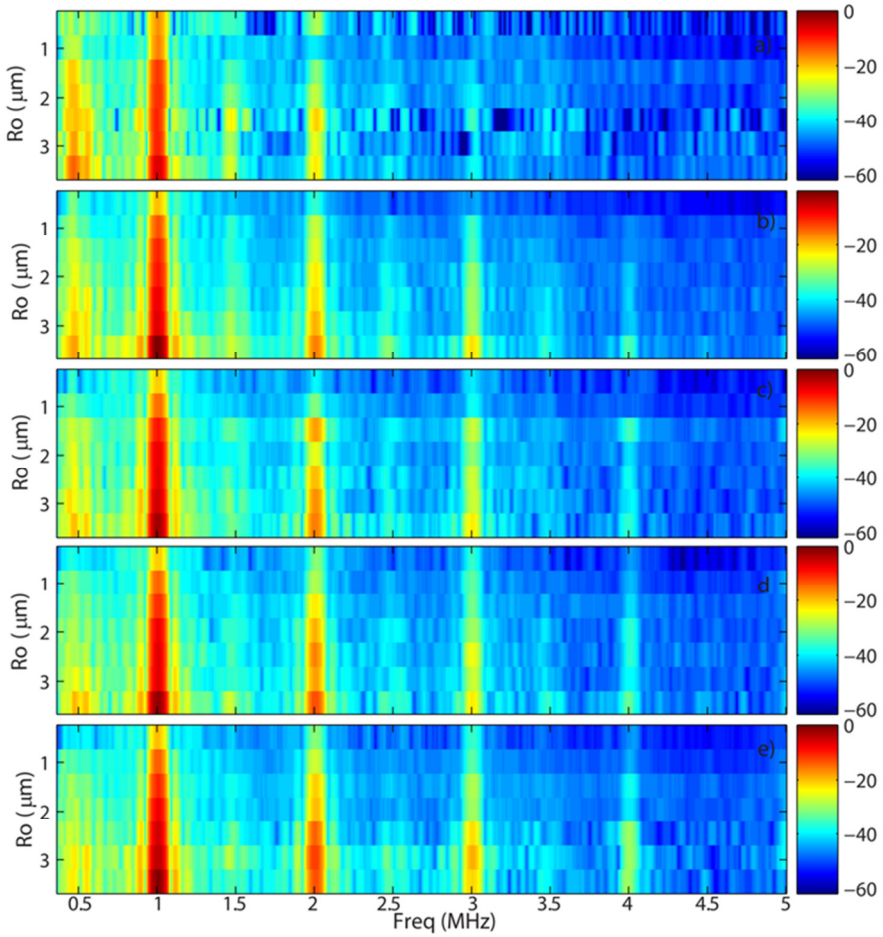

Figure 101. R(t) FFT's for five different pressure groups. Top is the lowest pressure (a = 50k Pa) and bottom is the highest pressure (e = 334 kPa). The disappearance of sub- and ultraharmonic components as pressure increases is evident, as is a corresponding increase in harmonic and broadband noise.

Finally, from the R(t) curves of the data it is possible to calculate (without the need of shell mechanical property fitting) the number of curves that behave in an expansion only or compression only behavior, calculated from relative radial excursions using equations presented elsewhere [214,215]. For Optison, expansion-only behavior ranged from 4-8% and compression only ranged from 0.7-4.5% of the entire population, as a function of driving pressure groups (Fig. 102).

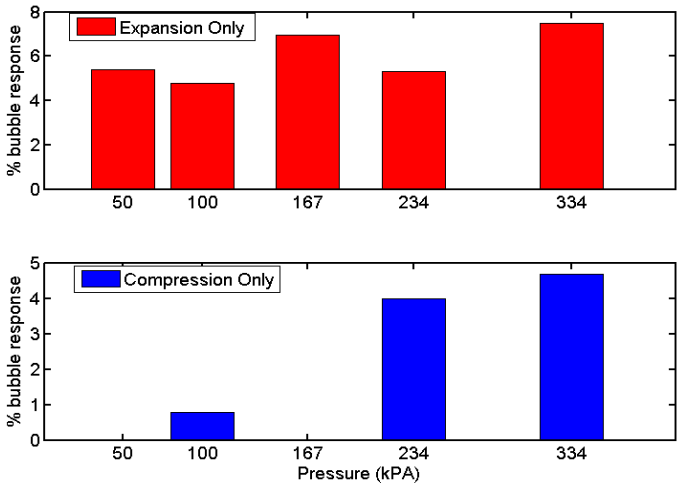

Figure 102. Expansion *vs*. compression only behavior for Optison (n = 570 MB, Table 8). It is displayed at several pressure settings in response to 20 cycles at 1 MHz frequency.

6.3.4 Discussion and Conclusion

The advantage of spectral analysis in our flow cytometry system is that there is no need to fit the shell mechanical properties, thus it can be implemented immediately after flow. One future improvement in this system would be to implement a real-time FFT algorithm that relatively compares the harmonic content between groups in flow cytometry (such as loaded *vs*. unloaded bubbles, discussed in a subsequent section). This would be particularly useful for developers of new targeted contrast agents, where the effects of small changes in the shell attachments on bubble dynamical behavior could then be quickly characterized and verified acoustically. Another advantage of spectral analysis with flow cytometry is that there is no limitation of bandwidth as there is using imaging probes. Typically with imaging probes, there is a transmission at f_0, and perhaps there could be detection of maximum two or three harmonics, granting the system is broadband and not very high q (poor resolution). Therefore, with light scattering it is possible to perform a relatively quick comparison of the spectral emission

between two types of bubbles (A or B) to a specific pulse ensemble and to quickly decide which population has statistically significant stronger harmonic oscillations for a specific imaging application. The light scattering collection of this system acts like a broadband hydrophone (*i.e.*, if light pulses are sampled at 20 MHz, then 10 harmonics at f_o=1 MHz can be collected) without worrying about bandwidth limitations.

Here, the mechanical properties of Optison using short transient (20 cycles) and long (steady state) acoustic fields are discussed and compared. To our knowledge, there is no study that compares the shell mechanical properties of MBs obtained from long (5 ms) *vs.* short (20 µs) pressure pulses. For the steady state case, the shell elastic modulus was found to be on average χ= 0.38 N/m (Table 8). For the transient case, it was found to be on average, χ= 1.04 N/m (Section 6.1), or about 3-fold larger, which is 1.04 N/m. This is within the range of values 0.9 - 1.3 N/m in the literature [197,204,216,217] and 1.3 N/m (internal GE report). This evident decrease in shell elasticity by increasing the ultrasound exposure is similar to a strain softening behavior of the MB, which has been mostly reported for lipid shelled MBs in the literature [206,218]. Strain softening has been defined as decreased association between constituent molecules in the encapsulation as its area increases [218], and has been shown as a decrease in elasticity as the deformation stress increases [206]. However, when comparing similar pressures between the present study and the previous section (Section 6.1), the parameter changing is not the pressure, but the exposure time. This suggests a combination of shell fatigue and strain softening due to a decreased elasticity caused by a timescale effect of ultrasound forcing at the bubble, by driving the contrast agent for a longer time.

The shell dilatational viscosity for the steady state study (Section 6.2) was found to be within the range of 0.3 - 2.3 x 10^{-7} kg/s (Table 8) and for the transient case, 0.3 - 1.4 x 10^{-6} kg/s, which spans 1 order of magnitude. In general, the lower shell viscosity suggests a shear thinning behavior that could be potentially caused by shell fatigue. Unlike the transient study, the ranges of viscosity of the current steady state system are within the published average values (7.6 x 10^{-8} kg/s and 1.2 x 10^{-8} kg/s, assuming a 15 nm shell) [197,204]. In addition, in the transient section (Section 6.1) the shell viscosity only increased by a factor of 3 over an approximately 6-fold increase in pressure, whereas in the steady state studies it is shown an 8-fold increase over an approximately 7-fold increase in pressure.

In the current CW study, the PZT is turned 'on' and the MBs are exposed to the steady state field from the time they enter the flow cell until they arrive to the interrogation region (and

beyond, but this is of no concern in the present context; see Fig. 78b), which takes approximately 6 ms. From the velocity steady state field 2D plot, shown in Fig. 79b, we can note that Optison MBs are undergoing oscillations prior to arriving to the interrogation region (Fig. 78b). The state of the shell is unknown and the shell properties can be modified due shell fatigue, characterized by temporal progression of changes in radii, which causes the shell to become more fragile with each pulse and an increasing resistance to compression [4,219]. Shell fatigue has been the subject of previous studies [219,220]. In addition Optison destruction threshold studies have identified 3 dominant mechanisms of destruction: 1) static diffusion [221], 2) acoustically-driven diffusion[222,223], and 3) rapid fragmentation due shell rupture or small imperfections in the shell that lead to a fast diffusion[222,223]. Optison destruction attributed to acoustically driven diffusion can happen in ~1 second timescales of ultrasound exposures at 3.5 MHz for pressure ranges between 0.1 and 0.4 MPa peak negative [222], which are the same range of pressure studied in this section. It is possible that the MB undergoes acoustically driven diffusion and it is manifested as a change in the mechanical properties that are reported in this section. It has been shown by Marmottant [192]; their Fig. 6) that UCA microbubbles subjected to several pulses over 50 ms produces changes in R_o and in the oscillation asymmetry (R(t) behavior) pulse-to-pulse, thus potentially changing the mechanical properties dynamically. Although this result was for lipid shells, the timescales and the thin shell UCA applies for Optison as well; thus we consider acoustically-induced, progressive modifications of shell properties to be a probable factor in the experiments we describe here. The main result is that using the same UCA, but exposing the UCA to MHz-frequency acoustic fields of several milliseconds duration and of similar pressures yields lower estimation of the shell mechanical properties.

6.4: Detecting Slight Shell Variations in Lipid and Protein Microbubbles

6.4.1 Introduction

There is a growing interest using microbubbles to mediate drug delivery or for dual modality imaging [4,26,38]. For these applications, drugs or fluorophores can be either loaded to the native bubble shell or dissolved within the layers of the shell, thus modifying their shell properties. In addition, custom formulations of microbubbles with physicochemical properties (*e.g.*, size and surface charge) 'tuned' for the desired biomedical application are often used. These changes in microbubble shell can modify the shell properties. Understanding how loading affects a MB's response is important for imaging and therapeutic applications. Also altering the components of the shell might lead to changes in the mechanical properties and therefore to the scattering properties of the contrast agents.

Research on targeted drug delivery using microbubbles (MBs) focuses on maximizing the binding efficacy of the targeted moieties, and trying to help them bind more efficiently[224,225]. Other major effort research area focus on the differentiation of targeted from free flowing using models[226,227], single bubble experiments[228,229], or using pulse echo data or advanced Doppler methods[230,231]. The bulk of latter effort is directed toward analyzing the mechanical response of the bound bubbles[232]. However, it is uncertain if the incorporation of a cargo, such as drugs or fluorescent markers, modifies the shell properties of the MB.

The bulk linear properties of monodisperse bubbles produced using flow-focusing microfluidic devices were reported to depend on both the radius and the acoustic pressure [207,233]. However, none of these studies investigated the properties of one specific lipid on the acoustic response MBs. Understanding the influence of this replacement on MB's acoustical stability and their response to ultrasound has potential benefits for targeted microbubbles local drug delivery and ultrasound molecular imaging applications.

Characterization of lipid shelled Definity and Sonovue MBs *via* acoustic spectroscopy and high speed imaging has been reported before [234–237]. Several lipid variations have also been characterized [55,238]. However these studies have not focused on a particular change of a shell material. High speed imaging has been used to study the distribution of lipids in the coating of two types of microbubbles, formulating using the lipids DPPC or DSPC [239]. DPPC has 16 carbon atoms, and is used in Definity (Lantheus Medical). The DSPC lipid has 18 carbon atoms

and is present in SonoVue (now called Lumason; Bracco), and also present the experimental agent BR14. The main difference observed was the DSPC coated bubbles showed heterogeneity in their lipid distribution as opposed to DPPC-coated lipid microbubbles, which revealed homogeneity in their lipid distribution of island domains. Similar results were also reported for mixtures of two or three of the components [240–243] that were used for the microbubble coating in the study by [239].

Recent studies using ultrasound spectroscopy and high speed imaging techniques revealed relative differences in the dynamics and shell dilatational viscosity between liposome-loaded and unloaded lipid-shelled bubbles, and even between DPSC and DSPE lipid shelled bubbles[215,244,245]. These studies estimate viscoelastic properties of the shell from the damping coefficient measurements and from fitting experimentally measured resonance curves to the bubbles diameter using a linear viscoelastic model. Regardless of the size of the molecule that has been incorporated to the shell (large liposomes, small fluorophores, or different main lipid) the modification of the shell changes the mechanical properties and dynamic behavior of MBs. Although the high speed imaging is a great direct visualization method for MBs, this approach does not allow statistical descriptions of bubble behaviors [244] as a function of size since the analyses typically look at only few tens of bubbles in each group, is very time consuming, and does not directly interrogate the R (t) behavior of each bubble.

Recently, atomic force microscopy (AFM) studies have also revealed relative changes in the shell stiffness and mechanical properties by incorporation or loading of small molecules such as actin molecules, PEG chains, and nanoparticles added to regular lipid shelled bubbles. [58,246,247].

Our acoustic flow cytometer has proved to be a fast and high throughput system to perform acoustic characterization of MBs[48,49,209,210,248]. Based on evidence from the literature, we formulated two hypotheses; *viz.*: 1) slight modifications in the shell of protein or lipid MBs could be manifested in a change of their mechanical properties, and 2) our modified acoustic flow cytometer would be capable of detecting the relative effect of loaded *vs.* unloaded MBs or ***slight modifications*** in the size-dependent mechanical properties for custom-made lipid and protein MBs with a statistically large sample. The data supported the hypotheses.

6.4.2 Materials and Methods

A flow cytometer modified with a PZT transducer was used to extract the shell properties of statistically significant numbers of MBs with methods described elsewhere[48,49]. In the experiments, three types of MBs were used: Optison, and two custom-made preparations. MBs were diluted in 0.45 µm filtered Isoton II electrolyte with an initial concentration of 6 x 10^8 bubbles/mL for Optison and for the custom-made lipid shelled bubbles, ~5.2 x 10^9 bubbles/mL

or ~3 x 10^8 bubbles/mL (Table 10), respectively, determined using a Coulter Multisizer M3. Experiments were done in triplicates at a sheath pressure of 41.3 kPa (6 PSI) and sample pressure of 43.4 kPa (6.3PSI), equivalent to a flow rate of 5 mL/min from the flow cell. Each run at a particular pressure setting lasted between 3-5 minutes, allowing us to collect about 100,000 MB events for each run. For size calibration of the flow cytometer, we used a size calibration kit containing nonfluorescent beads with diameters from 0.5-10 µm. The PMT voltage output was converted to a radius using Mie scattering theory [48,59,60].

Additional details of the acoustic and detection system are as follows: The acoustic driving signal consisted of a tone burst at a frequency of 1 MHz for Optison and 1.2 MHz for lipid bubbles. The reason for the use of slightly higher driving frequency with the custom-made bubbles was the expectation that the smaller, custom-made bubbles would produce more robust responses at the higher frequency. The light scattered from the MBs was collected by a PMT and routed to a custom high bandwidth (-6 dB at 5 MHz) current to voltage converter and logarithmic preamplifier similar to that described by Shapiro[41] and digitized by a 12 bit PXI- 5105 at 20 MHz for later analysis. For the purpose of characterizing the bubbles in this study, we used the flow cytometer's side scatter optical path. Custom built LabVIEW software was used to control the side scatter PMT gain setting.

Protein shelled Optison loaded vs. unloaded shell experiments

Optison was obtained directly from the manufacturer. The albumin shelled microbubbles encapsulate octafluoropropane (C_3F_8) gas, and are supplied in a 3mL vial at a concentration of 5 - 8 x 10^8 bubbles/mL, with a mean diameter between 2.0 - 4.5 µm (using a Coulter Multisizer II), with 93% smaller than 10 µm [221]. The shell thickness is assumed to be around 15 nm, consistent with one or few layers of albumin [249]. In order to study loading of the shell in protein-shelled bubbles, we reacted Optison MBs with Evans blue fluorescent dye (MW 960.8 Da, 960.8 g/mol, Sigma Aldrich, USA), which binds strongly with albumin, the protein in the shell of Optison™, using two Evans blue concentrations in the reaction mix (11 or 45 µM final concentrations). Evans blue fluoresces with excitation peaks at 470 and 540 nm and an emission peak at 680 nm [250]. Prior to Evans blue binding, excess albumin in the Optison was removed by slow speed centrifugation (120 g x 30 sec), and this process was performed twice (before and adding the dye) by re-suspending the bubble cream layer in filtered Isoton II. We refer subsequently to these Optison-Evans blue labeled MBs as "loaded bubbles". It has been shown that centrifugation speeds up to 170 g for 30 seconds are safe and do not change the

size distribution of Optison [251]. Shell loading was confirmed *via* fluorescent microscopy and flow cytometry (Fig. 103). For fluorescent microscopy binding confirmation a Nikon Eclipse 80i microscope (Nikon Instruments, NY) was used and details of the microscope are provided below: A 40X Nikon objective, green excitation laser: 560-580 nm (570 bandpass cwl), Texas Red filter used for collection: 600 - 650 nm (625cwl), and Dichroic: 590-665 bandpass, with 200 ms exposures. Binding rate was found to be close to 100% in every image (every bubble had fluorescent molecules). Control images revealed no fluorescence. For flow cytometry detection a 488 nm, 500 mW CW laser (Melles Griot) was used. Forward, side scattering and fluorescence signals were collected. For fluorescence detection we used a 690/30 (red filter). Size stability was performed using Coulter Multisizer before and after dye loading (Fig. 104a). The viscoelastic properties of Optison™ MBs (dye-loaded *vs*. unloaded) driven at 1 MHz were measured at 50kPa and 100kPa peak-positive pressures. Samples were diluted in Isoton to reach a final concentration between 2 - 5 x 10^6 bubbles/mL for flow cytometry experiments. Normalized spectral power was computed following the methods detailed in the previous section (section 6.3.2).

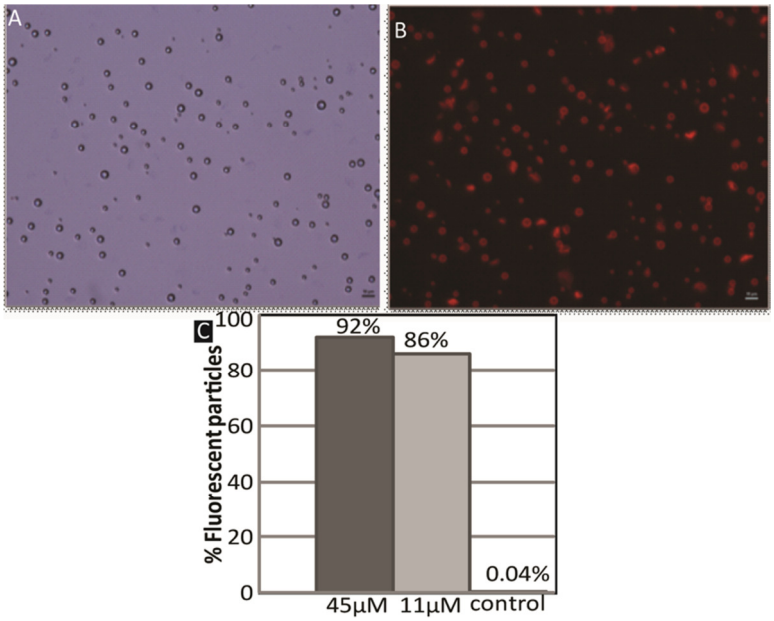

Figure 103. Summary of fluorescence microscopy and flow cytometry results. A) Brightfield (left) microscope image of Optison MB's and B) corresponding fluorescence Image obtained for Evan's blue loaded Optison. C) % fluorescence quantified *via* flow cytometry at 2 different concentrations of Evans blue. Scale bars are 10 microns.

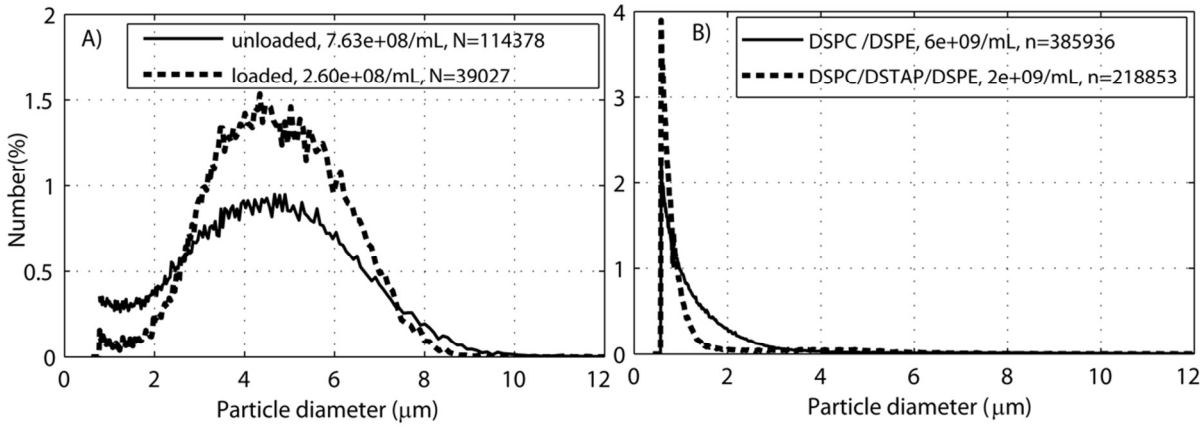

Figure 104. Size distributions: A) the unloaded and loaded Optison protein shelled bubbles and B) for the two different kinds of custom-made lipid bubbles from Table 10 (DSPC/DSPE and DSPC/DSTAP/DSPE samples).

Lipid shell modification experiments with custom-made lipid MBs:

In order to visualize shell differences in PEGylated lipid bubbles we studied two microbubble formulations that we call DSPC/DSPE and DSPC/DSTAP/DSPE in Table 10. The DSPC/DSPE MBs were comprised of a 9:1 molar ratio of 1,2-distearoyl-sn-glycero-3-phosphocholine (DSPC) : 1,2-distearoyl-sn-glycero-3-phosphoethanolamine-N-[amino(polyethyleneglycol)2000] (DSPE-PEG2000 Amine), while the DSPC/DSTAP/DSPE MBs were comprised of a total of a 7:2:1 ratio of DSPC : 1,2-distearoyl-3-trimethylammonium-propane (DSTAP) : DSPE-PEG2000 Amine. A total of 1 mg of lipid was delivered into a tube and dried overnight under vacuum. The lipid film was rehydrated in 1 mL solution of 10:10:80 (v/v/v) glycerol:propylene glycol:water at 67 ℃. The tube headspace was filled with perfluorobutane and amalgamated with a Vialmix® machine for 45 s. The MB solution was processed by differential centrifugation to remove micelles/free lipids and isolate MBs with diameters less than 2 μm as previously described [45]. Population size, concentration (Fig. 104b) and stability tests were performed using a Coulter M3 Multisizer. The viscoelastic properties of the lipid bubbles with different shell components, DSPC /DSPE (N=111) *vs.* DSPC/DSTAP/DSPE (N=53), driven at 1 or 1.2 MHz were measured at 167 kPa -400 kPa peak-positive pressures. Expansion only behaviors and compression only behaviors were calculated based on [215,244,245]. From Table 10 we can note that the latter one contains a cationic lipid and therefore has higher zeta potential. Normalized spectral power was computed following the methods detailed in the previous section (section 6.3.2).

Table 10. Lipid microbubble fabrication and characterization (See Appendix C for chemical structures of lipids below).

Bubble Type	Avg Radius (μm)	Concentration (MB/mL)	Avg Zeta Potential (mV)	DSPC	DSTAP	DSPE-2K Amine
DSPC/DSPE, 2K	0.482 ± 0.108	$5.17x10^9$	12.7 ± 0.8	28.73 μL		11.27 μL
DSPC/DSTAP/DSPE,2K	0.486 ± 0.189	$2.98x10^8$	29.8 ± 0.3	22.75 μL	5.79 μL	11.50 μL

6.4.3 Results

Protein Bubble Loaded vs. Unloaded

Our statistically significant results with loading the shell of protein MBs agree with previous findings for lipid shelled MBs [215,245,247]. Both loaded and unloaded MBs exhibited increased shell viscosity as a function of MB size and decreased viscosity as a function of shear rate (Fig. 105a and c, respectively). There was a statistically significant increase in the shell dilatational viscosity and shear rate of loaded MBs over unloaded MBs (Fig. 105b,d). In addition, spectral analysis (Fig. 107a) of hundreds (n=340 each group) of MB R(t) curves in the mean size range (R_0= 1.5 - 2.5 μm) revealed a statistically significant enhancement of +4.5, 5.5, 6.4 or 7.7dB increases in the second, third, fourth and fifth harmonic of the loaded MB spectra compared to the unloaded MB (averaged for N=340 MBs in each group). There is no significant variation in the ultraharmonic and broadband noise content between the two groups. The shell elastic modulus did not show statistically significant differences between groups (Fig. 110a). Loading did not significantly change MB size distribution (Fig. 104a).

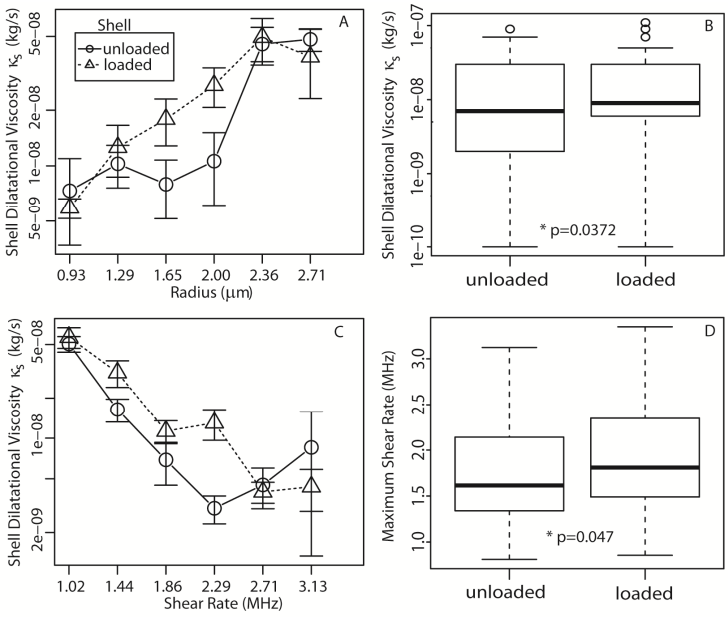

Figure 105. Optison Viscoelastic shell properties measured for N=100 bubbles driven at 50kPa. Error bars indicate 95% CI. A) Dilatational viscosity as a function of binned bubble radius (A) and as a function of shear rate (C). Box plot Comparing shell dilatational modulus and maximum shear rate (b and d). All results in B and D reveal statistical significance (shown on the figure).

Lipid MB Shell Variations

Lipid shelled MBs exhibited an increase in shell dilatational viscosity as a function of size and a decrease in viscosity as a function of shear rate (Fig. 106a, 106c, respectively), consistent with commercial lipid shelled bubbles properties shown before [48,49,60,206]. DSPC/DSTAP/DSPE MB's showed a significant increase in the shell dilatational viscosity and a significant decrease in the shear rate compared to DSPC /DSPE MBs (Fig. 106b and 106d). The shell elastic modulus did not show significant differences between size groups (0.2 and 0.22 N/m, respectively), suggesting that it is constant across bubble sizes, as previously reported [48,49,53–55,60,206]. These results suggest that there is a size dependent (and thus frequency dependent) effect of the viscosity and shear rate of the bubble. We also estimated the resonance frequency using Eg. 3, below) for 3 different sizes of the population studied with R = (0.25, 0.56, or 0.81 μm) and obtained for = 41, 14, and 8.5 MHz, respectively.

$$f_0 = \frac{1}{2\pi}\sqrt{\frac{1}{\rho R_0^2}\left[3\gamma P_0 + \frac{2(3\gamma-1)\sigma_\omega}{R_0} + \frac{4\chi}{R_0}\right]}. \qquad (6.1)$$

We saw differences in compression only behavior from the DSPC/DSPE group (8% of the total number of bubbles) compared the DSPC/DSTAP/DSPE group (0.9% of the total number). Expansion only behavior was less than 1% for both groups and not different. In addition, spectral analysis (Fig. 107b) of hundreds of MB R(t) curves in the mean size range (R= 0.2-1

μm) revealed a statistically significant enhancement of +9.7, 5.6, 6.9 increase in the second, third and fourth harmonic of the DSPC/DSPE MB spectra compared to the DSPC/DSTAP/DSPE MB (averaged for N=730, N=307 MB respectively). However, the content between the harmonics (broadband noise) and especially around the ultraharmonics is always higher for DSPC/DSTAP/DSPE MBs.

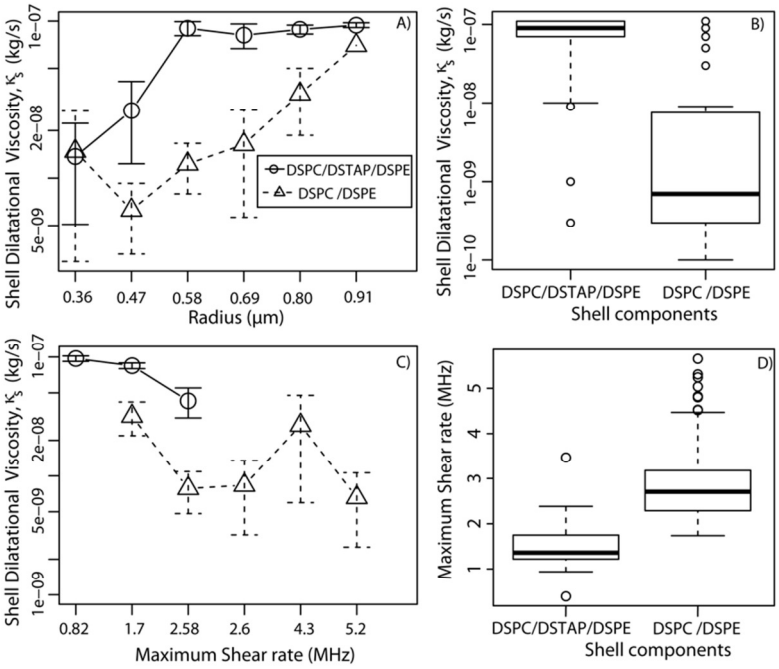

Figure 106. Illustration of size and viscoelastic property. Size and viscoelastic property analysis for a statistically large DSPC/DSTAP/DSPE lipid-shelled MB sample (N=53) and a DSPC/DSPE lipid shell sample, N=83. A) Shell dilatational viscosity as a function of Radius and shear rate (C. Box plot Comparing shell dilatational modulus and maximum shear rate (b and d). All results in B and D reveal statistical significance ($p<0.01$).

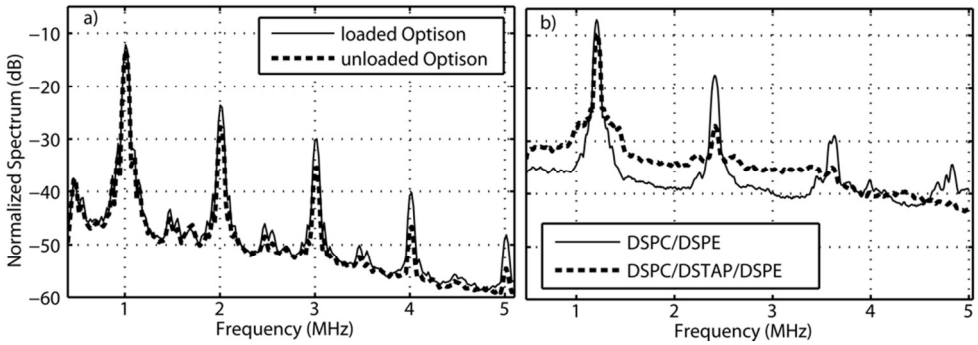

Figure 107. Spectral analysis for protein and lipid bubbles. A) Comparison between loaded (solid) vs. unloaded(dash) UCA, n=340 each group. b) Comparison between DSPC/DSPE (solid line, n=700) vs. DSPC-DSTAP-DSPE bubbles (dash,n=320).

Figures 108 and 109 compare the 2-D FFT (radius *vs*. frequency) with color representing the strength of the normalized FFT energy at a particular binned MB sized for the lipid and protein MBs, respectively. In Fig. 108, the lipid MB size-dependent spectra are compared. The spectral power content of the radial oscillations from DPSC/DSPE MBs (Fig 108a) is much larger at the harmonics (f_o, f_1, f_2, f_3) than the spectral power content from DPSC/DSTAP/DSPE MBs. However, the regions surrounding ultraharmonics (3/2 f_o, 5/2 f_o, 7/2 f_o) and the broadband noise are higher from the DPSC/DSTAP/DSPE MBs, similar to the averaged results shown in Fig. 107b. There is also a size dependent effect in the second harmonic (2.4 MHz) creating two regions (hot colorbar) of higher spectral power content at 0.6 and 0.96 μm radius for DPSC/DSPE, and three regions (0.3, 0.7, 0.98 μm) for DPSC/DSTAP/DSPE. These results suggest that there is a size dependent (and thus frequency dependent) effect with loading that affects the viscosity and shear rate of the bubble, and also that loaded MBs may enhance contrast signal strength.

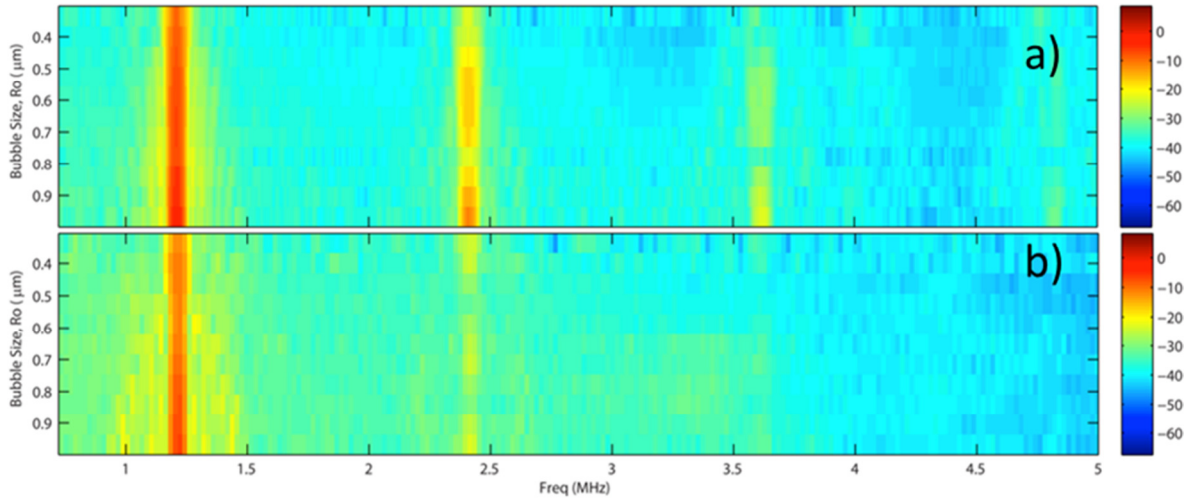

Figure 108. Bubble R vs. Frequency FFT spectra for a) DSPC/DSPE, and b) DSPC/DSTAP/DSPE. The strength of the spectral power content of the radial oscillations from the two lipid MB formulation is shown, where hot-color bar represents the strength level of the normalized FFT power at a particular binned MB sized for the lipid MBs

In Fig. 109, the loaded vs. unloaded Optison MB size-dependent spectra are compared. The spectral content of the radial oscillations from loaded MBs (Fig 109b) is slightly larger at the harmonics and ultraharmonics compared to the spectral content from unloaded MBs (Fig 109a), across several bubble sizes. The differences are more noticeable at the higher harmonics (e.g. f_3 and f_4) show larger differences across all sizes. In general, larger bubbles (3.2 μm in radius) contribute to higher spectral content compared to other sizes across all frequencies observed. These results suggest that there is a size dependent (and thus frequency dependent) effect with

loading that affects the viscosity and shear rate of the bubble, and also that loaded MBs may enhance contrast signal strength.

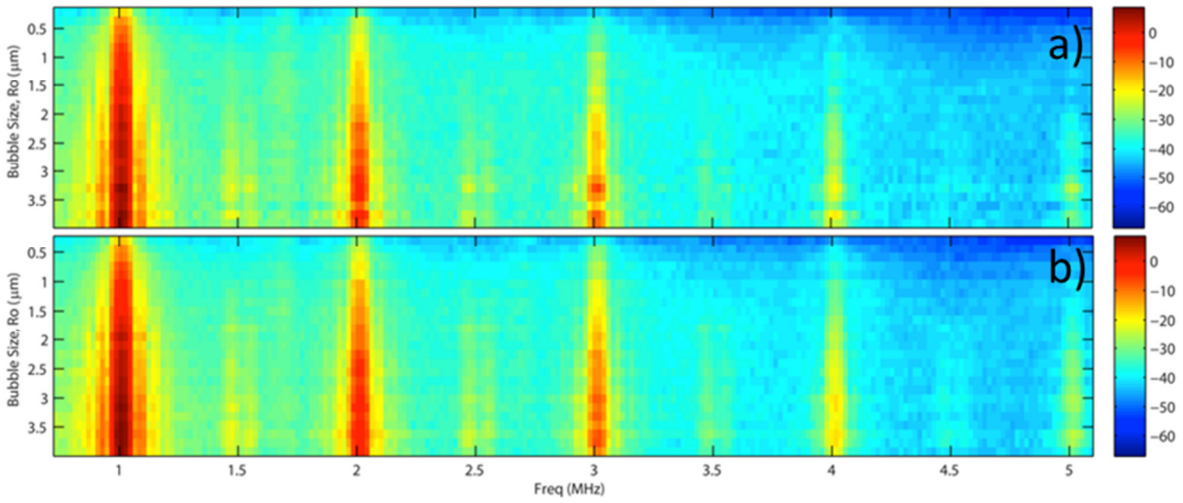

Figure 109. Bubble R vs. Frequency FFT spectra. a) Unloaded Optison b) Loaded Optison. The strength of the spectral power content of the radial oscillations from the two Optison MB formulations is shown, where hot-color bar represents the strength level of the normalized FFT power at a particular binned MB sized for the lipid MBs

The shell mechanical properties for the lipid MB formulations were also characterized at 1MHz. The lipid MBs exhibited an increase in shell dilatational viscosity as a function of size and a decrease in viscosity as a function of shear rate (Fig. 110b and d, respectively), consistent with published results for commercial lipid shelled bubbles properties[48,60,206]. The shell elastic modulus did not show significant differences between size groups (Fig. 104a), suggesting that it is constant across bubble sizes, also as reported previously [48]. These results suggest that there is a size dependent (and thus frequency dependent) effect of the viscosity and shear rate of the bubble. We also estimated the resonance frequency using Eqn (6.1) for 3 different sizes of the population studied, with R_o = 0.25, 0.56, or 0.81 μm and obtained f_o = 41, 14, and 8.5 MHz, respectively.

$$f_0 = \frac{1}{2\pi}\sqrt{\frac{1}{\rho R_0^2}\left[3\gamma P_0 + \frac{2(3\gamma-1)\sigma_\omega}{R_0} + \frac{4\chi}{R_0}\right]}. \qquad (6.1)$$

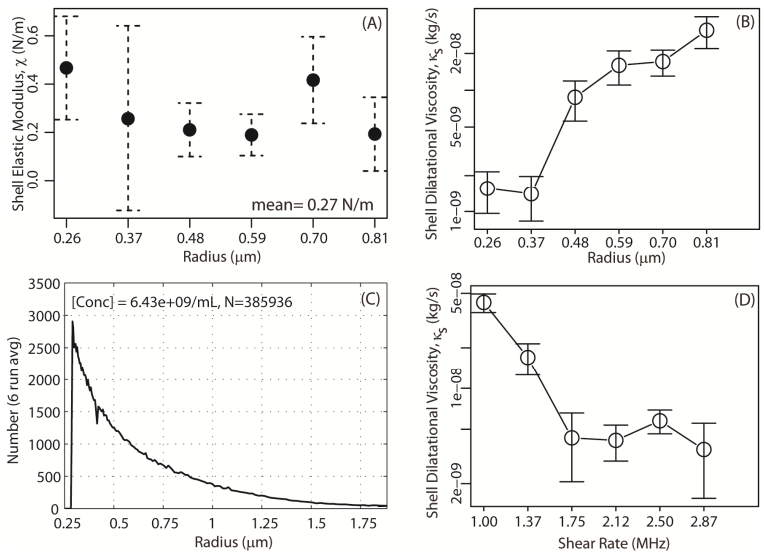

Figure 110. Size and viscoelastic property analysis for a statistically large slightly cationic lipid-shelled MB sample (N=111). A) Elastic modulus as a function of bubble size. Shell dilatational viscosity as a function of radius and shear rate (B and D, respectively). C) Population size distribution, and concentration (6 run average). In A, B and D, the number indicates the center of the bin.

6.4.4 Discussion

The results show a relative change in mechanical properties and bubble dynamics (confirmed *via* spectral analysis) due to modifications in the shell of both proteins and lipids. Modifying the mechanical properties of bubbles and the way the bubble responds to ultrasound by loading any particles to it has direct repercussions in the emerging field of drug delivery. For new MB (drug or fluorescent loaded vehicles), while coating or linking may be feasible from a biochemistry standpoint, the efficiency of drug loading remains a concern, especially when using drugs that are expensive or difficult to produce. On top of the expense of production and reagents cost, there is no current platform to quickly test and characterize the MBs before going to *in vivo* studies. Our acoustic flow cytometry represents a novel modification of off-the-shelf technology that is capable of quickly characterizing the acoustic response (*via* spectral analysis), sizing and determining the size-dependent mechanical properties of new MB's with a fluorescent or drug payload aimed for a drug delivery or molecular imaging application.

Comparisons were done at a single frequency and a single pressure setting. Therefore, the trend for the mechanical properties (relationships) at higher or lower pressures or different frequencies is not known. While a full pressure dependence characterization as shown in ([49,209–211,248]) should be performed to understand the pressure dependence of the shell property of each UCA, the goal of here was to understand the relative difference between two very similar

MB's with slight modification or variation to the shell constituents (loaded *vs*. unloaded protein shell of Optison and two very similar lipid MBs).

One of the most interesting results is that the slight changes in the shell of the lipid or protein MBs manifest themselves as changes in the shell dilatational viscosity from our R(t) fitted bubble dynamics data, but not in the shell elasticity. For lipids and protein there was no statistically significant differences between the elastic modulus between groups. For the protein bubble results in Figs. 105, 107a and 109, the Evans blue bound to the albumin shell could produce a slight change in the binding conformation of denatured albumin that manifests as a change in viscosity of the shell. Figure 107d shows a statistically significant increase the measured shear rate from the loaded compared with unloaded bubbles, which is correlated with higher averaged harmonics measured between groups in Fig. 107a. Figure `09 show the size dependent spectral amplitude, indicating higher harmonic content in the loaded MBs at all sizes. To our knowledge, this is the first study performed that characterizes changes in the shell incorporation to a protein shell (*viz*., Optison).

From Fig. 119b, it can be observed that the DSPCE/DSPE MBs had a significantly higher measured shear rate compared with DSPC/DPSTAP/DSPE bubbles ($p < 0.01$) , but exhibited a significantly lower shell dilatational viscosity compared with the latter group. From Figs. 107b and 108, we can see that the DSPCE/DSPE have significantly higher harmonic content compared to DSPCE/DPSTAP/DSPE MBs, but the former has higher ultraharmonic content. This effect might be due to a lowering of the shell elastic modulus, which was not observed in the protein results mentioned above. Our lipid bubble results agree with similar published work[244], where changing lipid type affected the MB stability and their response to ultrasound. Although the study used ultrahigh-speed imaging to compare the responses to ultrasound of DSPC or DPPC as the main lipid in the coating, there were changes in the shell viscosity which are similar to what we observed in our study. The biggest limitation with their studies is that the results are from small numbers of MBs (27 *vs*. 31) due to limitations from high speed imaging.

In previous published results, the number of carbon atoms (hydrophobic chain length) of the phospholipids incorporated into the microbubble shell was found to influence the dissolution and the acoustic stability (when exposed to ultrasound) of the MBs [252,253]. The influence of chain length on ultrasound-driven dissolution (*i.e*., acoustical stability) was different from that of passive dissolution. Helfield *et al.* [254] varied the shell microstructure using different cooling rates

and observed a change in subharmonic response. Kooiman *et al.* [239] revealed that the DSPC coated bubbles showed heterogeneity in their lipid distribution as opposed to DPPC-coated lipid microbubbles. Even relatively monodisperse bubbles produced by flow focusing have also shown dependence on the size and pressures, when determining their bulk mechanical properties[207,233]. This suggests a need for new models where non-linear rheological behaviors can be incorporated to predict nonlinear changes in the shell properties.

The replacement of only 2/9ths DSPC (Table 10) with the molecule DSTAP in the shell changed the viscosity but not to the elasticity of the shell. It might be because of the charge of the lipids that they tend to repel to each other and not want to move freely, the higher DSPC/DSTAP/DSPE charge with the DSTAP. Shell viscosity of lipid bubbles was found to depend on the coating composition and manufacturing method, and viscosity was lower when higher concentrations of emulsifier were used [255,256] explained this by the increased movements of lipids caused by the emulsifier. When manufacturing DSPC/DSTAP/DSPE MBs, not as many form because of the electrostatic repulsions. When the surfactant is cationic, an electric field is created and can affect the surfactant flux based on Govy-Chapman theory. As the frequency increases, the elastic modulus becomes independent of the charge, becoming dependent only on surface tension and concentration of surfactant on the surface. Although adding a different lipid type is changes the rheological or viscosity properties of the lipid shell, it is difficult to understand the relationship from the molecular structure of these very similar lipids (Appendix C).

Broadly speaking, it could be expected that a high molecular weight compound loading in the shell would increase constraints on MB dynamics. This is true, for example, for liposome loaded lipid shelled bubbles [215,245]. With constrained dynamics, there are thresholds by which bubbles do not respond. There has also been several publications by a similar group where lipid shedding and fluorophore shedding has been captured by high-speed camera [215,245]. Our a modified flow cytometry system can detect fluorescence total values, but one limitation of our current setup is that if the fluorophores are shed, but still within the laser interrogation region (60 µm), the fluorophores will emit light in all directions, and these 'artifact' emissions collected as though representing labeled cells. Therefore the time dependence of fluorescence shedding cannot be quantified.

6.4.5 Conclusion

Our acoustic flow cytometer was used to extract the shell mechanical properties of statistically significant numbers of protein and lipid shelled MBs. We incorporated Evans blue fluorescent dye (which strongly binds albumin) to the shell of Optison™ and measured changes in the viscoelastic properties of Optison™. MBs (dye-loaded *vs*. unloaded) driven at 1 MHz were measured at 50 kPa or 100 kPa peak-positive pressures. We modified the lipid content of two very similar lipid bubbles and also observed changes in the viscoelastic properties. Spectral analysis revealed changes in the scattering spectral amplitudes of the harmonics due to the slight shell changes. Small modifications to the shell can thus have significant effects not only on the mechanical properties but also in the acoustic response of MBs that impact drug delivery and molecular imaging applications.

6.5: Future Work: Characterization of Bound Targeted UCA-cell Systems

6.5.1 Introduction

In this section, preliminary data of binding and characterization of targeted microbubbles and leukemia cells is presented. The bound cell-bubble complex is characterized with our modified flow cytometer, together conventional microscopy. In addition, a position sensitive detector, developed by Swalwell *et al*. [198] capable of measuring relative position of particles in the flow with respect of the center of a laser beam is used. The future goals described in this section are to 1) detect the relative separation of bubble-cell *vs*. leukemia cells alone, 2) use light scattering to quantify their interaction, their dynamics, or the typical asymmetric oscillations described elsewhere [39] and 3) to calibrate the position sensitive detector so that the exact distance a particle has been shifted due to an US pulse is known. The initial binding efficiency, binding ratio, were determined in this preliminary study. We hypothesize that the acoustic flow cytometry is an adequate tool to characterize bound targeted UCA-cell, binding rate and binding efficiency. Here the interaction of streptavidin-coated microbubbles (Targestar-SA) linked to CCL-119 leukemia cells *via* biotinylated anti-CD7 antibodies is presented. The following preliminary results are used in part for the pending patent application below:

CAMILO, P. 2014 SYSTEMS, DEVICES, AND METHODS FOR SEPARATING, CONCENTRATING, AND/OR DIFFERENTIATING BETWEEN CELLS FROM A CELL SAMPLE. US 14/254,611 FILED 4/16/2014. PENDING.

6.5.2 Methods

Cell Line and Characterization:

A human leukemia line, CCL-119 (ATCC, immortal human acute lymphoblastic leukemia line) was grown in a suspension culture in RPMI 1640 medium supplemented with 10% fetal bovine serum and 1% penicillin-streptomycin solution. We identified the percentage of biomarkers expressed on the cell surface prior to choosing the cell line for study based on the fraction of cells expressing various surface antigens: CD3 B (37%), CD 4 (50%), CD5 (95%) and CD7 (77%). Biotinylated anti-CD7 antibody ([LT7](biotin conjugate), cat # ab34293, Abcam, USA) was then selected as the 'bridge molecule' because it was believed desirable to have most of the cells susceptible to binding to streptavidin-tagged MBs (Targestar-SA, Targeson Inc., San Diego, USA), but with a small significant fraction of the cells lacking the antigen. It was hoped that this would provide an internal control for efforts to sort cells on the basis of whether they had or had not associated with MBs.

A 5 µL aliquot (yielding 5 µg) of biotinylated anti-CD7, was added to a million cells concentrated by centrifugation to 1 million cells in 200 µL. This was estimated to provide an excess of roughly 5000-fold more anti-CD7 than needed to saturate the surface antigens on the cell surface. After reaction with the antibody, the cells were centrifuged using low-speed settings (400g's for 5 min). The Targestar-SA MBs were gently mixed for five minutes in a 25mL falcon tube with the now-antibody-labeled cells. Cells were prepared at two different concentrations to test which one obtained higher binding with an equal amount of Targeson-SA MBs: 2.35 million cells/mL and in 200,000 cells/mL, which has been found to be an optimal concentration for flow cytometry at the current flow rates (~76 µL/s, sheath fluid pressure ~7.5 Psi). In order to run the cells on the flow cytometer, the dynamic range of the amplifier (Log amp) was adjusted to detect cells within the higher limits of the amplifier (the mean size of this cells is 11 µm in diameter and its distribution is rather broad, containing cells around 8 to 15 µm in diameter (see Fig. 111b). The medium used as a sheath fluid for all the particles and as an environment for UCA and beads to guarantee their stability was 0.45 µm-filtered 0.9% NaCl. This is the same diluent used for our Coulter M3 and Z counting machines, so that we keep consistency throughout different machines. Cells were diluted and suspended in RPMI cell media to extend their consistency and stability (not maintained in regular saline). The antibody-labeled cells and streptavidin labeled bubbles incubation time was five minutes at 37 ° C, the MBs were added at a concentration of $2x10^6$ MBs/mL.

6.5.3 Preliminary Results and Discussion

Flow cytometry (Fig. 111a) shows that we distinguish a scattering pulse from a cell *vs*. a bubble by using size, time of flight and also superimposed ultrasound oscillations (red curve in Fig. 111a). The assessment of binding was performed using a microscopy stage system with Nikon 40x and 60x objective lenses which are air and water immersion objectives respectively. We used a high magnification microscope system (Nikon Eclipse 80i, Nikon Instruments, NY) to assess the binding efficiency and binding ratios of streptavidin coated, lipid shelled UCA, bound to biotinylated –antiCD7 and CCL119 cells. In Fig. 112 we observe some binding of MB's to leukemia cells. The binding rate was low and the maximum number of bubbles that we saw on a cell was four.

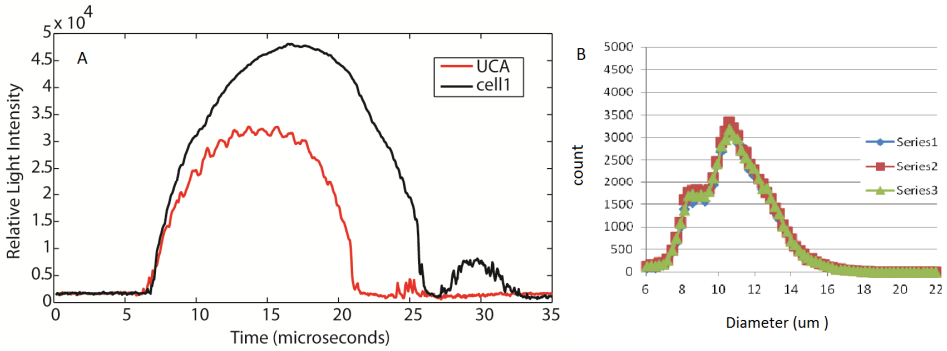

Figure 111. UCA *vs.* Leukemia cell relative size difference using flow and coulter system. A) Light intensity *vs.* interrogation time showing that two different signals (superimposed) which is a bubble in red and cell in black, showing that with the current electronics, we can easily resolve both at the flow rates used. Size distribution for current CCL-119 using Coulter M3.

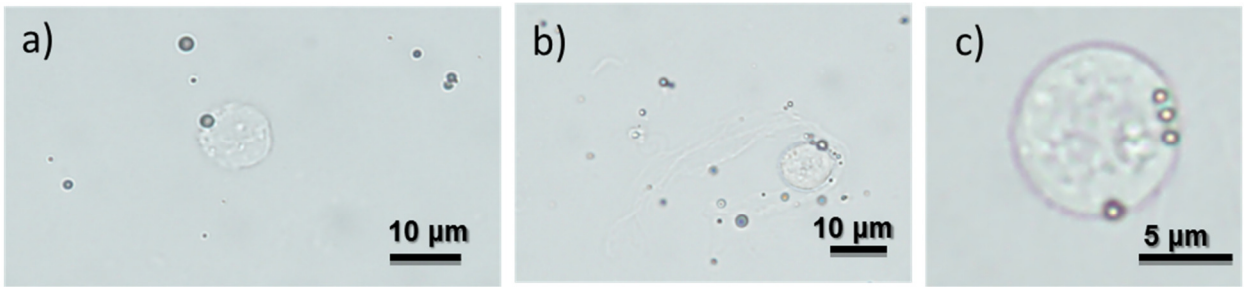

Figure 112. Microscopy images of microbubble and leukemia cell binding. a): Micrograph 60X of cell-bubble complex. b): Micrograph showing microbubbles alone and cells. c) Zoomed cell with 4 microbubbles apparently attached.

Swalwell et al, 2009[198] developed a position sensitive detector in order to introduce a sheathless flow cytometer, called the virtual core. The virtual core's principles are shown in Fig. 113. Briefly, it used a special alignment of optics in the forward scattered path in order to determine if a particle is or not in the focal region of the interrogation laser. This allows the detector to discriminate whether or not a particle has been through the cytometer laser center. A potential future use of the position detector would be to measure and quantify the displacement that a bubble-cell conjugate has experienced in response to applied acoustic radiation force and to use this principal as the basis of simple and direct antigen-specific cell sorting for diagnosis or cell phenotypic enrichment. The work is still in development, but progress has been made on the instrumentation.

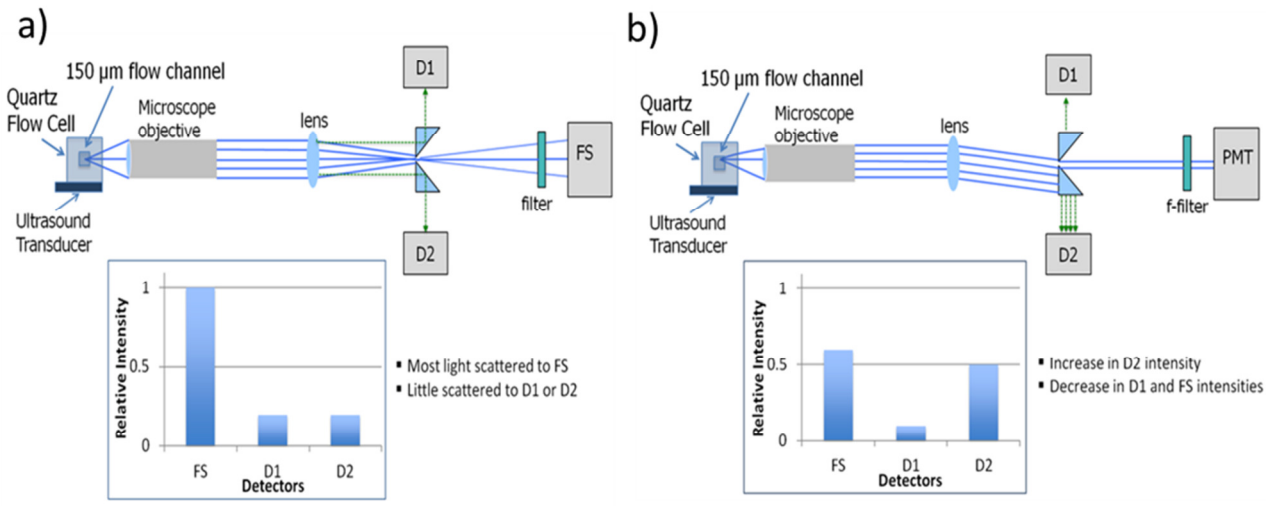

Figure 113. Position sensitive detector schematic. Forward scattering when the particle is centered (a) and when the particle is displaced to a side of the center (b). The relative intensity of the forward scattered (FS) goes down when the particle leaves the center of the laser (b). The detector D1 or D2, will increase in light intensity after the shift, since geometrically, is leaving the center towards one side or the other.

In Fig. 114 the principle of the detector is demonstrated. We can observe that there is position shift of calibration beads (D=8µms) caused by ultrasound radiation force.

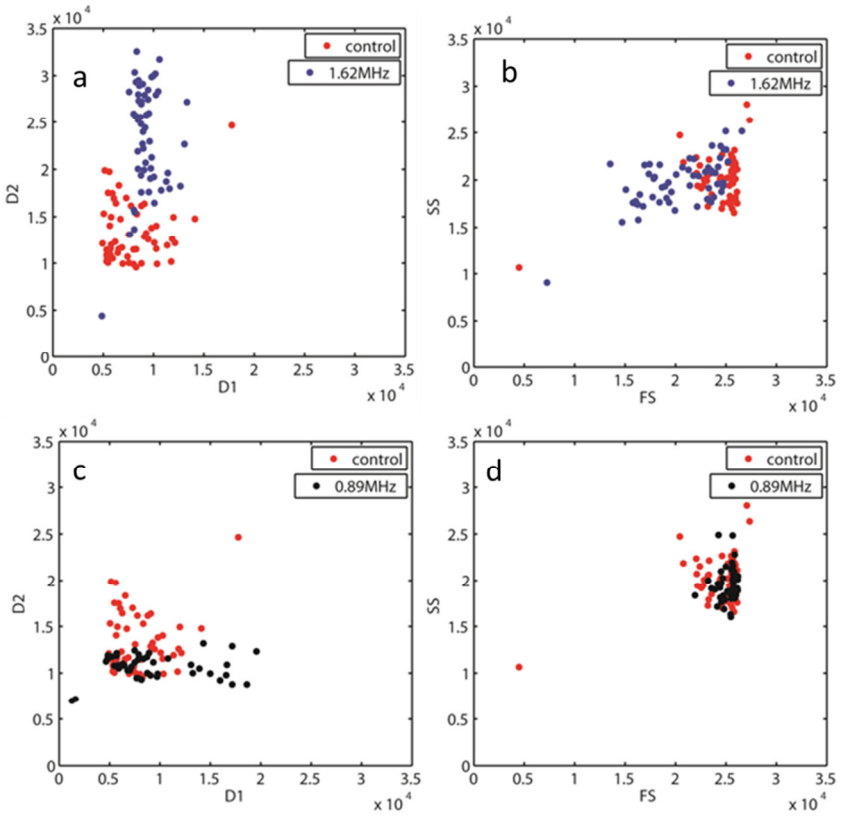

Figure 114. Detector principle. Top panels show detector D1 and D2 changes on (a) and FS, SS (b) for control and 1.6MHz 50 cycle burst. Bottom panel shows the same information for another frequency, 0.89 MHz. Varying frequency excites different standing patterns that might displace beads one way or the other.

Thus particle acoustic radiation force-induced particle displacements can be detected using the D1- and D2-augmented acoustic flow cytometer, offering the possibility of a straightforward means of sorting cells. While there is some support in the literature for the concept that cells (alone) can be segregated acoustically on the basis of subtle differences in their intrinsic properties, a more promising approach seems to be the one presented here; *viz.*, linking MBs with cells via specific antibodies. The challenges are several, however. Distinguishing between a complex (bubble+cell) *versus* just a big cell is challenging using only light scattering (flow cytometry). Ultrasound activation of the MB's helps one to know which signals come from bubbles and which ones come from cells, as shown in Fig. 113a. The cell-MB conjugates could be distinguished using a combination of PSD and light scattering signals. The position sensitive detector does not have the sensitivity to capture cell displacement of the cell alone to a transient pulse (cells are mostly water; therefore impedance mismatch between a cell and its surroundings is negligible). It might also be possible that bubbles detach from the cells before a displacement can be observed; this possibility must be investigated but seems a doable undertaking.

CHAPTER 7

Characterization of a Phase Change Dual Contrast Agent

7.1 Introduction

This remaining chapter is part of an interdepartmental collaboration study between the O'Donnell, Matula and Pozzo laboratories (*i.e.*, a uWAMIT collaboration). In this chapter, a nanoscale emulsion bead encapsulated with absorptive gold nanoparticles[257] recently proposed as a contrast agent for photoacoustic (PA) molecular imaging is investigated as a possible agent for dual laser and ultrasound-based therapy to achieve low cavitation thresholds. The nanoemulsion consists of a perfluorohexane core with a boiling temperature of 56 ℃ and a layer of gold nanospheres at the emulsion's oil-water interface that can be optically activated to generate cavitation nuclei with fairly lower laser fluence. By clustering gold nanospheres at high density on the emulsion bead surface, the optical absorption spectrum is broadened and red-shifted thereby enabling its use in deep tissue at near-infrared wavelengths (700 – 1000 nm).

Contrast-enhanced imaging with exogenous contrast agents is a rapidly developing technique for both photoacoustic (PA) and ultrasound (US) systems. Microbubbles have been used in US harmonic imaging [258] of vasculature, and for drug or therapeutic delivery [259]. Their large size (typically 1-10 µm), however, inhibits high penetrability into tissue through leaky vasculature (300 – 500 nm endothelial gaps) and nanoscale pores, and through active mechanisms such as cellular intake.

E Work published in part in:

Arnal B, **Perez C**, Wei C, Xia J, Lombardo M, Pelivanov I, Matula TJ, Pozzo LD, Donnell MO. Photoacoustics Sono-photoacoustic imaging of gold nanoemulsions : Part I . Exposure thresholds. Biochem Pharmacol Elsevier GmbH., 2015a;:1–8.

Arnal B, Wei C, **Perez C**, Nguyen T, Lombardo M, Pelivanov I, Pozzo LD, Donnell MO. Photoacoustics Sono-photoacoustic imaging of gold nanoemulsions : Part II . Real time imaging. Biochem Pharmacol Elsevier GmbH., 2015b;:1–9.

Wei C, Xia J, Lombardo M, **Perez C**, Arnal B, Larson-Smith K, Pelivanov I, Matula T, Pozzo L, O'Donnell M. Laser-induced cavitation in nanoemulsion with gold nanospheres for blood clot disruption: in vitro results. Opt Lett 2014a;39:2599–2602.

Wei CW, Lombardo M, Larson-Smith K, Pelivanov I, **Perez C**, Xia J, Matula T, Pozzo D, O'Donnell M. Nonlinear contrast enhancement in photoacoustic molecular imaging with gold nanosphere encapsulated nanoemulsions. Appl Phys Lett 2014b;104:1–4.

Making stable nanobubbles at the dimensions required for enhanced transport is currently a challenge [260]. To solve this problem, phase-change contrast agents, which change state from liquid to gas if exposed to thermal and/or acoustic energy, were introduced. Liquid perfluorocarbon nanodroplets with a low-boiling point and a physical dimension appropriate for enhanced penetrability into tissue have been developed [261–264]. The phase-transition of these nanodroplets into a microbubble (vaporization) produces high contrast for US imaging. Compared with other US contrast agents, nanoemulsions can have a long circulation time in the body (up to two hours [262]). Because of increased surface tension, however, US exposure parameters must be relatively high, usually involving high repetition rates [264] or long excitations (~100 ms)[263]. This means that heat can be involved in the vaporization, increasing the possibility of damage to surrounding tissues or limiting the frame rate of the imaging modality. This mechanism is also not efficient using low-frequency ultrasound because of low acoustic absorption.

To achieve molecular imaging at significant depths within tissue, laser-activated PA contrast agents have been introduced [265–269] at the nanoscale. Plasmonic absorption enhances the efficiency of compact nanoprobes (10 – 200 nm) in PA generation. However, a significant concentration is usually required to get single shot measurements for real-time *in vivo* imaging (*e.g.* ~10 nM)[265–269]. Recent studies have shown that combining nanodroplets with efficient optical absorbers in a single contrast agent can enhance the PA signal from the absorbers [266]. Here we build on this work to demonstrate a highly sensitive, and potentially specific, approach for molecular imaging and therapy using a nanoscale contrast agent integrating perfluorocarbon nanodroplets with plasmonic absorbers. In particular, we explore the non-linear acoustic response of these agents to simultaneous light and sound excitations at exposure levels well within safety limits for routine diagnostic imaging.

In our previous work, we introduced a nanoemulsion of perfluorohexane droplets (100-200 nm) surrounded by amphiphilic gold nanopsheres (12 nm in diameter). It was used as a non-linear PA contrast agent by inducing a phase transition of the oil through plasmonic absorption of light by the gold nanoparticles[270]. This approach can produce highly sensitive PA images with high background suppression (*i.e.*, also highly specific contrast), but it requires a relatively high optical fluence to observe non-linear contrast (at 750 nm, threshold at 4 mJ/cm^2, 10 dB contrast around 6 mJ/cm^2), limiting its use for deep imaging applications.

An approach to greatly reduce the optical fluence required for a non-linear response from these contrast agents is suggested by recent work showing that laser generation of water vapor bubbles around plasmonic absorbers can be enhanced by adding ultrasound pressure fields[271–273]. This technique, named "PA cavitation", enables high contrast imaging at lower exposure thresholds and concentrations. Building on this work, we investigate here the PA cavitation exposure thresholds needed to trigger vaporization of a nanoemulsion beads coated with gold nanospheres (NEB-GNS). This approach leverages short-lived (a few µs) bubbles made possible by the high boiling point (BP) of the perfluorocarbon used in this nanoemulsion. In contrast to another approach using long lifetime bubbles [266], a short-lifetime strategy using reversible phase transitions is preferred for molecular imaging applications requiring extended exposures.

In the remainder of this chapter we investigate the benefit of clustering small gold nanopsheres around high-BP perfluorocarbon droplets for combined PA/US applications. After introducing the physical characteristics of the NEB-GNS agent, high speed imaging results, photoacoustic nonlinear enhancement effects and vaporization thresholds are quantified and compared to single gold nanopsheres. The potential use of the vaporization signals for imaging is then studied and discussed. To specifically retrieve the vaporization signal in tissues loaded with NEB-GNS, photoacoustic and backscattered ultrasound signals must be cancelled by a procedure described in a the last section (7.3.4) called "sono-photoacoustic" imaging.

7.2 Materials and Methods

7.2.1 Nanoemulsion Samples

NEB-GNS were synthetized using the procedure described in previous reports[257,274]. Colloidal gold nanospheres (diameter 12 nm) were synthetized using a citrate reduction method[275]. The particles were functionalized using PEG-thiol and butane-thiol (Sigma Aldrich, St. Louis, MO, USA), with dosages of 0.8 chains/nm^2 Au and 700 molecules/nm^2 Au respectively. Attraction between the hydrophobic butane-thiol ligands resulted in clustered gold nanospheres dispersions. A solution of 1 vol. % perfluorohexane (Sigma Aldrich, St. Louis, MO, USA) and 0.012 vol. % Au clusters in water was sonicated (102C, Branson, Danbury, CT, USA, pulsed regime - 1 s on, 4 s off) for 13 s in a cold water bath. The absorbance was measured with a spectrophotometer (UV 1601, Shimatzu, Kyoto, Japan). The absorbance spectrum (Fig. 115a,

blue curve) exhibits a red shift of the resonance from 520 nm to 547 nm compared with the original gold nanopsheres (black curve) and a broad tail enhancing absorption in the optical window ([600 – 1100] nm wavelengths). The size was measured by DLS as a broad dispersion between 30 - 1200 nm with a peak at 132.1 nm and a mean size of 303 nm (Fig. 115b)). Additional complexes were identified between 2 and 6 µm, but DLS may not be quantitative in this range as it is heavily affected by sedimentation or flotation [276]. In our case, the effective density of perfluorohexane beads (1.7) can be increased by the gold nanospheres (density 19.3) resulting in sedimentation speeds depending on size.

To confirm the presence and quantify the micron-size particle number, the size distribution and concentration of the emulsion were obtained prior to and after all experiments using a Coulter Multisizer III (Beckman Coulter, Miami, FL). A 20 µm aperture was used, which can size particles with diameters from 0.56-12 µm; any count below 0.56 µm is considered as noise. The sample was diluted ~1250X in 0.2 µm filtered ISOTON II electrolyte. A 50 µL sample was used each time, and all measurements were repeated 6 times using a volumetric count mode. Individual particles were sized and binned in 300 evenly spaced bins with 0.039 µm width. All data are displayed as a histogram with count *vs.* diameter, with the count (bin height) showing the number of particles in each bin interval. The reported concentration is computed for all ranges in question and accounts for the dilution factor and sampling volume used above.

A near Gaussian distribution of NEB-GNSs was identified between 1 and 3 µm (inset of Fig. 115b). The sample was then split in two volumes. Assuming an ideal covering of the bead by gold nanopsheres (80% surface density), the weight of each bead size was calculated. Then, a basic model of sedimentation (Stokes force = gravity) was used to calculate the sedimentation speeds of different particles: *e.g.*, in 24 hours a 425 nm particle sinks 22 mm. In contrast, a 132 nm bead should sink only 6 mm in the same period. A sample of 10 ml was left to settle in a scintillation vial. As 22 mm was the height of our solution in the vial, we assumed that all particles larger than 425 nm would fall to the bottom. An 8 ml sample was carefully withdrawn from the top without provoking any agitation. This supernatant was sized again with the Coulter counter. There were no particles larger than 1 micron (inset Fig. 115b), which validated the purification process. These samples were used to compare the vaporization threshold before and after purification. The purified NEB-GNS sample showed a less broad tail than the original one (Fig. 115a), indicating that larger beads tend to broaden the extinction spectrum.

We performed discrete dipole approximation (DDA) simulations using DDscat [277] to estimate the contributions of scattering and absorption on NEB-GNS. An oil bead of 150 nm diameter was surrounded by 12 nm GNS positioned using an optimization code solving the Thomson problem, leaving a gap of 2 nm between spheres. The NEB-GNS structure was discretized using a step of 1.35 nm and the simulation was run with orientational averages. The broadening of the tail was observed for both absorption and scattering contributions, but scattering contributes to less than 20% of the extinction and is not particularly higher at the longer wavelength. Hence, it is likely that absorption dominates over scattering, at least for the purified sample, meaning NEB-GNS absorption can be related to the absorbance measurement.

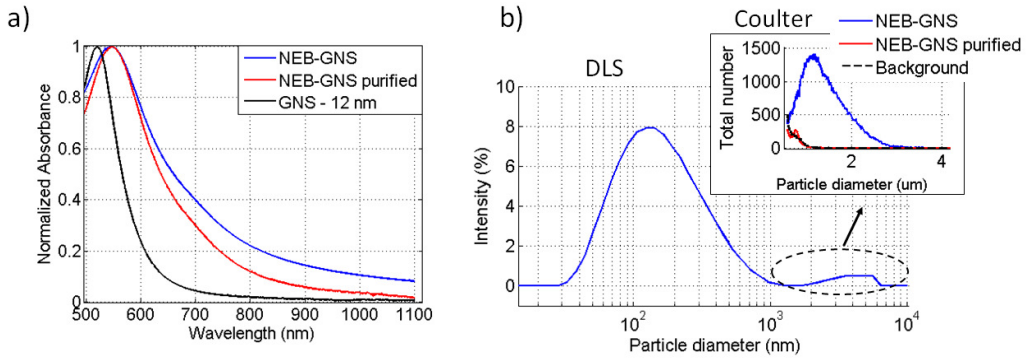

Figure 115. Emulsion size purification step. a) Absorbance spectra of the nanoemulsion before (blue) and after purification (red), and of gold nanopsheres in suspension (black). b) Sizing of the nanoemulsion by DLS (Intensity). Inset: Sizing in the micron range using a Coulter counter: nanoemulsion before (blue) and after purification (red); background signal is shown in black.

7.2.2 Sample Preparation

Using a size-dependent concentration measurement from DLS, we estimate the concentration of emulsion bead in the stock solution to be 1.32 x 10^{12} beads/ml (for sizes ranging from 100 to 8000 nm), or about 2.2 nM. For all experiments, the solution was diluted to a fixed absorbance of 0.25 cm^{-1} at 750 nm, leading to a concentration of 3.8×10^{10} beads/ml (or 63 pM) for the raw sample and 5.86 × 10^{10} beads/ml (or 94 pM) for the purified sample (lower tail after filtration, Fig. 115b).

A sample of GNS obtained after a citrate reduction method was diluted with citrate buffer (3.8 mM) to obtain an absorbance matching the NEB-GNS one at 520 nm (0.403 cm^{-1}). The concentration of GNS was then 2.59 × 10^{12} GNS/ml. The concentrations of GNS and NEB-GNS samples were estimated respectively to be 3.8×10^{12} GNS/ml and 5.9×10^{12} GNS/ml, *i.e.*, on the same order. The non-linearity of NEB-GNSs was studied using a tube phantom (SLTT-16-72,

Zeus, Orangeburg, SC, USA) with an energy-sweeping PA imaging system. A 532-nm pumped wavelength tunable OPO laser (Surelite OPO plus, Continuum, Santa Clara, CA, USA) delivered 800-nm laser pulses, with a 10-ns duration at a 20-Hz repetition rate, to generate PA signals and also induce microbubbles by heating the NEB-GNSs. Before being coupled into a fiber bundle (77526, Oriel Instruments, Stratford, CT, USA), laser pulses passed through a continuously variable neutral density filter (NDL-10C-2, Thorlabs, Newton, NJ, USA) mounted on a linear actuator motor (T-LA60A, Zaber, Vancouver, BC, Canada) moving laterally to change the energy into the fiber bundle, producing a laser fluence varying from 2.3 mJ/cm^2 to 16.7 mJ/cm^2 on the sample in the tube immersed in a water tank. An ultrasound linear array transducer (AT8L12-5 50 mm, Broadsound, Hsinchu, Taiwan) interfaced with an ultrasound imaging system (Verasonics, Redmond, WA, USA) was placed about 15 mm above the tube to receive PA signals. The central 128 elements of the transducer were used, yielding a 25.6 mm aperture with a detection angle of about 81 degrees. For comparison, a linear ink (Waterman, Paris, France) solution was used as a control. The absorption coefficient was adjusted to be the same, 2.5 cm^{-1}, for NEB-GNSs and ink at the irradiating wavelength.

7.2.3 Ultrasound Transducer Calibration

The pressure field generated by a focused ultrasound transducer (H-102, Sonic Concept, Woodinville, WA, USA, focused at 63 mm, f# 0.98, 1.24 MHz) in line with a 55 dB gain power amplifier (ENI-A150) was quantified using the fiber optic hydrophone described earlier. The HIFU transducer, mounted at one end of a degassed and deionized water bath, was driven by a 10 cycle sine wave burst produced by a function generator, , power amplifier and a customized matching network. A 10 MΩ high voltage oscilloscope probe (Teledyne LeCroy, Chestnut Ridge, NY) was inserted between the matching network and the power amplifier to measure the input voltage applied to the driving system. A 3D positioning system was used to move the fiber optic probe hydrophone at the focus. Hydrophone signals were digitized by an oscilloscope at 500 MSample/s. The FOPH 2000 software CALDEC was used to calculate the pressure from oscilloscope data and to deconvolve the signal to account for the frequency response of the system[107]. As minimal thermal effects result from ultrasound with a 10-cycle pulse at low repetition rate (5 Hz), peak negative (p-) pressure alone is reported and corresponds to the minimum pressure measured in the pulse.

7.2.4 Automated Setup for Light and Sound Exposure Threshold Study

A 532-nm pump beam was injected into a wavelength-tunable optical parametric oscillator (OPO) cavity (Surelite OPO plus, Continuum, Santa Clara, CA, USA) to produce 10-ns duration, 750-nm laser pulses. Before coupling the laser beam into a fiber bundle (77526, Oriel Instruments, Stratford, CT, USA) for delivery to the sample, the fluence was adjusted with a combination of neutral density filters that can be remotely switched with a six-position filter wheel (FW-103, Thorlabs, NJ, USA), as shown on the top left of Fig. 116a. The sample (diluted NEB-GNS suspension or GNS) was injected into a customized transfer pipet (3 ml, BD Falcon, NJ, USA) connected to a tube in a closed loop. The tubing was coupled to a peristaltic pump (Masterflex L/S model 7518-60, Cole-Parmer, IL, USA), allowing circulation of the sample between each dataset. The pump induced quasistatic pressure changes and was not operated during acquisitions.

The sample was immersed into ultra-pure degassed water and was positioned approximately at the focus of the transducer by maximizing the pulse-echo signal received on the focused transducer. Then, the laser was fired at a low fluence on the black marker spot and the PA signal was maximized on the focused transducer, allowing more precise positioning. An in-house PVDF unfocused sensor (bandwidth [0.05 - 30 MHz], aperture 6 mm diameter) was then positioned at the water surface 70 mm from the sample. The timing of ultrasound emissions and laser firing was adjusted. Note that the laser beam size of 6 mm is larger than the acoustic wavelength (1.2 mm) and covers multiple peak negative pressure sites. Thus, contrary to our preliminary experiment where the light was focused on a 1 mm area [278], the exact lasing time in the microsecond range will not affect the results. Broad illumination is also more representative of potential *in vivo* applications. The sample was then moved horizontally toward the transducer, allowing both the focal spot of the transducer and the laser spot to meet within the pipet bulb. As noted above, a 10-cycle ultrasound pulse emitted with the focused US transducer was used for all studies. The laser was fired at the arrival time of the 5th acoustic cycle at the transducer focus.

To cover all desired exposure ranges in terms of laser fluence and US pressure while recording enough data to perform statistics, an automated platform was designed. A TTL signal running at 20 Hz, corresponding to the flash lamp timing of the laser is used as an input trigger to an ADC board (Razor 14X2 Express CompuScope, Gage, Lockport, IL, USA) controlled with Matlab. When the software is running, a trigger out is sent by the ADC board immediately after being triggered. This signal is then delayed by 250 µs by a function generator (AFG-3252, Tektronix,

OR, USA) to trigger the laser Q-switch. This approach limits exposure of the samples since lasing only occurs when a signal is actually being recorded. Moreover, the repetition rate was limited to 5 Hz by the Matlab software. The second channel of the generator was used to drive an RF amplifier at a voltage also controlled by software to independently scan the pressure amplitude. Ultrasound was emitted earlier than the laser so that the pulses arrived synchronously. The PVDF transducer finally received both the laser-induced PA signals and the scattered pressure waves originating from the focused transducer. This RF signal was captured by the ADC, displayed in real-time and saved on the computer hard-drive for further analysis. At each set of exposure parameters, 200 recordings were performed. The laser fluence was gradually increased. For each laser fluence, the ultrasound pressure was raised until significant cavitation activity was noted.

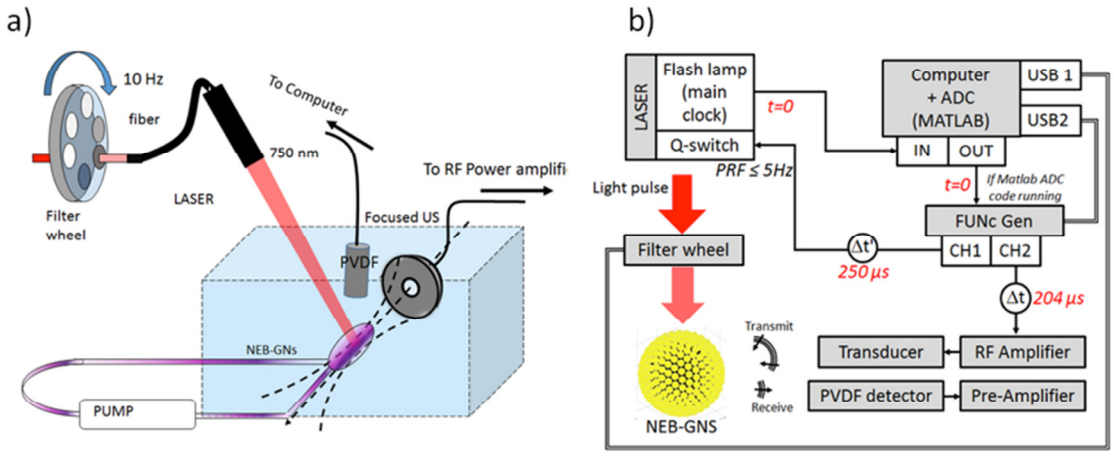

Figure 116. Setup for automated parameter scan of laser fluence and acoustic pressure. a) Light and sound delivery and sample position. b) Instrumentation with remote controls. The reader should follow the diagram starting from the flash lamp signal (t=0).

Fluence values were calibrated by placing an energy meter (J-power, Coherent, Santa Clara, California) at a position matching the focus of the US transducer. A 2 mm pinhole was used, ensuring that it was at the maximum energy position of the laser beam. Then, light attenuation through 60 mm of water was taken into account to report all fluence values.

Data analysis

For each set of exposure parameters, a reference signal recorded without laser firing was subtracted from the 200 signals to remove the US scattered wave contributions from the plastic container, similar to methods used in our previous studies [278,279]. This subtraction was robust and produced residual signals outside the time window of interest much smaller than those obtained during laser excitation studies. The broadband noise signal was computed in a time

window before the lasing time. If no bubble is present, the differential signal should correspond to pure noise. In contrast, the presence of vapor will automatically generate some scattered acoustic signals in all directions. To detect the vaporization events, a threshold on the magnitude of the signals equal to 2 times the noise value was chosen to count the number of cavitation events out of the 200 independent recordings. This threshold was set arbitrarily and the results were not highly influenced by its value, indicating that our detection method is very sensitive. A sigmoidal function was fit to all broadband noise dependencies at each laser fluence to compute the cavitation threshold, defined as the peak negative acoustic pressure corresponding to a 50% probability of a cavitation event.

7.2.5 High Speed Imaging

To view bubble formation resulting from a single laser pulse at the long wavelength edge of the optical window acting on NEB-GNSs, an inverted microscope (TE2000-U, Nikon, Japan) with a 40X water immersed objective (MRD07420 CFI Apo 40X W NIR, Nikon, Japan) was coupled to a high-speed camera (Imacon 200, Hadland Imaging LLC, Santa Cruz, CA, USA) and synchronized with a semiconductor fiber laser (HM 40W G3.1, SPI, South Hampton, UK). A small amount of NEB-GNS with a concentration of 7.6×10^{10} beads/ml was sandwiched between two plastic food wrap membranes (polyvinyldene chloride, Saran, Racine, WI, USA) with a thickness of about 300 µm and sealed with an O-ring. The sample was placed in a water tank and co-aligned with the objective. A 10 ns, 1064 nm laser pulse was delivered to the sample over a 0.7 mm diameter round illumination spot resulting in a fluence of about 70 mJ/cm^2. This wavelength (1064 nm) provides good penetration into the body for most biomedical applications. In addition, commercial fiber or diode-pumped Q-switched solid state lasers are available at 1064 nm that are inexpensive, compact, and high powered, enabling a potentially cost-effective solution for diagnostic and therapeutic needs. As shown in previously published results, the spectrum of the NEB-GNS nanosystem exhibits significant absorption at 1064 nm,[257,280] even though the absorption spectrum peaks at shorter wavelengths. The high speed camera can record bubble generation and dynamics with a maximum frame rate of 2×10^8 frames/s.

7.2.6 Blood Clot *In Vitro* Experiments

Fibrin gels were prepared according to the procedure described in a previous paper.[281] Briefly, human fibrinogen (Enzyme Research Laboratories, South Bend, IN) was defrosted from -80 ℃ to 37 ℃ and dialyzed into a pH 7.4 buffer solution (0.14 M NaCl and 44 mM HEPES). The

concentration was determined by spectroscopy at 280 nm with an extinction coefficient of 1.6 mg $ml^{-1}cm^{-1}$.[282] The gels were formed by adding $CaCl_2$ and human α-thrombin (Enzyme Research Laboratories, South Bend, IN) into the fibrinogen to convert it to fibrin. The final sample composition includes 2 mM $CaCl_2$, 0.16 units/ml thrombin, buffer solution, and 4 mg/ml fibrinogen. The gels were injected into a 1.6-mm tube (SLTT-16-72, Zeus, Orangeburg, SC, USA) and allowed to react for at least 1 hour before performing the experiment.

A small amount (~30 μL) of NEB-GNS with a concentration of ~1.17×10^{12} beads/ml dispersion (0.015 vol% Au, 1 vol% perfluorohexane) was added next to a 15-mm long fibrin clot in the tube. The tube was then connected to a water head at the NEB-GNS side, providing a pressure at the lower end of blood pressure in a human artery, 80 mm Hg, and immersed in a tank filled with deionized water for US pulse-echo and PA monitoring.

Two different wavelengths (750 or 1064 nm) within the therapeutic window (approximately 700-1100 nm) emitted by different lasers were employed to irradiate the emulsion-clot sample. As an initial demonstration to disrupt a clot with laser-activated cavitation from this new emulsion, an OPO laser (Surelite OPO plus, Continuum, Santa Clara, CA, USA) with a wavelength tuned to 750 nm was used. This wavelength is closer to the peak absorption of NEB-GNS [280] and thus considered more efficient than the 1064 nm wavelength used in the experiments conducted, the results of which are illustrated in Fig. 118. Nanosecond (7 ns at 1/e level) laser pulses were coupled into a fiber bundle (77526, Oriel Instruments, Stratford, CT, USA) to irradiate the emulsion-clot interface inside the tube, creating cavitation bubbles from NEB-GNSs, and also generating PA signals. The fluence was about 7 mJ/cm^2 and the pulse repetition rate was 20 Hz. Both the fluence and average irradiance are well within guidelines for safe operation at this wavelength.[283] A linear US array transducer (AT8L12-5 50 mm, Broadsound, Hsinchu, Taiwan) interfaced with a Verasonics imaging system (Redmond, WA, USA) was placed 16 mm above the tube to receive PA signals and also perform US pulse-echo imaging. A digital camera (DSC W230, Sony, Japan) was also used to record the process. We performed a clot disruption experiment at 750nm and repeated with the same 1064 nm fiber laser used to generate the data displayed for Fig. 118. The videos obtained can be found in the supplementary material of this publication ([278]). All the conditions are the same except the laser wavelength changed from 750 nm to 1064 nm with a repetition rate of 1 kHz.

7.3 Results:

We have demonstrated in previous work that this nanoemulsion with gold nanospheres (NEB-GNSs) exhibits strongly nonlinear PA signal response versus applied laser fluence due to bubble formation with dramatically enhanced thermal expansion.[279,280,284]

7.3.1. Proof of Concept via High Speed Imaging and Nonlinear Imaging:

In this section, optically-induced bubble formation is verified using a microscope coupled with a high-speed camera (microphotography), and a potential therapeutic application using this nanoagent for cardiovascular disease, blood clot disruption, is also demonstrated in an *in vitro* study. We also explore and discuss the possibility of manipulating the threshold for cavitation under simultaneous pulsed laser and US excitation, and report in the next section (7.3.2).

Figure 117 shows a series of images of bubble formation induced by a single laser pulse delivered at 120 ns relative to the start of recording. The image at the 200 – 300 ns window clearly shows generated microbubbles. Some expanded to a maximum diameter of about 10 μm in the image at 600 – 700 ns and then shrank. All bubbles were lost after 1400 ns (~1300 ns after the laser pulse), indicating that their lifetime is about 1 μs. Bubbles may disappear due to collapse (inertial cavitation) or re-condensation back into the liquid state.

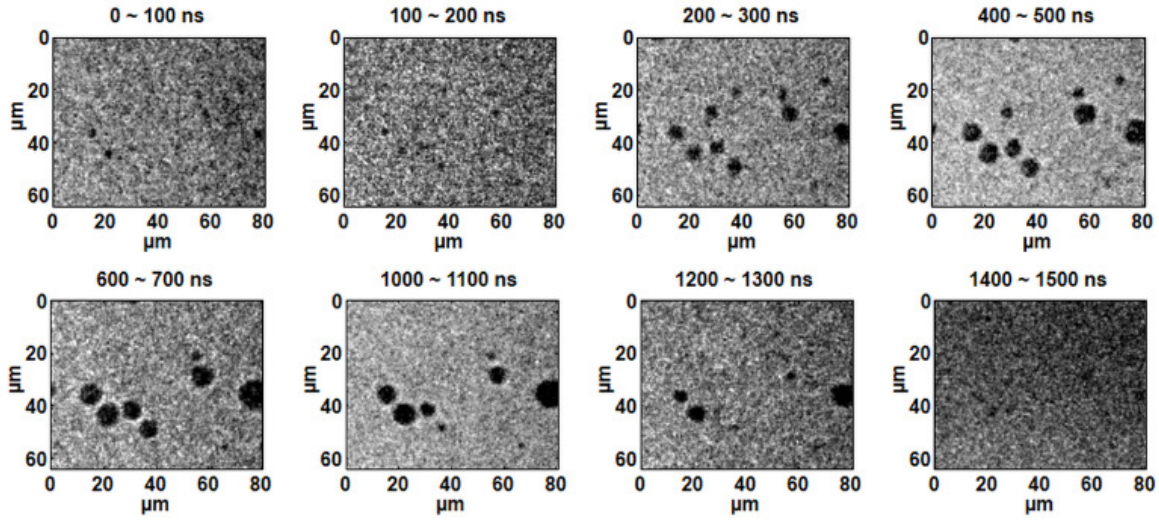

Figure 117. Images by a high speed camera: μm-sized bubble formation from nanometer-sized NEB-GNSs with one short (10 ns) laser pulse irradiating the sample at 120 ns relative to the start of data acquisition. The lifetime of the bubbles is about 1 μsec.

Clearly, 2 orders of magnitude growth in diameter (or 4 orders in volume) suggests the possibility of using NEB-GNSs for therapy. As a first application, the potential of using NEB-

GNSs for human blood clot disruption was investigated in an *in vitro* experiment. Although the absorption coefficient at this wavelength is significantly smaller than that at 750 nm, short-lived microbubbles appear at 70 mJ/cm^2 (as shown in Fig. 118). However, their effect on clot breakage depends on vessel size and geometry, and also on clot strength. In our case, sufficient microbubbles are formed at a fluence of 533 mJ/cm^2 to effectively break the clot. This was a preliminary result and the purpose was to test the feasibility of a clot breakage with a portable fiber laser. Although it takes less time (about 40 seconds) to break through the clot compared with the previous experiment, both the fluence (533 mJ/cm^2) and average radiance are well above safety limits at this wavelength.[283] In addition, depth-dependent light attenuation in turbid biological tissue makes it more difficult to deliver sufficient energy to target region at centimeters depth. Therefore, there is a need to explore a method that can significantly reduce both the laser fluence and light-activated cavitation threshold for clot breakage.

Figure 118. Laser-induced fibrin clot disruption. Figure of laser-induced fibrin clot disruption with NEB-GNSs in a tube using a 1064-nm laser with a pulse repetition rate of 1 kHz and a laser fluence of 533 mJ/cm^2.

Recent studies have shown that a significantly lower cavitation threshold can be achieved when a laser pulse is delivered to an absorbing medium negative pressure phase of an US pulse arrives simultaneously at the region of interest, compared with using either laser or US excitation alone.[272,273] Therefore, combining US with optically-activated cavitation using NEB-GNSs may provide a more effective treatment for thrombotic disease.

To explore the possibility of non-invasive, cavitation-based therapies in deep regions, an experiment using simultaneous laser-US excitation of NEB-GNSs with a concentration of 1.26 × 10^{12} beads/ml dispersion (0.005 vol% Au and 0.27 vol % perfluorohexane) in a 1.6-mm tube was performed with a low-frequency (center frequency at 1.24 MHz) focused transducer (H-102,; described earlier) and the 1064 nm fiber laser with a pulse width of 250 ns and a significantly reduced fluence (84 mJ/cm^2) compared with that used in the experiment summarized in Fig. 118. The tube was positioned in the focus of the low-frequency transducer. A homemade unfocussed wide-band PVDF transducer (100 kHz - 30 MHz bandwidth by 1/e level, 6-mm working aperture) was placed in water to detect both A-line laser-generated PA

signals and low frequency US signals reflected by the tube with NEB-GNSs with/without laser irradiation.

Figure 119 shows preliminary results of simultaneous laser/US excitation of NEB-GNSs. Both the original recorded signal and its “slow-time” differential signal, representing the difference between signals recorded on consecutive transducer firings (100 Hz repetition rate), are displayed. The peak negative acoustic pressure was 0.97 MPa.

Figures 119a and d show a sample RF A-line and the corresponding differential signal, respectively, for the case where laser irradiation was turned off. The received waveform represents simply the acoustic wave from the focused low-frequency transducer scattered by the tube filled with nanoemulsion. The differential signal shows that the residue was at the background noise level. Figures 119b and e show original/differential waveforms for the case where the laser pulse irradiated the tube at the arrival time of peak *positive* pressure. Clearly, the waveform is very close to that of the previous case, indicating that laser incidence at peak positive pressure did not induce a phase transition in the nanoemulsion. Significant cavitation was observed when laser pulses irradiate the sample at the time of arrival of the *negative* pressure phase of the acoustic wave (Figs. 119c and f). Before laser incidence, the waveform is unchanged from burst to burst and the differential signal is at the background noise level, similar to the previous two cases. In contrast, the waveform is greatly changed after the laser firing, demonstrating initial cavitation and subsequent bubble expansion and collapse from one laser pulse to the next as a widely varying differential signal. With simultaneous US delivery, the lifetime of the cavitation bubble extended to more than 5 μsec (and can be further extended with longer US excitation), as compared to 1 μsec for laser excitation alone, as shown in Fig. 117. A longer-lived cavitation bubble may be more effective for US-based treatment.

To demonstrate that these snapshots are relevant, cavitation probabilities were calculated using a set of 200 firings for all three cases. The energy of differential signals, representing the difference between signals and a fixed reference signal, were integrated and thresholded over the noise level for cavitation detection. The cavitation probabilities were 0%, 1.5%, and 86% for US only, laser at positive peak, and laser at negative peak, respectively, indicating greatly enhanced efficiency for cavitation based treatments.

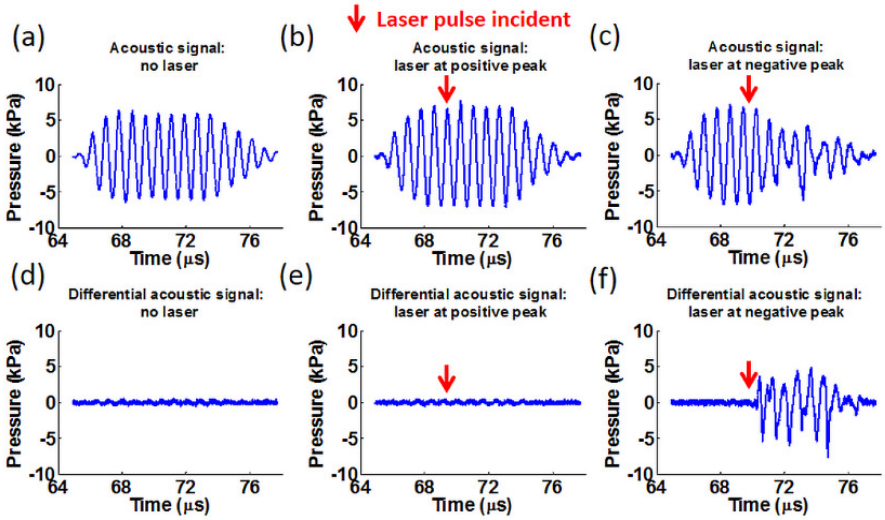

Figure 119. Preliminary results on manipulating bubble generation by NEB-GNSs with simultaneous laser/US excitation. Typical back-scattered RF A-line signals received by a broadband PVDF transducer when the laser was off (a), the laser pulse irradiates the emulsion at peak positive (b) and peak negative (c) pressure. RF signals associated with the slow-time difference when the laser was off (d), the laser pulse irradiates the emulsion at peak positive pressure (e) and peak negative (f) pressure.

In summary, cavitation bubbles are optically-induced in this new type of nanoemulsion with a single laser pulse, and they are demonstrated to help disrupt a fibrin clot in an *in vitro* experiment. With simultaneous low-frequency US excitation and laser (delivered at peak negative pressure), the cavitation threshold can be reduced and long-lived cavitation bubbles produced, making this nanoemulsion potentially effective for non-invasive therapeutic applications inside the body where the energies of both laser and US excitation are well below safety limits. High-intensity focused ultrasound (HIFU) assisted treatment (*i.e.*, histotripsy) will also be implemented into this NEB-GNS nanosystem to further break up and dissolve a clot,[285,286] minimizing potential circulation of small fragments detached from the clot after disruption (*i.e.*, embolism),[287] blocking blood flow in small vessels and causing more serious problems such as stroke, myocardial infarction, and deep vein thrombosis.

To demonstrate the nonlinear PA response of nanoemulsion beads with GNSs (NEB-GNS), a series of PA images were recorded in a phantom at different laser fluences. The relationship between PA signal amplitude and applied laser fluence was investigated for NEB-GNSs, and the results were compared with a linear control agent (black ink of the same optical absorption coefficient) mimicking background absorbers. A scale-differential scheme was also applied to demonstrate enhanced specificity by removing linear background signals.

PA images (cross-sectional view) of the two samples in the tube at three different laser fluences are shown in Fig. 120. Ink images (top row, a-c) depict typical PA images of an homogeneous cylindrical absorber detected by a band-limited ultrasound transducer. Only top and bottom boundaries can be seen, but not the middle part. The signal amplitude changes linearly with the applied laser fluence. In contrast, images of NEB-GNSs (bottom row, d-f) exhibit rapid signal growth as laser fluence increases due to nonlinear signal generation from bubble formation. Furthermore, the appearance of heterogeneous PA sources in the middle of the tube, especially at a laser fluence of 15 mJ/cm^2, is additional evidence of laser-induced transient bubble formation. Note that the display level for ink (maximum at –25 dB) and NEB-GNSs (maximum at 0 dB) is different to illustrate the amplitude difference between the two samples, and the larger dynamic range for NEB-GNSs (45 dB *vs*. 35 dB for ink) indicates greater nonlinear signal increase compared to the ink sample over the range of energies used. The maximum display level, 0 dB, is defined as the maximum value in the images of NEB-GNSs.

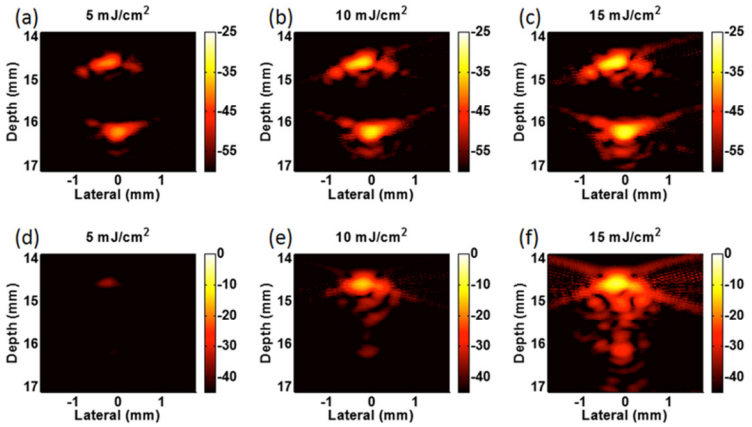

Figure 120. Two samples at three different laser fluences. Photoacoustic images of samples in the tube at different laser fluences: ink solution (a)-(c), and dispersion of nanoemulsion beads with gold nanospheres (d)-(f). Note that images are shown with different dynamic ranges and different levels. Ink: –60 dB to –25 dB. Nanoemulsion beads: –45 dB to 0 dB.

The PA image amplitude representing the sum of every pixel value within the tube is plotted as a function of laser fluence on a log-log scale in Fig. 121. For ink (blue circles), all data points can tightly fit to a linear equation (dotted line). For NEB-GNSs, this linear relation is only valid under a laser fluence threshold (~3.5 mJ/cm^2), and the amplitude grows non-linearly after the laser fluence exceeds this threshold. At 15 mJ/cm^2, the image amplitude of NEB-GNSs increases by more than 24 times (27.7 dB) that of the ink sample.

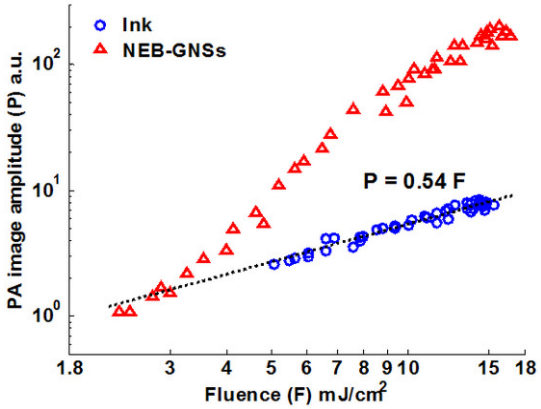

Figure 121. Photoacoustic image amplitude of ink (blue circle) and NEB-GNSs (red triangle) versus laser fluence.

To demonstrate that the nonlinear NEB-GNSs can be used to enhance detection specificity in PA molecular imaging, a scale-differential scheme was used. First, a reference image IM_{F0} at laser fluence F_0 was chosen. At every laser fluence F, a linearly-scaled image $SIM_{F/F0}$ can be obtained from IM_{F0} according to the ratio of F to $F_{0,}$

$$\mathrm{SIM_{F/F0}} = \mathrm{IM_{F0}} \times \frac{\mathrm{F}}{\mathrm{F_0}}. \tag{7.1}$$

The differential image $DIM_{F/F0}$ at laser fluence F is obtained by subtracting the scaled reference image from the image IM_F at that laser fluence,

$$\mathrm{DIM_{F/F0}} = \mathrm{IM_F} - \mathrm{SIM_{F/F0}}. \tag{7.2}$$

Fig. 120 presents examples of differential images of the ink sample (Fig. 121a) and NEB-GNSs (Fig. 121b), both normalized to the maximum (0 dB) of the original image. As expected, the differential image $DIM_{10/5}$ shows nearly complete subtraction for the linear ink sample. The small residue at the bottom of the tube is due to imperfect subtraction and is at the background noise level. In contrast, the differential image of NEB-GNSs, $DIM_{10/5}$, exhibits an enormous residue, with more than 40 dB contrast compared to the differential image of the ink sample. The images are shown with the same dynamic range (25 dB), but at a 30 dB level difference between NEB-GNSs (maximum at –15 dB) and ink (maximum at –45 dB). These results demonstrate the potential of the proposed contrast agent to enhance the specificity of detecting targeted objects in PA molecular imaging by suppressing any background absorber with a linear PA response.

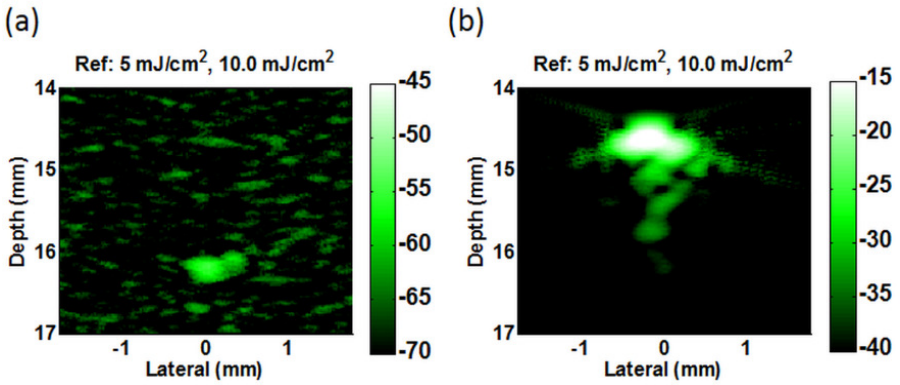

Figure 122. Differential photoacoustic images of ink (a) and NEB-GNSs (b) at a laser fluence of 10 mJ/cm^2. The reference image is at 5 mJ/cm^2. Images are normalized to the maximum of the original images in Fig. 120 (0 dB) and shown with a dynamic range of 25 dB. Note that images are shown at different levels: –70 dB to –45 dB for ink, and –40 dB to –15 dB for NEB-GNSs. The contrast between the two differential images is larger than 40 dB.

To further investigate the nonlinear behavior of NEB-GNSs, primarily determined by the nonlinear expansion of bubbles, various simple functions, such as parabolic, higher order polynomial functions, or exponentials, were used to fit the curve of NEB-GNSs in Fig. 121. Unfortunately, a simple functional form does not capture the behavior of the nonlinear curve. The amplitude obtained by summing all signals within the tube region may not be a valid way to express the behavior of bubble formation and subsequent acoustic generation of a single nanoagent, especially when the phantom is not illuminated homogeneously within the entire tube volume and not all agents are activated at the same time. Also, the characteristics of NEB-GNSs may change at every energy level. Quantification of this nonlinear phenomenon to better understand the relationship between PA amplitude and laser fluence may be feasible using a numerical simulation with a realistic physical model describing this process.

By consecutively sweeping the energy both up and down several times, reproducibility of the non-linearity was demonstrated for NEB-GNSs. However, the amplitude decreases slowly as scan time increases (*i.e.*, degradation toward a linear relation). This is evidence that not all agents are activated at the same time, and they may be slightly degraded on every sweep cycle.

Delivering an ultrasound probe pulse simultaneously, or right after laser-activated bubble generation, enables contrast-enhanced ultrasound imaging as well, in terms of increased backscattered signal and harmonic generation. This new agent and technique can be easily implemented in any integrated ultrasound/PA imaging system. With simultaneous laser/ultrasound probing, targeted contrast-enhanced ultrasound imaging and targeted therapy

with high intensity focused ultrasound (HIFU) can be envisioned for cardiovascular diagnostic and therapeutic (*i.e.*, theranostic) applications, such as blood clot detection and subsequent disruption. However, according to our previous studies,[279,284] the lifetime of the bubbles is about 1~2 µsec, which requires precise timing control to deliver the ultrasound pulse before the bubble collapses. Optimizing the laser irradiation parameters (*e.g.*, pulse duration and laser fluence) and nanoemulsion bead properties (*e.g.*, size and shell material) to create a long-lived bubble is one of the necessary next steps.

7.3.2 Cavitation Threshold Results

After removing the contribution from the tube using a reference signal, the recorded signals clearly exhibited the presence of cavitation. With the same exposure parameters, a small cavitation event can be distinguished in Fig. 123b from no cavitation in Fig 123a. Cavitation always occurred at the lasing time depicted by the red dotted line. A larger cavitation event is shown in Fig. 123c with 10-fold amplitude compared to the small cavitation (note scale change). Normalized spectra for both of these signals are shown in Fig. 123d. The broadband noise characteristics are present in both signals, although the main harmonic is relatively higher for the large cavitation event.

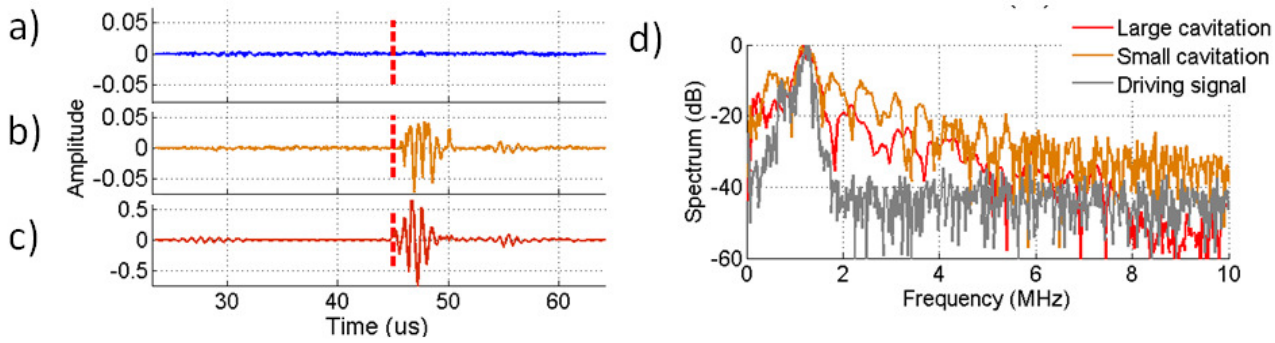

Figure 123. Wideband detection of cavitation events using a PVDF detector. Lasing time is shown with the red dotted line and the ultrasound 10-cycle pulse travels to the focus starting from the blue dotted line time. a-c) Signals after differentiation. a)-b) No cavitation and cavitation (probability 5%) with exposures of F_0 = 0.641 mJ/cm^2, P- = 1.74 MPa. c) Large cavitation (F_0 = 4.7 mJ/cm^2, P- = 1.43 MPa). d) Normalized spectra of differential signals for large (red), small (orange) and spectrum of the driving signal at 1.24 MHz.

Vaporization Probabilities

The resulting cavitation probabilities as a function of US peak negative pressure are shown for the NEB-GNS and purified NEB-GNS samples in Figs. 124a and b. For both samples, cavitation activity was not consistently observed using the 10-cycle ultrasound pulse alone, even at pressures exceeding 8 MPa (below 20% for the raw sample and 2% for the purified one; results not shown). In contrast, a small fluence (0.64 mJ/cm^2) already creates consistent vaporization at

1.5 MPa for the raw sample and at 2.5 MPa for the purified one. Higher fluences decrease the vaporization threshold. Note that for the purified sample, and at such a low concentration, a very high laser fluence of 27.7 mJ/cm^2 is only efficient for vaporization at 0.6 MPa, and that raising the fluence from 9.5 to 27.7 mJ/cm^2 doesn't change the cavitation threshold dramatically. These results show that combining light (transient heating) and short ultrasound pulse (pressure) exposures is much more efficient than using each of them separately.

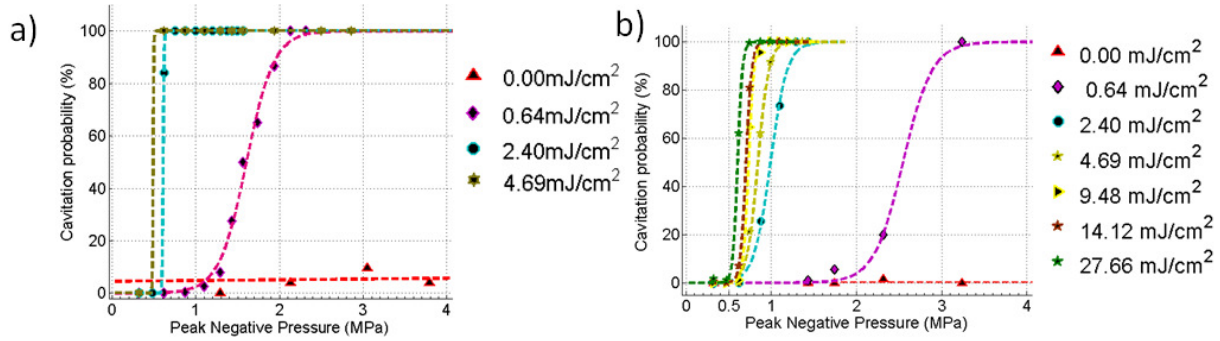

Figure 124. Photoacoustic cavitation probabilities of emulsion sample #1 before (a) and after (b) purification.

7.3.3 Vaporization Results and Comparison with a GNS Sample.

A summary of the vaporization threshold (50% probability) of the GNS-NEB samples (raw and purified) and the GNS 12 nm sample is presented in Fig. 125. For a peak negative pressure of 1.0 MPa, the fluence threshold of the GNS is reduced by a factor of 12 for the raw sample and by a factor of 6 for the filtered sample.

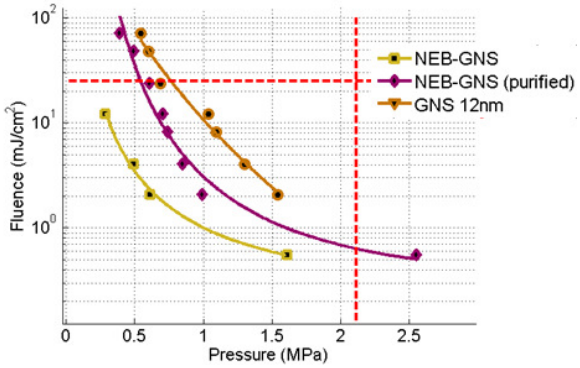

Figure 125. Summary of vaporization thresholds. Each point in the fluence / peak negative pressure plane corresponds to a 50% vaporization probability. NEB-GNS, NEB-GNS purified and GNS. The red dotted lines indicate: the mechanical index (MI) FDA limitation of 1.9 for ultrasound imaging (vertical) and the permissible optical fluence exposure of 25 mJ/cm^2 (horizontal).

7.3.4 Sono-photoacoustic Signal Enhancement

For imaging purposes, the amplitude emitted by the bubbles will determine detection sensitivity. In addition, the non-linear nature of sono-photoacoustic signal enhancement may lead to a

highly specific agent. To explore this hypothesis, the signals presenting cavitation within each data set were isolated. Then, the median value and the standard deviation of the maximum amplitude in time of these signals were calculated.

In Fig. 126, the sono-photoacoustic signal clearly evolves in a non-linear manner as a function of acoustic peak negative pressure for both the raw sample and the purified one. Note that amplitudes are higher in Fig. 126a than in Fig. 126b. The bubble signatures had in fact similar amplitudes at a fixed pressure. While the cavitation threshold decreases with laser fluence, the amplitude of cavitation events does not change with pressure when the fluence is above a threshold (above 2.4 mJ/cm^2 for both samples). This result suggests the potential for deep sono-photoacoustic imaging.

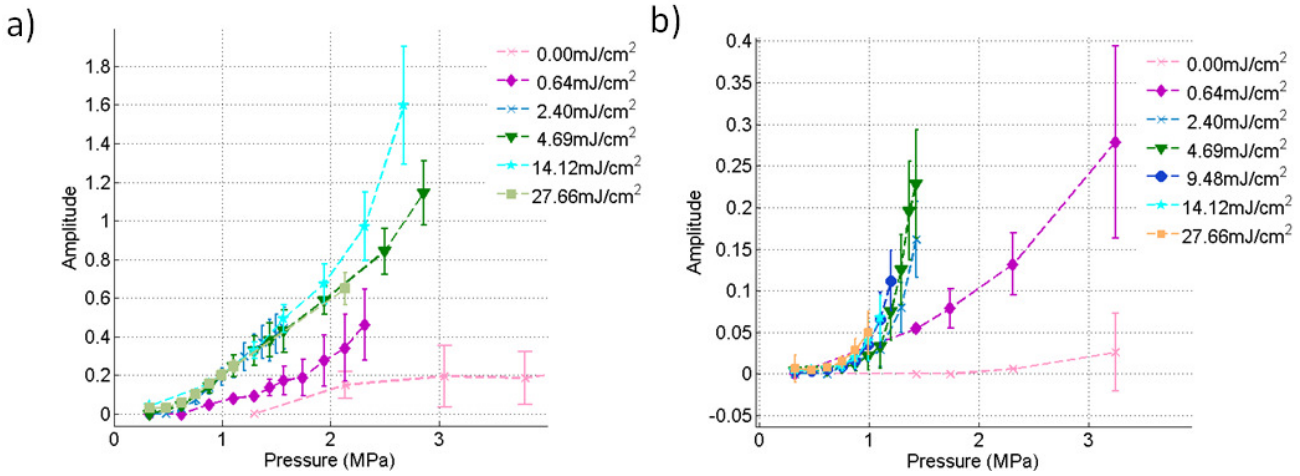

Figure 126. Amplitude of sono-photoacoustic signals as a function of acoustic pressure at different fluences. a) NEB-GNS sample. b) NEB-GNS purified sample.

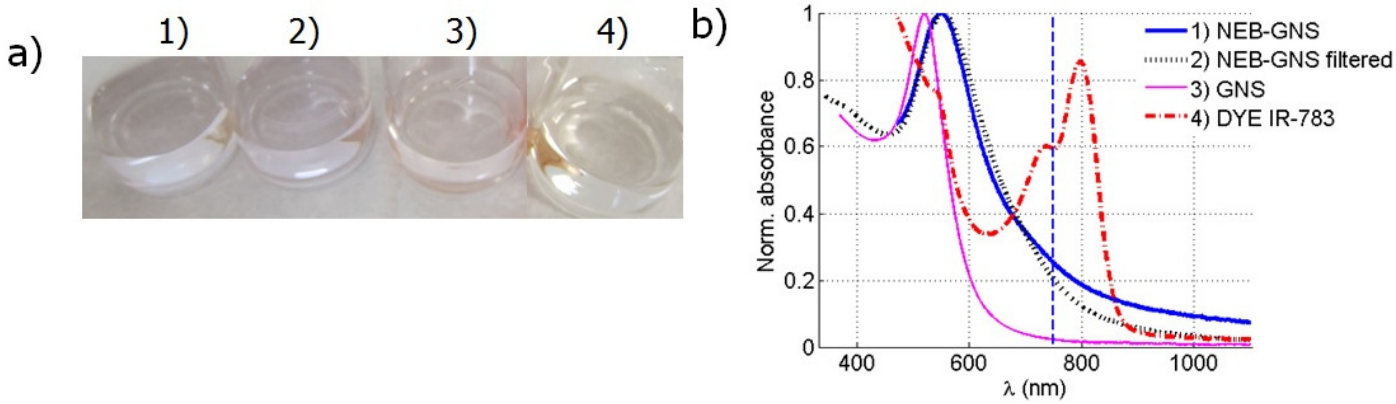

Figure 127. Different samples and their absorbance. a) Photograph of different samples at the dilution used in these experiments. b) Absorbance of the samples. 1) NEB-GNS (thick blue line); 2) NEB-GNS filtered (black dotted line); 3) GNS (12 nm diameter, thin pink line); 4) Dye IR-783 (red dash dotted line). All samples were diluted so their extinctions at 750 nm are 0.05 cm^{-1}, except for the GNS solution, which has an extinction of 0.009 cm^{-1} with same amount of GNS as in the NEB-GNS. The vertical blue dotted line indicates the operating wavelength of this study (750 nm).

7.3.5 Using NEB-GNS to Develop a New Imaging Modality.

The polyacrylamide gel phantom was synthesized with some nanoparticles or dye in the mixture following the thorough protocol described in[288]. A linear array (L7-4, 128 elements, ATL, Bothell, WA, USA) was controlled by a programmable ultrasound scanner (Vantage 128, Verasonics, Redmond, WA, USA) operating in a custom interleaved PA – US sequence. The maximum voltage of 96 V was used to maximize the pressure amplitude. The imaging sequence consisted of an US image obtained by ultrafast imaging [289] with coherent compounding [290] of 6 plane waves tilted at different angles (-5° to 5°, not depicted in Fig. 128). Then, the sono-photoacoustic acquisition (see Fig.128a) consisted of:

- *PA:* frame using laser only excitation (optional for SPA)
- US^+ : US frame with N cycles emission (3 MHz) and positive polarity with no laser firing
- US^- : US frame with N cycles emission (3 MHz) and negative polarity (opposite amplitude) with no laser firing
- ($PA + US^+$) : Laser + US image with N cycles US emission (3 MHz) and positive polarity
- ($PA + US^-$) : Laser + US image with N cycles US emission (3 MHz) and negative polarity

A lipstick hydrophone (Aperture: 200 um, SEA, Soquel, CA, USA) was used to validate the timing sequence, *i.e.* lasing time relative to acoustic propagation. The combination of pulsed light and US is depicted in Fig. 128b. For the (PA $+ US^{\pm}$) acquisitions, light emissions are performed when the US pulse reaches a desired depth z_2.

The emulsion nanodroplets are vaporized or cavitated at the lasing time and at all locations of peak negative pressure [279] if combinations of acoustic pressure and laser fluence pulses are used together at diagnostic exposures. Inverting the polarities will have a complementary effect on the locations of the vaporization sites. SPA images are formed by the following coherent combination (7.3):

$$SPA = \left\{\left(PA + US^{+}\right) - US^{+}\right\} - \left\{\left(PA + US^{-}\right) - US^{-}\right\} \qquad (7.3)$$

The role of both subtractions $\left(PA + US^{\pm}\right) - US^{\pm}$ is to cancel the US backscatter from tissue and isolate signals specific to the vaporization of the contrast agent. However, a linear PA signal (*e.g.*, signal from the optical absorbers without any phase conversion) remains in both terms.

The subtraction of both terms ensures that the linear PA signal is cancelled while the combination of both vaporization signals are complementary since the location of peak negative pressures are offset by half of the US wavelength. A step by step demonstration of this approach is given in Section 3.1. Note that the coherent combination (7.3) can be equivalently performed on RF signals before or after beam forming, as it is a linear operation. In both cases, the beam forming algorithm must use one-way delays since acoustic sources of interest are formed at the lasing time.

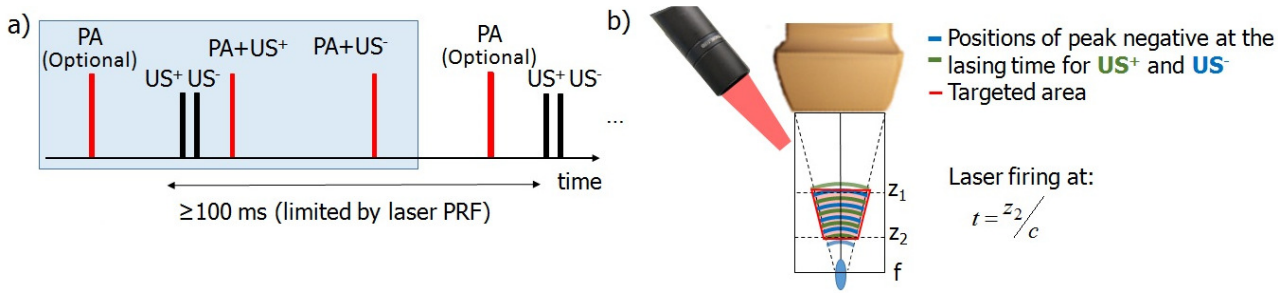

Figure 128. Sono-photoacoustic imaging setup using a Verasonics scanner and a diagnostic ultrasound probe in wide beam mode. a) Timing diagram. Note that PA firings can be removed in a real-time sequence since SPA does not use images formed with the laser excitation alone. b) Imaging setup: the laser pulse emission occurs when US reaches a depth of z2 resulting in a targeted area between z1 and z2 and delimited by the path of the US beam (indicated in red). A focused beam is used in the region before the focus to enhance the pressure amplitude while keeping a wide area under consideration. The blue and green lines indicate respectively where the positive and negative US peaks are at the lasing time.

It is possible to use this mode with plane wave insonification. However, to maximize the penetration of the technique, which is limited by the in-depth decay of laser fluence, the pressure amplitude resulting from a plane wave might not be optimal, at least with a conventional probe connected to a regular power supply. As shown in Fig. 128b, a wide-beam technique is introduced using a focused beam but the laser pulse intersects the US wave in a region prior to the transducer focus.

.

Transmission and reception bandwidth

US signals were sent at 3 MHz for SPA acquisitions. This frequency is at the edge of the bandwidth of the L7-4 array. The RF data were received within the bandwidth of [4 – 7] MHz with a high pass filter at a cutoff frequency of 3.5 MHz and implemented with Verasonics software. This made it possible to reduce linear US components scattered by bubbles over multiple cycles that can degrade axial resolution.

SPA imaging in solutions of NEB-GNS and control samples

The four suspensions prepared according to section II-B were imaged using the SPA algorithm described above. An 8-cycle US excitation at 3 MHz and focused at 50 mm synchronized with

lasing was used. In all cases, the fluence was set to 3.65 mJ/cm^2 and the pressure measured at 35 mm depth was 1.9 MPa (wide-beam focusing to depth of z= 50 mm). Figure 129 demonstrates all radio frequency (RF) signals needed to form an SPA image and recorded for an NEB GNS solution at one of the linear array channels. Figure 129a illustrates a very small PA signal generated inside the pipet with NEB GNS solution. The spike around 35 μs corresponds to the PA signal created at the front surface of the pipet due to small absorption of laser radiation inside the wall and/or emulsion beads attracted to the wall. To avoid the influence of the wall on the main signal from the emulsion, the pipet had a diameter bigger than the region of light and sound interaction (~10 mm (laterally) x 4 mm (axially)), which was centered at the middle of the pipet. In any event, even this wall signal was two orders of magnitude smaller than US and resulting SPA signals. Thus, we conclude that the linear PA response of NEB GNS emulsion (*e.g.*, without phase transition) was not distinguishable from noise at the current level of emulsion concentration.

The RF signals recorded for combined US and laser excitations but for US "+" and "-" polarities are correspondingly shown in Fig. 129b and c. Strong reflections from pipet walls are observed (the signals arriving at ~ 32μs and 47μs), but a signal induced by simultaneous light and sound excitation is clearly seen between the pipet wall signals. This indicates that the phase transition in the emulsion droplet produces a large cavitation/vaporization signal. It is around 3 orders of magnitude bigger than the linear PA signal (*e.g.*, without phase transition) produced at the same location with laser excitation alone, which was hardly recognizable from noise in Fig. 129a.

The coherent subtraction of the same polarity US signals, but with (PA+US$^+$) and without (US$^{+)}$ laser, gives the signals shown in Fig. 129d-e. This procedure removes the linear US signal, which is not specific to the emulsion. Here, for example, strong US wall signals are almost completely suppressed. The SPA signal illustrated in Fig. 129f is calculated to retrieve a NL sono-photoacoustic signal composed of vaporization and cavitation activity signatures occurring specifically at the nanoemulsion bead location.

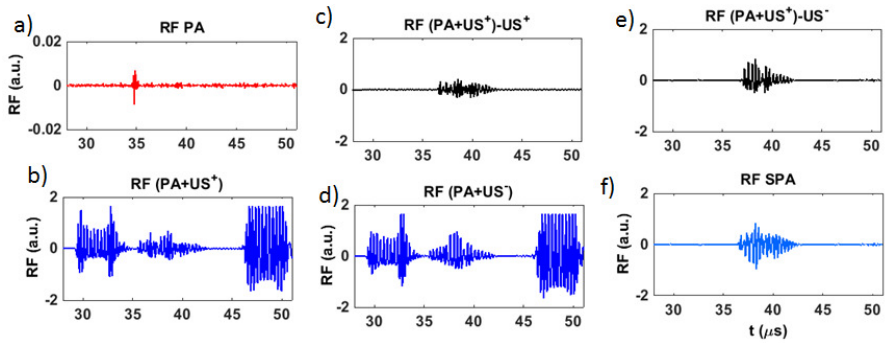

Figure 129. RF signals from one of the array channels for NEB-GNS solution. a) PA signal; b) (PA+US$^+$) signal; c) Subtraction of b) with US$^+$ signal, d) (PA+US$^-$) signal, e) Subtraction of c) with US$^-$ signal, f) SPA signal. An 8-cycle US excitation at 3 MHz is used and focused to 50 mm synchronized with lasing. In all cases, the fluence is 3.65 mJ/cm^2 and the pressure measured at 35 mm depth is 1.9 MPa.

This same procedure was applied to all four samples. A single SPA image of the NEB-GNS solution superimposed on the US B-scan is presented in Fig. 130a. The suspension concentration was estimated to be 12.6 pM. For the NEB-GNS filtered sample shown in Fig. 130b, signal enhancement can be obtained at the same exposure but not with a probability of 1 and within a smaller area. This is consistent with our previous results, which shows that both the vaporization threshold and signal enhancement depend on the size of the droplets. The reference sample, dye and GNS (Figs. 130c and d, correspondingly) do not show any signal enhancement among the 28 frames acquired for the current values of laser fluence and US excitation pressure. Hence, for NEB-GNS, signal enhancement of 35 dB appears when the cavitation threshold is reached, which could be very useful for real-time detection of low nanoagent concentrations.

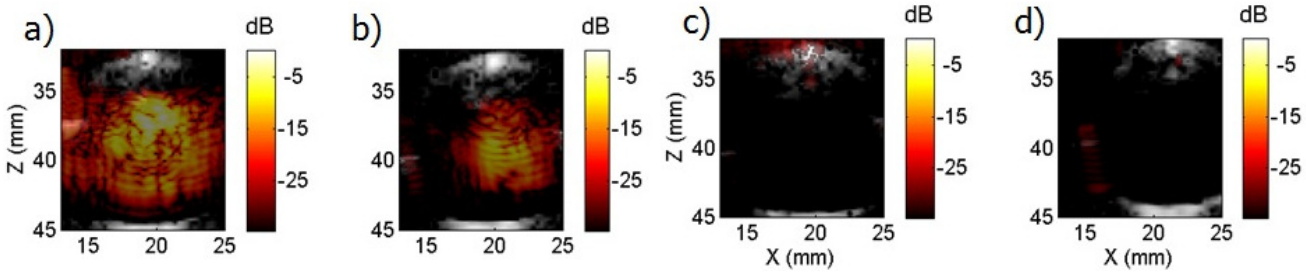

Figure 130. Sono-photoacoustic imaging of different absorbing solutions at ultra-low concentrations. a) NEB-GNS; b) NEB-GNS filtered; c) Molecular dye IR-783 nm; d) GNS-12 nm with a matching amount of gold particles as in NEB-GNS.

Note here, that SPA imaging can retrieve signals from the inside of a large homogeneous absorbing volume even when a band-limited array ([4 – 7] MHz) is used. The bubbles formed induce a highly heterogeneous PA source distribution with large fluctuations in thermal expansion as well as heterogeneous acoustic properties, producing a speckle image. In

contrast, a linear PA image would lead to signal only at the bottom/top of the pipette and at much lower amplitude given the dilution of the samples.

SPA imaging of NEB-GNS in polyacrylamide phantom

A PA signal can be seen at 33 µs in Fig. 131a, which summarizes results for the polyacrylamide gel infused with NEB-GNS. It comes from an acoustic absorber plate (blue color) that also absorbs light and generates a linear PA signal. No linear PA signal from the NEB-GNS was measured above the noise floor.

The combination of light and sound for both US polarities using 8-cycle emissions at 3 MHz focused at 60 mm can be observed in Figs. 131b-c. The laser fluence was 5.2 mJ/cm^2 and the acoustic peak negative pressure measured at z =3 5 mm was 1.6 MPa (wide-beam focusing at 60 mm). The RF signals in Figs. 131b and c include the PA signal at 33 µs, but it is obscured by the US backscatter. Subtraction of the same polarity US signals, but obtained with laser, (PA+US$^+$), or without the laser, US$^+$, gives the signal shown in Fig. 131d. It shows a difference in the response of the emulsion created by adding the laser pulse to the 8-cycle, 3MHz US signal. When the response of the emulsion is linear, this differential signal should be equal to the PA one illustrated in Fig. 131a. However, combining laser and US creates a phase transition in the emulsion beads resulting in a nonlinear contribution formed by bubble thermal expansion and nonlinear scattering of the probe 8-cycle US signal by the bubbles. Figure 131e shows the residual signal *(PA+US$^-$)- US$^-$*, similar to that illustrated in Fig. 131d, but obtained with the *US$^-$* excitation, *i.e.* with the signal inverted in polarity compared to US$^+$. Since the phase transition in the emulsion occurs at positions with maximum negative pressure (corresponding to the 8 negative peaks of the US excitation), bubbles will be formed at different locations compared to the one obtained with the US$^+$ excitation. Note that in both Figs. 131d and e the linear PA signal around 33 µsec is preserved. The final SPA signal in Fig. 131f is obtained by subtracting the signals shown in Figs. 131d and 131e. This suppresses all linear PA and US background signals not related to cavitation activity of the nanoemulsion. Figure 132 presents images summarizing these results on the phantom. Figure 132a shows a conventional US image; it was obtained with the same linear array, but used the whole transducer bandwidth in conventional imaging mode. The inclusion is seen as a black rectangle (see Fig. 132a).

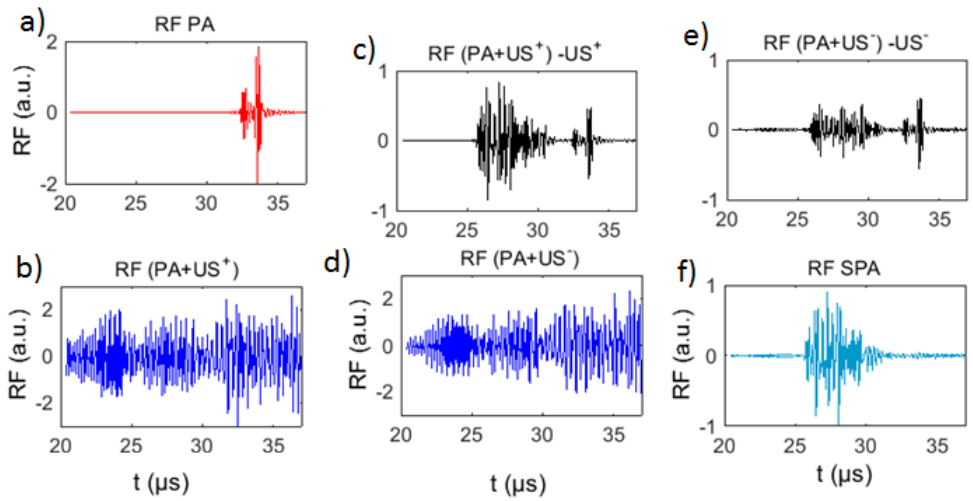

Figure 131. RF signals with NEB-GNS polyacrylamide inclusion. RF signals from one of the array channels for the phantom with a NEB-GNS polyacrylamide inclusion located inside an agarose gel. a) PA signal; b) (PA+US$^+$) signal; c) (PA+US$^-$) signal, d) Subtraction of b) with US$^+$ signal, e) Subtraction of c) with US$^-$ signal, f) SPA signal. An 8-cycle US excitation at 3 MHz and focused to 60 mm was synchronized with lasing. The acoustic pressure measured at 35 mm is 1.6 MPa, the laser fluence is 5.2 mJ/cm^2.

The surrounding medium was an agarose phantom with US scatterers providing speckles. The bright line situated at the bottom of the gel in the right corner corresponds to a blue acoustic absorber plate (AptFlex F28, Precision Acoustics, Dorchester, UK) placed there to reduce US reflections from the bottom of the container that could create reverberation throughout the container. The SPA image corresponds to a signal coming from the inclusion containing NEB-GNS (see Fig. 132c). This imaging sequence can suppress linear PA and US signals to retrieve the NL sono-photoacoustic signal composed of vaporization and cavitation activity signatures occurring specifically at the nanoemulsion bead location. In Fig. 132d, the SPA image (hot color bar) is overlaid onto the US image obtained in Fig. 132a.

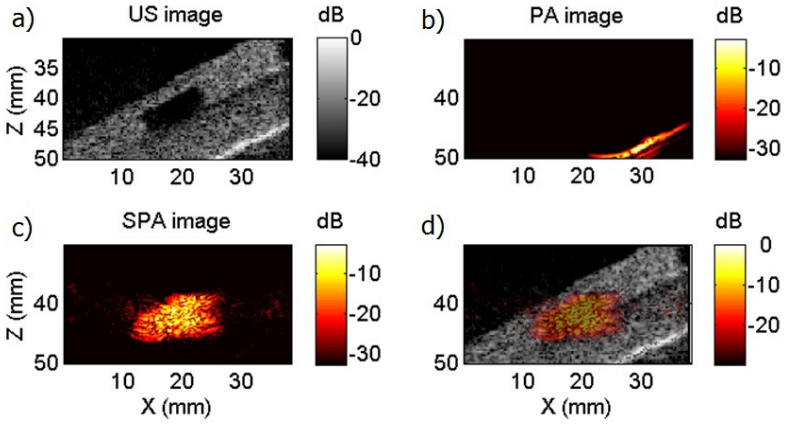

Figure 132. SPA imaging of a NEB-GNS polyacrylamide inclusion located inside an agarose gel. a) Ultrasound image, b) PA image, c) SPA image, d) SPA image overlaid on the US image. An 8-cycle US excitation at 3 MHz and focused to 60 mm was synchronized with lasing.

Comparison of SPA images in PA phantom for NEB-GNS with GNS and dye samples

Images for the agarose phantom containing 4 polyacrylamide inclusions are shown in Figs. 133. In all cases, the linear PA signal coming from the absorber was cancelled except a small residual visible in Fig. 133b that could correspond to a change in optical scattering due to varying bubble clouds between the two (PA + US) images or simply pulse energy fluctuation. However, the SPA image amplitude is generally much greater than the residuals and can clearly be identified without signal averaging. The average (over the inclusion) contrast between the inclusion and the gel in the image (in dB) were 21.0, 8.3, -7.3 and -19 dB for the four samples, respectively. The contrast to noise ratio (CNR) for the two phantoms with measureable SPA contrast were 26.8 and 18.4 dB respectively, enabling clear identification of the agent.

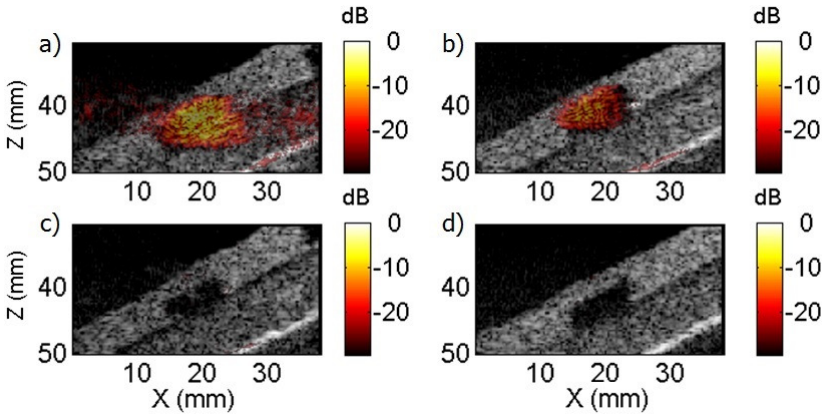

Figure 133. SPA imaging of different agents embedded into polyacrylamide inclusion located inside an agarose gel. a) NEB-GNS; b) NEB-GNS filtered; c) GNS-12 nm with the same amount of gold as NEB-GNS; d) Molecular dye IR-783 nm. The reference magnitude (0 dB) corresponds to the maximum of the SPA image. The laser fluence was 5.2mJ/cm^2 and the acoustic peak negative pressure measured at z=35 mm was 1.6 MPa (wide-beam focusing at 60 mm).

High resolution SPA imaging in solutions of NEB-GNS with a single-cycle US wave

Multiple cycle US pulses were used to cover a large area at once. However, as shown this section and in previous work [291], a laser-US nucleated bubble may keep oscillating over the remaining US pulse. The presence of an US field creates a bubble oscillation preventing re-condensation. It can result in degraded axial resolution since the bubbles backscatter until they condense or collapse. As an alternative, a single-cycle US pulse can be used, as shown in Fig. 134. In this example, a plane wave of 1.03 MPa (measured at a 35 mm depth) was emitted by the array and the laser fluence was set to 3.3 mJ/cm^2. Three frames recorded at different times in a continuous imaging sequence for the same conditions are displayed. The SPA signal is a horizontal stripe and no signal comes from either side. The position of the SPA signal is very

stable in time and depends only on the timing of the laser pulses relative to propagation of the plane wave. It shows that the SPA method can fully control the cavitation location for applications such as drug delivery, molecular imaging, with the potential for minimal impact to vital healthy surrounding tissues. If multiple areas are to be investigated or treated, the delay between laser and US emissions can be scanned and multiple images can be combined

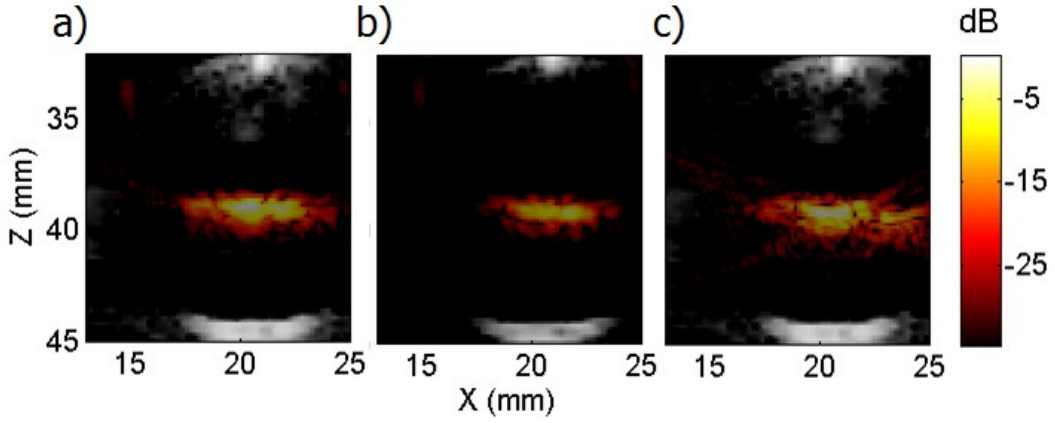

Figure 134. SPA obtained for NEB_GNS solution using a single-cycle US excitation. Panels a)-c) correspond to the detection at three different times in a continuous imaging sequence for exactly the same configuration. US plane wave of 1.03 MPa (measured at a 35 mm depth) is used for the excitation together with the laser fluence of 3.3 mJ/cm^2.

7.4 Discussion

In this chapter, we have demonstrated the potential of a novel contrast agent composed of nanoemulsion beads surrounded by gold nanospheres using simultaneous light and sound excitation. A robust emulsion characterization platform, which performs a 2D parameter scan (pressure and light) for cavitation threshold determination, was developed. This platform is expected to be particularly beneficial for future testing and comparison of new nanoemulsion contrast agent formulations.

The exposure parameters required to achieve PA cavitation were studied extensively at a picomolar concentration of contrast agent (2 - 6 x 10^{10} beads/mL). Ultrasound pressures were varied from 0.1 MPa - 9 MPa at focal peak negative pressures and laser fluences varied from 0.4-27.6 mJ/cm^2. As laser fluence increased, the cavitation threshold (in terms of US peak negative pressure) decreased to values far below the FDA mechanical index (MI < 1.9) limitation.

From Fig. 124, it is clear that the cavitation probability for ultrasound exposure alone remained low for pressures up to 4 MPa (<10%). The pressure for ultrasound exposure alone was

scanned up to 9 MPa (not shown in Fig. 124) yet we did not reach a 50% probability of cavitation (dashed pink line). Previous work with similar nanoemulsions, in terms of boiling points and sizes, explored acoustic droplet vaporization thresholds of dodecafluoropentane (DDFP, boiling point in bulk = 29°C) and of 2H, 3H-perfluoropentane (H-PFP, boiling point in bulk = 55°C) albumin-coated droplets with a mean diameter of approximately 260 nm, and 630 nm, respectively[292]. These nanoemulsions were included in albumin-acrylamide gel phantoms and sonicated with 10 cycle HIFU pulses (f = 2 MHz, pulse repetition = 5 s), similar to our setup (1.24 MHz). For DDFP, an ultrasound peak negative pressure threshold was found at 8.50 MPa. In the case of H-PFP, the pressure was increased up to 8.7 MPa without evidence of vaporization. Our results are consistent with this study[292]. When exposed to 5 MHz, micron-scale perfluoropentane droplets vaporization thresholds decreases with droplet diameter [293] as surface tension decreases. As the purification process removes particles larger than 600 nm, the observed increase of vaporization threshold is consistent with previous studies. Additionally, many studies reported a decreasing vaporization pressure as a function of increasing US frequency [294,295]. As mentioned earlier, heat seems to be necessary to overcome surface tension stabilization. Our study shows that this heat can be delivered in a controlled and targeted way by plasmonic light absorption.

Preliminary imaging experiments (not shown here) suggest that particles accumulated at the bottom of the sample. Single nanoparticles are mostly subject to diffusion and gravity can usually be neglected. In contrast, gravity effects can be dominant for large oil droplets (1.7 density) and is amplified by clustered gold. We took advantage of these effects to purify our sample. A centrifugation technique could have been used, but it was not preferred because it could increase the probability of aggregation of beads at the bottom of the container. Similarly, extrusion through membrane filters could lead to more consistent size distributions, but it could also generate new distributions of beads since extrusion can actually help create droplets. It could also result in the loss of products trapped on the membrane surface.

Previous high speed photomicrography studies on the same emulsion type showed the short lifetimes (~1.2 µs) of the vapor bubbles under light exposure only [278], suggesting that the perfluorocarbon beads also go back to the liquid state when the ultrasound field vanishes. The fate of the gold nanoparticles during bubble expansion and after condensation has not been studied yet. Nevertheless, additional experiments have also shown a strong consistency in the cavitation activity after several thousand shots, indicating that the gold particles remain

somehow coupled to the beads. Observing a single emulsion bead flowing into a small channel and exposed to light and sound could lead to better characterization.

Photoacoustic cavitation is surprisingly induced in the GNS sample composed of small particles (15 nm diameter) at a wavelength (750 nm) where optical absorption is very weak. Previous work has only studied photoacoustic cavitation of large diameter GNS (82 nm diameter) at the plasmonic resonance wavelength (532 nm)[271]. Here, the mean distance between GNS is 72 µm given the size and concentration, so coupling effects should not play a role in effective vapor bubble creation unless there is particle aggregation due to acoustic streaming, or other pressure-induced effects. Further modeling inspired by previous work [296,297] could focus on explaining this behavior. Compared with the emulsion beads, the liquid volume to vaporize is not the same and the total energies necessary to achieve vaporization might not be comparable.

As the probability of cavitation increases (see Fig. 126), we have shown that the amplitude of the resultant acoustic signal does not increase with laser fluence for fluences higher than 2.4 mJ/cm^2. This means that when the phase transition occurs, a higher laser fluence does not affect the vaporization signals as much as the US pressure does. The laser pulse induces heat within a short 30-40 ns time window, enabling the phase transition. Then, it appears that the bubble size is more influenced by the pressure field, which also controls the amplitude of bubble-generated acoustic waves. As extinction by soft tissue limits light penetration, a scenario of low laser fluence with a maximum permissible pressure would be ideal for contrast enhancement. Depending on the tissue types between the light source and the region of interest, such light penetration can be achieved from one to a few centimeters deep into tissue. A Monte Carlo simulation [296] of light transport was performed through skin (thickness ΔZ = 1.12 mm, absorption coefficient μ_a = 0.49 cm^{-1}, scattering coefficient μ_s = 82.6 cm^{-1}, anisotropy g = 0.75), fat (ΔZ = 2 mm, μ_a = 0.1 cm^{-1}, μ_s = 115 cm^{-1}, g = 0.9) and muscle (ΔZ = 30 mm, μ_a = 0.09 cm^{-1}, μ_s = 216 cm^{-1}, g = 0.9). Using a Gaussian beam (width: 2 cm, λ = 750 nm, maximum fluence: 25 mJ/cm^2), fluences of 2 mJ/cm^2 and 0.6 mJ/cm^2 were reached at depths of 1.6 and 2.0 cm, respectively. Future studies could explore the penetration limits for different imaging applications.

Finally, due to the clustering of gold nanopsheres on an emulsion bead, and to the resulting large signal from the bubble, these measurements succeeded even at low concentration in a

regime where single shot linear PA imaging fails (0.25 cm^{-1}). The nanoemulsion structure and synthesis can be further improved to reach higher efficiency, for example using another perfluorocarbon oil with a lower boiling point [293,298]. Based on this work, a real-time imaging system could achieve sono-photoacoustic imaging of NEB-GNS at depths exceeding several centimeters and at ultra-low concentration levels. This imaging approach could rely on single cycle or multiple cycles US excitations, depending on the desired imaging range. However, to use this technique for *in vivo* imaging, scattered ultrasound and photoacoustic signals must both be cancelled to retrieve the specificity of vaporization signals and perform accurate background suppression. A way to implement sono-photoacoustics in a real-time imaging sequence was also presented and discussed. Moreover, inertial cavitation produced by this nanoemulsion already has been exploited for *in vitro* sonothrombolysis[278]. Further work can rely on this study to optimize the delivery of this treatment and its monitoring.

7.5 Conclusion

This work showed the potential of gold-coated nanoemulsion beads excited simultaneously by pulsed laser and ultrasound. A fully automated setup for dual exposure parameter scanning was designed for quantitative assessment of vaporization thresholds of the NEB-GNS. A phase transition of the nanoemulsion bead occurred at much lower peak negative pressure when laser fluence increased. We demonstrated that NEB-GNS vaporization could be achieved at a reduced exposure compared to the vaporization of water surrounding single GNS. The high amplitude of vaporization signals produced by simultaneous pulsed light and ultrasound exposure could be used to design an imaging modality allowing both high specificity and sensitivity of nano-contrast agent detection. The results could also be applied to drug delivery using nanodroplets with high encapsulation energy and to localized or targeted therapies using nanoagents.

CHAPTER 8

Conclusion

8.1 Summary

The work presented in this thesis attempts to characterize the ultrasound pressure fields from clinical devices and understand the fields' interactions with contrast agents. For the characterization of pressure fields from clinical devices (therapeutic regimens using high pressure levels), tools such as high speed imaging, fiber optic hydrophones and wave propagation modeling were adapted to characterize these pressure fields, their bubble dynamics and their interaction. In order to characterize contrast agents or microbubbles, a similar approach to the problem was implemented. Tools such as laser Doppler vibrometry, hydrophones and finite element modeling were adapted to characterize the low pressure acoustic flow cytometer. Broadly speaking, an off-the shelf tool initially used for cell interrogation was modified in order to characterize microbubbles, and together with these tools the pressure fields inside the system and the bubble dynamics was determined.

As mentioned in the introduction of Chapter 2, bubbles can be induced by ultrasound, or they could be exogenously injected in the body, and ultimately, there are many questions about how bubbles respond to different pressure fields, let alone questions about what the acoustic pressure field is for each clinical device available. Each chapter partially addresses this question: In Chapter 3, a model-experiment approach was developed in order to characterize the acoustic field of a clinical shockwave device. For electromagnetic sources that generate single pulses, a method to measure the rise time accurately is introduced in this chapter, allowing proper characterization of the positive pulse and comparison with other sources available in the field. In addition, a powerful model is validated against the data, allowing it to be used in the future for *in vivo* field prediction, where measurement of the field is not possible. After fully characterizing, modeling and understanding the device, *in vivo* and *in vitro* application studies were presented. The importance and significance of independent characterization of medical devices is demonstrated in Chapter 3. More importantly, by showing the large differences between the regimes measured within the same device (non-linear *vs*. linear regimes), it was concluded that labeling devices such as "shockwave therapy" (SWT) devices provides conflicting information for the field, where even within the same device, varying settings could produce strong nonlinear therapeutic pulse *vs*. a very low level pressure pulse,

whereas the term shockwave therapy, for example, physically requires shockwaves. The American Institute of Ultrasound in Medicine (AIUM) has, unsuccessfully, been trying to encourage research groups and hospitals around the world to properly characterize their therapeutic ultrasound medical devices prior to use in clinical studies for decades, so that the medical success can be accurately attributed to a specific pressure field, and so that shockwave therapy research can potentially advance in a unified direction. I suggest that future experiments follow this thorough characterization approach for clinical devices in order to perform shockwave therapy studies on animal models. One potential interesting shock wave therapy study in would focus on the investigation of the evident angiogenic and osteogenic capabilities of transient-nonlinear pressure pulses emitted from these devices in a more related animal model (prior studies have been done in rat models, showing some success, but a more clinically relevant animal model is needed).

In Chapter 4, the acoustic field and bubble dynamics of a laser-induced clinical dental device used in periodontics and orthodontics for the removal of biofilms is performed. The device settings were fully characterized and understanding of the influence of PRF, pulse energy, pulse duration and position dependence was attained. The bubble collapses from this microwave-radiating laser pulse-based device were shown to agree with a heat-dampened collapse, which was validated with a heat-transfer model that agreed with the high speed measurements.

The remainder of the thesis focused on characterizing the interaction between ultrasound and contrast agents. This was done in order to characterize the contrast agent's specific response to ultrasound. As it is implied, first, the ultrasound field inside the system had to be characterized. Whether they were ultrasound or photoacoustic contrast agents (MBs or emulsions, respectively), the methods and tools implemented here slightly varied, but the methods, time series analysis and data analysis applied to characterization of both types of contrast agent were similar.

Chapter 5 introduced a powerful new tool; *viz.*, a flow cytometer modified in such a way as to allow MHz-frequency insonification of materials flowing through the region of laser interrogation. I then showed how the first iteration of the system was capable of characterizing thin (lipid, Definity) and thick (lysozyme protein) microbubble shells. System improvements to the detectors were also presented (fluorescence detection and position sensitive detectors implementation, and comparing the sizing capabilities to gold standards such as coulter).

For Chapter 6, two FEM methods were developed and validated. These models have already provided increasing value to our group: 1) increased general knowledge of FEM validation, optimization and testing. Our group has already developed similar models to allow researchers in other projects to predict pressures in their systems. 2) It provides us with a platform to optimize current systems. For the flow cytometer systems, the models are particularly useful to predict the pressure in new applications such as focused sources for radiation force studies.

In Chapter 6, two broadly similar techniques were developed to characterize the pressure inside the acoustic flow cytometer's channel. Determining the pressure allowed faster characterization of MBs. The model-experiment methods determined the steady state and transient forcing functions to drive MBs, and both validations were rigorously performed and allowed us to flow MBs at one-thousand bubbles per second rates, and obtain their individual mechanical properties in less than 1 minute per bubble. In the last sections of Chapter 6, the calibrated tool was used to detect differences in loading between two very similar protein shelled MBs (dye-loaded *vs*. unloaded Optison) and between two slightly different kinds of lipid-shelled MBs. Differences in the harmonic oscillations and shell properties were observed. The acoustic flow cytometer thus has the sensitivity to detect relatively slight changes in the shell of MBs as revealed by their effect on forced microbubble dynamics.

8.2 Research Vision and Proposed Future Work

Future work related to this thesis is presented. As briefly mentioned in Chapter 6.5, using radiation force studies to separate MB's attached to cells *vs*. cells alone and thereby effect sorting is the next goal. The position detectors already in place will be used to sense changes in position between one group and the other as the ultrasound pulses the particles in flow. To accomplish this goal, the position sensitive detectors must be calibrated to convert light

scattering changes in position to distance using calibration beads. Then, the detectors can be used to determine changes on position of the coupled system due to acoustic radiation force. Hopefully, this tool can quickly isolate MB-cell bound complexes from regular cells. Several applications such as rare circulating cancer cell detection are drivers of this potential future direction. In addition to characterizing the position changes, the acoustic cytometer is capable of estimating binding efficiency and binding rates of cell-MB systems.

I suggest that future experiments compare loaded *vs*. unloaded MBs, similar to Chapter 6.4, as follows: Four different model compounds of Optison UCA's with different molecular weights should be used. The goals of the experiment would be to determine shell properties from MBS with different degrees of loading. Based on current results in Chapter 6.4 and recent literature (see section 6.4), it is hypothesized that relative differences in shell properties and dynamic properties of MBs with different degrees of loading to the shell.

Currently, while a MB is interrogated in the flow cytometer inside the laser region, there is not enough time to observe bubble dissolution, size changes, or fatigue effects from MB oscillations. One potential future improvement or modification of the system could be to incorporate several lasers so that the R(t) behavior can be tracked as a function of multiple acoustic pulses to observe, for example, lipid shedding (quantified by fluorescence loss as a function of time) or to quantify time dependent payload delivery in loaded MBs.

In Chapter 7, emulsion droplets were characterized and a vaporization threshold of the droplet *via* dual sound and light activation was determined. An imaging approach was introduced that took advantage of the acoustic emissions and photoacoustic emissions of dual contrast agents (reducing the linear component and taking advantage of the nonlinear emissions) that showed significant improvement over current photoacoustic contrast agents or regular MBs alone. A similar implementation of Chapter 7 inside the acoustic flow cytometer is also part of a potential future experiment, where the characterization time would hopefully be shortened (currently a parameter scan can take 3 hours per sample). I suggest a future study that plans to investigate several energy settings for the dual laser-ultrasound emulsion activation. The acoustic flow cytometer with an addition of an activation laser could then determine not only the size, but also the dynamics (and lifetime) of individual vaporized droplets.

Finally, there are several potential improvements to the acoustic flow cytometer system that could lead to a more industry-relevant specialty instrument and to a wider, clinical translation: The first one is to design a custom flow cell with wider channel so that a hydrophone with enough sensitivity can be introduced. This will allow routine calibration by inserting a hydrophone without depending on a model. The second potential improvement is to collaborate with an imaging expert to use typical imaging sequences (pulse inversion, amplitude modulation) used in commercial ultrasound scanners to excite ultrasound contrast agents, and not long bursts. This will allow potential opportunities for the study and development of new imaging sequences to take advantage of the dynamic properties of newly developed contrast agents. The current system is limited to the flow channel, where reflections of the pulse are inevitable, therefore a new setup could be designed where reflections can be dissipated or mitigated. Submerging the current system and use of a thin capillary as opposed to a flow cell could be possibilities to create such system. The final improvement to the system is the implementation of pseudo-real-time MB shell property fitting. A faster implementation of the code (using C++, for example) can be embedded in the current electronics of the cytometer to perform pseudo-real-time MB characterization.

It is concluded that the acoustic flow cytometer has a potential to revolutionize the MB characterization research field, by providing size distribution data, characterizing shell properties and dynamic responses of MBs at very high throughputs. In addition, it is our hope that acoustic flow cytometry can become a platform for drug delivery MB research, where conventional drug loading is very expensive, and the ability to quickly characterize and determine if the drug loaded MB’s will respond well can be obtained with a single device.

REFERENCES:

1. Miller, D. L. *et al.* Overview of therapeutic ultrasound applications and safety considerations. *J. ultrasound Med.* **31,** 623–34 (2012).
2. Dalecki, D. Mechanical bioeffects of ultrasound. *Annu. Rev. Biomed. Eng.* **6,** 229–48 (2004).
3. Hokland, S. L. *et al.* MRI-guided focused ultrasound: methodology and applications. *IEEE Trans. Med. Imaging* **25,** 723–31 (2006).
4. Stride, E. & Saffari, N. Microbubble ultrasound contrast agents: a review. *Proc. Inst. Mech. Eng. H.* **217,** 429–47 (2003).
5. Frenkel, V. Ultrasound mediated delivery of drugs and genes to solid tumors. *Adv. Drug Deliv. Rev.* **60,** 1193–208 (2008).
6. Dromi, S. *et al.* Pulsed-high intensity focused ultrasound and low temperature - Sensitive liposomes for enhanced targeted drug delivery and antitumor effect. *Clin. Cancer Res.* **13,** 2722–2727 (2007).
7. Fink, M. Time reversal of ultrasonic fields. I. Basic principles. *IEEE Trans. Ultrason. Ferroelectr. Freq. Control* **39,** 555–566 (1992).
8. Thomas, J. L., Wu, F. & Fink, M. Time reversal focusing applied to lithotripsy. *Ultrason. Imaging* **18,** 106–121 (1996).
9. Khokhlova, V. A., Bobkova, S. M. & Gavrilov, L. R. Focus splitting associated with propagation of focused ultrasound through the rib cage. *Acoust. Phys.* **56,** 665–674 (2010).
10. Perez, C., Chen, H., Matula, T. J., Karzova, M. & Khokhlova, V. A. Acoustic field characterization of the Duolith: measurements and modeling of a clinical shock wave therapy device. *J. Acoust. Soc. Am.* **134,** 1663–74 (2013).
11. Chitnis, P. V. & Cleveland, R. O. Acoustic and Cavitation Fields of Shock Wave Therapy Devices. in *AIP Conference Proceedings* 440–444 (American Institute of Physics, 2006).
12. Cleveland, R. O., Chitnis, P. V & McClure, S. R. Acoustic field of a ballistic shock wave therapy device. *Ultrasound Med. Biol.* **33,** 1327–35 (2007).
13. Mehier-Humbert, S., Bettinger, T., Yan, F. & Guy, R. H. Plasma membrane poration induced by ultrasound exposure: implication for drug delivery. *J. Control. release* **104,** 213–22 (2005).

14. Wondergem, N. & De La Rosette, J. J. M. C. H. HIFU and cryoablation-non or minimal touch techniques for the treatment of prostate cancer. Is there a role for contrast enhanced ultrasound? *Minim. invasive Ther. allied Technol.* **16,** 22–30 (2007).

15. Hwang, J. H. *et al.* Preclinical in vivo evaluation of an extracorporeal HIFU device for ablation of pancreatic tumors. *Ultrasound Med. Biol.* **35,** 967–75 (2009).

16. Hwang, J. H. & Crum, L. A. Current status of clinical high-intensity focused ultrasound. *Conf. Proc. IEEE Eng. Med. Biol. Soc.* **2009,** 130–3 (2009).

17. Damianou, C. In vitro and in vivo ablation of porcine renal tissues using high-intensity focused ultrasound. *Ultrasound Med. Biol.* **29,** 1321–1330 (2003).

18. Maxwell, A. D. *et al.* Noninvasive thrombolysis using pulsed ultrasound cavitation therapy - histotripsy. *Ultrasound Med. Biol.* **35,** 1982–94 (2009).

19. Wang, Y.-N., Khokhlova, T., Bailey, M., Hwang, J. H. & Khokhlova, V. Histological and Biochemical Analysis of Mechanical and Thermal Bioeffects in Boiling Histotripsy Lesions Induced by High Intensity Focused Ultrasound. *Ultrasound Med. Biol.* 1–15 (2013). doi:10.1016/j.ultrasmedbio.2012.10.012

20. Skyba, D. M., Price, R. J., Linka, A. Z., Skalak, T. C. & Kaul, S. Direct in vivo visualization of intravascular destruction of microbubbles by ultrasound and its local effects on tissue. *Circulation* **98,** 290–293 (1998).

21. Liang, H.-D., Tang, J., Halliwell, M. & Wells, P. N. T. Sonoporation, drug delivery, and gene therapy. *Proc. Inst. Mech. Eng. Part H J. Eng. Med.* **224,** 343–361 (2010).

22. Nyborg, W. L. Ultrasonic microstreaming and related phenomena. *Br. J. Cancer. Suppl.* **5,** 156–60 (1982).

23. Chapelon, J. Y. *et al.* In vivo effects of high-intensity ultrasound on prostatic adenocarcinoma Dunning R3327. *Cancer Res.* **15,** 6353–6357 (1992).

24. Bailey, M. R., Khokhlova, V. A., Sapozhnikov, O. A., Kargl, S. G. & Crum, L. A. Physical mechanisms of the therapeutic effect of ultrasound (a review). *Acoust. Phys.* **49,** 369–388 (2003).

25. Ferrara, K. W. Driving delivery vehicles with ultrasound. *Adv. Drug Deliv. Rev.* **60,** 1097–102 (2008).

26. Ferrara, K., Pollard, R. & Borden, M. Ultrasound microbubble contrast agents: fundamentals and application to gene and drug delivery. *Annu. Rev. Biomed. Eng.* **9,** 415–47 (2007).

27. Khokhlova, V. A. *et al.* Effects of nonlinear propagation, cavitation, and boiling in lesion formation by high intensity focused ultrasound in a gel phantom. *J. Acoust. Soc. Am.* **119,** 1834 (2006).

28. Cho, J. A. *et al.* Hyperthermia-treated mesenchymal stem cells exert antitumor effects on human carcinoma cell line. *Cancer* **115,** 311–23 (2009).

29. Dewhirst, M. W., Viglianti, B. L., Lora-Michiels, M., Hanson, M. & Hoopes, P. J. Basic principles of thermal dosimetry and thermal thresholds for tissue damage from hyperthermia. *Int. J. Hyperthermia* **19,** 267–94 (2007).

30. Ta, T., Convertine, A. J., Reyes, C. R., Stayton, P. S. & Porter, T. M. Thermosensitive liposomes modified with poly(N-isopropylacrylamide-co-propylacrylic acid) copolymers for triggered release of doxorubicin. *Biomacromolecules* **11,** 1915–20 (2010).

31. Deckers, R. & Moonen, C. T. W. Ultrasound triggered, image guided, local drug delivery. *J. Control. Release* **148,** 25–33 (2010).

32. Hwang, J. H. & Crum, L. a. Current status of clinical high-intensity focused ultrasound. *Conf. Proc. IEEE Eng. Med. Biol. Soc.* **2009,** 130–3 (2009).

33. Sirsi, S. & Borden, M. Microbubble Compositions, Properties and Biomedical Applications. *Bubble Sci. Eng. Technol.* **1,** 3–17 (2009).

34. Cosgrove, D. & Harvey, C. Clinical uses of microbubbles in diagnosis and treatment. *Med. Biol. Eng. Comput.* **47,** 813–826 (2009).

35. Cavalieri, F., Zhou, M. & Ashokkumar, M. The Design of Multifunctional Microbubbles for Ultrasound Image-Guided Cancer Therapy. *Curr. Top. Med. Chem.* **10,** 1198–1210 (2010).

36. FDA Approved Drug Product List B, U. S. F. and D. A. *Approved Drug Product List B.* (2015).

37. Unnikrishnan, S. & Klibanov, A. L. Microbubbles as ultrasound contrast agents for molecular imaging: preparation and application. *AJR. Am. J. Roentgenol.* **199,** 292–9 (2012).

38. Kang, S.-T. & Yeh, C.-K. Ultrasound microbubble contrast agents for diagnostic and therapeutic applications: current status and future design. *Chang Gung Med. J.* **35,** 125–39 (2011).

39. Faez, T., Skachkov, I., Versluis, M., Kooiman, K. & de Jong, N. In vivo characterization of ultrasound contrast agents: microbubble spectroscopy in a chicken embryo. *Ultrasound Med. Biol.* **38,** 1608–17 (2012).

40. Pellerito, J. & Polak, J. *Introduction to Vascular Ultrasonography*. (Saunders, Elsevier, 2012).

41. Shapiro, H. M. *Practical Flow Cytometry*. (John Wiley & Sons, 2003).

42. Nolan, J. P. & Condello, D. Spectral flow cytometry. *Curr. Protoc. Cytom.* **1,** (2013).

43. Shapiro, H. M. The evolution of cytometers. *Cytometry. A* **58,** 13–20 (2004).

44. Shapiro, H. M. Fluorescent dyes for differential counts by flow cytometry: does histochemistry tell us much more than cell geometry? *J. Histochem. Cytochem.* **25,** 976–89 (1977).

45. Feshitan, J. A., Chen, C. C., Kwan, J. J. & Borden, M. A. Microbubble size isolation by differential centrifugation. *J. Colloid Interface Sci.* **329,** 316–24 (2009).

46. Sirsi, S., Feshitan, J., Kwan, J., Homma, S. & Borden, M. Effect of microbubble size on fundamental mode high frequency ultrasound imaging in mice. *Ultrasound Med. Biol.* **36,** 935–48 (2010).

47. Satinover, S. J., Dove, J. D. & Borden, M. A. Single-particle optical sizing of microbubbles. *Ultrasound Med. Biol.* **40,** 138–47 (2014).

48. Tu, J. *et al.* Microbubble sizing and shell characterization using flow cytometry. *IEEE Trans. Ultrason. Ferroelectr. Freq. Control* **58,** 955–963 (2011).

49. Cavalieri, F. *et al.* Mechanical characterization of ultrasonically synthesized microbubble shells by flow cytometry and AFM. *ACS Appl. Mater. Interfaces* **5,** 10920–10925 (2013).

50. Chang, P. H., Shung, K. K., Wu, S. J. & Levene, H. B. Second harmonic imaging and harmonic Doppler measurements with Albunex. *IEEE Trans. Ultrason. Ferroelectr. Freq. Control* **42,** 1020–1027 (1995).

51. Sboros, V. *et al.* Nanointerrogation of ultrasonic contrast agent microbubbles using atomic force microscopy. *Ultrasound Med. Biol.* **32,** 579–585 (2006).

52. Gorce, J. M., Arditi, M. & Schneider, M. Influence of bubble size distribution on the echogenicity of ultrasound contrast agents: a study of SonoVue. *Invest. Radiol.* **35,** 661–71 (2000).

53. Morgan, K. E. *et al.* Experimental and theoretical evaluation of microbubble behavior: effect of transmitted phase and bubble size. *IEEE Trans. Ultrason. Ferroelectr. Freq. Control* **47,** 1494–509 (2000).

54. Dayton, P. A., Morgan, K. E., Klibanov, A. L., Brandenburger, G. H. & Ferrara, K. W. Optical and acoustical observations of the effects of ultrasound on contrast agents. *IEEE Trans. Ultrason. Ferroelectr. Freq. Control* **46,** 220–32 (1999).

55. Van der Meer, S. M. *et al.* Microbubble spectroscopy of ultrasound contrast agents. *J. Acoust. Soc. Am.* **121,** 648–656 (2007).

56. Glynos, E. *et al.* Nanomechanics of biocompatible hollow thin-shell polymer microspheres. *Langmuir* **25,** 7514–7522 (2009).

57. Grant, C. A., McKendry, J. E. & Evans, S. D. Temperature dependent stiffness and visco-elastic behaviour of lipid coated microbubbles using atomic force microscopy. *Soft Matter* **8,** 1321–1326 (2012).

58. Santos, E. B., Morris, J. K., Glynos, E., Sboros, V. & Koutsos, V. Nanomechanical properties of phospholipid microbubbles. *Langmuir* **28,** 5753–5760 (2012).

59. Guan, J. & Matula, T. J. Using light scattering to measure the response of individual ultrasound contrast microbubbles subjected to pulsed ultrasound in vitro. *J. Acoust. Soc. Am.* **116,** 2832–42 (2004).

60. Tu, J., Guan, J., Qiu, Y. & Matula, T. J. Estimating the shell parameters of SonoVue microbubbles using light scattering. *J. Acoust. Soc. Am.* **126,** 2954–62 (2009).

61. Kudo, P. *et al.* Randomized, placebo-controlled, double-blind clinical trial evaluating the treatment of plantar fasciitis with an extracoporeal shockwave therapy (ESWT) device: a North American confirmatory study. *J. Orthop. Res.* **24,** 115–23 (2006).

62. Rompe, J. D., Decking, J., Schoellner, C. & Nafe, B. Shock Wave Application for Chronic Plantar Fasciitis in Running Athletes: A Prospective, Randomized, Placebo-Controlled Trial. *Am. J. Sport. Med.* **31,** 268–275 (2003).

63. Gerdesmeyer, L. *et al.* Extracorporeal shock wave therapy for the treatment of chronic calcifying tendonitis of the rotator cuff: a randomized controlled trial. *JAMA-J. Am. Med. Assoc.* **290,** 2573–80 (2003).

64. Furia, J. P. Safety and efficacy of extracorporeal shock wave therapy for chronic lateral epicondylitis. *Am. J. Orthop. (Belle Mead NJ).* **34,** 13–19 (2005).

65. Rompe, J. D. Repetitive Low-Energy Shock Wave Treatment for Chronic Lateral Epicondylitis in Tennis Players. *Am. J. Sport. Med.* **32,** 734–743 (2004).

66. Peers, K. *Extracorporeal Shock Wave Therapy in Chronic Achilles and Patellar Tendinopathy*. (Leuven University Press, 2003, 2003).

67. Yoo, S. D. *et al.* Effects of extracorporeal shockwave therapy on nanostructural and biomechanical responses in the collagenase-induced Achilles tendinitis animal model. *Laser. Med. Sci.* **27,** 1195–1204 (2012).

68. Valchanou, V. D. & Michailov, P. High energy shock waves in the treatment of delayed and nonunion of fractures. *Int. Orthop.* **15,** 181–184 (1991).

69. Peng, Y. *et al.* Effects of extracorporeal cardiac shock wave therapy in patients with ischemic heart failure. *Chinese J. Cardiovasc. Dis.* **40,** 141–6 (2012).

70. Fukumoto, Y. *et al.* Extracorporeal cardiac shock wave therapy ameliorates myocardial ischemia in patients with severe coronary artery disease. *Coron. Artery Dis.* **17,** 63–70 (2006).

71. Yang, P. *et al.* Randomized and double-blind controlled clinical trial of extracorporeal cardiac shock wave therapy for coronary heart disease. *Heart Vessels* **28,** 284–91 (2013).

72. Nishida, T. *et al.* Extracorporeal cardiac shock wave therapy markedly ameliorates ischemia-induced myocardial dysfunction in pigs in vivo. *Circulation* **110,** 3055–61 (2004).

73. Ito, Y. *et al.* Cardiac shock wave therapy ameliorates left ventricular remodeling after myocardial ischemia–reperfusion injury in pigs in vivo. *Coron. Artery Dis.* **21,** 304–311 (2010).

74. Wang, C.-J. *et al.* Shock wave therapy induces neovascularization at the tendon-bone junction. A study in rabbits. *J. Orthop. Res.* **21,** 984–9 (2003).

75. Meirer, R. *et al.* Comparison of the effectiveness of gene therapy with vascular endothelial growth factor or shock wave therapy to reduce ischaemic necrosis in an epigastric skin flap model in rats. *J. Plast. Reconstr. Aesthet. Surg.* **60,** 266–71 (2007).

76. Meirer, R. *et al.* Shock Wave Therapy Reduces Necrotic Flap Zones and Induces VEGF Expression in Animal Epigastric Skin Flap Model. *J. Reconstr. Microsurg.* **23,** 231–235 (2007).

77. Wang, C.-J. *et al.* Extracorporeal shockwave therapy shows time-dependent chondroprotective effects in osteoarthritis of the knee in rats. *J. Surg. Res.* 1–10 (2012).

78. Wang, C.-J. Extracorporeal shockwave therapy in musculoskeletal disorders. *J. Orthop. Surg. Res.* 7–11 (2012).

79. Wang, C.-J. An overview of shock wave therapy in musculoskeletal disorders. *Chang Gung Med. J.* **26,** 220–32 (2003).

80. Mariotto, S. *et al.* Extracorporeal shock waves: from lithotripsy to anti-inflammatory action by NO production. *Nitric. Oxide-Biol. Ch.* **12,** 89–96 (2005).

81. Ito, K., Fukumoto, Y. & Shimokawa, H. Extracorporeal Shock Wave Therapy as a New and Non-invasive Angiogenic Strategy. *Tohoku. J. Exp. Med.* **219,** 1–9 (2009).

82. Notarnicola, a *et al.* Extracorporeal shockwaves versus surgery in the treatment of pseudoarthrosis of the carpal scaphoid. *Ultrasound Med. Biol.* **36,** 1306–13 (2010).

83. Coleman, A. J. & Saunders, J. E. A survey of the acoustic output of comercial extracorporeal shock wave lithotripters. *Ultrasound Med. Biol.* **15,** 213–227 (1989).

84. Buizza, A., Dell'Aquila, T., Giribona, P. & Spagno, C. The performance of different pressure pulse generators for extracorporeal lithotripsy: A comparison based on commercial lithotripters for kidney stones. *Ultrasound Med. Biol.* **21,** 259–272 (1995).

85. Cleveland, R. O. *et al.* Design and characterization of a research electrohydraulic lithotripter patterned after the Dornier HM3. *Rev. Sci. Instrum.* **71,** 2514–25 (2000).

86. Cleveland, R. O. & McAteer, J. A. *Physics of Shockwave Lithotripsy in Smith's Textbook of Endourology*. (Wiley-Blackwell, 2012).

87. Gollwitzer, H., Diehl, P., von Korff, A., Rahlfs, V. W. & Gerdesmeyer, L. Extracorporeal shock wave therapy for chronic painful heel syndrome: a prospective, double blind, randomized trial assessing the efficacy of a new electromagnetic shock wave device. *J. Foot Ankle Surg.* **46,** 348–57 (2000).

88. Müller, P., Guggenheim, B., Attin, T., Marlinghaus, E. & Schmidlin, P. R. Potential of shock waves to remove calculus and biofilm. *Clin. Oral . Investig.* **15,** 959–65 (2011).

89. Tinazzi, E. *et al.* Effects of shock wave therapy in the skin of patients with progressive systemic sclerosis: a pilot study. *Rheumatol. Int.* **31,** 651–56 (2011).

90. Zimmermann, R. *et al.* Extracorporeal shock-wave therapy for treating chronic pelvic pain syndrome: a feasibility study and the first clinical results. *BJU Int.* **102,** 976–80 (2008).

91. Zimmermann, R., Cumpanas, A., Miclea, F. & Janetschek, G. Extracorporeal shock wave therapy for the treatment of chronic pelvic pain syndrome in males: a randomised, double-blind, placebo-controlled study. *Eur. Urol.* **56,** 418–24 (2009).

92. Lauer, U. *et al.* Shock wave permeabilization as a new gene transfer method. *Gene. Ther.* **4,** 710–5 (1997).

93. Bao, S., Thrall, B. D., Gies, R. A. & Miller, D. L. In vivo transfection of melanoma cells by lithotripter shock waves. *Cancer. Res.* **58,** 219–21 (1998).

94. Rompe, J. D., Rosendahl, T., Schöllner, C. & Theis, C. High-energy extracorporeal shock wave treatment of nonunions. *Clin. Orthop. Relat. Res.* 102–11 (2001).

95. Schoellner, C., Rompe, J. D., Decking, J. & Heine, J. High energy extracorporeal shockwave therapy (ESWT) in pseudarthrosis. *Orthopade* **31,** 658–62 (2002).

96. Ludwig, J. *et al.* High-energy shock wave treatment of femoral head necrosis in adults. *Clin. Orthop. Relat. Res.* 119–26 (2001).

97. Vogel, J., Rompe, J. D., Hopf, C., Heine, J. & Bürger, R. High-energy extracorporeal shock-wave therapy (ESWT) in the treatment of pseudarthrosis. *Z Orthop Ihre Grenzgeb* **135,** 145–9 (1997).

98. Endres, S., Weiskirch, M., Hinz, C., Hütter, F. & Wilke, A. Extracorporeal shock-wave therapy in the treatment of pseudoarthrosis: a case report. *Cases. J.* **1,** 276 (2008).

99. Palmieri, A. *et al.* A first prospective, randomized, double-blind, placebo-controlled clinical trial evaluating extracorporeal shock wave therapy for the treatment of Peyronie's disease. *Eur. Urol.* **56,** 363–9 (2009).

100. Moen, M. H. *et al.* Shockwave treatment for medial tibial stress syndrome in athletes; a prospective controlled study. *Br. J. Sport. Med.* **46,** 253–7 (2012).

101. Nazer, B. *et al.* Therapeutic Ultrasound Promotes Reperfusion and Angiogenesis in a Rat Model of Peripheral Arterial Disease. *Circ. J.* (2015). doi:10.1253/circj.CJ-15-0366

102. Kreider, W. *et al.* Acoustic measurements and holographic reconstruction of the Philips MR-guided HIFU source. in *Program and Abstract Book 'Current and Future Applications of MR-guided Focused Ultrasound 2010', 2nd International Symposium, 17–20 October 2010, Washington DC* 79 (2010).

103. Khokhlova, V. A., Ponomarev, A. E., Averkiou, M. A. & Crum, L. A. Nonlinear pulsed ultrasound beams radiated by rectangular focused diagnostic transducers. *Acoust. Phys.* **52,** 481–489 (2006).

104. Khokhlova, V. A., Souchon, R., Tavakkoli, J., Sapozhnikov, O. A. & Cathignol, D. Numerical modeling of finite-amplitude sound beams: Shock formation in the near field of a cw plane piston source. *J. Acoust. Soc. Am.* **110,** 95–108 (2001).

105. Averkiou, M. A. & Cleveland, R. O. Modeling of an electrohydraulic lithotripter with the KZK equation. *J. Acoust. Soc. Am.* **106,** 102–12 (1999).

106. Canney, M. S., Bailey, M. R., Crum, L. A., Khokhlova, V. A. & Sapozhnikov, O. A. Acoustic characterization of high intensity focused ultrasound fields: a combined measurement and modeling approach. *J. Acoust. Soc. Am.* **124,** 2406–20 (2008).

107. Eisenmenger, W. & Staudenraus, J. Fibre-optic probe hydrophone for ultrasonic and shock-wave measurements in water. *Ultrasonics* **31,** 267–273 (1993).

108. IEC61846. *Ultrasonics - Pressure pulse lithotriptors - Characteristics of fields, T.-. Ultrasonics, Editor*. (1998).

109. Averiyanov, M., Ollivier, S., Khokhlova, V. & Blanc-Benon, P. Random focusing of nonlinear acoustic N-waves in fully developed turbulence: laboratory scale experiment. *J. Acoust. Soc. Am.* **130,** 3595–607 (2011).

110. Yuldashev, P. *et al.* Nonlinear propagation of spark-generated N-waves in air: modeling and measurements using acoustical and optical methods. *J. Acoust. Soc. Am.* **128,** 3321–33 (2010).

111. Hamilton, M. F. & Blackstock, D. T. *Nonlinear Acoustics*. (Academic Press, 1998).

112. Kurganov, A. & Tadmor, E. New High-Resolution Central Schemes for Nonlinear Conservation Laws and Convection–Diffusion Equations. *J. Comput. Phys.* **160,** 241–282 (2000).

113. Karzova, M. M., Averiyanov, M. V., Sapozhnikov, O. A. & Khokhlova, V. A. Mechanisms for saturation of nonlinear pulsed and periodic signals in focused acoustic beams. *Acoust. Phys.* **58,** 81–89 (2012).

114. Averiyanov, M., Blanc-Benon, P., Cleveland, R. O. & Khokhlova, V. Nonlinear and diffraction effects in propagation of N-waves in randomly inhomogeneous moving media. *J. Acoust. Soc. Am.* **129,** 1760–72 (2011).

115. Bessonova, O. V, Khokhlova, V. A., Bailey, M. R., Canney, M. S. & Crum, L. A. Focusing of high power ultrasound beams and limiting values of shock wave parameters. *Acoust. Phys.* **55,** 463–476 (2009).

116. Lokhandwalla, M., McAteer, J. A., Williams, J. C. & Sturtevant, B. Mechanical haemolysis in shock wave lithotripsy (SWL): II. In vitro cell lysis due to shear. *Phys. Med. Bio.* **46,** 1245–64 (2001).

117. Lokhandwalla, M. & Sturtevant, B. Mechanical haemolysis in shock wave lithotripsy (SWL): I. Analysis of cell deformation due to SWL flow-fields. *Phys. Med. Bio.* **46,** 413–37 (2001).

118. Wang, N., Tytell, J. D. & Ingber, D. E. Mechanotransduction at a distance: mechanically coupling the extracellular matrix with the nucleus. *Nat. Rev. Mol. Cell. Biol.* **10,** 75–82 (2009).

119. Fagnan, K. M., Leveque, R. J., Matula, T. J. & MacConaghy, B. in *Hyperbolic Problems: Theory, Numerics, Applications* (eds. Benzoni-Gavage, S. & Serre, D.) **m,** 503–510 (Springer Berlin Heidelberg, 2008).

120. Matula, T. J., MacConaghy, B., Ching, R., Fagnan, K. & LeVeque, R. J. Measurements of acoustic energy deflection in the presence of replica bone. *ISMST Newsl.* **6,** 20–22 (2010).

121. Chen, H., Brayman, A. a, Bailey, M. R. & Matula, T. J. Blood vessel rupture by cavitation. *Urol. Res.* **38,** 321–6 (2010).

122. Chen, H., Kreider, W., Brayman, A., Bailey, M. & Matula, T. Blood Vessel Deformations on Microsecond Time Scales by Ultrasonic Cavitation. *Phys. Rev. Lett.* **106,** 1–4 (2011).

123. Freund, J. B. Suppression of shocked-bubble expansion due to tissue confinement with application to shock-wave lithotripsy. *J. Acoust. Soc. Am.* **123,** 2867–74 (2008).

124. Zhong, P., Zhou, Y. & Zhu, S. Dynamics of bubble oscillation in constrained media and mechanisms of vessel rupture in SWL. *Ultrasound Med. Biol.* **27,** 119–134 (2001).

125. Navarro, A. *et al.* Bacterial biofilm disruption using laser-generated shockwaves. *Proc. SPIE* **8214,** 82141H–82141H–8 (2012).

126. Kizhner, V., Krespi, Y. P., Hall-Stoodley, L. & Stoodley, P. Laser-generated shockwave for clearing medical device biofilms. *Photomed. Laser Surg.* **29,** 277–82 (2011).

127. Kumon, R. E. *et al.* Ultrasound-induced calcium oscillations and waves in Chinese hamster ovary cells in the presence of microbubbles. *Biophys. J.* **93,** L29–L31 (2007).

128. Kudo, N., Okada, K. & Yamamoto, K. Sonoporation by single-shot pulsed ultrasound with microbubbles adjacent to cells. *Biophys. J.* **96,** 4866–4876 (2009).

129. Reher, P., Doan, N., Bradnock, B., Meghji, S. & Harris, M. Effect of ultrasound on the production of IL-8, basic FGF and VEGF. *Cytokine* **11,** 416–423 (1999).

130. Doan, N., Reher, P., Meghji, S. & Harris, M. In vitro effects of therapeutic ultrasound on cell proliferation, protein synthesis, and cytokine production by human fibroblasts,

osteoblasts, and monocytes. *J. Oral Maxillofac. Surg.* **57,** 409–419; discussion 420 (1999).

131. Vogel, A. Shock wave emission and cavitation bubble generation by picosecond and nanosecond optical breakdown in water. *J. Acoust. Soc. Am.* **100,** 148 (1996).

132. Vogel, A., Lauterborn, W. & Timm, R. Optical and acoustic investigations of the dynamics of laser-produced cavitation bubbles near a solid boundary. *J. Fluid Mech.* **206,** 299–388 (1989).

133. Vogel, A. & Lauterborn, W. Acoustic transient generation by laser-produced cavitation bubbles near solid boundaries. *J. Acoust. Soc. Am.* **84,** 719–731 (1988).

134. Vogel, A. & Venugopalan, V. *Optical-Thermal Response of Laser-Irradiated Tissue*. (Springer Netherlands, 2011). doi:10.1007/978-90-481-8831-4

135. Verleng, M., Verdaasdonk, R., van der Veen, A., Lemberg, V. & Boutoussov, D. Cavitation bubbles induced by Erbium lasers: implications for dentistry. in *Proc. SPIE 8929, Lasers in Dentistry XX, 89290B*

136. Blanken, J., De Moor, R. J. G., Meire, M. & Verdaasdonk, R. Laser induced explosive vapor and cavitation resulting in effective irrigation of the root canal. Part 1: A visualization study. *Lasers Surg. Med.* **41,** 514–519 (2009).

137. Blanken, J. & Verdaasdonk, R. Cavitation as a working mechanism of the Er, Cr: YSGG laser in endodontics: a visualization study. *J Oral Laser Appl* **7,** 97–106 (2007).

138. Asshauer, T., Rink, K. & Delacrétaz, G. Acoustic transient generation by holmium-laser-induced cavitation bubbles. *J. Appl. Phys.* **76,** 5007 (1994).

139. Oskoee, P., Kimyai, S., Ebrahimi, M., Rikhtegaran, S. & Pournaghi-Azar, F. Cervical Margin Integrity of Class II Resin Composite Restorations in Laser- and Bur-Prepared Cavities Using Three Different Adhesive Systems. *Oper. Dent.* **37,** 316–323 (2012).

140. Subramaniam, P. & Pandey, A. Effect of erbium, chromium: yttrium, scandium, gallium, garnet laser and casein phosphopeptide-amorphous calcium phosphate on surface micro-hardness of primary tooth enamel. *Eur. J. Dent.* **8,** 402 (2014).

141. Korkmaz, F. M., Baygin, O., Tuzuner, T., Bagis, B. & Arslan, I. The effect of an erbium, chromium: Yttrium-scandium-gallium-garnet laser on the microleakage and bond strength of silorane and micro-hybrid composite restorations. *Eur. J. Dent.* **7,** 33–40 (2013).

142. Hatipoğlu, M. & Barutcigil, Ç. Effects of erbium - and chromium - doped yttrium scandium gallium garnet and diode lasers on the surfaces of restorative dental materials : A scanning electron microscope study. **18,** (2015).

143. Aydemir, S., Cimilli, H., Hazar Yoruç, A. & Kartal, N. Evaluation of two different root-end cavity preparation techniques: A scanning electron microscope study. *Eur. J. Dent.* **7,** 186 (2013).

144. Sullivan, J., Pileggi, R. & Varella, C. Evaluation of Root-End Resections Performed by Er, Cr: YSGG Laser with and without Placement of a Root-End Filling Material. *Int. J. Dent.* **2009,** 798786 (2009).

145. Polenik, P. & Netolicky, J. Deposition of Fluorescent Magnetic Nanoparticles into Dentinal Tubules. 1–5 (2014).

146. Ith, M., Pratisto, H., Altermatt, H. J., Frenz, M. & Weber, H. P. Dynamics of laser-induced channel formation in water and influence of pulse duration on the ablation of biotissue under water with pulsed erbium-laser radiation. *Appl. Phys. B - Lasers Opt.* **59,** 621–629 (1994).

147. Jansen, E. D. *et al.* Effect of pulse duration on bubble formation and laser-induced pressure waves during holmium laser ablation. *Lasers Surg. Med.* **18,** 278–93 (1996).

148. Lü, T., Xiao, Q., Xia, D., Ruan, K. & Li, Z. Cavitation effect of holmium laser pulse applied to ablation of hard tissue underwater. *J. Biomed. Opt.* **15,** 048002 (2014).

149. Palanker, D., Turovets, I. & Lewis, A. Dynamics of ArF excimer laser-induced cavitation bubbles in gel surrounded by a liquid medium. *Lasers Surg. Med.* **21,** 294–300 (1997).

150. Shangguan, H., Casperson, L. W., Paisley, D. L. & Prahl, S. a. Photographic studies of laser-induced bubble formation in absorbing liquids and on submerged targets: implications for drug delivery with microsecond laser pulses. *Soc. Photo-Optical Instrum. Eng. Opt Eng* **37,** 2217–2226 (1998).

151. Shangguan, H., Casperson, L. W., Shearin, A., Paisley, D. L. & Prahl, S. A. Effects of Material Properties on Laser-induced Bubble Formation in Absorbing Liquids and On Submerged Targets. *Proc SPIE* **2869,** 783–791 (1997).

152. Howard, D. & Sturtevant, B. In vitro study of the mechanical effects of shock-wave lithotripsy. *Ultrasound Med. Biol.* **23,** 1107–1122 (1997).

153. Notarnicola, A. *et al.* Extracorporeal shockwaves versus surgery in the treatment of pseudoarthrosis of the carpal scaphoid. *Ultrasound Med. Biol.* **36,** 1306–13 (2010).

154. Wang, C.-J., Huang, H.-Y. & Pai, C.-H. Shock wave-enhanced neovascularization at the tendon-bone junction: An experiment in dogs. *J. Foot Ankle Surg.* **41,** 16–22 (2002).

155. Kreider, W., Crum, L. A., Bailey, M. R. & Sapozhnikov, O. A. A reduced-order, single-bubble cavitation model with applications to therapeutic ultrasound. *J. Acoust. Soc. Am.* **130,** 3511–30 (2011).

156. Kreider, W., Crum, L. A., Bailey, M. R. & Sapozhnikov, O. A. Observations of the collapses and rebounds of millimeter-sized lithotripsy bubbles. *J. Acoust. Soc. Am.* **130,** 3531–40 (2011).

157. Versluis, M., Schmitz, B., von Der Heydt, A. & Lohse, D. How Snapping Shrimp Snap: Through Cavitating Bubbles. *Science (80-.).* **289,** 2114–2117 (2000).

158. Matula, T. J. Bubble levitation and translation under single-bubble sonoluminescence conditions. *J. Acoust. Soc. Am.* **114,** 775–781 (2003).

159. Matula, T., Cordry, S., Roy, R. & Crum, L. Bjerknes force and bubble levitation under single-bubble sonoluminescence conditions. *J. Acoust. …* **102,** 1522–1527 (1997).

160. Plesset, M. S. & Zwick, S. A. A nonsteady heat diffusion problem with spherical symmetry. *J. Appl. Phys.* **23,** 95–98 (1952).

161. Cole, R. H. *Underwater Explosions*. (Princeton University Press, 1948).

162. Samokhin, a a, Klimentov, S. M. & Pivovarov, P. a. Acoustic diagnostics of the explosive boiling up of a transparent liquid on an absorbing substrate induced by two nanosecond laser pulses. *Quantum Electron.* **37,** 967–970 (2007).

163. Samokhin, A. ., Vovchenko, V. I. & Il'ichev, N. N. Photoacoustics and evaporation pressure signals in water irradiated with erbium laser pulses.pdf. *Phys. Wave Phenom.* **16,** 275–282 (2008).

164. Samokhin, A. ., Vovchenko, V. I., Il'ichev, N. N. & Shapkin, P. V. Features of the explosive boiling up of water irradiated by a Q-switched erbium laser.pdf. *Quantum Electron.* **37,** 1141–1142 (2007).

165. Samokhin, A. . & Il'ichev, N. N. On Photoacoustic monitoring of laser evaporation front movement. *Quantum Electron.* **40,** 659–660 (2010).

166. Pecha, R. & Gompf, B. Microimplosions: Cavitation Collapse and Shock Wave Emission on a Nanosecond Time Scale. *Phys. Rev. Lett.* **84,** 1328–1330 (2000).

167. Matula, T. J. *et al.* The acoustic emissions from single-bubble sonoluminescence. *J. Acoust. Soc. Am.* **103,** 1377–1382 (1998).

168. Perez, C. *et al.* Acoustic field characterization of the Waterlase2: Acoustic characterization and high speed photomicrography of a clinical laser generated shock wave therapy device for the treatment of periodontal biofilms in orthodontics and periodontics. *J. Acoust. Soc. Am.* **136,** 2279–2279 (2014).

169. Zhang, Y.-R., Du, W., Zhou, X.-D. & Yu, H.-Y. Review of research on the mechanical properties of the human tooth. *Int. J. Oral Sci.* 1–9 (2014). doi:10.1038/ijos.2014.21

170. Imbeni, V., Nalla, R. K., Bosi, C., Kinney, J. H. & Ritchie, R. O. In vitro fracture toughness of human dentin. *J. Biomed. Mater. Res. A* **66,** 1–9 (2003).

171. Cavalieri, F., Ashokkumar, M., Grieser, F. & Caruso, F. Ultrasonic synthesis of stable, functional lysozyme microbubbles. *Langmuir* **24,** 10078–83 (2008).

172. Cavalieri, F., Zhou, M., Caruso, F. & Ashokkumar, M. One-pot ultrasonic synthesis of multifunctional microbubbles and microcapsules using synthetic thiolated macromolecules. *Chem. Commun. (Camb).* **47,** 4096–4098 (2011).

173. Zhou, M., Cavalieri, F. & Ashokkumar, M. Tailoring the properties of ultrasonically synthesised microbubbles. *Soft Matter* **7,** 623 (2011).

174. Zhou, M., Cavalieri, F., Caruso, F. & Ashokkumar, M. Confinement of acoustic cavitation for the synthesis of protein-shelled nanobubbles for diagnostics and nucleic acid delivery. *ACS Macro Lett.* **1,** 853–856 (2012).

175. Melino, S. *et al.* Molecular properties of lysozyme-microbubbles: towards the protein and nucleic acid delivery. *Amino Acids* **43,** 885–896 (2012).

176. Cavalieri, F. *et al.* Antimicrobial and Biosensing Ultrasound-Responsive Lysozyme-Shelled Microbubbles. *ACS Appl. Mater. Interfaces* **5,** 464–471 (2013).

177. Cavalieri, F. *et al.* Influence of the Morphology of Lysozyme-Shelled Microparticles on the Cellular Association, Uptake, and Degradation in Human Breast Adenocarcinoma Cells. *Part. Part. Syst. Charact.* **30,** 695–705 (2013).

178. Tao, S. L. & Desai, T. a. Micromachined devices: The impact of controlled geometry from cell-targeting to bioavailability. *J. Control. Release* **109,** 127–138 (2005).

179. Doshi, N., Zahr, A. S., Bhaskar, S., Lahann, J. & Mitragotri, S. Red blood cell-mimicking synthetic biomaterial particles. *Proc. Natl. Acad. Sci. U. S. A.* **106,** 21495–21499 (2009).

180. Merkel, T. J. *et al.* Using mechanobiological mimicry of red blood cells to extend circulation times of hydrogel microparticles. *Proc. Natl. Acad. Sci. U. S. A.* **108,** 586–591 (2011).

181. Wang, J., Byrne, J. D., Napier, M. E. & Desimone, J. M. More effective nanomedicines through particle design. *Small* **7,** 1919–1931 (2011).

182. Aden, A. L. & Kerker, M. Scattering of electromagnetic waves from two concentric spheres. *J. Appl. Phys.* **22,** 1242–1246 (1951).

183. Marston, P. L. Colors observed when sunlight is scattered by bubble clouds in seawater. *Appl. Opt.* **30,** 3479–84 (1991).

184. Marston, P. L., Billete, B. & Dean, C. E. Scattering of light by a coated bubble in water near the critical and Brewster scattering angles. *SPIE 925 Ocean Opt. IX* **925,** 308–316 (1988).

185. Bohren, C. & Huffman, D. *Absorption and Scattering of light by small particles*. (J. Wiley and Sons, 1988).

186. Van der Meer, S. M. *et al.* Microbubble spectroscopy of ultrasound contrast agents. *J. Acoust. Soc. Am.* **121,** 648 (2007).

187. Elsner, N., Dubreuil, F. & Weinkamer, R. Mechanical properties of freestanding polyelectrolyte capsules: a quantitative approach based on shell theory. *… Polym. Surfaces …* (2006).

188. Lulevich, V. V. & Vinogradova, O. I. Effect of pH and Salt on the Stiffness of Polyelectrolyte Multilayer Microcapsules. *Langmuir* **20,** 2874–2878 (2004).

189. Schmidt, S. *et al.* Release properties of pressurized microgel templated capsules. *Adv. Funct. Mater.* **21,** 1411–1418 (2011).

190. Feng, W. W. & Yang, W.-H. On the Contact Problem of an Inflated Spherical Nonlinear Membrane. *J. Appl. Mech.* **40,** 209 (1973).

191. Gregory, R. D., Milac, T. I. & Wan, F. Y. M. The Axisymmetric Deformation of a Thin, or Moderately Thick, Elastic Spherical Cap. *Stud. Appl. Math.* **100,** 67–94 (1998).

192. Marmottant, P. *et al.* A model for large amplitude oscillations of coated bubbles accounting for buckling and rupture. *J. Acoust. Soc. Am.* **118,** 3499 (2005).

193. Flynn, H. G. Cavitation dynamics. I. A mathematical formulation. *J. Acoust. Soc. Am.* **57,** 1379 (1975).

194. Flynn, H. G. Transient pulsations of small gas bubbles in water. *J. Acoust. Soc. Am.* **84,** 1863–1876 (1988).

195. De Jong, N. & Hoff, L. Ultrasound scattering microspheres properties of Albunex. *Ultrasonics* **31,** 175–181 (1993).

196. Hoff, L. *Acoustic Characterization of Contrast Agents for Medical Ultrasound Imaging*. (Kluwer Academic Publishers, 2001).

197. Chatterjee, D. & Sarkar, K. A Newtonian rheological model for the interface of microbubble contrast agents. *Ultrasound Med. Biol.* **29,** 1749–1757 (2003).

198. Swalwell, J. E., Petersen, T. W. & van den Engh, G. Virtual-core flow cytometry. *Cytometry. A* **75,** 960–5 (2009).

199. Tu, J. *et al.* Microbubble sizing and shell characterization using flow cytometry. *IEEE Trans. Ultrason. Ferroelectr. Freq. Control* **58,** 955–63 (2011).

200. Shapiro, H. M. *Practical Flow Cytometry*. (John Wiley & Sons, 1994).

201. Feshitan, J. A., Chen, C. C., Kwan, J. J. & Borden, M. A. Microbubble size isolation by differential centrifugation. *J. Colloid Interface Sci.* **329,** 316–324 (2009).

202. Chitnis, P. V *et al.* Rupture threshold characterization of polymer-shelled ultrasound contrast agents subjected to static overpressure. *J. Appl. Phys.* **109,** 84906–8490610 (2011).

203. Lubinski, M. A., Emelianov, S. Y. & O'Donnell, M. Speckle Tracking Methods for Ultrasonic Elasticity Imaging Using Short-Time Correlation. *IEEE Trans. Ultrason. Ferroelectr. Freq. Control* **46,** 82–96 (1999).

204. Santin, M. D. *et al.* Encapsulated contrast microbubble radial oscillation associated with postexcitation pressure peaks. *J. Acoust. Soc. Am.* **127,** 1156–1164 (2010).

205. Shi, W. T. *et al.* Subharmonic imaging with microbubble contrast agents: initial results. *Ultrason. Imaging* **21,** 79–94 (1999).

206. Doinikov, A., Haac, J. F. & Dayton, P. A. Modeling of nonlinear viscous stress in encapsulating shells of lipid-coated contrast agent microbubbles. *Ultrasonics* **49,** 269–275 (2009).

207. Gong, Y., Cabodi, M. & Porter, T. M. Acoustic investigation of pressure-dependent resonance and shell elasticity of lipid-coated monodisperse microbubbles. *Appl. Phys. Lett.* **104,** 074103 (2014).

208. Frinking, P. J. A. & de Jong, N. Acoustic modeling of shell-encapsulated gas bubbles. *Ultrasound Med. Biol.* **24,** 523–533 (1998).

209. Perez, C. *et al.* Characterizing the pressure field in a modified flow cytometer quartz flow cell: A combined measurement and model approach to validate the internal pressure. *J. Acoust. Soc. Am.* **136,** 2095–2095 (2014).

210. Wang, C.-H. *et al.* Characterizing the pressure field in a modified microbubble flow cytometer: Using a laser Doppler vibrometer to validate the internal pressure. *J. Acoust. Soc. Am.* **137,** 2423–2424 (2015).

211. Perez, C. *et al.* Acoustic and optical characterization of targeted ultrasound contrast agents. *J. Acoust. Soc. Am.* **133,** 3261 (2013).

212. Shi, W. T. *et al.* Subharmonic imaging with microbubble contrast agents: initial results. *Ultrason. Imaging* **21,** 79–94 (1999).

213. Shi, W. & Forsberg, F. Ultrasonic characterization of the nonlinear properties of contrast microbubbles. *Ultrasound Med. Biol.* **26,** 93–104 (2000).

214. De Jong, N. *et al.* 'Compression-Only' Behavior of Phospholipid-Coated Contrast Bubbles. *Ultrasound Med. Biol.* **33,** 653–656 (2007).

215. Luan, Y. *et al.* Acoustical properties of individual liposome-loaded microbubbles. *Ultrasound Med. Biol.* **38,** 2174–85 (2012).

216. Church, C. The effects of an elastic solid surface layer on the radial pulsations of gas bubbles. *J. Acoust. Soc. Am.* **97,** 1510–1521 (1995).

217. Coussios, C. C. *et al.* In vitro characterization of liposomes and Optison® by acoustic scattering at 3.5 MHz. *Ultrasound Med. Biol.* **30,** 181–190 (2004).

218. Paul, S. *et al.* Material characterization of the encapsulation of an ultrasound contrast microbubble and its subharmonic response: strain-softening interfacial elasticity model. *J. Acoust. Soc. Am.* **127,** 3846–57 (2010).

219. Deng, C. X. *et al.* Study of ultrasonic contrast agents using a dual-frequency band technique. *Ultrasound Med. Biol.* **26,** 819–831 (2000).

220. Chen, W.-S., Matula, T. J., Brayman, A. A. & Crum, L. A. A comparison of the fragmentation thresholds and inertial cavitation doses of different ultrasound contrast agents. *J. Acoust. Soc. Am.* **113,** 643 (2003).

221. Podell, S. *et al.* Physical and biochemical stability of Optison, an injectable ultrasound contrast agent. *Biotechnol. Appl. Biochem.* **30 (Pt 3),** 213–223 (1999).

222. Porter, T. M., Smith, D. A. B. & Holland, C. K. Acoustic techniques for assessing the Optison destruction threshold. *J. ultrasound Med.* **25,** 1519–1529 (2006).

223. Chômas, J. E., Dayton, P., Alien, J., Morgan, K. & Ferrara, K. W. Mechanisms of contrast agent destruction. *IEEE Trans. Ultrason. Ferroelectr. Freq. Control* **48,** 232–248 (2001).

224. Yamakoshi, Y. & Miwa, T. Microbubble adhesion to target wall by ultrasonic wave frequency sweep method. *Jpn. J. Appl. Phys.* **48,** 0–6 (2009).

225. Zhao, S. *et al.* Radiation-Force Assisted Targeting Facilitates Ultrasonic Molecular Imaging. *Mol. Imaging* **3,** 135–148 (2004).

226. Doinikov, A. a, Aired, L. & Bouakaz, A. Acoustic scattering from a contrast agent microbubble near an elastic wall of finite thickness. *Phys. Med. Biol.* **56,** 6951–6967 (2011).

227. Doinikov, A. A., Zhao, S. & Dayton, P. A. Modeling of the acoustic response from contrast agent microbubbles near a rigid wall Alexander. *Ultrasonics* **49,** 195–201 (2008).

228. Sprague, M. R., Chérin, E., Goertz, D. E. & Foster, F. S. Nonlinear Emission from Individual Bound Microbubbles at High Frequencies. *Ultrasound Med. Biol.* **36,** 313–324 (2010).

229. Overvelde, M. *et al.* Dynamics of Coated Microbubbles Adherent to a Wall. *Ultrasound Med. Biol.* **37,** 1500–1508 (2011).

230. Mahue, V., Mari, J. M., Eckersley, J. & Tang, M. Pulse Inversion Doppler. *IEEE Trans. Ultrason. Ferroelectr. Freq. Control* **58,** 73–81 (2011).

231. Needles, A., Couture, O. & Foster, F. S. A Method for Differentiating Targeted Microbubbles in Real Time Using Subharmonic Micro-Ultrasound and Interframe Filtering. *Ultrasound Med. Biol.* **35,** 1564–1573 (2009).

232. Loughran, J., Sennoga, C., J Eckersley, R. & Tang, M.-X. Effect of ultrasound on adherent microbubble contrast agents. *Phys. Med. Biol.* **57,** 6999–7014 (2012).

233. Parrales, M. a., Fernandez, J. M., Perez-Saborid, M., Kopechek, J. a. & Porter, T. M. Acoustic characterization of monodisperse lipid-coated microbubbles: Relationship between size and shell viscoelastic properties. *J. Acoust. Soc. Am.* **136,** 1077–1084 (2014).

234. Chetty, K., Stride, E., Sennoga, C., Hajnal, J. & Eckersley, R. High-speed optical observations and simulation results of SonoVue microbubbles at low-pressure insonation. *IEEE Trans. Ultrason. Ferroelectr. Freq. Control* **55,** 1333–1342 (2008).

235. Faez, T., Goertz, D. & De Jong, N. Characterization of Definity™ Ultrasound Contrast Agent at Frequency Range of 5-15 MHz. *Ultrasound Med. Biol.* **37,** 338–342 (2011).

236. Gorce, J. M., Arditi, M. & Schneider, M. Influence of bubble size distribution on the echogenicity of ultrasound contrast agents: a study of SonoVue. *Invest. Radiol.* **35,** 661–671 (2000).

237. Helfield, B. L. & Goertz, D. E. Nonlinear resonance behavior and linear shell estimates for Definity TM and MicroMarker TM assessed with acoustic microbubble spectroscopy. *J. Acoust. Soc. Am.* **133,** 1158–1168 (2014).

238. Pu, G., Borden, M. A. & Longo, M. L. Collapse and shedding transitions in binary lipid monolayers coating microbubbles. *Langmuir* **22,** 2993–2999 (2006).

239. Kooiman, K. *et al.* DSPC or DPPC as main shell component influences ligand distribution and binding area of lipid-coated targeted microbubbles. *Eur. J. Lipid Sci. Technol.* **116,** 1217–1227 (2014).

240. Lozano, M. M. & Longo, M. L. Microbubbles coated with disaturated lipids and DSPE-PEG2000: Phase behavior, collapse transitions, and permeability. *Langmuir* **25,** 3705–3712 (2009).

241. Borden, M. A. *et al.* Lateral phase separation in lipid-coated microbubbles. *Langmuir* **22,** 4291–4297 (2006).

242. Kim, D. H., Costello, M. J., Duncan, P. B. & Needham, D. Mechanical properties and microstructure of polycrystalline phospholipid monolayer shells: Novel solid microparticles. *Langmuir* **19,** 8455–8466 (2003).

243. Lozano, M. M. & Longo, M. L. Complex formation and other phase transformations mapped in saturated phosphatidylcholine/DSPE-PEG2000 monolayers. *Soft Matter* **5,** 1822 (2009).

244. Van Rooij, T. *et al.* Non-linear Response and Viscoelastic Properties of Lipid-Coated Microbubbles: DSPC versus DPPC. *Ultrasound Med. Biol.* **41,** 1432–1445 (2015).

245. Luan, Y. *et al.* Lipid shedding from single oscillating microbubbles. *Ultrasound Med. Biol.* **40,** 1834–1846 (2014).

246. Heath, G. R. *et al.* Self-assembly of actin scaffolds on lipid microbubbles. *Soft Matter* **10,** 694–700 (2014).

247. Abou-saleh, R. H., Peyman, S. A., Critchley, K., Evans, S. D. & Thomson, N. H. Nanomechanics of lipid encapsulated microbubbles with functional coatings. *Langmuir* (2013).

248. Perez, C. *et al.* Acoustic and optical characterization of ultrasound contrast agents via flow cytometry. *J. Acoust. Soc. Am.* **132,** 1906 (2012).

249. Myrset, A. H., Nicolaysen, H., Toft, K., Christiansen, C. & Skotland, T. Structure and organization of albumin molecules forming the shell of air-filled microspheres: evidence for a monolayer of albumin molecules of multiple orientations stabilizing the enclosed air. *Biotechnol. Appl. Biochem.* **24 (Pt 2),** 145–53 (1996).

250. Hed, J., Dahlgren, C. & Rundquist, I. A simple fluorescence technique to stain the plasma membrane of human neutrophils. *Histochemistry* **79,** 105–110 (1983).

251. Hellebust, H., Christiansen, C. & Skotland, T. Biochemical characterization of air-filled albumin microspheres. *Biotechnol. Appl. Biochem.* **18 (Pt 3),** 227–37 (1993).

252. Borden, M. A. & Longo, M. L. Dissolution behavior of lipid monolayer-coated, air-filled microbubbles: Effect of lipid hydrophobic chain length. *Langmuir* **18,** 9225–9233 (2002).

253. Garg, S., Thomas, A. A. & Borden, M. A. The effect of lipid monolayer in-plane rigidity on invivo microbubble circulation persistence. *Biomaterials* **34,** 6862–6870 (2013).

254. Helfield, B. L., Cherin, E., Foster, F. S. & Goertz, D. E. Investigating the Subharmonic Response of Individual Phospholipid Encapsulated Microbubbles at High Frequencies: A Comparative Study of Five Agents. *Ultrasound Med. Biol.* **38,** 846–863 (2012).

255. Hosny, N. A. *et al.* Mapping microbubble viscosity using fluorescence lifetime imaging of molecular rotors. *Proc. Natl. Acad. Sci. U. S. A.* **110,** 9225–30 (2013).

256. Wang, C. H. & Yeh, C. K. Controlling the Size Distribution of Lipid-Coated Bubbles via Fluidity Regulation. *Ultrasound Med. Biol.* **39,** 882–892 (2013).

257. Larson-smith, K. & Pozzo, D. C. Pickering Emulsions Stabilized by Nanoparticle Surfactants. *Langmuir* **28,** 11725–11732 (2012).

258. Wei, K. *et al.* Quantification of myocardial blood flow with ultrasound-induced destruction of microbubbles administered as a constant venous infusion. *Circulation* **97,** 473–483 (1998).

259. Unger, E. C. *et al.* Therapeutic applications of lipid-coated microbubbles. *Advanced Drug Delivery Reviews* **56,** 1291–1314 (2004).

260. Cavalli, R. *et al.* New chitosan nanobubbles for ultrasound-mediated gene delivery: Preparation and in vitro characterization. *Int. J. Nanomedicine* **7,** 3309–3318 (2012).

261. Rapoport, N., Gao, Z. & Kennedy, A. Multifunctional nanoparticles for combining ultrasonic tumor imaging and targeted chemotherapy. *J. Natl. Cancer Inst.* **99,** 1095–106 (2007).

262. Rapoport, N. *et al.* Ultrasound-mediated tumor imaging and nanotherapy using drug loaded, block copolymer stabilized perfluorocarbon nanoemulsions. *J. Control. Release* **153,** 4–15 (2011).

263. Giesecke, T. & Hynynen, K. Ultrasound-mediated cavitation thresholds of liquid perfluorocarbon droplets in vitro. *Ultrasound Med. Biol.* **29,** 1359–1365 (2003).

264. Kripfgans, O., Fowlkes, J. & Miller, D. Acoustic droplet vaporization for therapeutic and diagnostic applications. *Ultrasound Med.* **26,** 1177–1189 (2000).

265. Kim, K. *et al.* Photoacoustic imaging of early inflammatory response using gold nanorods. *Appl. Phys. Lett.* **90,** 223901 (2007).

266. Wilson, K., Homan, K. & Emelianov, S. Biomedical photoacoustics beyond thermal expansion using triggered nanodroplet vaporization for contrast-enhanced imaging. *Nature Communications* **3,** 618 (2012).

267. Li, P.-C. *et al.* Photoacoustic imaging of multiple targets using gold nanorods. *IEEE transactions on ultrasonics, ferroelectrics, and frequency control* **54,** 1642–1647 (2007).

268. Chen, Y. S. *et al.* Silica-coated gold nanorods as photoacoustic signal nanoamplifiers. *Nano Lett.* **11,** 348–354 (2011).

269. Agarwal, A. *et al.* Targeted gold nanorod contrast agent for prostate cancer detection by photoacoustic imaging. *J. Appl. Phys.* **102,** (2007).

270. Wei, C.-W. *et al.* Nonlinear contrast enhancement in photoacoustic molecular imaging with gold nanosphere encapsulated nanoemulsions. *Appl. Phys. Lett.* **104,** 033701 (2014).

271. Ju, H., Roy, R. a & Murray, T. W. Gold nanoparticle targeted photoacoustic cavitation for potential deep tissue imaging and therapy. *Biomed. Opt. Express* **4,** 66–76 (2013).

272. Farny Caleb H, Wu Tianming, Holt Glynn R, Murray Todd W, R. R. A. Nucleating cavitation from laser-illuminated nano-particles. *Acoust. Res. Lett. Online* **6,** 138–143

273. McLaughlan, J. R., Roy, R. a, Ju, H. & Murray, T. W. Ultrasonic enhancement of photoacoustic emissions by nanoparticle-targeted cavitation. *Opt. Lett.* **35,** 2127–2129 (2010).

274. Larson-smith, K. & Pozzo, D. C. Scalable synthesis of self-assembling nanoparticle clusters based on controlled steric interactions. *Soft Matter* **7,** 5339–5347 (2011).

275. Frens, G. Controlled Nucleation for the Regulation of the Particle Size in Monodisperse Gold Suspensions. *Nat. Phys. Sci.* **241,** 20–22 (1973).

276. Fattaccioli, J. *et al.* Size and fluorescence measurements of individual droplets by flow cytometry. *Soft Matter* **5,** 2232 (2009).

277. Draine, B. T. & Flatau, P. J. Discrete-dipole approximation for scattering calculations. *Journal of the Optical Society of America A* **11,** 1491 (1994).

278. Wei, C. *et al.* Laser-induced cavitation in nanoemulsion with gold nanospheres for blood clot disruption: in vitro results. *Opt. Lett.* **39,** 2599–2602 (2014).

279. Wei, C. W. *et al.* Nonlinear contrast enhancement in photoacoustic molecular imaging with gold nanosphere encapsulated nanoemulsions. *Appl. Phys. Lett.* **104,** 1–4 (2014).

280. Xia, J. *et al.* Emulsion-aided laser clot disruption using a portable low-cost highrepetition rate fiber laser with simultaneous photoacoustic imaging. in *IEEE Ultrasonics Symposium, Prague, CR* IUS1–C3–4 (2013).

281. Weigandt, K. M. *et al.* Fibrin clot structure and mechanics associated with specific oxidation of methionine residues in fibrinogen. *Biophys. J.* **103,** 2399–2407 (2012).

282. Carr, M. E. & Hermans, J. Size and density of fibrin fibers from turbidity. *Macromolecules* **11,** 46–50 (1978).

283. York, N. ANSI Procedures for the National Adoption of ISO and IEC Standards as American National Standards. (2007).

284. Chen-Wei, W. *et al.* Emulsion-aided laser clot disruption using a portable low-cost highrepetition rate fiber laser with simultaneous photoacoustic imaging. in *IEEE Ultrasonics Symposium, Prague, CR* (2013).

285. Burgess, A. *et al.* High-intensity focused ultrasound (HIFU) for dissolution of clots in a rabbit model of embolic stroke. *PLoS One* **7,** 1–7 (2012).

286. Maxwell, A. D. *et al.* Noninvasive treatment of deep venous thrombosis using pulsed ultrasound cavitation therapy (histotripsy) in a porcine model. *J. Vasc. Interv. Radiol.* **22,** 369–377 (2011).

287. V, K., AK, A., N, F. & JA., A. *Pathologic Basis of Disease*. (Elsevier Inc., 2009).

288. Arnal, B. *et al.* Photoacoustics Sono-photoacoustic imaging of gold nanoemulsions : Part II . Real time imaging. *Biochem. Pharmacol.* 1–9 (2015). doi:10.1016/j.pacs.2015.01.001

289. Tanter, M., Bercoff, J., Sandrin, L. & Fink, M. Ultrafast compound imaging for 2-D motion vector estimation: Application to transient elastography. *IEEE Trans. Ultrason. Ferroelectr. Freq. Control* **49,** 1363–1374 (2002).

290. Montaldo, G., Tanter, M., Bercoff, J., Benech, N. & Fink, M. Coherent plane-wave compounding for very high frame rate ultrasonography and transient elastography. *IEEE Trans. Ultrason. Ferroelectr. Freq. Control* **56,** 489–506 (2009).

291. Arnal, B. *et al.* Photoacoustics Sono-photoacoustic imaging of gold nanoemulsions : Part I . Exposure thresholds. *Biochem. Pharmacol.* 1–8 (2015). doi:10.1016/j.pacs.2014.12.001

292. Zhang, P. & Porter, T. An in vitro study of a phase-shift nanoemulsion: a potential nucleation agent for bubble-enhanced HIFU tumor ablation. *Ultrasound Med. Biol.* **36,** 1856–66 (2010).

293. Sheeran, P. S., Luois, S. H., Mullin, L. B., Matsunaga, T. O. & Dayton, P. A. Design of ultrasonically-activatable nanoparticles using low boiling point perfluorocarbons. *Biomaterials* **33,** 3262–9 (2012).

294. Kripfgans, O. D., Fowlkes, J. B., Woydt, M., Eldevik, O. P. & Carson, P. L. In vivo droplet vaporization for occlusion therapy and phase aberration correction. *IEEE Trans. Ultrason. Ferroelectr. Freq. Control* **49,** 726–38 (2002).

295. Schad, K. C. & Hynynen, K. In vitro characterization of perfluorocarbon droplets for focused ultrasound therapy. *Phys. Med. Biol.* **55,** 4933–47 (2010).

296. Wang, L., Jacques, S. L. & Zheng, L. MCML--Monte Carlo modeling of light transport in multi-layered tissues. *Comput. Methods Programs Biomed.* **47,** 131–146 (1995).

297. Wu, T., Farny, C. H., Roy, R. A. & Holt, R. G. Modeling cavitation nucleation from laser-illuminated nanoparticles subjected to acoustic stress. *The Journal of the Acoustical Society of America* **130,** 3252 (2011).

298. Sheeran, P. S. *et al.* Decafluorobutane as a phase-change contrast agent for low-energy extravascular ultrasonic imaging. *Ultrasound Med. Biol.* **37,** 1518–30 (2011).

APPENDIX A

Supplementary Information Chapter 4, Tables

The tables below summarize the characterization of the parameter space in Chapter 4.

Table 11. Measured p+ of the flat tip, H mode, as a function of energy and tip diameter.

	Pressure (MPa), Depth Corrected, H Mode							
Tip →	**200µm Flat**				**300µm Flat**			
Energy (mJ)	**Primary Pulse**	**First Collapse**	**Second Collapse**	**Third Collapse**	**Primary Pulse**	**First Collapse**	**Second Collapse**	**Third Collapse**
20	0.065	0.071	0.0223	0.0056	0.1245	0.1095	0.1444	0.0215
50					0.1245	0.1095	0.1444	0.0215
100	0.1032	0.7172	0.2521	0.056	0.2634	0.5888	0.3059	0.1147
150					0.1883	0.8856	0.3339	0.0921
200	0.7344	0.7069	0.6725	0.1715	0.1867	1.2108	0.4394	0.1106
250					0.1974	1.354	0.464	0.1134
300					0.2838	1.4732	0.6796	0.1273
350								
400								

Table 12. Measured p+ of the tapered tip, H mode, as a function of energy and tip diameter.

	Pressure (MPa), Depth Corrected, H Mode											
Tip →	**200µm Tapered**				**300µm Tapered**				**400µm Tapered**			
Energy (mJ)	**Primary Pulse**	**First Collapse**	**Second Collapse**	**Third Collapse**	**Primary Pulse**	**First Collapse**	**Second Collapse**	**Third Collapse**	**Primary Pulse**	**First Collapse**	**Second Collapse**	**Third Collapse**
20	0.1244	0.136	0.039	0.0097	0.0908	0.0272	0.0734	0.0025	0.0473	0.1214	0.0505	0.0036
50	0.2005	0.1163	0.2951	0.0315	0.1345	0.2571	0.4373	0.0476	0.1071	0.3601	0.3509	0.0521
100	0.2128	0.1567	0.7063	0.1643	0.2021	0.3147	0.7359	0.1435	0.1378	0.5283	0.4718	0.2435
150	0.2524	0.1895	0.9737	0.3145	0.2758	0.3334	0.9602	0.2841	0.2038	0.4753	0.8851	0.3037
200	0.4529	0.9496	1.3248	0.4133	0.1744	0.4382	1.0556	0.3496	0.1296	0.7021	1.0617	0.2939
250					0.2304	0.4976	0.9747	0.4151	0.2359	0.8783	1.0432	0.4686
300					0.2614	0.5787	1.2531	0.3628	0.1971	0.9428	1.2799	0.3719
350									0.2959	0.8804	1.2865	0.5041
400									0.3105	1.0794	1.3857	0.6772

Table 13. Measured p+ of the 300 µm tip, S mode, as a function of energy and tip geometry.

	Pressure (MPa), Depth Corrected, S Mode							
Tip →	**300µm Flat**				**300µm Tapered**			
Energy (mJ)	**Primary Pulse**	**First Collapse**	**Second Collapse**	**Third Collapse**	**Primary Pulse**	**First Collapse**	**Second Collapse**	**Third Collapse**
20	0.0072	0.0057	0.0019	0.0018	0.0112	0.0154		
50	0.0096	0.0097	0.0012	0.0012				
100	0.0112	0.0478	0.0573	0.0397	0.0185	0.0022		
150	0.0054	0.0611	0.068	0.0331				
200	0.0114	0.0747	0.068	0.0627	0.0093	0.0029		
250	0.0074	0.1065	0.0979	0.0432				
300	0.0113	0.0536	0.129	0.1064	0.0083	0.0024		

Table 14. Primary and rebound bubble radius measured for all tips, energies, pulse modes and device settings.

	Max Radius (mm) H Mode *(Flat (F), Tapered (T))*										**Max R (mm) S Mode**	
Tip →	**200µm F**	**200µm F**	**300µm F**	**300µm F**	**200µm T**	**200µm T**	**300µm T**	**300µm T**	**400µm T**	**400µm T**	**300µm F**	**300 µm T**
Energy (mJ)	Primary Bubble	Rebound Bubble	Primary Bubble	Rebound Bubble	Primary Bubble	Rebound Bubble	Primary Bubble	Rebound Bubble	Primary Bubble	Rebound Bubble	Primary Bubble	Primary Bubble
20	0.55	0.26	0.4	0.06	0.8	0.27	0.63	0.47	0.69	0.6	0.1	0.13
50			0.675	0.34	1.34	0.62	1.21	0.75	1.21	0.79	0.48	
100	1.16	0.63	1.14	0.6	2.1	0.97	1.93	1.04	1.78	1.05	0.75	1.032
150			1.35	0.75	2.61	1.17	2.42	1.25	2.18	1.206	0.77	
200	2	1.04	1.8	0.94	3.16	1.64	3.01	1.58	2.51	1.375	0.81	1.56
250			1.87	0.941			3.04	1.6	2.77	1.51	0.91	
300			2.17	1.07			3.28	1.78	3.02	1.7	1.03	1.91
350									3.22	1.82		
400									3.4	2		

APPENDIX B

Manufacturing Custom Lipid and Protein Shell Microbubbles

Fabrication and Characterization of homemade lipid-shelled and protein-shelled microbubbles: Here, custom made UCA (protein shelled and lipid shelled) protocols are discussed, and their characterization is presented.

Lipid Shelled “Definity-like” Protocol:

Materials: Nitrogen, Perfluropropane gas, MPEG 5000 DPPE,DPPA, DPPC, Chloroform, Propylene Glycol, Glycerin, Sodium Phosphate Monobasic Monohydrate

Sodium Phosphate Dibasic Heptahydrate, Sodium Chloride, Fume Hood, Bath Sonicator 1.5 mL amber vials with open cap and resealing septum, 18.5 gauge needles (or lower gauge), 23.5 gauge needles, Flasks for storing stocks, Chloroform-proof vials for storing chloroform stocks.

1. Prepare the stock solutions of Propylene Glycol, Glycerine, and both Sodium Phosphates. Their final concentrations in the 1 mL pipetted into the tubes should be as follows: Propylene Glycol- 103.5 mg/mL, Glycerin-126.2 mg/mL, Sodium Phosphate Monobasic- 2.34 mg/mL, Sodium Phosphate Dibasic- 2.16 mg/mL, Sodium Chloride -4.77 mg/mL. The combined aqueous solution should also have these concentrations

2. Combine stocks into single, aqueous solution.

3. Create stock solutions for each of the lipids in chloroform.

The final concentration of each lipid in the amber vial should be as follows:
-MPEG 5000 DPPE: .304 mg/mL
-DPPA: .045 mg/mL
-DPPC: .401 mg/mL

4. Under the fume hood, place 20 µL of each chloroform/lipid solutions into each vial being created. Once there is 60 µL of lipid solution in each vial, use a gassing apparatus to flow nitrogen over the vials in order to evaporate chloroform. Gas the vials for 45 minutes with a gentle stream.

5. When finished flowing the nitrogen over the vials, place the vials in the desiccator and vacuum them in order to further ensure no residual chloroform remains. Vacuum the vials for at least three hours, preferably overnight.

6. Filter 100 mL of the aqueous working solution through a .45 µm filter in order to purify it. Store the rest of the working solution, labeled, so that it can be used in the future. Once it has

been filtered and capped, it does not need to be refiltered unless it is left uncapped for long periods of time.

7. Once the vials have been vacuumed, add 1 mL of aqueous solution to each vial, cap them (with a septum) and place them in the bath sonicator. The water in the sonicator should be prepared so that it is 60 degrees C. Run the sonicator for ten minutes or until there are no visible chunks of lipids in the solution.

8. Fit the vials to a gassing apparatus attached with a three-way valve to vacuum and perfluropropane gas. Turn the vacuum and perfluropropane on, and set the valve so that the vacuum is flowing to the vials. After three seconds, switch the valve so that the gas is flowing gently into the vials. After three seconds, turn the switch back to vacuum and repeat this procedure three to four times.

9. Once the perfluropropane has been added, seal the vials' caps further with parafilm and store in the refrigerator until they are to be used.

10. Once the vials are to be used, place them in a vialmix and shake for 45 seconds**.** Place the vials on ice for a short amount of time before and during use in order to compensate for mechanical heating caused by the vialmix. While using vials, draw bubbles out with a 18.5 gauge needle and inject perfluropropane (compensate for loss of volume by replacing with gas in the headspace) with a 23.5 gauge needle.

Protein Shelled protocol:

Materials: Tris buffer (tris(hydroxymethyl)amino methane), lysozyme from hen egg white, DL-dithiothreitol (DTT), were purchased from Sigma–Aldrich (USA). Milli-Q filtered water (18 MΩ cm−1) was used to prepare all solutions. Materials needed: Lysozyme, DL Dithiothreitol, Tris, hydroxylmethyl,DI water, and a pH meter.

1. Make Tris buffer. Solution should have concentration of 30 mM or .03 Molar. Once the buffer has been created, its pH should be tested. If the buffer's pH is 8-8.2, it doesn't need to be adjusted. If it is above 8.2 pH, use HCl to adjust. If below 8 pH, use NaOH to adjust.

2. In a 15 mL Falcon Tube, combine 1 mL of Tris buffer created in Step 1 with 50 mg of Lysozyme.

3. Add 30 mg of DL-DTT to the solution from the previous step. Stir the solution using a stirring rod for about five minutes in order to denature the proteins.

4. After five minutes, place the beaker of water under the sonicator. Position the falcon tube so that the protein solution rests 1 or 2 cm below the water level (this will help keep it cool while sonicating) and clamp the tube into place. Position the Sonicator so that it rests directly on the

interface between the solution and the air in a way such that it does not touch and will not touch the sides of the falcon tube during sonication.

5. Sonicate for 30 seconds at 40% amplitude (Sonics Vibra Cell, 28kHz, small tip).

6. Once the sonication is complete, remove the tube from the clamp, place tube in a holder, and add DI water until there is approximately 13 mL in the tube. Allow tube to sit at room temperature for 10 minutes so that bubbles rise to the top and the debris sinks to the bottom.

7. After 10 minutes, insert syringe into tube and position the syringe so that it is sitting in the lower layer of debris (which should appear whiter and cloudier than the water above it) and remove 7-8 mL of the solution in order to "wash" the bubbles. When this is completed, refill the tube with DI water and repeat 2-3 more times.

Results:

The main results for testing the ability to manufacture and characterize the agents are sizing studies using a Coulter Multisizer M3 (Beckman Coulter, FL, USA) using a 30 µm aperture. The fabrication and testing process for lipids need 2 days (1 day for overnight lipid drying and then the second day everything can be activated and within 2 or 3 hours of open should be consumed. Typical bubble size distribution for protein and lipid -shelled bubbles are shown in Schem 1 below.

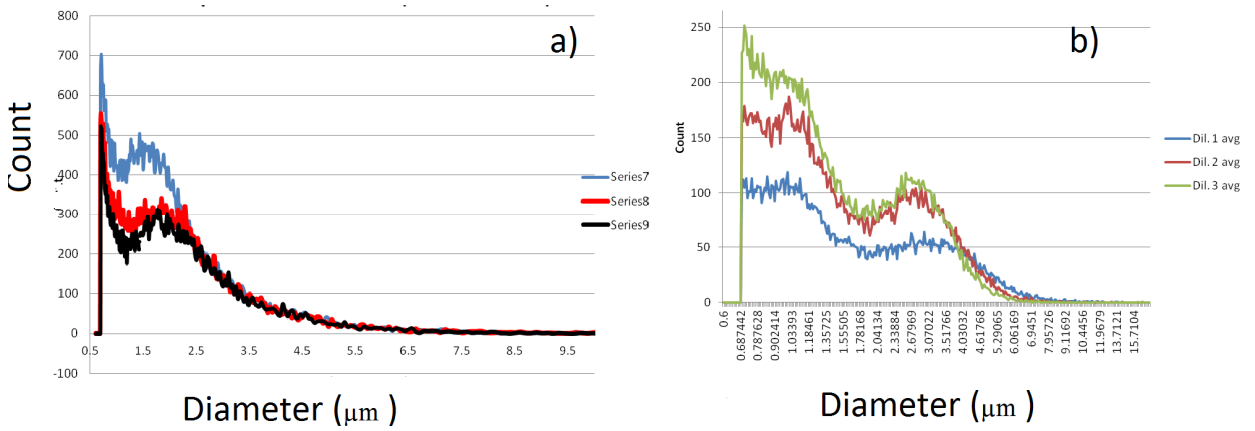

Schem A1. Lipid bubble size distribution (definity recipe, a) and Lyzozyme-protiein shelled microbubbles typical size distribution (b).

Two kinds of stability analysis for lipid microbubbles were performed. The first test (#1) by stirring a 200mL solution of diluted MB (~100,000/mL) using Coulter Stirring setup (speed setting 2) where the MBs where diluted in Isoton II solution (air saturated). The dilution used in test 1 was 30µL in 20mL of ISOTON II. Coulter sizing occurred every 5 minutes for one hour. Schem A2 (a) shows what happens to the same population of MBs in an air saturated saline solution over time. The next stability study (test #2) assessed the change in population and size

of the custom made MB inside the vial after drawing 30µL aliquots at a given time. The results of this repeated sampling stability over time are shown in Schem A2 (b).

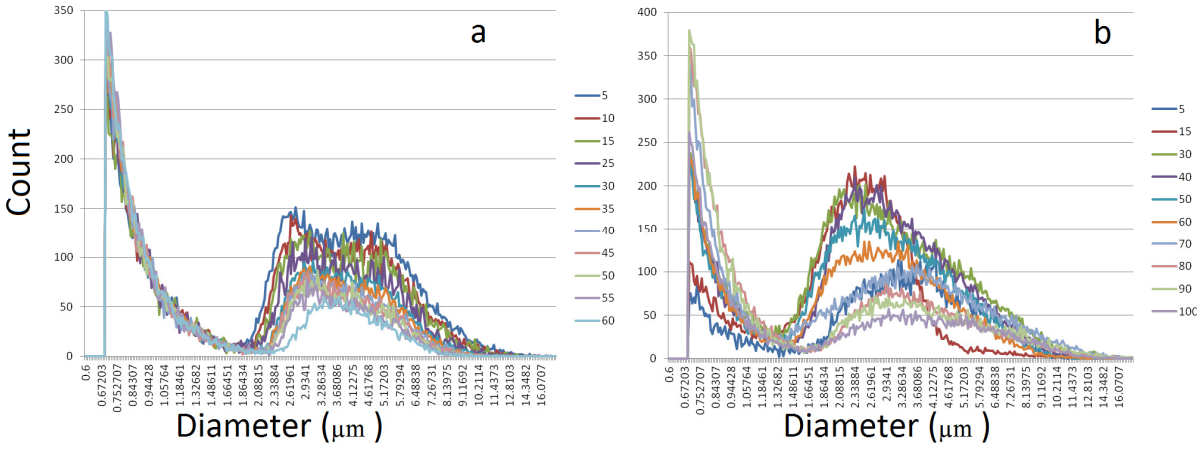

Schem A2. Sizing bubbles as a function of time. Stability test # 1 (a) and stability test # 2 (b).

Finally the stability of the contrast agent Optison is displayed in Schem A3 for comparison to the stability tests #1 and # 2 shown in Schem A2. For both panels shown in Schem A3, the concentration of the agent remains ½ of the initial concentration after 35 minutes, consistent with the custom made MBs shown in Schem A2.

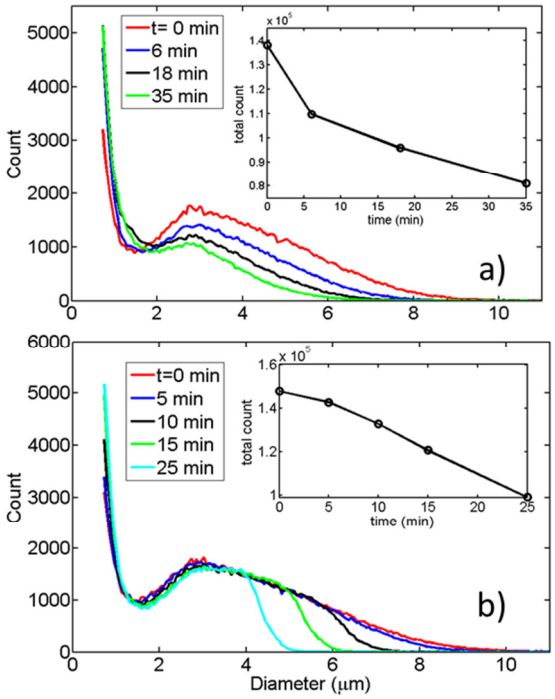

Schem A3. Sizing bubbles as a function of time. Stability test # 1 (a) and stability test # 2 (b).

APPENDIX C

Chemical Structure for Lipid Formulations Used in Chapter 6.4

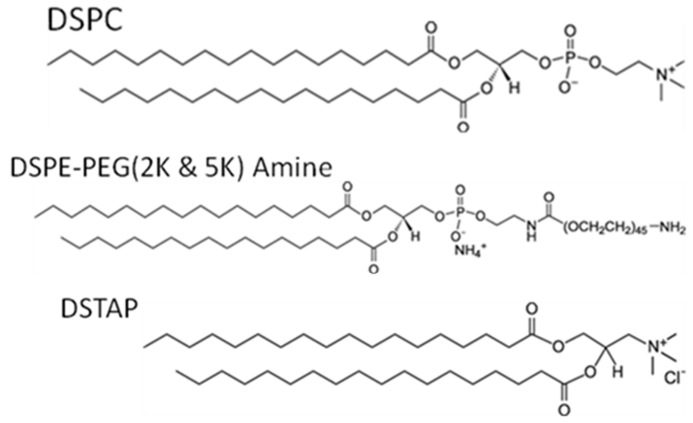

Slightly Cationic (SCat) MBs: 9 DSPC : 1 DSPE-PEG2000 Amine

Cationic (Cat) MBs: 7 DSPC : 2 DSTAP : 1 DSPE-PEG2000 Amine

VITA

Education

U. of Washington*, PhD. in Bioengineering* *Seattle, WA* (10/2010 – Present)
THESIS: *Characterizing ultrasound pressure fields, microbubbles & their interaction.*
Advisors: Dr. Thomas J Matula and Dr. Lawrence Crum.
University of Delaware, ***BSc. Electrical Engineering*** *Newark, DE* (08/2006 – 06/2010)
Minors: Mathematics and Bioelectrical engineering.
La Quinta Del Puente HS, ***High School Diploma, Honors*** *Bucaramanga, Colombia* (01/1996 – 06-2006) ORIGINAL DEGREE: *Bachiller Académico con énfasis en Ciencias & Multimedia*.

Selected Patents & Inventions:

CAMILO, P. 2014 SYSTEMS, DEVICES, AND METHODS FOR SEPARATING, CONCENTRATING, AND/OR DIFFERENTIATING BETWEEN CELLS FROM A CELL SAMPLE. US 14/254,611 FILED 4/16/2014. PENDING.
CAMILO, P. 2014 TECH 47247 – "DELIVERY OF VOLATILE ANESTHETICS WITH MICROBUBBLES" AND STAGE = TECHNOLOGY EVALUATION, INNOVATION STAGE.

PUBLISHED JOURNAL ARTICLES:

1. **C. Perez,** H. Chen, T. J. Matula, M. Karzova, and V. A. Khokhlova, "Acoustic field characterization of the Duolith: measurements and modeling of a clinical shock wave therapy device.," *J. Acoust. Soc. Am.*, vol. 134, no. 2, pp. 1663–74, 2013
2. F. Cavalieri, J. P. Best, **C. Perez**, J. Tu, F. Caruso, T. J. Matula, and M. Ashokkumar, "Mechanical characterization of ultrasonically synthesized microbubble shells by flow cytometry and AFM," *ACS Appl. Mater. Interfaces*, vol. 5, pp. 10920–10925, 2013
3. C. Wei, J. Xia, M. Lombardo, **C. Perez**, B. Arnal, K. Larson-Smith, I. Pelivanov, T. Matula, L. Pozzo, and M. O'Donnell, "Laser-induced cavitation in nanoemulsion with gold nanospheres for blood clot disruption: in vitro results," *Opt. Lett.*, vol. 39, no. 9, pp. 2599–2602, 2014.
4. C. W. Wei, M. Lombardo, K. Larson-Smith, I. Pelivanov, **C. Perez**, J. Xia, T. Matula, D. Pozzo, and M. O'Donnell, "Nonlinear contrast enhancement in photoacoustic molecular imaging with gold nanosphere encapsulated nanoemulsions," *Appl. Phys. Lett.*, vol. 104, no. 3, pp. 1–4, 2014.
5. B. Nazer, F. Ghahghaie, R. Kashima, T. Khokhlova, **C. Perez**, L. Crum, T. Matula, and A. Hata, "Therapeutic Ultrasound Promotes Reperfusion and Angiogenesis in a Rat Model of Peripheral Arterial Disease," *Circ. J.*, 2015
6. B. Arnal, C. Wei, **C. Perez**, T. Nguyen, M. Lombardo, I. Pelivanov, L. D. Pozzo, and M. O. Donnell, "Photoacoustics Sono-photoacoustic imaging of gold nanoemulsions : Part II . Real time imaging," *Biochem. Pharmacol.*, pp. 1–9, 2015.
7. B. Arnal, **C. Perez**, C. Wei, J. Xia, M. Lombardo, I. Pelivanov, T. J. Matula, L. D. Pozzo, and M. O. Donnell, "Photoacoustics Sono-photoacoustic imaging of gold nanoemulsions : Part I . Exposure thresholds," Biochem. Pharmacol., pp. 1–8, 2015.

SUMBITTED JOURNAL ARTICLES or IN-PREPARATION:

1. **C. Perez**, C.H. Wang, J. Swalwell, J. Tu, A. Brayman, T. Matula, "Microbubble shell characterization in a flow cytometer using a combined measurement-modeling approach. Part I: transient response.," *Ultrasound in Medicine and Biology, Submitted 07/2015.*
2. **C. Perez**, C.H. Wang, J. Swalwell, J. Tu, A. Brayman, T. Matula, "Microbubble shell characterization in a flow cytometer using a combined measurement-modeling approach; 2: Steady state response.," *Ultrasound in Medicine and Biology, Submitted 08/2015.*
3. **C. Perez**, Y-N. Wang, W. Kreider, T. J. Matula, A. Sivriver, V. Netchitailo, D. Boutoussov, "Acoustic field characterization of a commercial dental laser (Waterlase iPlus:) for orthodontics and periodontics.," *J. Acoust. Soc. Am, In preparation.*
4. **C. Perez**, Y. Zhong, K. Tan, S. Pun, M. Bruce ,T Matula, "Ultrasound-activated flow cytometry to detect small changes in the shell of lipid and protein ultrasound contrast agents .," *Ultrasound in Medicine and Biology, In preparation.*

SELECTED CONFERENCE PAPERS AND ORAL PRESENTATIONS (+10):

1. Acoustical Society of America (ASA), Biomedical Acoustics 2 Oral Talks. *Indianapolis, IN* (08/29/2014) Title: Characterization of the Waterlase II: A clinical dental laser & Characterization of the steady state acoustic field of an acoustic flow cytometer: Measurement & model approach.
2. Biomedical Engineering Society (BMES), Oral talk and proceedings *Seattle, WA* (05/26/2013) The transient acoustic field of an acoustic flow cytometer: Measurement and modeling approach.
3. International Congress on Acoustics, Oral talk, proceedings & poster. *Montreal, Canada* (06/16/2013) Title: Characterization of the acoustic field of an acoustic flow cytometer.
4. Acoustical Society of America (ASA), Biomedical & Physical Acoustics Talks. *Seattle, WA* (05/26/2011) Titles: High speed imaging of shockwave induced dynamics of cavitation bubbles and vessel walls & Characterization of the acoustic field of a clinical electromagnetic shockwave therapy device.

CONFERENCE ORAL PRESENTATIONS AND PROCEEDINGS:

Characterization of the acoustic field of a clinical electromagnetic shockwave therapy device.

Camilo Perez, Hong Chen and Thomas J. Matula J. Acoust. Soc. Am. **129**, 2679 (2011);

Temporal and spatial characteristics of nonlinear acoustic field generated by an extracorporeal shockwave therapy device: Modeling and measurements

Maria Karzova, Vera Khokhlova, Camilo Perez and Thomas Matula J. Acoust. Soc. Am. **133**, 3587 (2013);

High speed imaging of shockwave-induced dynamics of cavitation bubbles and vessel wall. Hong Chen, Camilo Perez, Andrew A. Brayman and Thomas J. Matula J. Acoust. Soc. Am. **129**, 2374 (2011)

Acoustic and optical characterization of ultrasound contrast agents via flow cytometry Camilo Perez, Andrew Brayman, Juan Tu, Jarred Swalwell, Hong Chen and Tom Matula J. Acoust. Soc. Am. **132**, 1906 (2012);

Acoustic and optical characterization of targeted ultrasound contrast agents Camilo Perez, Jarred Swalwell, Juan Tu, Hong Chen, Andrew Brayman and Thomas J. Matula J. Acoust. Soc. Am. **133**, 3261 (2013);

Acoustic field characterization of the Duolith: Measurements and modeling of a clinical shock wave therapy device Camilo Perez, Hong Chen, Thomas J. Matula, Maria Karzova and Vera A. Khokhlova J. Acoust. Soc. Am. **134**, 1663 (2013);

Characterizing the pressure field in a modified flow cytometer quartz flow cell: A combined measurement and model approach to validate the internal pressure Camilo Perez, *et al*. Soc. Am. **136**, 2095 (2014)

Acoustic field characterization of the Waterlase2: Acoustic characterization and high speed photomicrography of a clinical laser generated shock wave therapy device for the treatment of periodontal biofilms in orthodontics and periodontics Camilo Perez, Yak-Nam Wang, Alina Sivriver, Dmitri Boutoussov, Vladimir Netchitailo andThomas J. Matula J. Acoust. Soc. Am. **136**, 2279 (2014);

Characterizing the pressure field in a modified microbubble flow cytometer: Using a laser Doppler vibrometer to validate the internal pressure J. Acoust. Soc. Am. **137**, 2423 (2015);

Additional Experience

Seattle Student Chapter Acoustical Society (SSCASA) Treasurer. *Seattle* (2014 – Present)
Chapter co-founder, and responsible to manage annual budget for acoustics events and outreach.

ASA Student Council Member & College of Fellows' Liaison. *USA* (2014 – Present)
Organize student activities during conferences. Bridge communication between students & fellows.

Grading and Teaching Assistant*, Bioengineering, Univ. of Washington.* Seattle, WA
Topics: Heat Transfer, mechanical testing methods, fluid dynamics and Comsol modeling.

Grants & Scholarships

TA of the year: Outstanding teaching assistant of the year in bioengineering. (2012-2013)
Athletic Scholarship: Recruited athlete for NCAA Men's Tennis Division I. (2006-2010)
R. M. Lewis Award: Selected for personal & professional development at UD. (2008-2009)
Bangalore T. L. Award: Outstanding Engineering student scholarship. (2007-2008)